Alma Mater Studiorum – Università di Bologna
in cotutela con
Ecole Nationale Supérieure de Chimie de Montpellier

DOTTORATO DI RICERCA IN

CHIMICA

Ciclo XXIX

Settore Concorsuale di afferenza: **03/C2**

Settore Scientifico disciplinare: **CHIM/04**

CHEMICAL-LOOP APPROACH IN BIO-ALCOHOLS REFORMING

Presentata da: **Olena Vozniuk**

Coordinatore Dottorato   Relatore

Chiar.mo Prof. Aldo Roda   **Prof. Fabrizio Cavani**

                                                                     Relatore

                                       Prof. Francesco Di Renzo

Esame finale anno 2017

Chemical-Loop Reforming

Water Splitting

Hydrogen production

Spinel oxides

Mössbauer spectroscopy

Magnetic measurements

TPR/O

in-situ XPS

in-situ DRIFTS

TABLE OF CONTENTS

ABSTRACT

Nowadays, hydrogen production is mainly based on the reforming of natural gas or naphtha. Less energy intensive and more sustainable processes for hydrogen production are appealing for both industry and consumer applications. Chemical-loop steam reforming is one of the possible ways to produce H_2 starting from either conventional or renewable sources. Differently from classical reforming, separation costs can be avoided by splitting the process into two alternated steps in order to detach H_2 and CO_x streams. One of the advantages of this technology relates to its feedstock flexibility.

This PhD project deals with an investigation of a new process, named as Chemical-Loop Reforming (CLR) process, aimed to produce "*clean H_2*" with an inherent CO_x separation. The main principle of the CLR process is that an oxygen-storage material is first reduced by an ethanol stream (T-450°C) and then re-oxidized by water (T-450°C) to produce hydrogen and to restore the original oxidation state of the looping-material. The choice of ethanol as a reducing agent has several advantages: its renewable origin together with the possibility to decompose at a relatively lower temperature with a formation of the hydrogen-rich mixture.

Different M-modified spinel-type mixed oxides: TYPE I — MFe_2O_4 and TYPE II — $M_{0.6}Fe_{2.4}O_y$ viz. modified ferrospinels (where M=Cu, Co, Mn, Mg, Ca and Cu/Co, Cu/Mn, Co/Mn), as potentially attractive ionic oxygen and electron carrier looping materials, were prepared via co-precipitation method and tested in terms of both redox properties and catalytic activity to generate hydrogen by oxidation with steam, after a reductive step carried out with ethanol. Particularly, the focus on the reactivity behavior of binary/ternary materials explained by their ability to form thermodynamically stable spinel oxides which allow us to re-obtain the initial spinel phase upon cycling and in turn increase a stability of the looping material itself. In addition, the research includes in-situ DRIFTS and in-situ XPS studies that allowed to extract information at a molecular level and to follow surface changes within the reduction/re-oxidation processes during ethanol chemical-loop reforming. Bulk characterizations have been done using XRD, TPR/O, TEM/SEM/EDX, Magnetic measurements and Raman/Mössbauer spectroscopic techniques. Moreover, a modification of the conventional CLR process with an addition of the 3rd regeneration step (carried out with air) was done to increase the stability of the looping material and to overcome the deactivation problems, such as: a coke deposition/accumulation and an incomplete re-oxidation of M^0 during the 2nd step; the obtained results are compared to a conventional 2 steps CLR process.

RÉSUMÉ

Aujourd'hui, la production d'hydrogène est basée essentiellement sur le reformage du gaz naturel   ou des essences légères. Des procédés moins énergivores et plus durables pour la production d'hydrogène sont intéressants tant pour des applications industrielles que pour des produits pour grand public. Le reformage à la vapeur par cycle redox est une des voies possibles pour produire de l'H_2 à partir de sources traditionnelles comme de sources. A différence du reformage classique, les coûts de séparation peuvent être évités en séparant le procédé en en deux étapes alternées pour isoler les débits d'H_2 et CO_x. L'un des avantages de cette technologie est lié à sa flexibilité envers les matières premières utilisées.

Le sujet de thèse est l'étude exploratoire d'un nouveau procédé de reformage par cycle redox (CLR : Chemical-Loop Reforming) avec séparation intrinsèque des CO_x, visant la production d'"*H_2 propre*. Le principe essentiel du procédé CLR est basé sur le cycle redox d'un matériau de stockage d'oxygène, qui est d'abord réduit par un flux d'éthanol (T-450°C) et ensuite réoxydé par de la vapeur d'eau (T-450°C) pour produire de l'hydrogène et rétablir l'état d'oxydation initial du matériau à cycle redox. Le choix de l'éthanol comme agent réducteur présente plusieurs avantages, de son origine renouvelable à sa propriété de décomposition à une température relativement basse avec la formation d'un mélange riche en hydrogène.

Les oxydes mixtes de structure spinelle (ferrospinelles modifiées) sont des matériaux potentiellement intéressants pour le cyclage redox d'ions oxygènes et porteurs d'électrons. Plusieurs de ces spinelles M-modifiée de TYPE I – MFe_2O_4 et TYPE II – $M_{0.6}Fe_{2.4}O_y$ M-modifiée de TYPE I – MFe_2O_4 et TYPE II – $M_{0.6}Fe_{2.4}O_y$ avec M=Cu, Co, Mn, Mg, Ca et Cu/Co, Cu/Mn, Co/Mn) ont été préparées par une méthode de coprécipitation et elles ont été évaluées soit de par leurs propriétés redox et leur activité catalytique dans la production d'hydrogène par oxydation par la vapeur d'eau après une étape de réduction à l'éthanol. En particulier, l'attention a été portée sur la réactivité des matériaux binaires/ternaires à cause de leur propriété de former des spinelles thermodynamiquement stables, ce qui nous a permis de réobtenir la phase spinelle initiale après cyclage redox tout en augmentant la stabilité du matériau de cyclage. De plus, l'activité de recherché a inclut des études in-situ, DRIFTS et XPS, qui ont permis d'obtenir des informations au niveau moléculaire et de suivre les modifications de surface du matériau au cours des étapes de réduction et réoxydation pendant le reformage de l'éthanol par cyclage redox. Les matériaux ont été caractérisés par DRX, TPR/O, MET/MEB/EDX, mesures magnétiques et techniques spectroscopiques Raman/Mössbauer. De plus, une modification du procédé CLR conventionnel avec l'addition d'une troisième étape de régénération à l'air a permis d'augmenter la stabilité du matériau de cyclage redox et de surmonter les problèmes de désactivation, tels que le dépôt/accumulation de coke et la réoxydation incomplète de M^0 pendant l'étape de réoxydation à la vapeur d'eau. Les résultats obtenus ont été comparées à un procédé CLR conventionnel à deux étapes.

OBJECTIFS DU PROJET DE RECHERCHE

Le travail de recherché présenté ici est étude sur un nouveau procédé de reformage par cyclage redox (Chemical-Loop Reforming: CLR) pour produire de l'"*H₂ propre*" avec une séparation intrinsèque des *CO$_x$*. Le principe de base du procédé CLR est le cyclage d'un matériau de stockage d'oxygène, qui est d'abord réduit par un flux d'éthanol (T-450°C) et ensuite réoxydé par de la vapeur d'eau (T-450°C) pour produire de l'hydrogène et rétablir l'état d'oxydation initial du matériau de cyclage (Figure 1).
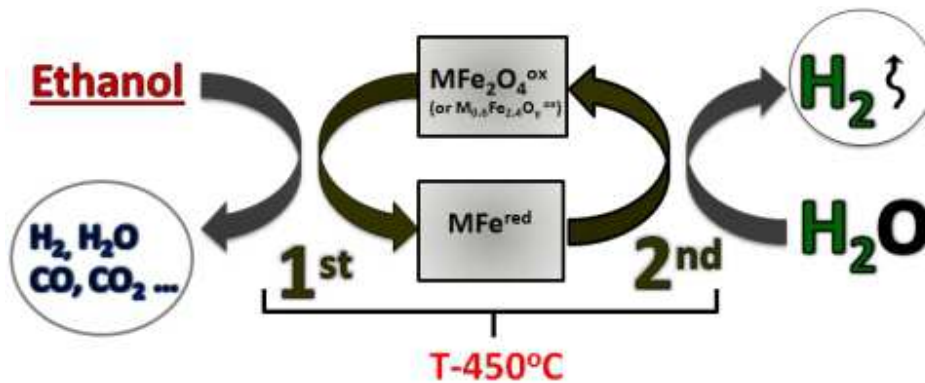
Figure 1. Reformage par cyclage redox de l'éthanol sur ferrospinelles modifiées

Le choix de l'éthanol comme agent réducteur présente plusieurs:

- L'éthanol peut être obtenu à partir de biomasse, ce qui peut contribuer à développer la production d'hydrogène à partir de matières premières différentes des combustibles fossiles;
- L'éthanol est un liquide non toxique, facile à transporter et manipuler, assez stable à température ambiante, bien adapté pour des usages dans des produits pour le grand public;
- L'utilisation de bioalcohol en reformage par cycle redox a jusqu'à présent attiré peu d'attention dans la littérature;

La tâche initiale du projet a été la définition des conditions et matériaux adaptés pour l'obtention d'un procédé optimise pour la production d'un flux d'hydrogène qui ne demande aucune opération de séparation ou purification supplémentaire. Par conséquent, plusieurs oxydes mixtes de type spinelle M-modifiées (TYPE I – *MFe₂O₄* et TYPE II – *M$_{0.6}$Fe$_{2.4}$O$_y$*) ont été synthétisés et testés comme matériaux de cyclage d'ions oxygènes et porteurs d'électrons dans la génération d'hydrogène par oxydation à la vapeur d'eau après une étape de réduction à l'éthanol. Plus spécifiquement, l'attention a été portée sur la réactivité des spinelles secondaires et tertiaires , grâce à leur capacité de former des oxydes thermodynamiquement stables qui pouvaient recouvrer leur phase initiale

après un cyclage redox. La composition de ferrospinelles MFe_2O_4 et $M_{0.6}Fe_{2.4}O_y$ a été variée avec des ions de métaux de transition (Co, Mn, Cu ou Cu/Co, Cu/Mn, Co/Mn) et des ions de métaux alcalinoterreux: Ca, Mg. L'objectif de ces modifications des matériaux a été la recherche d'une sélectivité améliorée pour obtenir des produits valorisables au cours de la première étape de réduction et une plus grande pureté de l'hydrogène produit dans la deuxième étape de réoxydation.

La deuxième tâche a été l'étude de la chimie du procédé, à travers des techniques de caractérisation in-situ et ex-situ et l'étude des propriétés des oxydes mixtes, en terme de propriétés redox, morphologiques et physico-chimiques, en incluant des études de propriétés de chimie de l'état solide des matériaux avant et après cyclage redox.

La recherche a été conduite sur les sites de trois institutions, les détails sur l'organisation du travail étant résumés dans la Figure 2.
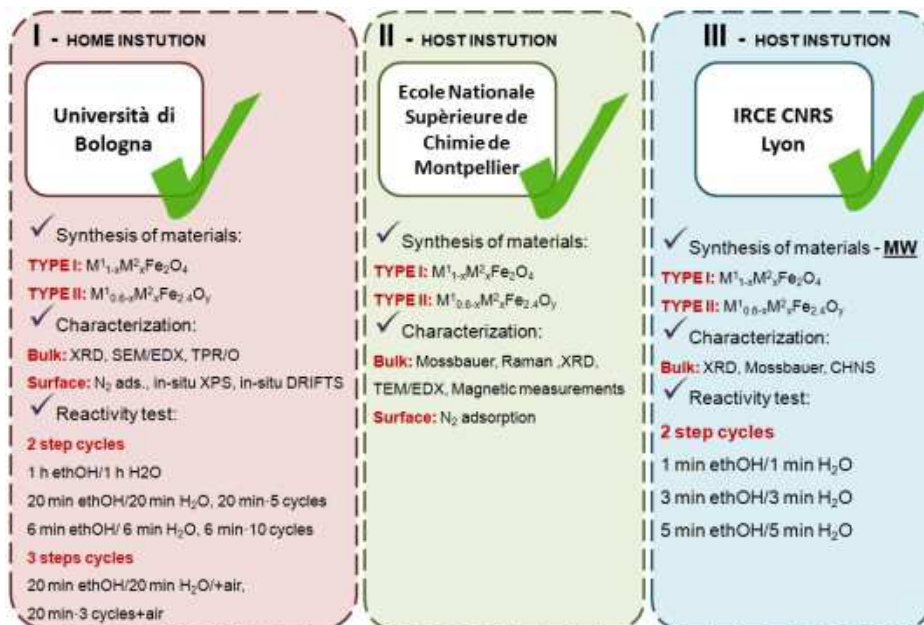
Figure 2. Travail accompli pendant les trois années de recherché doctorale

DIFFRACTION DES RAYONS X ET ADSORPTION DE N_2

La structure des ferrospinelles de TYPE I (MFe_2O_4) et TYPE II ($M_{0.6}Fe_{2.4}O_y$) préparées par coprécipitation a été identifiée par les diffractogrammes de poudres reportés en Figures 3. Les diffractogrammes indiquent la formation de spinelles comme phases principals pour tous les échantillons MFe_2O_4 et $M_{0.6}Fe_{2.4}O_y$. Un clair élargissement des raies de diffraction a été observé préférentiellement pour les ferrospinelles des deux types contenant du manganèse, comme $MnFe_2O_4$, $Cu_{0.5}Mn_{0.5}Fe_2O_4$, $Co_{0.5}Mn_{0.5}Fe_2O_4$ and $Mn_{0.6}Fe_{2.4}O_y$, $Co_{0.3}Mn_{0.3}Fe_{2.4}O_y$, $Cu_{0.3}Mn_{0.3}Fe_{2.4}O_y$,

$Co_{0.54}Mn_{0.06}Fe_{2.4}O_y$. Cet effet a été attribué à une diminution de la taille des particules ou à une baisse de cristallinité. Dans le Tableau 1 sont indiquées les valeurs de surface spécifique (SSA), taille des cristallites (calculée par l'équation de Scherrer ou la méthode de Williamson-hall) et taille des particules des échantillons calcinés à 450°C pour 8 h.

Figure 3. Diffractogrammes de poudres des spinelles MFe_2O_4 (en haut) et $M_{0.6}Fe_{2.4}O_y$ (en bas) calcinées à 450°C en flux d'air pour 8 h

Tableau 1. Surface spécifique (SSA) et taille des cristallites/particules des ferrites MFe_2O_4 and $M_{0.6}Fe_{2.4}O_y$

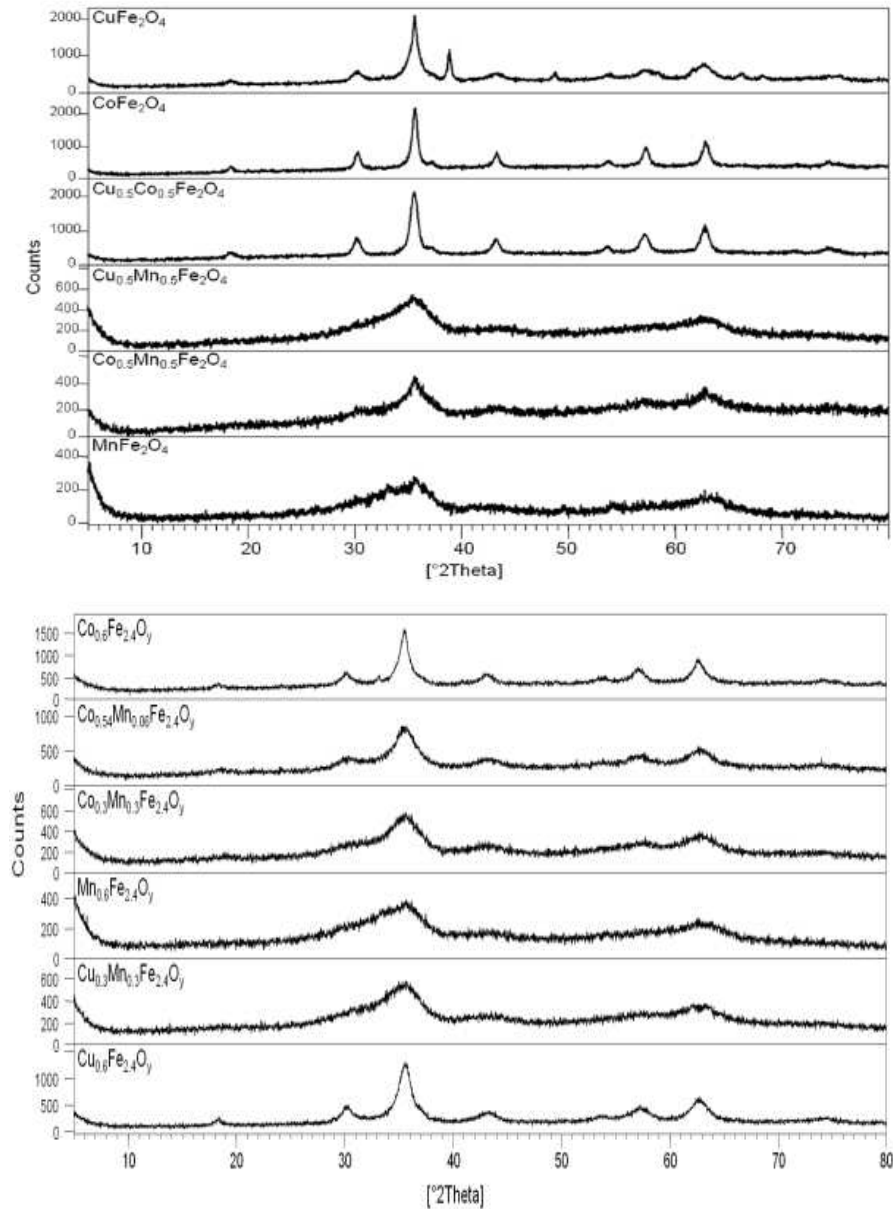| Sample name	SSA $_{fresh}$, m^2/g	Crystallite size (Scherrer eq.) $_{fresh}$, nm	Particle size (d_{BET}), nm
TYPE I: MFe_2O_4			
$CuFe_2O_4$	60	6.9	18.3
$Cu_{0.5}Co_{0.5}Fe_2O_4$	67	10.4	16.5
$CoFe_2O_4$	69	12	16.2
$Co_{0.5}Mn_{0.5}Fe_2O_4$	141	3.5	8
$Cu_{0.5}Mn_{0.5}Fe_2O_4$	112	-	10
$MnFe_2O_4$	165	-	6.9
TYPE II: $M_{0.6}Fe_{2.4}O_y$			
$Co_{0.6}Fe_{2.4}O_y$	71	7	16
$Co_{0.54}Mn_{0.06}Fe_{2.4}O_y$	88	4	13
$Co_{0.3}Mn_{0.3}Fe_{2.4}O_y$	138	3	8
$Mn_{0.6}Fe_{2.4}O_y$	157	-	7
$Cu_{0.3}Mn_{0.3}Fe_{2.4}O_y$	131	-	9
$Cu_{0.6}Fe_{2.4}O_y$	72	5	15

Toutes les ferrites contenant du Mn présentent une surface spécifique plus élevée aussi après traitement thermique. Cet effet peut être attribué d'abord à la présence de plus petites particules ainsi qu'à la présence d'une phase amorphe, en bon accord avec les résultats de diffraction présentés plus haut. Une confirmation ultérieure a été obtenue par la comparaison de la taille des cristallites obtenue par exploitation de la largeur des raies de diffraction avec la taille des particules calculée à partir de la SSA à travers une supposition sur la forme des particules, assumées sphériques et non poreuses pour les besoins du calcul.

REDUCTION À TEMPÉRATURE PROGRAMMÉE (TPR)

La réduction des oxydes de fer[(II,III)] ($Fe_3O_4 \rightarrow FeO \rightarrow Fe$) dépend fortement de la présence d'autres oxydes métalliques dans la ferrite M-modifiée résultante. Selon les résultats de DRX discutés plus haut, la phase principale obtenue au bout de la procédure de préparation est une phase spinelle de type Fe_3O_4 avec une formule générale $MFe_2O_4/M_{0.6}Fe_{2.4}O_y$. Dans les courbes TPR profiles des ferrites

M-modifiées reportées en Figure 4, on reconnaît deux étapes principales du processus de réduction : la réduction de l'oxyde de fer à fer métalliques et le processus propre de réduction de l'autre oxyde métallique incorporé à son métal. Toutefois, il est difficile de séparer les étapes de réduction puisque certaines étapes se fondent sans transition, en se superposant l'une dans l'autre. Néanmoins, les résultats obtenus et leur élaboration ultérieure, basée sur la nature des métaux additionnels (M^{2+}), leurs potentiels de réduction et les quantités d'H_2 consommées, nous ont permis de définir des étapes probables du processus de réduction des MFe_2O_4, étapes qui sont résumées dans la Figure 5.

En considérant le profil TPR profile de $CuFe_2O_4$, le premier pic à 240°C peut être attribué à une réduction rapide de l'oxydes de cuivre présent dans l'échantillon (CuO~$21\%_w$) à cuivre métallique (Cu^0), ce qui conduit à une fraction de consommation d'H_2 α~16%. Le deuxième pic à ~ 340°C a été attribué à la première étape de réduction de la spinelle selon le mécanisme I de Figure 5, avec la formation de phases Cu^0 et Fe_3O_4 (α~27%). La réduction ultérieure de Fe_3O_4 à FeO et FeO à Fe^0 se manifeste à plus haute température jusqu'à α~70%. La réduction des échantillons $Cu_{0.5}Mn_{0.5}Fe_2O_4$ et $Cu_{0.5}Co_{0.5}Fe_2O_4$ suit le mécanisme III de Figure 5, dans lequel le premier pic à basse température correspond à la démixtion par étapes et/ou la réduction des cations M incorporés pour former des phases M (Cu^0), MO (MnO/CoO) et Fe_3O_4.
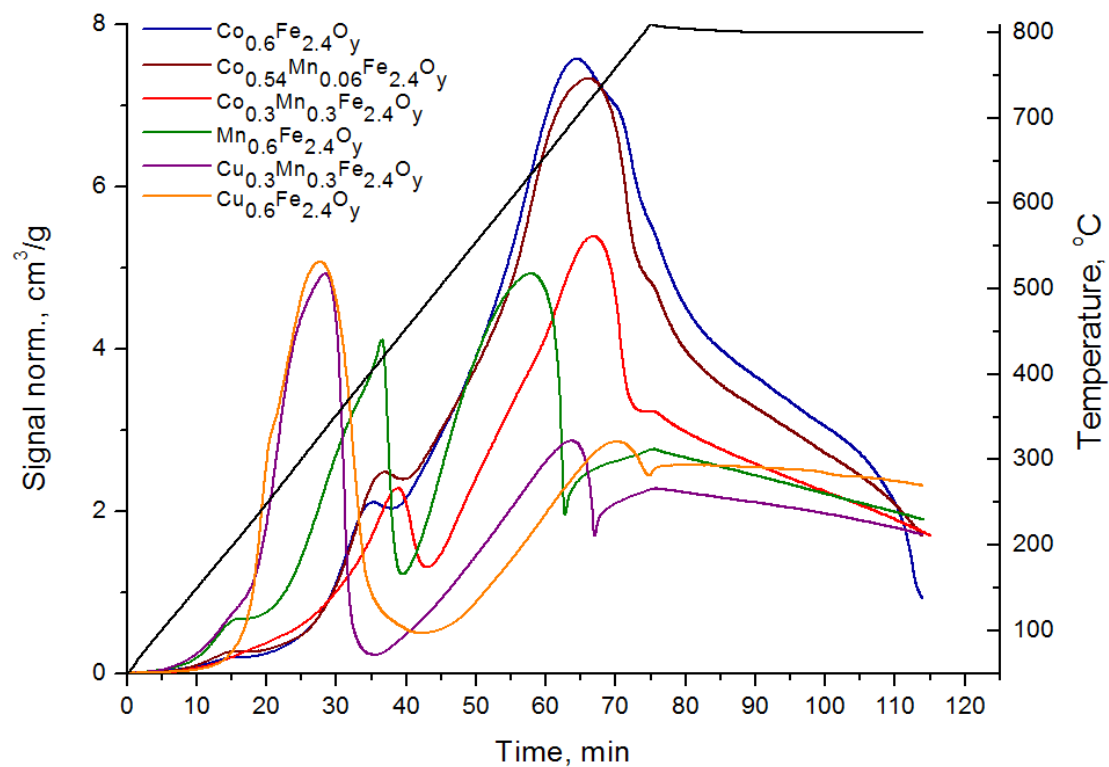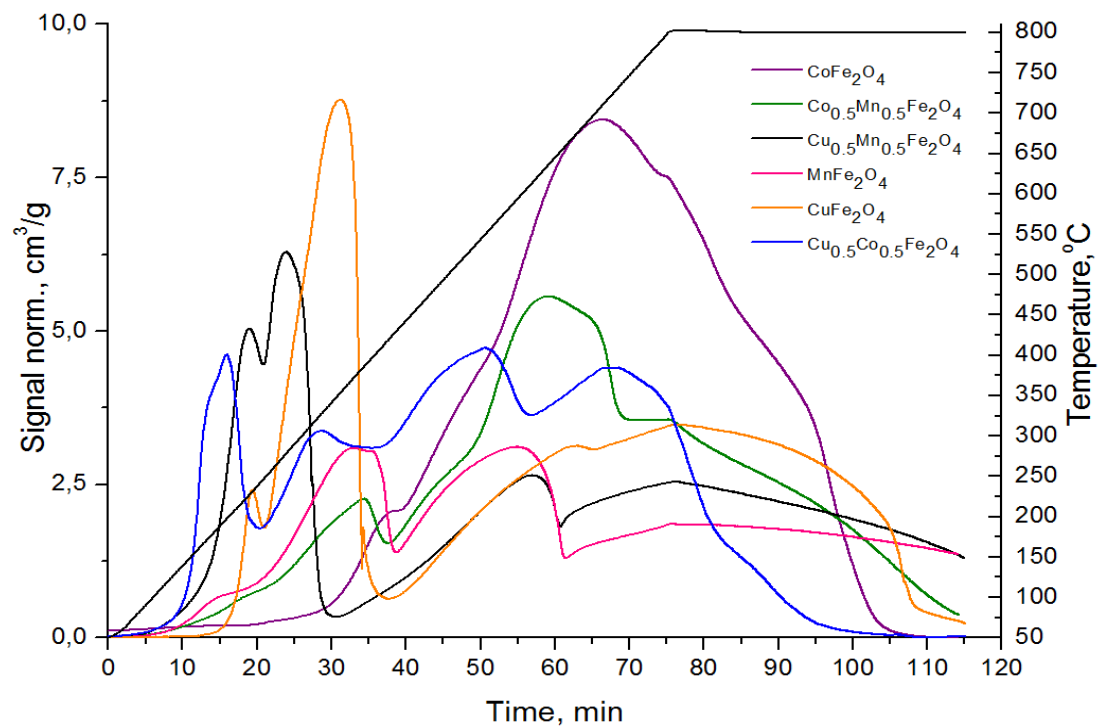
Figure 4. Courbes TPR de ferrites MFe$_2$O$_4$ (en haut) et M$_{0.6}$Fe$_{2.4}$O$_y$ (en bas) avec programmation de température de 50 to 800°C suivie d'une isotherme at 800°C pour 40 min
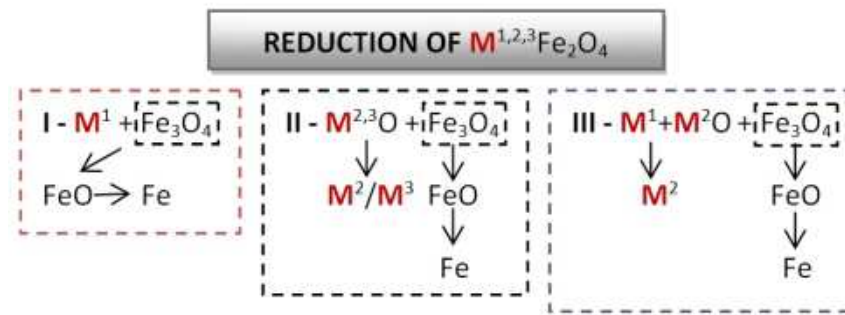
Figure 5. Schéma de réduction des ferrites MFe₂O₄

La réduction ultérieure des ferrites $Cu_{0.5}Co_{0.5}Fe_2O_4$ passe par les étapes suivantes: (1) $Fe_3O_4 \rightarrow FeO$ (+0,77eV), (2) $CoO \rightarrow Co^0$ (-0.28 eV), (3) $FeO \rightarrow Fe^0_{incom}$ (-0.44 eV) et atteint une α~65%. D'autre côté, la deuxième phase de réduction des ferrites $Cu_{0.5}Mn_{0.5}Fe_2O_4$ peut être ainsi schématisée: (1) $Fe_3O_4 \rightarrow FeO$, (2) $FeO \rightarrow Fe^0_{incom}$, ce qui correspond à α~65%. Il en résulte qu'il est difficile de réduire MnO à son correspondant métallique Mn^0, à cause de son potentiel de réduction très négatif (-1.18 eV), donc cette étape peut avoir lieu seulement à des températures très élevées. La réduction des échantillons $CoFe_2O_4$, $Co_{0.5}Mn_{0.5}Fe_2O_4$ et $MnFe_2O_4$ suit le mécanisme II de Figure 5. Dans le cas de $CoFe_2O_4$, le premier petit pic à 400^oC peut être attribué à la réduction initiale de la spinelle avec une étape de formation de phases CoO et Fe_3O_4 (correspondant à α~8%), tandis que dans les ferrites contenant du manganèse ($MnFe_2O_4$ et $Co_{0.5}Mn_{0.5}Fe_2O_4$) cette étape commence à plus basse température. Cependant, le degré de réduction final de $CoFe_2O_4$ (α~86%) a été bien plus élevé que celui des échantillons $Co_{0.5}Mn_{0.5}Fe_2O_4$ (61%) et $MnFe_2O_4$ (45%), ce qui peut être expliqué par la formation de la phase MnO, difficile à réduire en tant que telle ou sous forme de solution solide Mn_xFe_yO.

Les mécanismes de réduction proposés sur la base des résultats obtenus sur les ferrospinelles de TYPE I (MFe_2O_4), reportés en Figure 5, peuvent être appliqués aux courbes TPR des échantillons de TYPE II ($M_{0.6}Fe_{2.4}O_y$). Un épaulement de réduction à basse température, près de ~200∘C, qui correspond à ~5% de la réduction totale, observé expérimentalement pour les échantillons contenant Co, Co/Mn et Mn, a été attribué à la réduction de $M_{0.57}Fe_{2.28}O_4$ à $M_{0.6}Fe_{2.4}O_4$, engendrée par la présence de lacunes cationiques dans des matériaux suroxydés hautement défectif. On remarque que la présence de fer seulement sous forme de cations Fe^{3+} dans les échantillons initiaux a été confirmée par expériences Mössbauer où les valeurs d'IS (δ) sont dans le domaine typique des espèces Fe^{3+}: 0.31-0.35 mm/s, ce qui implique une suroxydation pour ces échantillons surstoechiométriques en fer. La réduction ultérieure des échantillons $Co_{0.6}Fe_{2.4}O_y^{(A)}$, $Co_{0.54}Mn_{0.06}Fe_{2.4}O_y^{(B)}$, $Co_{0.3}Mn_{0.3}Fe_{2.4}O_y^{(C)}$ et $Mn_{0.6}Fe_{2.4}O_y^{(D)}$ suit les mêmes étapes des ferrospinelles

TYPE I avec Co, Co/Mn et Mn (mécanisme II en Figure 5). Le premier petit pic à ~400°C a été attribué à la réduction initiale de la spinelle avec formation par étapes de phases CoO et Fe_3O_4 (ou CoO, MnO et Fe_3O_4), ce qui corresponds à un degré d'avancement de la réduction α~8%, tandis que dans la ferrite au manganèse $Mn_{0.6}Fe_{2.4}O_y$, cette étape commence à la plus basse température de ~380°C ($Mn_{0.6}Fe_{2.4}O_4 + 0.2\ H_2$ donne $0.6\ MnO + 0.8\ Fe_3O_4 + 0.2\ H_2O$). De toute façon, les échantillons au cobalt atteignent un degré de réduction significativement plus élevé (α~80[A], 75[B] and 55[C]%) par rapport à l'échantillon au manganèse (α~58[D]%), ce qui a été encore une fois attribué à la formation d'une phase difficilement réductible, sous la forme de MnO ou d'un oxyde mixte Mn_xFe_yO à structure wustite. Dans les courbes TPR des ferrites $Cu_{0.6}Fe_{2.4}O_y$[E] et $Cu_{0.3}Mn_{0.3}Fe_{2.4}O_y$[F], le premier pic à ~350°C a été attribué à la première étape de réduction de la spinelle avec formation finale de phases $Cu^{0[E]}$/Cu^0+MnO[F] et Fe_3O_4, correspondant à α~23[E]/16[F]%), suivant les mécanismes I[E]/III[F] de Figure 5. Les étapes ultérieures de réduction $Fe_3O_4 \rightarrow FeO$ et $FeO \rightarrow Fe^0$ se déroulent à plus haute température avec un degré de réduction global de ~52[E]/46[F]%. Comme expliqué plus haut pour les ferrospinelles avec Co/Mn et Mn, la réduction $MnO \rightarrow Mn^0$ (-1.18 eV) peut avoir lieu seulement à des températures très élevées, ce qui favorise la formation de phases difficilement réductibles MnO/Mn_xFe_yO.

EXPÉRIENCES DE RÉACTIVITÉ SUR FERROSPINELLES TYPE I ET TYPE II

Le choix de conditions de réaction et temps de cycle a été basé sur les études précédents de Cocchi (méthanol comme agent réducteur, T_{red} – 300 et 420°C/T_{re-ox} – 420°C, matériaux de cyclage : Fe_3O_4, $CoFe_2O_4$ et $NiFe_2O_4$) et Trevisanut (éthanol comme agent réducteur, $T_{screen\ red}$ – 400 et 450°C/T_{re-ox} – 450°C, matériau de cyclage: Fe_3O_4, $CoFe_2O_4$ et $NiFe_2O_4$). Il faut remarquer que le but essentiel de l'étape de réduction était de maximiser le niveau de réduction tout en améliorant la reproductibilité des cycles redox en minimisant la désactivation du matériau de cyclage, conséquence d'une accumulation de coke. Ces résultats précédents ont suggéré comme meilleures conditions de réaction une première étape de réduction par l'éthanol à T_{red}-450°C et une deuxième étape de réoxydation par la vapeur d'eau à T_{re-ox}-450°C. Le temps de cyclage a été choisi sur les même bases et a été divisé en cycles longs (durée d'un cycle complet: 1 h $_{red}$/1 h $_{re-ox}$) et cycles courts (durée d'un cycle complet: 20 min $_{red}$/20 min $_{re-ox}$ ou 6 min $_{red}$/6 min $_{re-ox}$). La durée optimisée pour chaque étape a été fixée à 20 minutes par cycle. Cependant, les moles globales d'H_2 formées pendant la deuxième étape ont été comparée à la même durée globale pour des cycles à rythme différent: par exemple 1h (total$\rightarrow$60 min) = 3 cyc·20 min (total$\rightarrow$60 min) = 10 cyc·6 min (total$\rightarrow$60 min). La composition des

ferrospinelles $M_{0.6}Fe_{2.4}O_y$ a aussi été variée en changeant les métaux de transition Co, Mn, Cu ou les métaux alcalinoterreux Ca, Mg. L'objectif de ces modifications a été l'obtention d'une plus grande sélectivité vers des produits valorisables dans la première étape de réduction ainsi qu0une plus grande pureté del'H_2 produit dans la deuxième étape de réoxydation.

Dans la Figure 6 sont résumées les valeurs intégrales de production d'H_2 au cours de l'étape de réduction de l'eau au terme d'un cycle redox complet de 20 minutes sur ferrospinelles MFe_2O_4 et $M_{0.6}Fe_{2.4}O_y$. Pour comprendre les résultats d'un point de vue différent, des données de réactivité importantes sont résumé dans le Tableau 2. Plusieurs éléments sont à mettre en évidence, en prenant comme étalon le premier matériau de cyclage redox proposé - Fe_3O_4:

- Un aspect positif de l'incorporation de manganèse dans les ferrites $MFe_2O_4/M_{0.6}Fe_{2.4}O_y$ est la diminution de la quantité de coke produite, qui tend à s'accumuler pendant la première étape de réduction à l'éthanol, comme montré par les valeurs $C\%_w$ (CHNS) en Table 2;
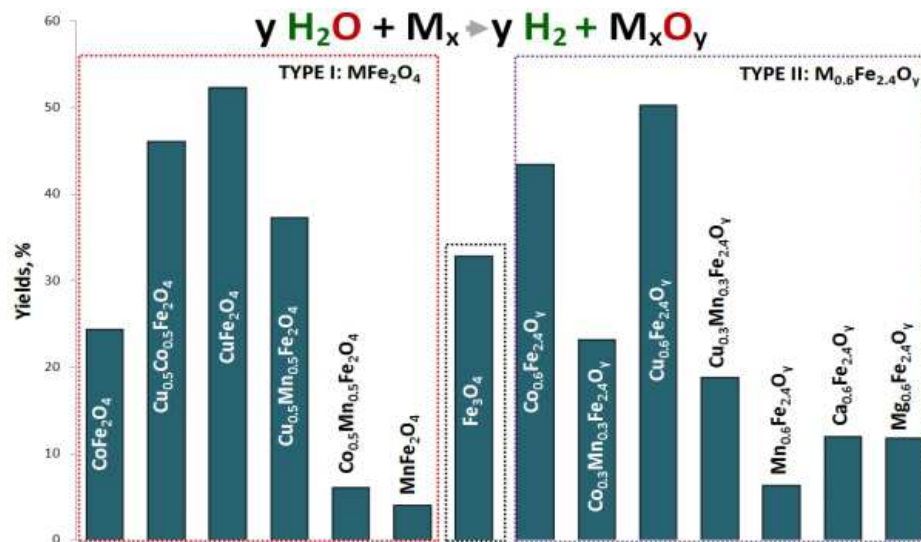
Figure 6. Rendements intégrés de production d'H_2 pendant la deuxième étape (réoxydation àla vapeur d'eau) à 450°C sur ferrospinelles MFe_2O_4 et $M_{0.6}Fe_{2.4}O_y$ (valeurs obtenues au terme d'un cycle redox complet de 20 min)

- Par conséquent, l'incorporation de manganèse augmente le rapport **H_2/CO_x**, (*à remarquer*: plus élevé le rapport **H_2/CO_x**, plus 'pure' est H_2 engendré pendant la deuxième étape de réoxydation). On peut comparer le rapport **$H_2/CO_x=3.5$** sur Fe_3O_4 avec des valeurs **$H_2/CO_x=15$** pour les TYPE I $MnFe_2O_4$ et $Co_{0.5}Mn_{0.5}Fe_2O_4$ et, pour le TYPE II, **$H_2/CO_x=14$** sur $Mn_{0.6}Fe_{2.4}O_y$ et **$H_2/CO_x=7$** sur $Co_{0.3}Mn_{0.3}Fe_{2.4}O_y$. D'autres valeurs **$H_2/CO_x$** sont données au Tableau 2;

- L'incorporation de métaux de transition, comme Cu/Co/Mn, avec le rapport Fe:Cu ou Fe: (-Co,-Mn) étant 2 or 2.4, a des effets bénéfiques sur la quantité totale d'H_2 produit par

réduction de H_2O par rapport à la spinelle Fe_3O_4 non modifiée. Les meilleurs rendements ont été obtenus sur ces ferrospinelles M-modifiées binaires/ternaires: TYPE I - $CuFe_2O_4$ (Y-52%), $Cu_{0.5}Co_{0.5}Fe_2O_4$ (Y-46%), $Cu_{0.5}Mn_{0.5}Fe_2O_4$ (Y-37%) et TYPE II – $Cu_{0.6}Fe_{2.4}O_y$ (Y-50%), $Co_{0.6}Fe_{2.4}O_y$;

Table 2. Paramètres de réactivité de ferrites MFe_2O_4 et $M_{0.6}Fe_{2.4}O_y$ (*valeurs obtenues après un cycle redox complet de 20 min*)

	$C \%_w$ after 20 min red with ethanol	H_2/CO_x	Moles of H_2/Moles of Ethanol (n_{H2}/n_{Eth})
TYPE I: MFe_2O_4			
$CoFe_2O_4$	11.6	6	0.5
$Cu_{0.5}Co_{0.5}Fe_2O_4$	16.3	3	1.0
$CuFe_2O_4$	**6.9**	**3**	**1.2**
$Cu_{0.5}Mn_{0.5}Fe_2O_4$	6.1	3	0.8
$Co_{0.5}Mn_{0.5}Fe_2O_4$	1.5	15	0.1
$MnFe_2O_4$	1.7	15	0.09
REFERENCE MATERIAL			
Fe_3O_4	**5.3**	**3.5**	**0.7**
TYPE II: $M_{0.6}Fe_{2.4}O_y$			
$Co_{0.6}Fe_{2.4}O_y$	**9.7**	**3**	**1.0**
$Co_{0.3}Mn_{0.3}Fe_{2.4}O_y$	7.9	7	0.5
$Cu_{0.6}Fe_{2.4}O_y$	9.8	3	1.1
$Cu_{0.3}Mn_{0.3}Fe_{2.4}O_y$	5.0	4	0.4
$Mn_{0.6}Fe_{2.4}O_y$	2.2	14	0.1
$Ca_{0.6}Fe_{2.4}O_y$	-	3	0.3
$Mg_{0.6}Fe2.4Oy$	-	7	0.3

- L'incorporation de cations Cu/Co- induit une augmentation du rapport n_{H2}/n_{Eth}, comme pour les TYPE I: $CuFe_2O_4$ (n_{H2}/n_{Eth}=1.2), $Cu_{0.5}Co_{0.5}Fe_{2.4}O_y$ (n_{H2}/n_{Eth}=1.0) et les TYPE II: $Cu_{0.6}Fe_{2.4}O_y$ (n_{H2}/n_{Eth}=1.1), $Co_{0.6}Fe_{2.4}O_y$ (n_{H2}/n_{Eth}=1.0).

- On pourrait suggérer une corrélation entre la facilité de former H_2 à partir de bioéthanol et la différence entre les potentiels calorifiques d'H_2 et éthanol (exprimés comme **LHV (Lower Heating Value)**, MJ/kg): **119,96** pour H_2 and **28.86** pour éthanol. En d'autres mots, le rapport n_{H2}/n_{Eth}, élevé permet une efficacité potentielle élevée pour le procédé CLR à partir d'éthanol. Evidemment, il y a beaucoup d'autres éléments qu'il faut prendre en compte pour évaluer e coût réel d'un procédé CLR et pour estimer un prix final raisonnable pour H_2 produit par cette technologie. L'objectif final reste une évaluation comparative de l'intérêt

économique du procédé CLR par rapport aux procédés existants, ce qui n'a pas pu être porté à terme dans la présente étude.

À complément des données d'activité reportées plus haut, une ultérieure comparaison entre ferrospinelles TYPE I and TYPE II est présentée en Figure 7 et Tableau 3, axée sur les quantités d'H_2 produites pendant plusieurs cycles consécutifs (notamment 3 cycles complets de 20 min de réduction et 20 min de réoxydation). On ne présente ici que les données pour les échantillons qui ont donné les meilleurs rendements en hydrogène (voir Figure 6). On peut remarquer que:
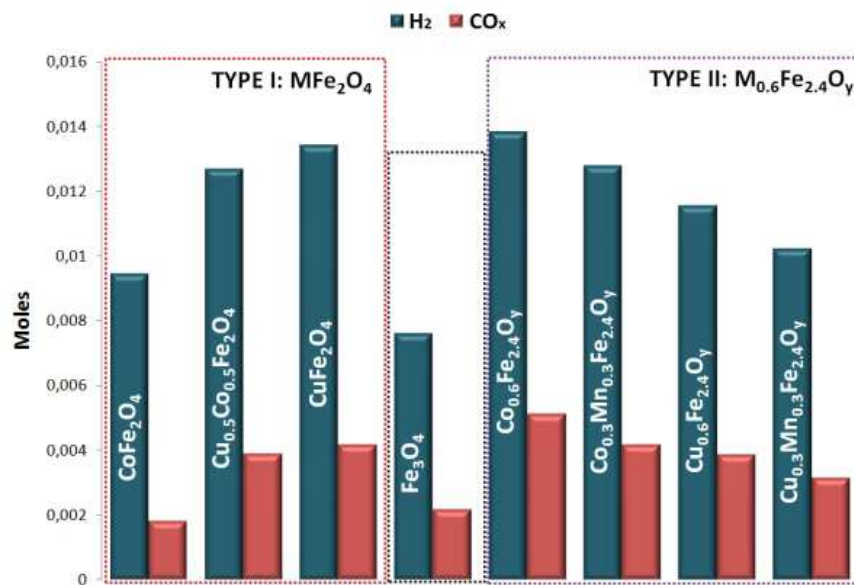

Figure 7. Quantités intégrées de H_2 et CO_x produites pendant les deuxième étapes de réoxydation à la vapeur d'eau à 450°C sur ferrospinelles MFe_2O_4 et $M_{0.6}Fe_{2.4}O_y$ (*note*: valeurs obtenues sur 3 cycles complets à étapes de 20 min)

Tableau 3. Paramètres d'activité calculés pour ferrites MFe_2O_4 et $M_{0.6}Fe_{2.4}O_y$ ferrites (*note*: valeurs obtenues sur 3 cycles complets à étapes de 20 min)

	H_2/CO_x	Moles of H_2/Moles of Ethanol
TYPE I: MFe_2O_4		
$CoFe_2O_4$	5	0.7
$Cu_{0.5}Co_{0.5}Fe_2O_4$	3	0.9
$CuFe_2O_4$	**3**	**1.0**
REFERENCE MATERIAL		
Fe_3O_4	**3**	**0.5**
TYPE II: $M_{0.6}Fe_{2.4}O_y$		
$Co_{0.6}Fe_{2.4}O_y$	**3**	**1.0**
$Co_{0.3}Mn_{0.3}Fe_{2.4}O_y$	3	0.9

Cu$_{0.6}$Fe$_{2.4}$O$_y$	3	0.8
Cu$_{0.3}$Mn$_{0.3}$Fe$_{2.4}$O$_y$	3	0.7

- L'utilisation de ferrospinelles TYPE I: CoFe$_2$O$_4$, CuFe$_2$O$_4$, Cu$_{0.5}$Co$_{0.5}$Fe$_2$O$_4$ et TYPE II: Co$_{0.6}$Fe$_{2.4}$O$_y$, Co$_{0.3}$Mn$_{0.3}$Fe$_{2.4}$O$_y$, Cu$_{0.6}$Fe$_{2.4}$O$_y$, Cu$_{0.3}$Mn$_{0.3}$Fe$_{2.4}$O$_y$, Co$_{0.3}$Mn$_{0.3}$Fe$_{2.4}$O$_y$ comme matériaux de cyclage redox en plusieurs cycles consécutifs conduit à la production d'une quantité d'hydrogène (*exprimée en moles en Figure 7*) bien supérieure à la valeur obtenue sur le matériau de référence Fe$_3$O$_4$ (voir Figure 7);

- L'augmentation du temps total *tos* (il s'agit du temps total des étapes de réduction ou réoxydation) de 20 à 60 min entraîne une forte diminution du rapport **H$_2$/CO$_x$** ratio, avec une diminution conséquente de la pureté du gaz objectif – H$_2$ (*note* : ce problème peut être résolu par un procédé CLR à trois étapes, la troisième étape étant une réoxydation à l'air);

- **CuFe$_2$O$_4$** (à l'intérieur du groupe de matériaux ferrospinelles **TYPE I**) et **Co$_{0.6}$Fe$_{2.4}$O$_y$** (à l'intérieur du groupe de matériaux ferrospinelles **TYPE**) montrent le rapport **n$_{H2}$/n$_{Eth}$** le plus élevé: **1** (en considérant les valeurs intégrées sur 3 cycles consécutifs), ce qui est bien le double de la valeur obtenue sur Fe$_3$O$_4$ (**n$_{H2}$/n$_{Eth}$=0.5**).

CONCLUSIONS

On peut compléter la comparaison entre ferrospinelles substituées TYPE I (MFe$_2$O$_4$, où Fe/M=2/1) et TYPE II (M$_{0.6}$Fe$_{2.4}$O$_y$, où Fe/M=4/1) et le matériau de référence – Fe$_3$O$_4$:

- L'incorporation de métaux (comme Cu, Co, Mn or Cu/Co, Co/Mn, Cu/Mn) modifie profondément les propriétés redox des matériaux ferrospinelles MFe$_2$O$_4$ and M$_{0.6}$Fe$_{2.4}$O$_y$. De plus, la présence de M en plus petite quantité (dans le TYPE II - M$_{0.6}$Fe$_{2.4}$O$_y$ avec Fe/M=4/1) a déjà été suffisante pour observer des effets positifs sur la production de H$_2$ par CLR à deux étapes du bioéthanol par rapport aux résultats obtenus sur Fe$_3$O$_4$ non modifiée. Une ultérieure augmentation de la fraction de M n'apporte aucune amélioration additionnelle aux performances des matériaux (comme pour le TYPE I - MFe$_2$O$_4$ avec Fe/M=2/1 mais, au contraire, montre un effet opposé (comme dans le cas des ferrites CoFe$_2$O$_4$ et Co$_{0.6}$Fe$_{2.4}$O$_y$, où le phénomène est expliqué par la faible tendance du Co^0 à être ré-oxydé avec l'eau comme seul agent oxydant). Ce qui implique que l'utilisation des ferrospinelles de TYPE II - M$_{0.6}$Fe$_{2.4}$O$_y$ comme matériaux porteurs d'oxygène et électrons est la plus attractive pour le CLR du bioethanol à deux étapes, puisque la réoxidation par la vapeur d'eau dans la

deuxième étape conduit à la réoxydation incomplète des composantes métalliques (Co^0 et Cu^0) formées dans l'étape précédente de réduction. On en conclu que plus de Co et Cu sont présents dans le matériau final M-modifié, moins de matériau sera disponible sous sa forme réoxydée pour être réduit dans les cycles successifs.

En conclusion: bien que plusieurs matériaux améliorés de cyclage redox aient été identifies, la compréhension complète de leurs performances et ultérieures études d'optimisation sont nécessaires pour évaluer correctement l'efficacité, l'ingénierie et l'économie du procédé de reformage de l'éthanol par cyclage redox.

1. INTRODUCTION

Current processes for the industrial production of hydrogen are mainly based on the reforming of natural gas/naphtha or coil gasification. Such processes are highly energy demanding. Hence, less energy-intensive and more sustainable technologies, exploiting renewable feedstocks (such as biomass, bio-alcohols and water) and renewable primary energy sources (e.g. sunlight, wind, wave or hydro-power), appear to be very attractive for both industry and consumer applications. A variety of new technologies offering a non-fossil based route for hydrogen production are in a different stage of development, and each offers unique opportunities, benefits and challenges.[1–10]

Chemical-Loop Steam Reforming is one of the possible ways to produce H_2 starting from either conventional or renewable sources. Differently from classical reforming, separation costs can be avoided by splitting the process into two alternated steps in order to detach H_2 and CO_x streams. One of the advantages of this technology relates to its feedstock flexibility. The chemical-loop process can be performed using a number of different reductants, such as gas resulting from coal[11] or biomass[12–14] gasification, light hydrocarbons reforming,[15] methane,[16–18] CH_4/CO_2 and CH_4/H_2 mixture,[18,19] pyrolysis oil,[20,21] methanol[22] and pure H_2 (as a method for H_2 storage).[23,24] Furthermore, the nature of the oxide, used as the ionic oxygen and electron carrier, and the reaction conditions are important parameters since they determine the potential for low costs and high efficiency of this process in order to have a commercial impact.

1.1. Hydrogen applications

Hydrogen is one of the key starting materials used in the chemical industry with an annual worldwide production of about 50 million tonnes. Currently, the largest amount (~95%) of the total manufactured hydrogen is consumed mainly by two industrial segments: the chemical sector, accounting for 65% of the market share (ammonia and methanol synthesis ~63%; liquid hydrocarbons and higher alcohols synthesis ~2%) and the refining sector, which accounts for 30% of the market share (hydrotreating and hydrocracking processes for

obtaining high grade petrochemical products). The other present uses, with ~5% of the total consumption, include the food industry (sorbitol and fat processing), the metallurgical industry (direct reduction of iron ore), the semiconductor industry, and etc (Figure 1-1).

In conclusion, there is a fast-growing need for increased hydrogen production, since H_2 itself may become an important "energy vector" with key applications as a carbon free fuel and as a fuel for hydrogen driven fuel cells for automotive uses. However, there are still several major problems to be overcome before it can be used in this way, including its manufacture, storage and distribution.
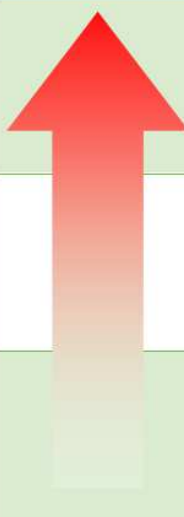
INDUSTRIAL SECTOR	KEY APPLICATIONS	H_2 demand
CHEMICAL ~ 65%	-AMMONIA PRODUCTION (mix. H_2 +N_2) -METHANOL PRODUCTION (mix. H_2+CO)	
REFINING ~ 30%	-HYDROTREATING (S,N,O-removal; olefins and aromatics saturation) - HYDROCRACKING (break C-C bond)	
OTHERS ~ 5%	-FOOD INDUSTRY (hardening of edible oil) -METALLURGICAL INDUSTRY (iron reduction; blanketing gas; forming gas) -SEMICONDUCTOR INDUSTRY, etc.	

Figure 1-1. Main segments of hydrogen consumption

1.1.1. Fuel cells

Fuel cells are devices that generate electricity based on a chemical reaction and are often referred to as continuously operating batteries. They exploit electrolysis reactions in a similar manner to traditional batteries however the reagents are constantly supplied to the cell, which actually and determines its difference compared to the traditional dischargeable batteries. There are several kinds of fuel cells though the main operating principle remains the same: hydrogen atoms at the anode break down to form electrons and H^+ ions (1), the

latter ones migrate through the electrolyte to the cathode (2), where each H^+ ion combines with the oxygen to form water (5) (also emitting heat), while the electrons run through the electrical circuit (4), producing a current (3) (Figure 1-2).
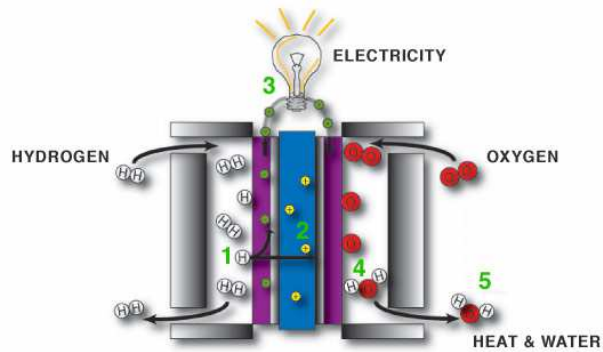

Figure 1-2. General scheme of the fuel cell technology

Nevertheless, its applications can vary depending on the type of hydrogen fed to the anode (they can be chemical elements containing hydrogen) and the nature of the electrolytes (Figure 1-3).
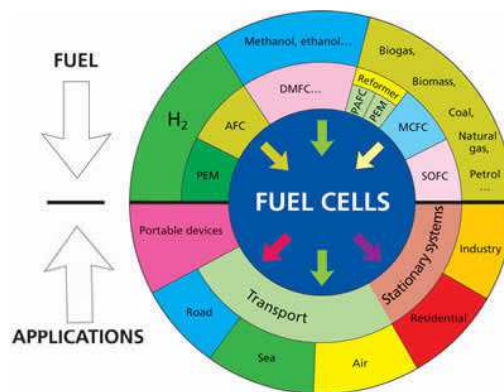

Figure 1-3. Lower segment: main application of the fuel cell technology; Upper segment: fuel and fuel cell types (taken from https://ec.europa.eu):

- AFC: Alkaline (especially in the space sector)
- PEMFC: Polymer Exchange Membrane
- DMFC: Direct Membrane
- PAFC: Phosphoric Acid

- MCFC: Molten Carbonate
- SOFC: Solid Oxide

1.2. Hydrogen production

1.2.1. Common feedstocks

Hydrogen can be produced from different resources including conventional fossil fuels, as natural gas, naphtha and coal, or either using renewable sources such as wind, solar, geothermal, biomass and etc. A variety of new technologies offering a non-fossil based route for hydrogen production are in a different stage of development, and each offers unique opportunities, benefits and challenges. A list of the various feedstocks and process technologies is presented in Figure 1-4.

Figure 1-4. Summary of the various feedstocks and process alternatives for H_2 production

1.2.2. Common processes for H_2 production

Hydrogen can be produced using a number of different processes (as illustrated in Figure 1-5). Thermochemical processes use heat and chemical reactions to release hydrogen from organic materials such as fossil fuels and biomass. Water (H_2O) can be split into hydrogen (H_2) and oxygen (O_2) using electrolysis or solar energy. Microorganisms such as bacteria and algae can produce hydrogen through biological processes. This session encompasses the most relevant information about the existing processes to manufacture hydrogen.
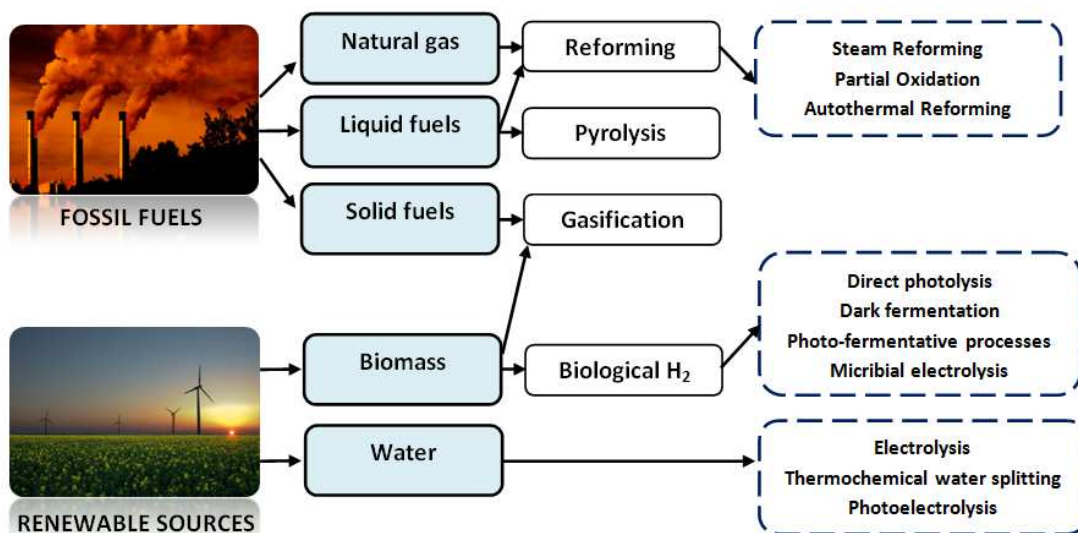

Figure 1-5. An overview of existing hydrogen production processes from different sources

1.2.3. Hydrogen via Reforming Processes

Reforming processes are based on the endothermic or exothermic conversion of the feedstock materials with $H_2O/CO_2/O_2$ into synthetic gas mixture ($CO+H_2$). The most commonly used feedstocks for the reforming processes are methane or either other light hydrocarbons obtained from oil. Several chemical processes have been developed in order to produce hydrogen via reforming route:

1) Steam Reforming (SMR),

2) Auto Thermal reforming (ATR),

3) Partial Oxidation (POX),

4) Dry Reforming of methane (DMR),

5) Combined Reforming of Methane (CMR),

6) Reforming with Membrane,

7) Tri-Reforming of Methane (TMR)[25].

The first three are widely used industrial processes, whereas the last four are recent innovative processes developed with the aim to minimize environmental impact and energy consumption together with the improvements of already existing methods.

Steam Methane Reforming (SMR) and Water Gas Shift (WGS) reaction

$$CH_4 + H_2O \rightarrow 3H_2 + CO \qquad \Delta H° = +225{,}4 \; kJ/mol$$

Steam Methane Reforming (SMR) is the most common way to produce hydrogen rich syngas mixture (H_2+ CO). A conventional steam reformer unit consists of several hundred fixed-bed reactor tubes filled with a catalyst, which can vary in its size and geometry. High temperatures (> 600°C) and low pressures favour the formation of the H_2 and CO products (Le Chatelier's Principle). However, in practice, the natural gas steam reformer is operated under the pressure of about 20-30 atm (for kinetic reasons) with an exit temperature of 800-870°C (but the tube wall temperature can range from 700°C up to a maximum hot spot of 920°C), where methane and steam are converted into synthesis gas. Primary steam reforming catalysts are nickel based catalyst: 10-20% Ni supported on α–Al_2O_3, calcium or magnesium aluminate with a life time from 3 to 5 years. Cobalt and noble metals are also active, but more expensive. Attempts to use non-metallic catalysts have not had commercial success because of the low activity. The catalyst properties are dictated by the severe operating conditions, i.e. temperatures of 450-950°C and steam partial pressures of up to 30 bar.

Normally, the subsequent stage of the SMR process includes WGS reactions which further convert carbon monoxide to carbon dioxide, while generating more hydrogen.

$$CO + H_2O \rightarrow H_2 + CO_2 \qquad \Delta H° = -42 \, kJ/mol$$

In the first stage, refers to a high temperature shift reaction, the gas is mixed with steam and passed over an Fe/Cr or Fe/Cr/Mg mixed oxide catalyst at T= 300-450°C in a fixed bed reactor; which decreases the carbon monoxide concentration down to 2-3%. In the second stage, the low temperature shift reaction, the mixture of gases is passed over a Cu/Zn oxide catalyst at T=190-220°C, where the carbon monoxide concentration is reduced to 0.1-0.2%. Further hydrogen purification can be achieved using:

- Methanation
- Pressure Swing Adsorption (PSA)
- Membrane reactors and etc.

Steam Naphtha Reforming

If naphtha is used as the feedstock, an extra reforming stage is needed. The naphtha is heated to form a vapour, mixed with steam and passed through tubes, heated at T=450-500°C and packed with a catalyst, nickel supported on a mixture of aluminium and magnesium oxides. The main product is methane together with carbon oxides (CO_x), which then processed by SMR, as if it was natural gas, followed by the shift reaction.

Dry Methane Reforming (DMR)

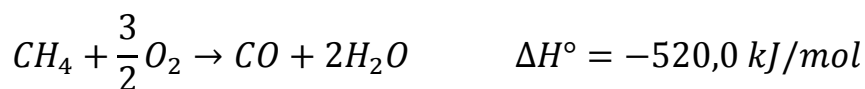$$CH_4 + CO_2 \rightarrow 2H_2 + 2CO \qquad \Delta H° = +260,5 \, kJ/mol$$

The DMR process is characterized by a very low intrinsic activity, in addition to the simultaneous occurrence of the reverse water gas shift (RWGS) reaction resulting in a syngas ratio less than unity. Dry reforming of methane has been investigated with noble (Rh, Ru, Pd and Pt) and non-noble metal (Ni, Co and Fe) based catalysts. Noble metal catalysts have drawn attention for their superior coking resistance, higher stability and

activity especially for higher temperature applications. However, for large scale industrial applications, development of the active catalyst is still under investigation.

Autothermal Reforming (ATR)

Autothermal reforming (ATR) is an important industrial process used to produce syngas with a low H_2/CO ratio (from 1.5 to 3) desired for synthesis of methanol and higher molecular weight hydrocarbons (via Fischer-Tropsch process). The main concept based on a combination of non-catalytic partial oxidation and adiabatic catalytic steam reforming, where the reactor temperature is maintained using the heat emitted from the partial oxidation of the hydrocarbon feedstock, typically methane, with a sub-stoichiometric amount of oxygen.

$$CH_4 + \frac{3}{2}O_2 \rightarrow CO + 2H_2O \qquad \Delta H° = -520,0 \ kJ/mol$$

$$CH_4 + H_2O \rightarrow 3H_2 + CO \qquad \Delta H° = +225,4 \ kJ/mol$$

This process was developed by Haldor Topsoe A/S with the aim to perform the POx (partial oxidation) and the SR (steam reforming) in a single ATR reactor. The very high temperatures in the ATR unit require a high thermal stability catalyst, which is typically the nickel-based catalyst on a stabilized Al or Mg-Al support.

Partial oxidation (POX)

$$CH_4 + \frac{1}{2}O_2 \rightarrow CO + 2H_2 \qquad \Delta H° = -36,0 \ kJ/mol$$
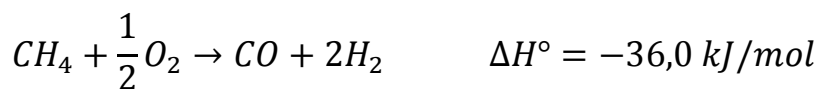
An alternative way to produce hydrogen based on the partial oxidation of a sub-stoichiometric fuel-air mixture which results in a formation of H_2-rich syngas. Partial oxidation is an exothermic reaction and, thus, considered to be more economically feasible than the processes of steam or dry reforming. The exothermic nature of reaction has certain drawbacks that it induces hot spots on catalyst arising from a poor heat removal rate

causing the difficulties in operation control. A difference is made between *thermal partial oxidation* (TPOX) and *catalytic partial oxidation* (CPOX).

Thermal (non-catalytic) Partial Oxidation

TPOX is a non-catalytic process in which the feed is partially combusted with a sub-stoichiometric amount of air, oxygen, or enriched air to obtain $CO+H_2$ mixture, where the production of syngas depends on the oxygen/fuel ratio at operating temperature range of 1200-1500°C. Feedstock is used for the TPOX can be almost any carbonaceous material, from natural gas through liquid feeds such as fuel oils and gas oils as well as coal. A non-catalytic partial oxidation process was developed by Texaco and Shell which results in high syngas yields at high temperature and pressures[26].

Catalytic Partial Oxidation

CPOX is a catalytic process in which the feed with sub-stoichiometric amount of oxygen (or air) is catalytically converted into $CO+H_2$ mixture. The use of a catalyst lowers the required reaction temperature down to 800-900°C. Commonly used catalysts are noble (Pt, Rh, Ir, Pd) or non-noble (Ni, Co) metal based catalysts. Catalytic partial oxidation can be performed only if a sulfur content of the feed is below 50 ppm, since the higher sulfur content would poison the catalyst (in such case non-catalytic partial oxidation is more suitable for the use).

1.2.4. Hydrogen via Chemical-Loop (CL) processes

CL processes are based on the looping approach that usually consists of two temporarily/spatially separated steps: reduction and re-oxidation. During the reduction step, a transfer of the oxygen to the fuel mediated by a metal oxide carrier material (Me_xO_y), which is put in a contact with a reducing stream, thus being reduced and at the same time converting the fuel into products, mainly CO_x, H_2O and H_2. Subsequent oxidation step is performed over the previously reduced material ($Me/Me_xO_{y-\delta}$) with air/H_2O (water splitting) in order to restore its original oxidation state (Me_xO_y) and to produce H_2 (when the re-oxidation step is carried out with a steam). The difference is made whenever air or water

steam are used to regenerate the oxygen carrier material. Re-oxidation step performed with air is varied between *Steam Reforming integrated to Chemical-Looping Combustion process (SR-CLC),* where CLC is used to energy supply needed for the conventional catalytic steam reforming and *Chemical-Looping Reforming process (CLR)* where primary products from the Chemical-Looping system are H_2 and CO. Other processes use the property of some oxygen depleted materials to react with water steam to generate pure H_2, also known as "water splitting". In this category, it can be found *Chemical-Looping Hydrogen (CLH)* or *One Step Decarbonization (OSD) processes*, and the so-called Chemical-Looping Gasification technologies: *Syngas Chemical-Looping process (SCL)* and *Coal Direct Chemical-Looping process (CDCL) and etc.* Usually the later processes need several oxidation steps, like an air treatment, which sometimes required for the final regeneration of the oxygen carrier material[27]. One of the fundamental parameters, that determines the overall efficiency of many chemical looping processes, lies in the effectiveness of the oxygen carrier materials. Hence many research groups focus their attention on further improving the activity and the stability of oxygen carrying materials.

Chemical-Loop Reforming (CLR) for Hydrogen Generation

CLR for Hydrogen Generation is developed as an alternative way to produce H_2 starting from either conventional or renewable sources. The Chemical-Loop process can be performed using a number of different reductants, such as gas resulting from coal[11] or biomass[12–14] gasification, light hydrocarbons reforming,[15] methane,[16–18] CH_4/CO_2 and CH_4/H_2 mixture,[18,19] pyrolysis oil,[20,21] methanol[22] and pure H_2 (as a method for H_2 storage).[23,24]Differently from a classical reforming, separation costs can be avoided by splitting the process into two/three alternated steps in order to detach H_2/CO_x streams and fully re-oxidize the oxygen carrier material (Figure 1-6). Generally, the reducing fuel (C_nH_{2m}) is fed to the FR, where it reacts with the oxygen carrier material (M_xO_y) according to the following equation:

(FR) – (n+m/2) M_xO_y + C_nH_{2m} → (n+m/2) M_xO_{y-2} + m H_2O + n CO_2
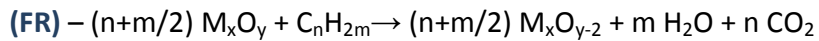
After the first step, previously reduced oxygen carrier material is transferred to the steam reactor (SR), where it is oxidized by a water steam to restore its original oxidation state:

(SR) – (n+m/2) M_xO_{y-2} + m H_2O → (n+m/2) M_xO_{y-1} + m H_2
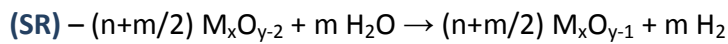
A general statement, made on the basis of the results obtained independently by several research groups: as the oxygen ratio in the system decreases, there is a higher tendency towards carbon formation, which in its turn leads to the lowering of the purity of the produced hydrogen. According to Cho et al. [28], the rate of carbon formation increased rapidly when more than 80 % of the available oxygen in the Ni-based oxygen carrier was consumed. Galvita and Sundmacher reported that a maximum Fe reduction of 60 % largely minimized carbon formation and a high purity hydrogen stream (< 20 ppm CO) could be obtained[29].

Usually, the difficulty to re-obtain original oxidation state of the oxygen carrier material by means of only water steam can lead to the necessity of an additional oxidation step, like an air treatment:

(AR) – (n+m/2) M_xO_{y-1} + ½ O_2 → (n+m/2) M_xO_y
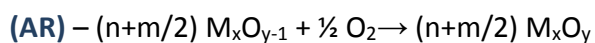
Oxygen carrier material (M_xO_y), in its fully oxidized form, is further re-circulated to the fuel reactor (FR) for subsequent cycles.
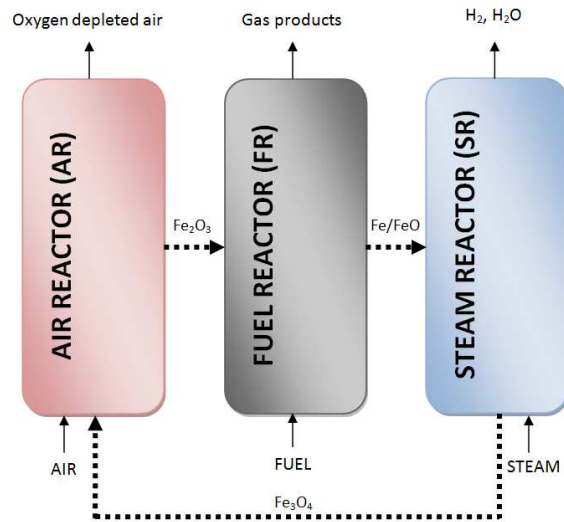
Figure 1-6. Schematic representation of CLR for Hydrogen Generation over Fe-based oxygen carrier material

Important aspects for the overall effectiveness of the process lie in the choice of operation conditions, reactors design and identification of suitable candidates to be used as corresponding oxygen carrier materials. Appropriate oxygen carriers should have sufficiently high conversion rates in redox reactions, high agglomeration/sintering resistance, complete fuel conversion, negligible carbon deposition, and be economical and environmentally friendly[30].

Oxygen carrier materials

As it has been already mentioned, a choice of the suitable oxygen carrier material for any type of Chemical-Loop process is an important parameter which has to be considered, taking into account several properties: reaction kinetics, thermodynamic feasibility of oxygen transfer, redox properties, oxygen content, long term recyclability and durability, attrition resistance, heat capacity, melting points, tendency to form coke, resistance to carbon deposition, low cost, toxicity and etc [27]. However, one of the most important requirements is the thermodynamic aspect of a suitable redox couple – M_xO_y/M_x, which determines the final effectiveness of the process together with a choice of operating conditions. Figure 1-7 shows the Gibbs free energies (ΔG) as a function of temperature for

some frequently studied oxygen carrier materials; moreover, the values for oxygen transport capacity are listed in Table 1-1.
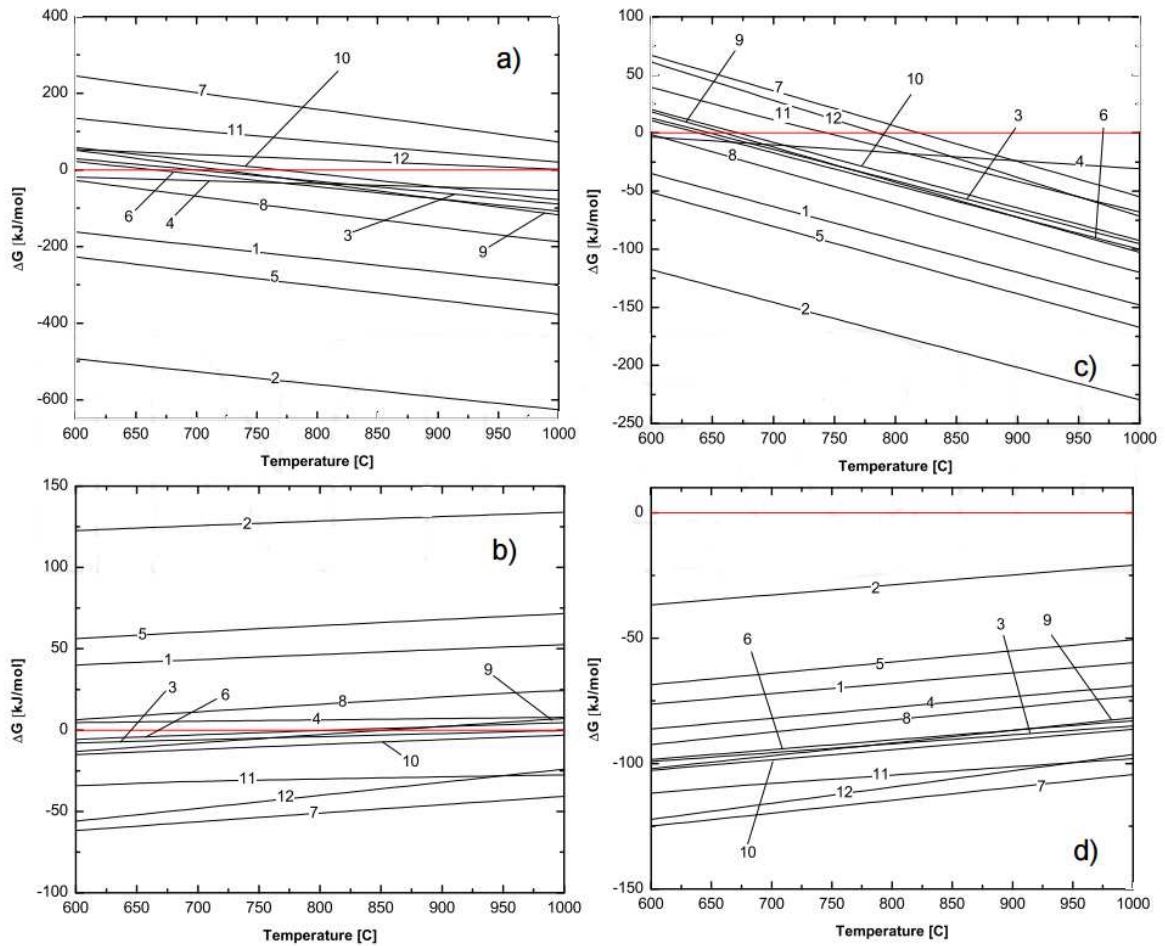

Figure 1-7. Gibbs free energies for the following redox reactions[31]: I. Reduction of oxygen carrier with a CH_4-fuel: a - CH_4 total combustion ($CH_4 + 4/y\ M_xO_y \rightarrow CO_2 + 2\ H_2O + 4x/y\ M$), b - CH_4 partial oxidation ($CH_4 + 1/y\ M_xO_y \rightarrow CO + 2H_2 + x/y\ M$); II. Re-oxidation of reduced oxygen carrier with a steam/air: c – H_2O oxidation ($x\ M + y\ H_2O \rightarrow M_xO_y + y\ H_2$), d - air oxidation ($x\ M + y/2\ O_2 \rightarrow M_xO_y$), *see Table 1-1 for the numeric legends

Table 1-1. Common redox couples[31]

*	Redox couple	Oxygen transport capacity, kg/kg-metal
1	NiO/Ni	0.27
2	CuO/Cu	0.25
3	Fe_3O_4/Fe	0.38

4	MnO_2/Mn	0.58
5	Co_3O_4/Co	0.36
6	WO_3/W	0.26
7	ZnO/Zn	0.24
8	SnO/Sn	0.13
9	In_2O_3/In	0.21
10	MoO_2/Mo	0.33
11	V_2O_5/V	0.78
12	CeO_2/Ce_2O_3	0.06

According to the listed data, oxygen carrier materials can be conventionally divided into the materials that are capable to partially oxidize methane, like ZnO/Zn, V_2O_5/V or CeO_2/Ce_2O_3. Whereas some redox couples, as NiO/Ni, Co_3O_4/Co and CuO/Cu, favor total methane oxidation; in addition, their further re-oxidation is also favorable over a wide temperature range, as supported by the negative ΔG values in Figure. Thus, oxygen carrier materials based on the Ni, Co and Cu elements are often regarded as good candidates for Chemical-Loop applications.

A comprehensive review on different oxygen carrier materials for the hydrogen production via Chemical-Loop processes was recently published by Protasova et al[30]. The review encompasses information on the different perovskites and Ni/Fe/Cu/Ce-based oxygen carrier materials. Perovskites showed good results for the partial oxidation of methane; whereas with Fe-based materials promising results also have been obtained (moreover they are considered to replace Ni-based oxygen carriers because of their price and toxicity). Several research groups have been exploring modifications of simple iron oxide (Fe_3O_4 and Fe_2O_3) in order to prevent deactivation,[32] to lower the operating temperature[33] and to increase the structural stability and reducibility,[34,35] the reaction rate for oxidation and total efficiency of the process.[36,37] Several studies were dedicated to different metal additives to iron oxide.[38,39] In addition, ternary metal systems have also been considered in the search for a better synergetic effect.[40,41] Several research groups have been investigated the effect

of various M-additives on the stability and redox behavior of iron oxide for chemical hydrogen storage using Pd, Pt, Rh, Ru, Al, Ce, Ti, Zr[42] and Al, Cr, Zr, Ga, V , Mo[43]. And it was found out that Pd, Pt, Rh and Ru additives have an effect on promoting the reduction and lowering the re-oxidation temperature of iron oxide. At the same time, Al, Ce, Ti, Zr, Cr, Ga and V additives prevent deactivation and sintering of iron oxide during repeated redox cycles. Some recent studies on developing of the novel and efficient oxygen carrier materials for Chemical-Loop applications highlight the special interest in spinel oxides[16,24,32,36,37,44–56] which, first of all, can be explained by their ability to form thermodynamically stable spinel oxides which allow to re-obtain the initial spinel phase upon cycling and in turn increase the stability of the looping material itself.

1.3. Spinel oxides: AB_2O_4

Spinel oxides with a generic formula of AB_2O_4 are chemically and thermally stable materials suitable for variety applications including catalysis (Figure 1-8). Many of them are used as magnetic pigments[57], nanodevices[58], photoelectric devices[59], sensors and microwave devices[60,61]. Besides, spinel ferrites (AFe_2O_4) are attractive because of the importance in ferrofluids[62,63], magnetic drug delivery[64,65] and hyperthermia for cancer treatment[66]. At the same time, they have well-established catalytic properties for many reactions, such as: oxidative dehydrogenation of hydrocarbons[67,68], decomposition of alcohols[69,70], selective oxidation reactions[71,72,73], CO[74] and CO_2 removal[75], VOCs[76] and propane total oxidation[77], methanol steam reforming[78], hydrogen peroxide decomposition[79,80], NO_x selective reduction[81] and WGS reaction[82,83]. The catalytic effectiveness of these systems explained by the ability of metallic ions to migrate between the sub-lattices without altering the structure, which makes the catalyst efficient for many organic transformation reactions[84]. Versatile catalytic properties are dependent on the chemical composition and nature of substituted ions, charges and their distribution among the O_h and T_d sites, and this is determined by the synthesis methods[85–88].

Figure 1-8. Main fields of the spinel oxide application

Structure of AB_2O_4 oxides

The crystallographic structure of spinel oxide group is formed by a nearly closed-packed face centered cubic (fcc) of anions (Figure 1-9) with two unequivalent sites for cations, which differ in oxygen coordination[89,88]. A tetrahedral site, **AO_4,** is comprised of the cation at the center of a cube and four oxygen atoms in the nonadjacent corners. The octahedral site, **BO_6,** consists of a cation surrounded by six oxygen atoms, two along each dimensional axis, to form a octahedron [88,90]. The preference of the individual ions for the two types of lattice sites (**O_h**vs**T_d**) is determined by:

- the ionic radii of the specific ions;
- the size of the interstices;
- the temperature;
- the orbital preference for specific coordination [88]

On the basis of a cation valency occupation in the molecule of the spinel oxide they can be subdivided into three basic types:

1. $M_1^{2+}M_2^{3+}O_4$, (2-3 spinel): Fe_3O_4, $NiFe_2O_4$, $CuFe_2O_4$

2. $M_1^{4+}M_2^{2+}O_4$, (4-2 spinel): $GeFe_2O_4$, $TiFe_2O_4$

3. $M_1^{6+}M_2^{1+}O_4$, (6-1 spinel): $MoLi_2O_4$, WAg_2O_4

However, the most common type is 2-3 spinel which comprises of M^1(II) and M^2(III) metal cations in the molecular unit.

B site – one metal with six nearest-neighbour oxygens→ O_h

A site – one metal with four nearest-neighbour oxygens→T_d

A^{II} = a divalent cation like Mg, Cr, Mn, Fe, Co, Ni, Cu, Zn, Cd, Sn
B^{III} = a trivalent cation like Al, Ga, In, Ti, V, Cr, Mn, Fe, Co, Ni
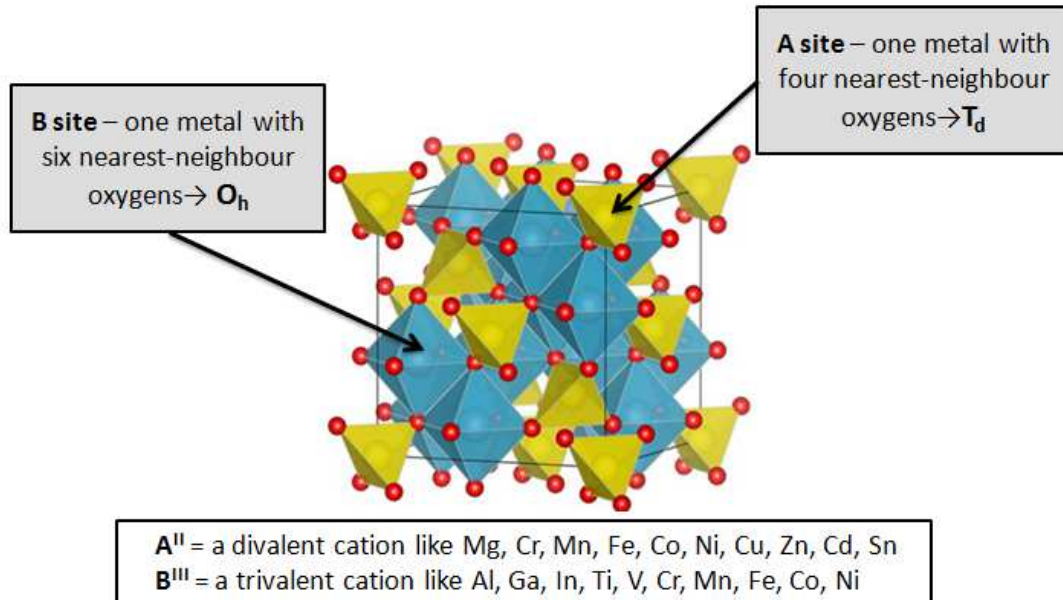
Figure 1-9. Spinel oxide unit cell

According to the distribution of A and B cations between T_d and O_h sites, there are two types of spinel oxides: normal and inverse spinels. In the **normal spinel**, the A cations (divalent) occupy all the tetrahedral sites, and the B cations (trivalent) fill the octahedral sites. Since tetrahedral holes are smaller than octahedral holes, the A ions should be smaller than the B ions. In fact, this condition is not fulfilled in many spinels, and thus there is another type of spinels, which is more common in nature, so called the inverse spinel, just to indicate that they were the opposite of what had already been described. In **inverse spinel**, the B cations occupy the tetrahedral sites, and the octahedral sites contains a mixture of B and A cations[89,91,88]. Important parameter which is used to describe the degree of spinel inversion denotes as an inversion parameter (δ), and is equal to **0** in a case of the **normal spinel** and **1** for the **inverse spinel**.

1.4. Aim of the research project

The research work presented here investigates a new process, named as Chemical-Loop Reforming (CLR) process, to produce "*clean H_2*" with an inherent CO_x separation. The main principle of the CLR process is that an oxygen-storage material is first reduced by ethanol stream (T-450°C), and then re-oxidized by water (T-450°C) to produce hydrogen and to restore the original oxidation state of the looping-material (Figure 1-10).
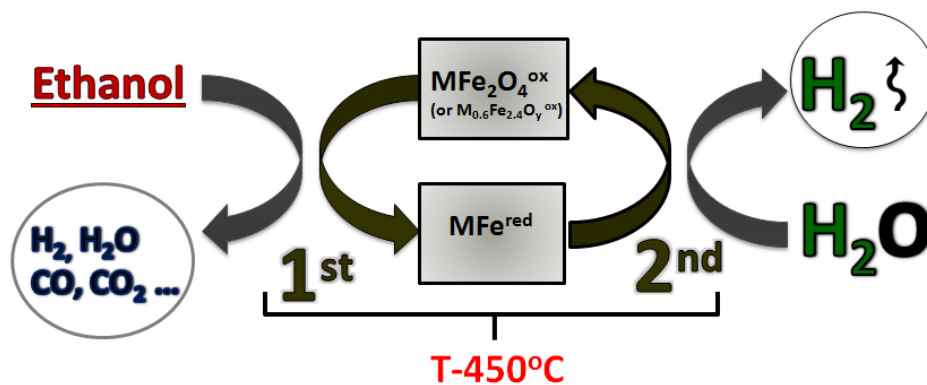
Figure 1-10. The chemical-loop reforming of ethanol over modified ferrospinels

The choice of ethanol as a reducing agent has its several advantages:

- The use of bio-alcohols in cycle reforming has not yet been much studied in literature;
- Ethanol can be obtained from biomasses, that might contribute to unlink the production of hydrogen from fossil fuels;
- Ethanol is a non-toxic liquid, easy to transport and handle, relatively stable at room temperature.

The initial task of the project is to define conditions and materials that may lead to an optimized process, allowing producing a hydrogen stream that does not require any additional purification or separation treatment. Hence, different M-modified spinel-type mixed oxides (TYPE I – MFe_2O_4 and TYPE II – $M_{0.6}Fe_{2.4}O_y$) are synthesized and tested as potentially attractive ionic oxygen and electron carrier looping materials to generate hydrogen by oxidation with steam, after a reductive step carried out with ethanol.

Particularly, the focus on the reactivity behavior of secondary/ternary materials explained by their ability to form thermodynamically stable spinel oxides which allow us to re-obtain the initial spinel phase upon cycling and in turn increase the stability of looping material itself. The composition of MFe_2O_4 and $M_{0.6}Fe_{2.4}O_y$ ferrospinels is varied in between transition metals: Co, Mn, Cu or Cu/Co, Cu/Mn, Co/Mn and alkaline earth metals: Ca, Mg. The aim of the following modifications is to pursue a higher selectivity to some valuable chemicals produced on the 1st reduction step along with a high purity H_2 produced during the 2nd re-oxidation step.

The secondary task is to explore the chemistry of the process, by means of both in-situ and ex-situ techniques, and the characteristics of the mixed oxides, in terms of redox properties, morphology and chemical-physical features which also encompasses the solid-state chemistry investigations of the fresh and cycled looping materials.

This research was apportioned between three institutions, all details about the accomplished work are summarized in Figure 1-11.

I - HOME INSTUTION

Università di Bologna

✓ Synthesis of materials:
TYPE I: $M^1_{1-x}M^2_xFe_2O_4$
TYPE II: $M^1_{0.6-x}M^2_xFe_{2.4}O_y$
✓ Characterization:
Bulk: XRD, SEM/EDX, TPR/O
Surface: N_2 ads., in-situ XPS, in-situ DRIFTS
✓ Reactivity test:
2 step cycles
1 h ethOH/1 h H2O
20 min ethOH/20 min H_2O, 20 min·5 cycles
6 min ethOH/ 6 min H_2O, 6 min·10 cycles
3 steps cycles
20 min ethOH/20 min H_2O/+air,
20 min·3 cycles+air

II - HOST INSTUTION

Ecole Nationale Supèrieure de Chimie de Montpellier

✓ Synthesis of materials:
TYPE I: $M^1_{1-x}M^2_xFe_2O_4$
TYPE II: $M^1_{0.6-x}M^2_xFe_{2.4}O_y$
✓ Characterization:
Bulk: Mossbauer, Raman ,XRD, TEM/EDX, Magnetic measurements
Surface: N_2 adsorption

III - HOST INSTUTION

IRCE CNRS Lyon

✓ Synthesis of materials - **MW**
TYPE I: $M^1_{1-x}M^2_xFe_2O_4$
TYPE II: $M^1_{0.6-x}M^2_xFe_{2.4}O_y$
✓ Characterization:
Bulk: XRD, Mossbauer, CHNS
✓ Reactivity test:
2 step cycles
1 min ethOH/1 min H_2O
3 min ethOH/3 min H_2O
5 min ethOH/5 min H_2O

Figure 1-11. Accomplished work during the three years of PhD research

2. CHARACTERIZATION TECHNIQUES AND SET-UP OF LABORATORY PLANT

This chapter includes the information on several characterization techniques used to study bulk and surface properties of the fresh/used looping materials (ferrospinels of TYPE I – MFe_2O_4 and TYPE II – $M_{0.6}Fe_{2.4}O_y$, where M: Cu, Co, Mn, Mg, Ca and Cu/Co, Cu/Mn, Co/Mn). All the solids were tested in a laboratory-scale plant designed to carry out the Ethanol Chemical-Loop Reforming experiments. In addition, the chapter contains a description of the analysis method used for identification and quantification of the reactants/products including the calculation protocols.

2.1. X-ray diffraction (XRD)

X-ray diffraction is a primary technique used to determine nature of the crystalline phases and to measure a size, shape and internal stress of small crystalline regions. Information on the sample is given by the position, intensity, sharpness and width of the diffraction lines. The diffraction angle 2θ and the spacing between two planes (h,k,l) d are related by the Bragg's law:

$$2\ d\ sin\theta = n\ \lambda$$

Where:

λ – the wavelength of incident X-ray

n – the diffraction order
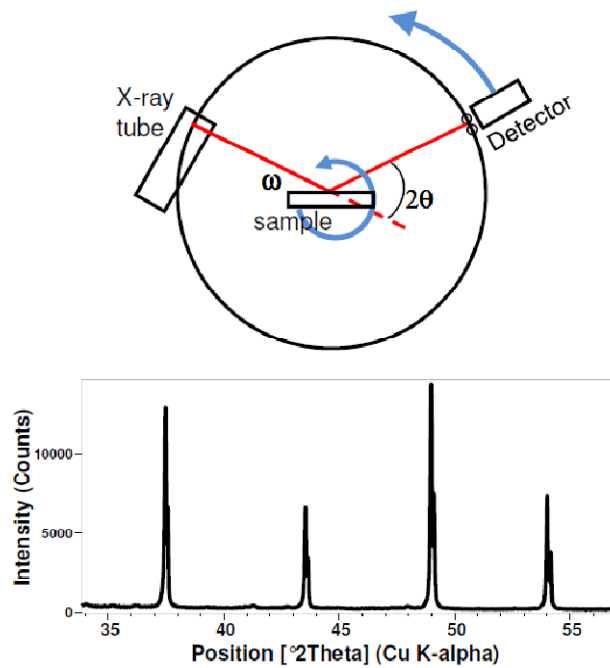
Figure 2-1. Schematization of the X-ray diffraction experimental setup

In the present study, the powder X-ray diffraction (XRD) patterns were measured on Bruker D8 Advance diffractometer (using Cu K$_\alpha$ radiation with λ = 1.5406 Å) with a Bragg-Brentano geometry and equipped with a Bruker Lynx Eye detector. The data were recorded varied from 5 to 80° 2θ diffraction angle with an acquisition time of 1 s per each step (0,01 degree).

The Debye-Scherrer equation was used for the calculation of a crystallite size, which is related to the FWHM (Full Width at Half Maximum) through the formula:

$$\tau = \frac{K\lambda}{\beta cos\theta}$$

Where:

τ – the mean size of the ordered (crystalline) domains, which may be smaller or equal to the grain size

K – the dimensionless shape factor, with a value close to unity (K is typically eq. to 0.9)

λ – the X-ray wavelength

β – the line broadening at half the maximum intensity (FWHM), after subtracting the instrumental line broadening

θ – the Bragg angle

TOPAS-4.2 program was used to refine the unit cell parameters of the crystalline phases and to calculate the relative phase content in the fresh/used samples. The calculations are based on the Rietveld refinement method, which permits the reproduction of the whole diffractogram, through the optimization of both structural (peak position and intensity) and non-structural (peaks shape) data.

2.2. Raman Spectroscopy

Raman spectroscopy is used to observe the differences in the vibrational modes of the samples with respect to the composition which causes local distortions that are not seen by x-ray diffraction. Raman spectra were recorded using a Bruker spectrometer with a 633 nm He/Ne laser source (filter: $P_{laser} \div 10$; slit 100 μm) equipped with a microscope (50X lens). Each spectrum was taken with 300 sec exposure time and 1 accumulation.
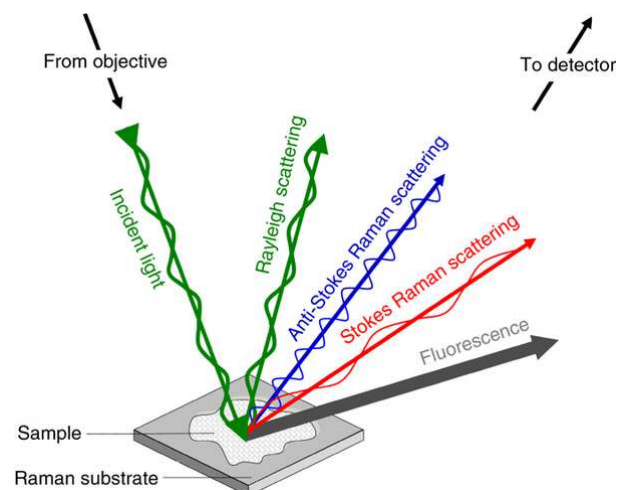
Figure 2-2. Schematic identifying light scattering after laser exposure on a sample surface

2.3. Mössbauer Spectroscopy

The Mössbauer effect consists of the "recoilless" emission of γ-ray photons from certain radioactive nuclei, and the selective re-absorption of those photons by other nearby nuclei. The process is sensitive to small differences between the structure of the emitting and the absorbing nuclei. Mössbauer spectroscopy uses this phenomenon to explore the nuclear and atomic structure of materials.

Through Mössbauer spectroscopy it is possible to obtain important information on the oxidation state and the structure of Fe species in a solid. The main nuclear interactions used for the interpretation of the resonance spectra are three:

- Isomer Shift (IS), which is the shift in nuclear energy levels induced by the static charge of nearby atomic electrons
- Quadrupole Splitting (QS) which is the shift in nuclear energy levels induced by a strong electric field gradient due to nearly electrons and
- Magnetic (or Hyperfine) Splitting (HS) corresponding to the energy level splitting in a nucleus due to the magnetic fields induced by the nearby atomic electrons.

The Mössbauer spectrometer was a homemade apparatus using a ^{57}Co/Rh γ-ray source and a conventional constant acceleration Mössbauer spectrometer. The solids were pressed into thin discs and the analysis took about one day to be completed (in some cases it can require even longer time).

Isomer shifts were given with respect to α-Fe. All spectra were taken at room temperature and ambient atmosphere; samples were diluted in sucrose at about 50%$_w$ concentration. Integrated areas under individual deconvoluted peaks were used to obtain the relative populations of different iron species, assuming an equal recoil-free fraction for all the species.

The calculations were made using pure Lorentzian functions. The parameters characterizing a Mössbauer spectrum were determined by least-squares fitting and the goodness of the fit statistics by minimizing the χ^2 quadratic function:

$$\chi^2 = \sum_i \frac{(y_i th - y_i exp)^2}{y_i exp} \cdot \frac{1}{N-K}$$

Where:

N - the number of measured points

K - the number of the parameters to be determined

$y_i exp$ and $y_i th$ – measured and calculated spectral values in velocity for each point i

Another ^{57}Fe Mössbauer spectra (taken in Montpellier and discussed in the Paragraph 5.11) were measured using a conventional constant acceleration spectrometer, and a commercial ^{57}Co:Rh γ-ray source. Both the sample and the absorber were kept at room temperature. The velocity calibration was performed using a α-iron absorber, and the isomer shift (δ) values are given relative to α-Fe metal. The collected spectra were least-square fitted by appropriate combinations of Lorentzian profiles, either with several discrete quadrupole doublets corresponding to different iron environments, or by assuming a distribution of the magnetic hyperfine fields (BHF), corresponding to the continuous distribution of non-equivalent magnetic interactions in the sample.

2.4. Surface area measurements

The specific surface area was measured applying the single point BET method. The instrument used for this analysis was a Carlo Erba Sorpty 1750 Fisons Instrument.

The method calculates the surface area of the sample from the volume of the gas corresponding to the monolayer adsorption. So, the variable that has to be measured from the analysis is the gas volume for the monolayer adsorption. The single-point approximation is based only on one measurement of the pressure of adsorption and the corresponding gas volume adsorbed; the formula used is here reported:

$$\frac{P}{V(P_s - P)} = \frac{c-1}{V_m \cdot c} \cdot \frac{P}{P_s} + \frac{1}{V_m \cdot c}$$

where P is the pressure, P_s is the surface tension of the adsorbed gas (nitrogen in this case), V is the adsorbed gas volume, V_m is the monolayer gas volume and c is a constant related to the gas-surface interaction. A second approximation made by the instrument software is that the constant c is very high compared to the other variables and so the final equation is

$$\frac{P}{V(P_s - P)} = \frac{1}{V_m} \cdot \frac{P}{P_s}$$

The percent error that derives from these approximations is about 7% on values over 3 m^2; below this limit, the surface area calculated cannot be considered reliable.

For the analysis, around an amount of 0.5 g of the sample was placed inside the sample holder and then heated at 150°C under vacuum ($\leq$4 Pa) to release water, air, CO_2 or other molecules adsorbed. Subsequently, the sample was placed in liquid nitrogen, and the adsorption of the gaseous N_2 was carried out.

The particle size (*d*) was calculated on the basis of the following correlation:

$$d = \frac{6}{SSA \cdot \rho}$$

Where:

SSA – value of the specific surface area, m^2/g

ρ – density of the sample, g/m^3

2.5.   SEM/TEM-EDX analysis

TEM/EDX characterisation, samples were suspended in ethanol and homogenized using ultrasonication (for 5 min). The suspension was deposited on a holey-carbon film Cu-grid for TEM analysis, then dried at 100°C. The analyses were carried out by a microscope TEM/STEM FEI TECNAI F20 at 200 keV.

SEM/EDX analyses were performed by using a SEM Zeiss EP EVO 50 with a tungsten electron source, secondary and backscattered electrons detectors. The EDX system is an Oxford Instruments INCA ENERGY 350 including a Si(Li) detector equipped with an ultrathin window (Z>4 (Be)).The images were collected in high vacuum mode @ EHT = 20 keV and the spectra were registered for 60s collection time.

2.6.   Temperature programmed reduction/oxidation (TPR1/O/R2)

The objectives of this technique are essentially the following:

1. To find the most efficient redox conditions

2. To characterize complex systems of M-modified ferrospinels: MFe_2O_4 and $M_{0.6}Fe_{2.4}O_y$ (where M=Cu, Co, Mn, Mg, Ca and Cu/Mn, Co/Mn, Cu/Co) in order to determine the role of each component on the reduction evolution of the whole material.

The instrument used for TPR/O analysis was the 1100 Micromeritics AutoChem II. 2920 V 4.05 Chemisorption Analyzer. The samples were first pre-treated at 450^oC for 45 min in He flow (30 min/min). Reduction 1/Reduction 2 (TPR-1/TPR-2) was carried out with 5 % H_2 in the Ar flow (30 ml/min). The oxidation stream (TPO) was 5% O_2 in the He flow (30 ml/min). Temperature program started at 50^oC and then the temperature increased up to 800°C (with ramp 10°C/min) and maintained there for 40 min. This last step was repeated for all the experiments (TPR-1/TPO/TPR-2).

2.7.   Carbon content measurements (CHNS)

The carbon contents of the materials after the each one of the two steps was determined using a CHNS/Oxygen automatic elemental analyzer Thermo Scientific MASS 200R. The samples were homogenized and loaded in small aluminum capsules and analyzed. For each samples two analyses were carried out in order to check for the homogeneity of the solid. Results were given as weight % of C, and the precision of the measurement was 0.3%.

2.8.   Magnetic measurements

Static magnetization and low-temperature hysteretic properties (at 300 K) of the AFeNi, AFeMn, and AFeCo samples were measured using a Quantum Design MPMS SQUID magnetometer, equipped with a superconducting magnet producing fields up to 50 kOe.

2.9.   In-situ X-ray Photoelectron Spectroscopy (XPS) experiments

X-ray Photoelectron Spectroscopy allows the direct characterization of a surface and it is widely used in catalyst characterization. The technique provides data, via expulsion and analysis of the related energies, of electrons from the solid and gives pieces of information

on the composition and chemical status of the elements on the solid surface before/after reaction test. XPS is exciting 'core' electrons by means of a soft X-ray beam (i.e. Mg/Al K$_\alpha$). The emitted electrons bring to us the information coming from a depth of 1-10 nm, so providing a good surface picture without its damage (Figure 2-3). The use of XPS in catalyst investigation is increasing and nowadays the availability of synchrotron light instrumentation (super ESCA) is favouring the XPS investigations because they are of great help in surmounting also the sensitivity problem[92].
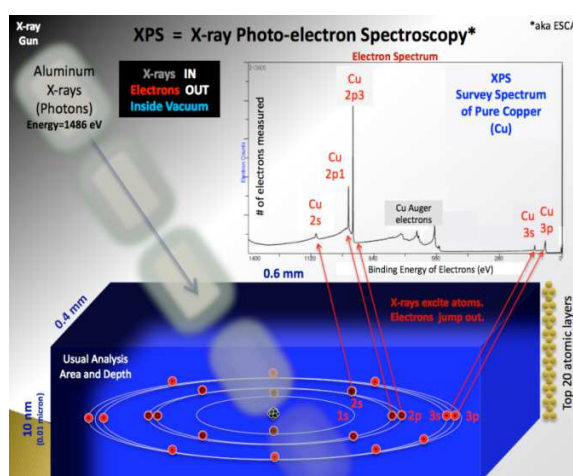
Figure 2-3. X-ray photoelectron spectroscopy physics (https://en.wikipedia.org/wiki/X-ray_photoelectron_spectroscopy)

X-ray Photoemission Spectroscopy (XPS) data were acquired using non-monochromatized AlKα (1486.6 eV) x-ray source, and an Omicron EA125 electron analyser (Figure 2-4). The measurements were carried out in a custom built ultra-high-vacuum system operating at the base pressure of 5×10^{-10} mbar equipped with facilities for sample heating and controlled gas dosing. The spectra were acquired at room temperature (RT) on drop casted films of powder samples suspended in water. Different sample treatments have been carried out: annealing in UHV at 450°C, reduction with ethanol at 450°C (5×10^{-6} mbar) and re-oxidation at 450°C in water ambient (2×10^{-4} mbar). For each of four M-modified ferrospinels (referring to $Co_{0.6-x}Mn_xFe_{2.4}O_y$) Fe 2$p$, O1$s$ and Co 2p and/or Mn 2p photoemission spectra were recorded sequentially after introduction in the UHV systems ("as received"), after annealing

in UHV for 30 min at 450°C, after exposure to ethanol at 450°C and after H_2O exposure at 450°C.
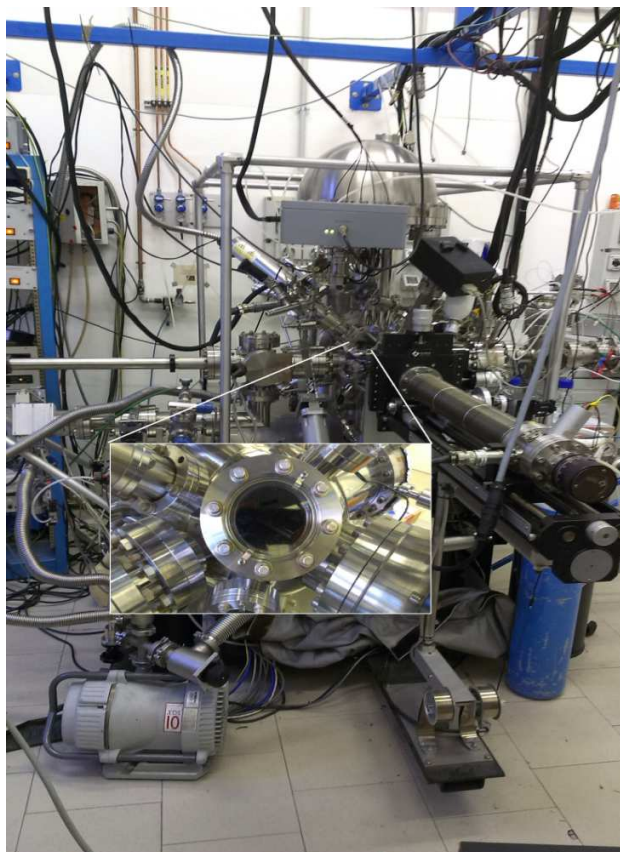
Figure 2-4. In-situ XPS apparatus

2.10.   Diffuse-Reflectance Infrared FT spectroscopy (DRIFTS) experiments

As shown in Figure 2-5, when an infrared beam reaches a sample, the incoming light may be partly reflected regularly (specular reflection) by the sample surface, partly scattered diffusely, and partly penetrates into the sample. The latter part may be absorbed within the particles or be diffracted at grain boundaries, giving rise to diffusely scattered light in all directions. This component of the radiation exits the sample at any angle but, since the light that leaves the surface has traveled through the particles, it contains data on the absorption properties of the material.
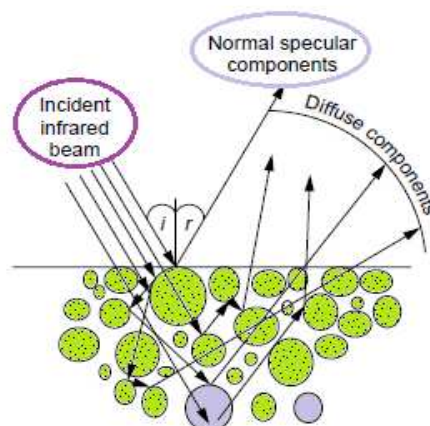
Figure 2-5. Representation of DRIFTS principle

In diffuse reflectance spectroscopy, there is no linear relation between the reflected light intensity (band intensity) and concentration, in contrast to traditional transmission spectroscopy in which the band intensity is directly proportional to concentration. Therefore, quantitative analyzes by DRIFTS are rather complicated. The empirical Kubelka-Munk equation relates the intensity of the reflected radiation to the concentration that can be used for quantitative evaluation. The Kubelka-Munk equation is defined as:

$$F(R) = (1-R)^2/2R = k/s = Ac/s$$

Where:

R - reflectance

k - absorption coefficient

s - scattering coefficient

c - concentration of the absorbing species
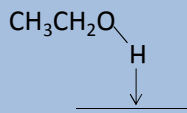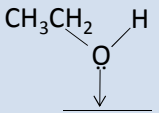
A - absorbance

In Kubelka-Munk equation it is assumed that s is the independent of wavelength and the sample is weakly absorbing. The former condition is achieved by proper sample preparation and the latter by dilution of strong absorbing samples with non-absorbing substrate powder (such as KBr or KCl). Therefore, to obtain reproducible results, particle size, sample packing and dilution should be carefully controlled, especially for quantitative analysis[93]

Diffuse-Reflectance Infrared FT spectroscopy, coupled with a quadrupole mass spectrometer (DRIFTS-MS) was used to characterise the surface features of materials, the scheme of the instrument is depicted in Figure 2-6. During a standard procedure, the sample was pre-treated at 450°C in a He flow (5mL/min) for 1 h in order to remove molecules possibly adsorbed on the material, mainly carbon dioxide and water. Then the sample was cooled down to 30°C, and the IR background was collected. Afterward ethanol was fed at 0.6 µL/min until saturation was reached (as seen by IR and MS; around 20 min) and whereupon the He flow was maintained until the weakly adsorbed ethanol was evacuated from the cell with loaded catalyst. During evacuation, the DRIFT and mass spectra were taken to follow stabilization of the system. When the mass and DRIFT spectra were stable, the temperature was increased up to 150°C for 2 min and then the system was cooled down to 30°C to record the spectra. This last step was repeated for the other temperatures (150, 200, 250, 300, 350 and 400°C).[94]

The adsorption of alcohols over metal oxides can lead to different kind of adsorbed species depending on the surface properties of the material under study. Table 2-1 shows the most representative intermediates and collects the characteristic infrared bands for the adsorption of ethanol according to the literature[94–99].

Table 2-1. Common species upon adsorption of ethanol and other compounds on catalysts surfaces

SPECIES		Characteristic frequencies (cm^{-1})
Hydrogen bonded ethanol	CH_3CH_2O H ↓	3000-3700 OH ν 1380 CH_3 δ 1500-1200 OH δ (broad)
Chemisorbed undissociated ethanol	CH_3CH_2 H O ↓	3500-3700 OH ν 1380 CH_3 δ 1270 OH δ (sharp)

Species	Structure	Vibrations
Adsorbed ethoxide	CH_3CH_2—O (on surface)	2970 $CH_3 \nu_{(as)}$ 2930 $CH_2 \nu_{(as)}$ / $CH_3 \nu_{(s)}$ 2875 $CH_2 \nu_{(as)}$ 1107 $CO\nu_{(as)\,monodent}$ 1065 $CO\nu_{(as)\,bident}$ / $CC \nu_{(as)}$
η^1-Acetaldehyde	CH_3CH—O (on surface)	1650-1700 $CO\nu$
η^2-Aldehyde	CH_3—$\overset{H}{C}$—O (on surface)	2755 $CH\nu$ 1348 $CH_3 \delta$ 1275 $CO\nu$ 1148 $CC \nu$ 972 $CH_3 \rho$
Acyl	CH_3—C=O (on surface)	2978 $CH_3 \nu_{(as)}$ 2901 $CH_2 \nu_{(as)}$ / $CH_3 \nu_{(s)}$ 1636 $CO\nu$
Acetate	CH_3—C—O···O (on surface)	1547 $OCO\nu_{(as)}$ 1445 $OCO\nu_{(s)}$ 1338 $CH_3 \delta_{(s)}$
Carbonate	O···C···O / O (on surface)	1547 $OCO\nu_{(as)}$ 1318 $OCO\nu_{(s)}$
Acetone	CH_3CCH_3, O (on surface)	1735-1723 $CO\nu_{(as)}$ 1437/1365 $CH_3 \delta_{(s)}$ / $CH_3 \delta_{(as)}$ 1207-1225 C-Cν
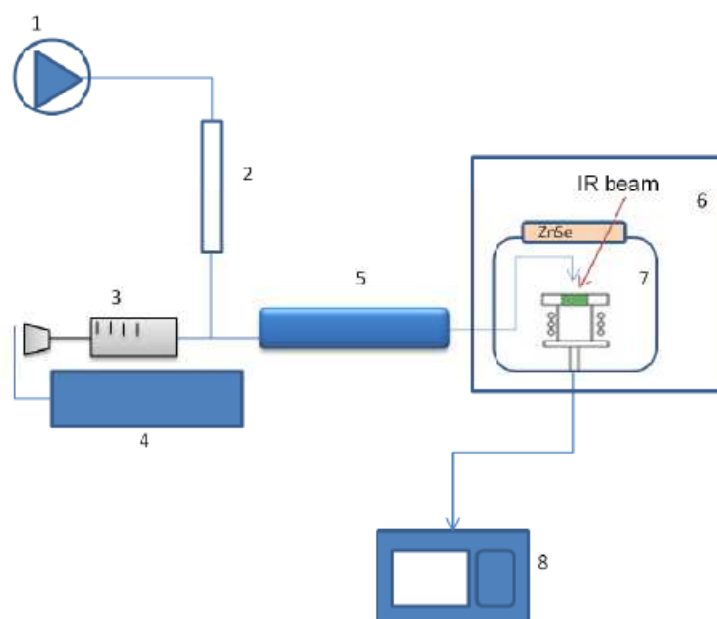
Figure 2-6. DRIFT-MASS scheme

1. Inert feed (He)	5. Heating stripe
2. Bubble flow meter	6. DRIFT apparatus
3. Syringe for liquid feed	7. High temperature cell
4. Syringe pump	8. MASS analyzer

2.11. Reactivity experiments: Chemical-Loop Reforming (CLR) process

The choice of reaction conditions and cycling time was adopted according to the study of Cocchi (reducing agent: methanol, T_{red} – 300 and 420°C/T_{re-ox} – 420°C, looping materials: Fe_3O_4, $CoFe_2O_4$ and $NiFe_2O_4$)[100] and Trevisanut (reducing agent: ethanol, T_{red}– 400 and 450°C/T_{re-ox} – 450°C, looping materials: Fe_3O_4, $CoFe_2O_4$ and $NiFe_2O_4$)[101]. Hence, previously obtained results suggested that the best reaction conditions have to be as follows: 1st step – ethanol reduction at T_{red}-450°C and 2nd step – water re-oxidation at T_{re-ox}-450°C. Reactivity experiments were carried out by loading app. 400 mg of M-modified ferrite, shaped in particles with diameter ranging from 0.25 to 0.6 mm; the reduction/re-oxidation step was carried out by feeding continuously a stream of ethanol (15.6 mol %)/water (29.3 mol %) vapors in N_2. Modifications to the conventional process were made in order to achieve its better effectiveness.

Laboratory-scale reactor

The reactivity tests were carried out in a laboratory-scale plant, depicted in Figure 2-7. Schematically, the plant can be subdivided into three zones: 1. Feeding Zone ("FZ"), 2. Reaction Zone ("RZ"), 3. Analysis Zone ("AZ").

In the 1st "FZ" a flow of carrier gases, mainly N_2, was controlled by two mass flow-meters (at v=30 mL/min); the outgoing gas was sent through a pre-heated pipe (T-150°C) where it was further mixed with a vaporized ethanol/water stream. Liquid reagents, like ethanol/water, were fed by means of a syringe pump set at a desired rate (ethanol - 0.8 mL/h; water - 0.55 mL/h).

The 2nd "RZ" is the zone where Chemical-Loop Reforming (CLR) reactions took place. The reactivity experiments were carried out in the fixed-bed quartz flow reactor (with an internal diameter of 12 mm and a length of 30 cm; the catalytic bed height was less than 5 mm) inserted into a furnace; while the temperature of the catalytic was measured by means of an axial thermocouple placed inside.

The third part is the "AZ", where the exit flow is sent to a micro-GC connected to a computer. Two different configurations were adopted for this zone, depending on the used reagent: during the reduction step carried out with ethanol, the stream, containing the products and the unconverted reagent, was sent directly through a heated line to the micro-GC; whereas during the re-oxidation step, carried out with water, the out flowing gases first passed through a water trap and only after that were sent to the micro-GC (such installation was made in order to avoid a damage of the GC-columns). The instrument used was an Agilent 3000A micro-GC installed on-line. The instrument was equipped with 3 columns: (a) a Plot Q column, carrier He, for the separation of CH_4, CO_2, H_2O, ethane, ethylene and propane; (b) a OV1 column, carrier He, for the separation of ethanol, acetaldehyde, H_2O, acetone, diethylether, ethylacetate, acetic acid, crotonaldehyde, pentanone-2, toluene; (c) a Molecular Sieve 5A column, carrier Ar, for the separation of H_2, O_2, N_2, CH_4, and CO. A Plot U backflash column was installed in order to avoid CO_2 and H_2O poisoning of the third column.

The instrument allowed carry out an analysis every 5 min during the 1st step and every 2 min during the 2nd step. This resulted in a large amount of data to be treated; therefore, the use of an Excel "macro" was necessary[101].
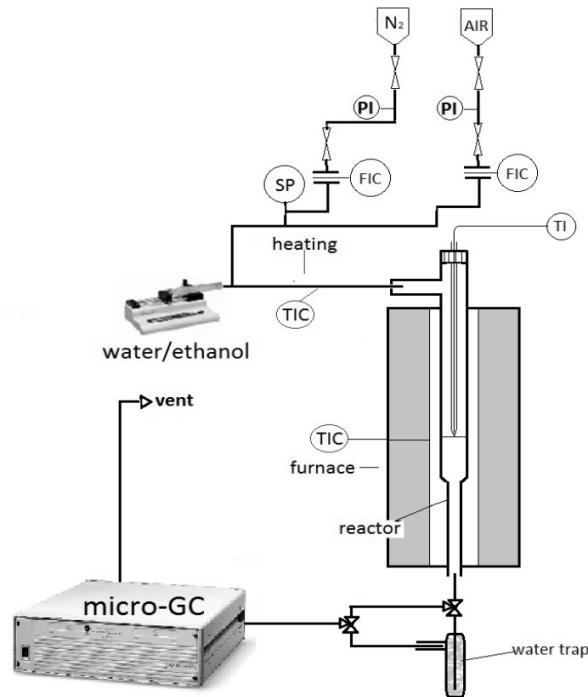
Figure 2-7. Schematic representation of the laboratory-scale plant

Data processing and parameters calculation

<u>*1st step – reduction*</u>

For the reduction step, we decided to feed a flowing gas containing 15.6 % of ethanol in 30 ml/min of nitrogen [100], at T-450°C. The resulting contact time (τ), app. 0.27 s, was calculated using the following equation:

$$\tau = \frac{\text{Vcat(ml)}}{\text{V'tot (ml/s)}}$$

Results obtained from the micro-GC analysis were expressed as $\%_v$ in the outlet stream. In order to calculate yields and conversion the following formulas were used:

$$Y_{P,A} = \frac{n_{P,out}}{n_{A,in}} = \frac{\%_v^{P,out} * \dot{V}_{tot}^{out}}{\%_v^{A,in} * \dot{V}_{tot}^{in}} = \frac{\%_v^{P,out}}{\%_v^{A,in}} * F_{vol}$$

$$X_A = \frac{\dot{n}^{A,in} - \dot{n}^{A,out}}{\dot{n}^{A,in}} = 1 - \frac{\%_v^{A,out}}{\%_v^{A,in} * F_{vol}}$$

* Considering a generic reaction A→P

F_{vol} is volumetric factor, which is obtained experimentally using N_2 as internal standard, and represents the change of the volumetric flow due to the variation of the number of moles.

$$F_{vol} = \frac{\%_v^{N_2,in}}{\%_v^{N_2,out}}$$

After a calibration, it was possible to determine the "instantaneous" molar yield (relative to the sampling instant) of the following compounds: CO, CO_2, CH_4, acetaldehyde, ethylene, ethane, ethylacetate, diethylether, acetic acid, propylene, propane, pentanone, toluene, acetone, H_2 and H_2O.

As the solid released oxygen to form products, until complete reduction was achieved, and due to the fact that coke or carbonaceous residues might accumulate on the solid during reaction, it was not possible to make an atomic balance neither of O atoms nor of C atoms. Therefore, an instantaneous balance on H atoms (the only species which was not contained in an accumulation term in material balances for the flow reactor) was carried out, which allowed to calculate: (a) the instantaneous balance on C and hence the amount of C accumulating on catalyst (expressed with the term "coke"), (b) the instantaneous balance of O and hence the amount of O released from the catalyst, and (c) the reduction degree of the solid.

2nd step – re-oxidation

For the oxidation step, since water was trapped before the GC inlet and therefore was not analyzed, it was necessary to determine the concentration of the different products, considering also water, by means of these equations:

$$\text{Conc}^{\text{vol,i}} = \%_{\text{GC}}^{\text{vol,i}} * \frac{\%_{\text{in}}^{\text{vol,N2}}}{\%_{\text{GC}}^{\text{vol,N2}}} \qquad \text{(where i} = H_2O, CO_2, CO, CH_4)$$

$$\text{Conc}^{\text{vol,H2O}} = 100 - \text{Conc}^{\text{vol,H2}} - \%_{\text{in}}^{\text{vol,N2}}$$

$$\%_{\text{real}}^{\text{vol,j}} = \frac{\text{Conc}^{\text{vol,j}}}{\sum \text{Conc}^{\text{vol,j}} + \%_{\text{in}}^{\text{vol,N2}}} \qquad \text{(where j} = H_2O, CO_2, CO, CH_4)$$

From the obtained concentrations, it was possible to calculate yields and conversions for the 2nd steps.

3rd step – regeneration

The regeneration step was carried out in air (20 mL/min) at 450$^{\text{o}}$C in order to increase the stability of the looping material and to overcome the deactivation problems, such as: a coke deposition/accumulation and an incomplete re-oxidation of M^0 phase after the first two steps. The reaction time was varied according to the amount of the remained coke (the end of the regeneration step was correlated to the amount of produced $CO_x \approx$ reached a value << 1 %$_{\text{vol}}$).

Chemical-Loop Reforming and Cycling Time variations

I. Conventional Chemical-Loop process, named as "2 steps CLR", consists of:

1st step – reduction - carried out with ethanol in N_2 flow at 450$^{\text{o}}$C;

2nd step – re-oxidation – carried out with water in N_2 flow at 450$^{\text{o}}$C.

II. Modified Chemical-Loop process, named as "3 steps CLR" consists of:

1st step – reduction - carried out with ethanol in N_2 flow at 450$^{\text{o}}$C;

2nd step – re-oxidation – carried out with water in N_2 flow at 450°C;

3rd step – regeneration – carried out in air at 450°C.

III. Cycling Time (CL) variations:

- Short cycles: 1, 3, 5 and 6 min;
- Long cycles: 20 and 60 min.

3. MATERIALS PREPARATION

All the ferrites used have been prepared using the co-precipitation method described elsewhere[102].

Co-precipitation

TYPE I SPINELS: MFe$_2$O$_4$ (where Fe/M=2/1 or Fe/M^1/M^2=4/1/1)

MFe$_2$O$_4$ferrospinels with different atomic ratio Fe/M (where M=Co, Cu, Mn or Cu/Co, Cu/Mn, Co/Mn) were prepared by the co-precipitation method (Figure 3-1). Nitrate precursors were used for all of the synthesized materials. The mixed solutions of metal precursors containing 100mL of 1M Fe(NO$_3$)$_3$·9H$_2$O, 100 mL of 0.5M M(NO$_3$)$_2$·xH$_2$O (or 100 mLof 0.25M M^1(NO$_3$)$_2$·xH$_2$O and 100 mL of M^2(NO$_3$)$_2$·xH$_2$O solutions)were put into a separation funnel and then drop-by-drop added into the reaction vessel containing 0.5L of 2 M NaOH aqueous solution at the temperature of 50°C under vigorous stirring with a constant speed. The suspensions were stirred for 2h at the constant temperature of 50°C adding NaOH 3M in order to maintain the pH above 13. The precipitates were separated by vacuum filtration by means of a Büchner funnel and then washed with about 1.5Lof distilled water at room temperature (RT), to remove sodium and nitrates ions.

TYPE II SPINELS: M$_{0.6}$Fe$_{2.4}$O$_y$ (where Fe/M=4/1 or Fe/M^1/M^2=8/1/1)

MFe$_2$O$_4$ferrospinels with different atomic ratio Fe/M (where M=Co, Cu, Mn, Mg, Ca or Cu/Co, Cu/Mn, Co/Mn) were prepared by the co-precipitation method (Figure 3-1). Nitrate precursors were used for all of the synthesized materials. The mixed solutions of metal precursors containing100mLof 1M Fe(NO$_3$)$_3$·9H$_2$O, 50 mL of 0.5M M(NO$_3$)$_2$·xH$_2$O (or 50 mL of 0.25M M^1(NO$_3$)$_2$·xH$_2$O and 50 mL of M^2(NO$_3$)$_2$·xH$_2$O solutions)were put into a separation funnel and then drop-by-drop added into the reaction vessel containing 0.5L of 2 M NaOH aqueous solution at the temperature of 50°C under vigorous stirring with a constant speed. The suspensions were stirred for 2h at the constant temperature of 50°C adding NaOH 3M in order to maintain the pH above 13. The precipitates were separated by vacuum filtration

by means of a Büchner funnel and then washed with about 1.5Lof distilled water at room temperature (RT), to remove sodium and nitrates ions.

Thermal treatments

All the washed samples (TYPE I and II) were dried at 120°C in air for 12 h, milled in agate mortar and then calcined in static air at 450°C for 8h with the heating rate of 10°C/min.

NOTE: A high surface area is important in order to make easier ferrites reduction, as explained by Cocchi and et al[103]. It has been shown that by increasing the calcination temperature, the surface area decreased continuously. Moreover, the annealing temperature cannot be lower than the reaction temperature. And, as reported by Trevisanut[101], the lower reaction temperature at which it was possible to obtain a fast enough reduction of MFe_2O_4(M=Fe, Co, Ni) ferrites is T-450°C. Taking into account these statements, the calcination temperature of *TYPE I* and *TYPE II* ferrites was maintained at 450°C.
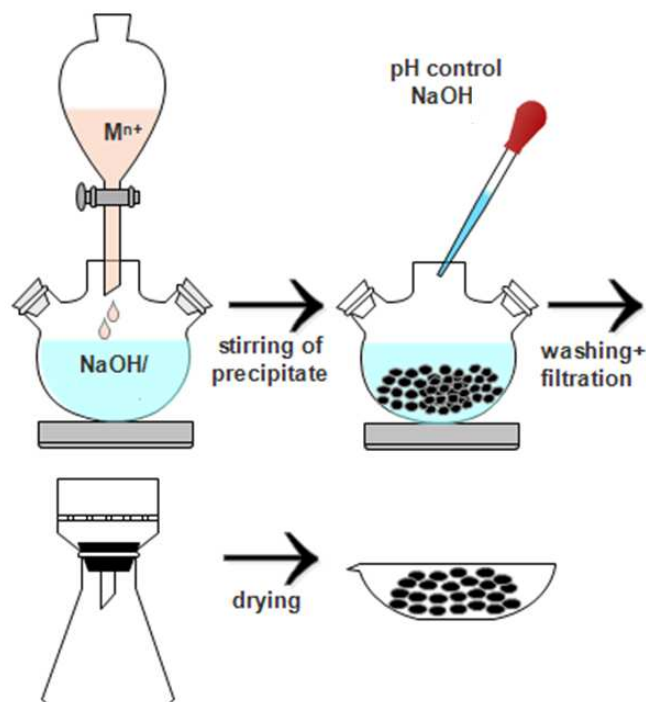
Figure 3-1. Scheme of the ferrospinels preparation

4. RESULTS AND DISCUSSION, PART I: TYPE I SPINELS (MFe$_2$O$_4$)

Bulk characterization of fresh materials

The section includes a discussion of the results obtained from several characterization techniques over fresh MFe$_2$O$_4$ (M-Co, Cu, Mn or Cu/Co, Cu/Mn, Co/Mn) samples: EDX analysis, XRD, N$_2$ adsorption, Raman Spectroscopy, TPR/TPO used to study bulk properties of freshly prepared ferrospinels.

4.1. Energy dispersive spectroscopy (EDX)

EDX is an addition characterization technique used for the elemental analysis or chemical characterization of the samples (the overall analytical accuracy is app. ± 2%). It is worth noting, that the EDX is a surface analysis technique, however it can be assimilated to a bulk analysis for nanoparticles smaller than the depth of penetration of the incident beam $x \sim 0.1 * E^{1.5}/\rho$[104] where x is in μm, E in keV and ρ in kg m^{-3}. For E 15 keV and ρ~6 the penetration depth is about 1 μm, so the EDX analysis of particles up to 2μ can be considered representative of the bulk composition.

Table 4-1 shows theoretical and measured ratios between Fe/M (M-foreign metal: Co, Cu, Mn or Cu/Co, Cu/Mn, Co/Mn). In all the cases the real ratio of Fe/M is slightly different from the expected one. This difference can first of all come from a weighing error and an incomplete pouring of the metal precursor solutions or to the slight hydration of the samples powders. Moreover, according to EDX analysis there is also a presence of Na < 1%$_w$ (as a residual which comes from the synthesis procedure).

Table 4-1. Results of EDX analysis

SAMPLE	Theoretical ratio, *Fe/M*	Measured ratio, *Fe/M*
CuFe$_2$O$_4$	Fe/Cu - 2/1	Fe/Co –2.16/1
Cu$_{0.5}$Co$_{0.5}$Fe$_2$O$_4$	Fe/Co - 4/1	Fe/Co –3.85/1
	Fe/Cu - 4/1	Fe/Cu– 4.21/1

CoFe$_2$O$_4$	Fe/Co - 2/1	Fe/Co –1.99/1
Co$_{0.5}$Mn$_{0.5}$Fe$_2$O$_4$	Fe/Co - 4/1	Fe/Co–4.39/1
	Fe/Mn - 4/1	Fe/Mn – 4.02/1
Cu$_{0.5}$Mn$_{0.5}$Fe$_2$O$_4$	Fe/Cu - 4/1	Fe/Cu –5.25/1
	Fe/Mn - 4/1	Fe/Mn –4.04/1
MnFe$_2$O$_4$	Fe/Mn - 2/1	Fe/Mn–1.89/1

4.2. XRD and N$_2$ adsorption
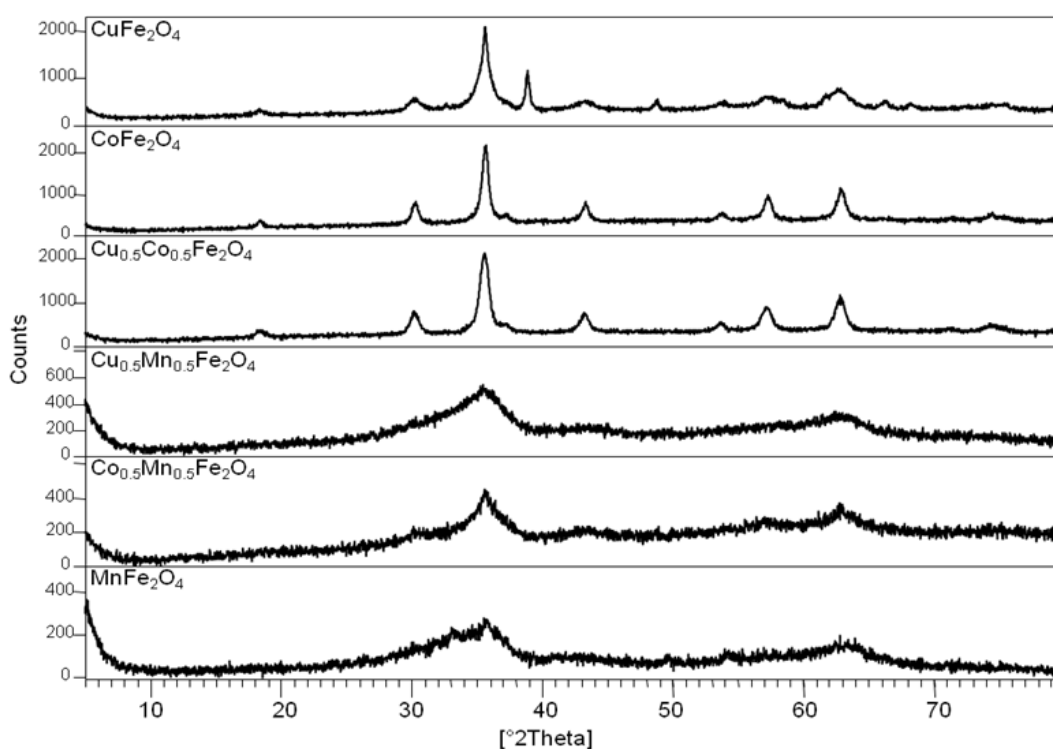
Figure 4-1. XRD patterns of fresh MFe$_2$O$_4$ samples calcined at 450°C for 8 h

The structure of fine powders is defined from XRD patterns (Figure 4-1). Resulted patterns confirm the formation of a spinel oxide, as the main phase for all the samples. However, the presence of CuO with a reflection at 38.8^o is detected for the Cu-modified sample (CuFe$_2$O$_4$

ferrite). Using Rietveld refinement, CuO is present as 21%$_w$ in the freshly prepared sample and this is taken into account for further calculations. Apparent broadening of the diffraction patters observed for the Mn-incorporated samples ($MnFe_2O_4$, $Co_{0.5}Mn_{0.5}Fe_2O_4$, $Cu_{0.5}Mn_{0.5}Fe_2O_4$) was attributed to a decrease in a particle size or as a fact of a lower crystallinity[105]. Similar results were previously obtained with Mn-substituted in $Co/Cu_{0.6-x}Mn_xFe_{2.4}O_y$ system (see PART II)[106]. In the Table 4-2are listed results of a specific surface area (SSA), a crystallite size (calculated by Scherrer eq. and) and a particle size (calculations are based on N_2 adsorption (BET) data) of the fresh powders calcined at 450^oC for 8 h.

Table 4-2. Specific surface area results (SSA) and crystallite/particle size of MFe_2O_4 ferrites

Sample name	SSA $_{fresh}$, m^2/g	Crystallite size (Scherrer eq.) $_{fresh}$, nm	Particle size (d$_{BET}$), nm
$CuFe_2O_4$	60	6.9	18.3
$Cu_{0.5}Co_{0.5}Fe_2O_4$	67	10.4	16.5
$CoFe_2O_4$	69	12.0	16.2
$Co_{0.5}Mn_{0.5}Fe_2O_4$	141	3.5	8.0
$Cu_{0.5}Mn_{0.5}Fe_2O_4$	112	-	10.0
$MnFe_2O_4$	165	-	6.9

All Mn-substituted ferrites exhibit a higher surface area even after the thermal treatment which first of all can be attributed to the presence of smaller particles (Table 4-2) along with the existence of an amorphous phase.

4.3. Raman Spectroscopy

Raman spectra of fresh materials calcined at $450^{\circ}C$ are shown in Figure 4-2. Cu/Co-substituted ferrites (Figure 4-2, D-F) reveal 5 distinct Raman modes, predicted by the literature: $A_{1g(1)}$ (690 cm^{-1}), $F_{2g(3)}$ (560 cm^{-1}), $F_{2g(2)}$ (472 cm^{-1}), E_g (305 cm^{-1}). The literature is discrepant to the assignment of the Raman active modes within a spinel lattice. However, the highest frequency mode ($A_{1g(1)}$) at 690 cm^{-1} is usually assigned to the symmetric stretching of the M-O bond in a T_d void[107,108,109]. In addition to the 5 theoretically predicted modes, samples D and E exhibit an additional peak at $A_{1g(2)}$ 616 cm^{-1}, which caused by disorder effects of M^{2+} and Fe^{3+} over the Td and Oh sites[109]. This shoulder for a $CoFe_2O_4$ spinel was also observed by Chandramohan and others[107]. They correlated an increase in the intensity of $A_{1g(2)}$ mode with lowering of inversion parameter in the following spinel, which also being supported by Mössbauer studies.
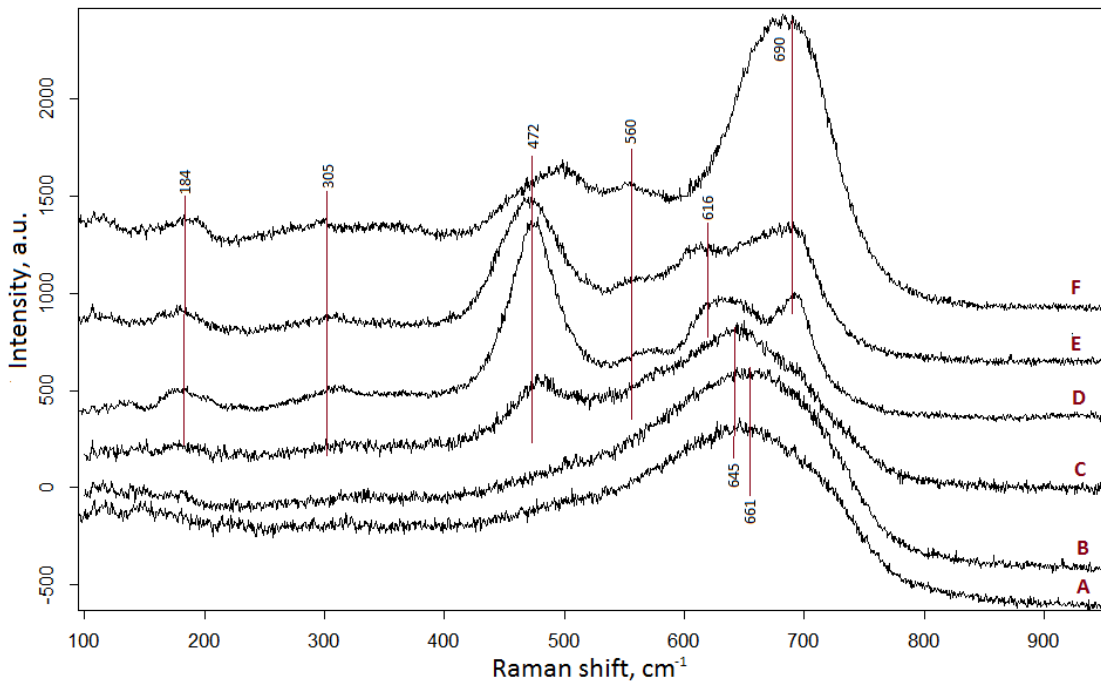
Figure 4-2. Raman spectra of MFe_2O_4 ferrites: A-$MnFe_2O_4$, B-$Cu_{0.5}Mn_{0.5}Fe_2O_4$, C-$Co_{0.5}Mn_{0.5}Fe_2O_4$,D-$CoFe_2O_4$,E-$Cu_{0.5}Co_{0.5}Fe_2O_4$ and F-$CuFe_2O_4$

Looking at the spectra of A-C samples (Mn-substituted ferrites), the position of the $A_{1g(1)}$ shifts to a lower frequency at about 661 cm^{-1} along with a distinct broadening of the

following spectra. The similar behavior was observed for Co/Mn-incorporation[106]. Hence, Mn^{2+} ions are proposed to partially replace Fe^{3+} ions in the Td sites, which may cause the change of the inversion degree towards the formation of the normal spinel.[110,111] The low intensity of the peaks and partial energy shifts can be related also to a lack of a long range in the small dimension systems along with an effect due to high defectivity[107] and a low crystallinity as confirmed by XRD.

4.4. Temperature programmed reduction/oxidation (TPR1/O/R2)

TPR curves: signal-vs-T

The reduction of the iron$^{(II,III)}$oxide: $Fe_3O_4 \rightarrow FeO \rightarrow Fe$ strongly depends on the presence of another metal oxide in the resulted M-modified ferrite [112–115,82,106,116]. According to the XRD and Raman results, discussed previously, the main phase obtained at the end of the preparation procedure was a Fe_3O_4-like spinel oxide phase with a generic formula of MFe_2O_4. Following the TPR profiles of M-modified ferrites, plotted in Figure 4-4,mainly two steps of the reduction processes can be distinguished: the reduction of iron oxide to metallic iron and the reduction process of other incorporated metal oxide to its metal. However, it's difficult to distinguish each stage of the reduction since some steps seamlessly flow from one to another which finally causes an overlap. Nevertheless, the obtained results and its further elaboration based on the nature of the foreign metals (M^{2+}), their reduction potentials and the amount of consumed H_2helped us to track back possible steps of the MFe_2O_4 reduction process, which are summarized in Figure 4-3.
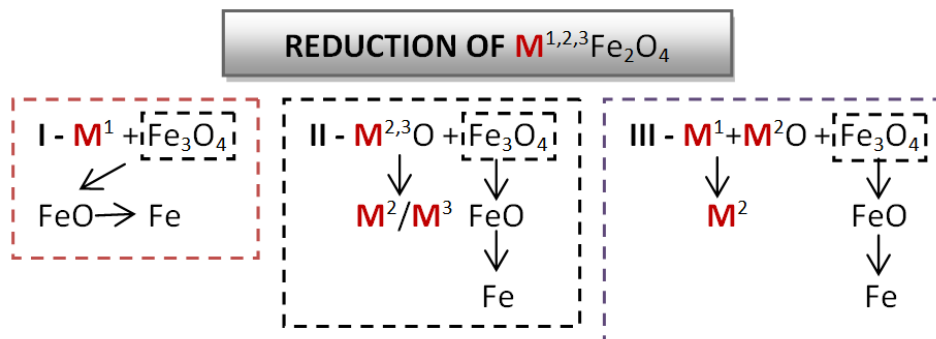
Figure 4-3. Reduction scheme of MFe_2O_4 ferrites

Looking at the TPR profile of $CuFe_2O_4$, the first peak at 240^oC can be attributed to a starting reduction of the initially present copper oxide ($CuO \sim 21\%_w$) to the metallic copper (Cu^0), which contributes to $\alpha \sim 16\%$. The second peak at $\sim 340^oC$ was attributed to a primary stepwise reduction of the spinel with a final formation of Cu^0 and Fe_3O_4 phases ($\alpha \sim 27\%$), following the pass I (Figure 4-3); the further reduction of the Fe_3O_4 to FeO and FeO to Fe^0_{incom} appears at higher temperatures with a total $\alpha \sim 70\%$. The reduction of $Cu_{0.5}Mn_{0.5}Fe_2O_4$ and $Cu_{0.5}Co_{0.5}Fe_2O_4$ samples follows the pass III (Figure 4-3), where the first peak at lower temperature corresponds to the stepwise exclusion or/and reduction of the M-incorporated cations to form M (Cu^0), MO (MnO/CoO) and Fe_3O_4 phases. Further reduction of the $Cu_{0.5}Co_{0.5}Fe_2O_4$ ferrite goes through the following stages: (1) $Fe_3O_4 \rightarrow FeO$ (+0,77eV), (2) $CoO \rightarrow Co^0$ (-0.28 eV), (3) $FeO \rightarrow Fe^0_{incom}$ (-0.44 eV), reaching $\alpha \sim 65\%$. On the other hand, the reduction of $Cu_{0.5}Mn_{0.5}Fe_2O_4$ ferrite can be schematized as follows: (1) $Fe_3O_4 \rightarrow FeO$, (2) $FeO \rightarrow Fe^0_{incom}$, which corresponds to $\alpha \sim 65\%$. It turned out that it is difficult for MnO to be reduced to its metallic component Mn^0, due to its highly negative reduction potential (-1.18 eV)[106] and thus this step can occur only at very extreme temperatures (see ΔG^0_{react}, Table 4-3). The reduction of the $CoFe_2O_4$, $Co_{0.5}Mn_{0.5}Fe_2O_4$ and $MnFe_2O_4$ samples follows the pass II in Figure 4-3. In a case of $CoFe_2O_4$, the first small peak at 400^oC can be attributed to the primary spinel reduction with a stepwise formation of CoO and Fe_3O_4 phases (which corresponds to $\alpha \sim 8\%$), whereas in Mn-incorporated ferrites ($MnFe_2O_4$ and $Co_{0.5}Mn_{0.5}Fe_2O_4$) this step starts at lower temperature. However, the total reduction extent of $CoFe_2O_4$ ($\alpha \sim 86\%$) was much higher than of the $Co_{0.5}Mn_{0.5}Fe_2O_4$ (61%) and $MnFe_2O_4$ (45%) samples and can be explained by the formation of the hardly reducible phase of MnO (or in the form of Mn_xFe_yO oxide).

COMPLETE REDUCTION SCHEME OF MFe$_2$O$_4$ FERROSPINELS

Cu$_{0.5}$Mn$_{0.5}$Fe$_2$O$_4$
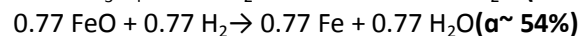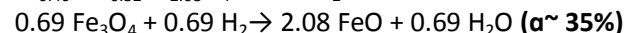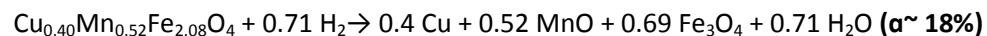
Cu$_{0.40}$Mn$_{0.52}$Fe$_{2.08}$O$_4$ + 0.71 H$_2$ → 0.4 Cu + 0.52 MnO + 0.69 Fe$_3$O$_4$ + 0.71 H$_2$O **(α~ 18%)**

0.69 Fe$_3$O$_4$ + 0.69 H$_2$ → 2.08 FeO + 0.69 H$_2$O **(α~ 35%)**

0.77 FeO + 0.77 H$_2$ → 0.77 Fe + 0.77 H$_2$O **(α~ 54%)**

At the end of TPR1: incomplete reduction of FeO and MnO phases: Mn$_x$Fe$_y$O

→Mn$_{0.29}$Fe$_{0.72}$O

CuFe$_2$O$_4$ (CuO*~ 21 %$_w$)

CuO* + H$_2$ → Cu + H$_2$O **(α~ 16%)**

Cu$_{0.4}$Fe$_{2.6}$O$_4$ + 0.52 H$_2$ → 0.4Cu + 0.87 Fe$_3$O$_4$ + 0.52 H$_2$O **(α~ 27%)**

0.87 Fe$_3$O$_4$ + 0.87 H$_2$ → 2.61 FeO + 0.87 H$_2$O **(α~ 45%)**

1.17 FeO + 1.17 H$_2$ → 1.17 Fe + 1.17 H$_2$O **(α~ 70%)**
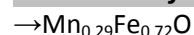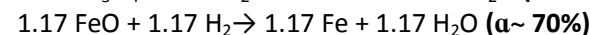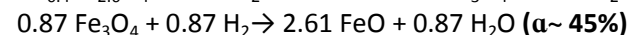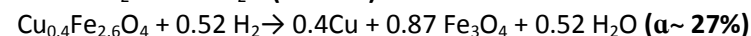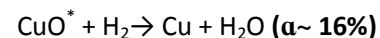
At the end of TPR1: incomplete reduction of FeO phase

* the reduction of segregated CuO phase

Cu$_{0.5}$Co$_{0.5}$Fe$_2$O$_4$
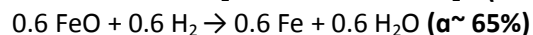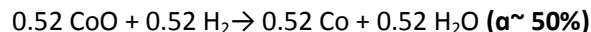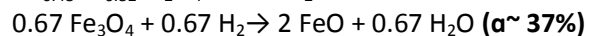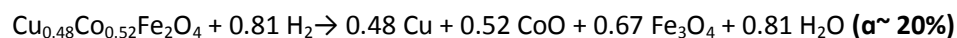
Cu$_{0.48}$Co$_{0.52}$Fe$_2$O$_4$ + 0.81 H$_2$ → 0.48 Cu + 0.52 CoO + 0.67 Fe$_3$O$_4$ + 0.81 H$_2$O **(α~ 20%)**

0.67 Fe$_3$O$_4$ + 0.67 H$_2$ → 2 FeO + 0.67 H$_2$O **(α~ 37%)**

0.52 CoO + 0.52 H$_2$ → 0.52 Co + 0.52 H$_2$O **(α~ 50%)**

0.6 FeO + 0.6 H$_2$ → 0.6 Fe + 0.6 H$_2$O **(α~ 65%)**

At the end of TPR1: incomplete reduction of FeO phase

CoFe$_2$O$_4$

CoFe$_2$O$_4$ + 0.33 H$_2$ → CoO + 0.67 Fe$_3$O$_4$ + 0.33 H$_2$O **(α~ 8%)**

0.67 Fe$_3$O$_4$ + 0.67 H$_2$ → 2 FeO + 0.67 H$_2$O **(α~ 25%)**

CoO + H$_2$ → Co + H$_2$O **(α~ 50%)**

1.44 FeO + 1.44 H$_2$ → 1.44 Fe + 1.44 H$_2$O **(α~ 86%)**
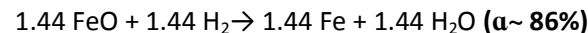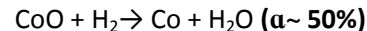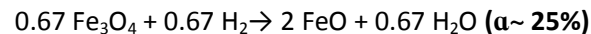
At the end of TPR1: incomplete reduction of FeO phase

Co$_{0.5}$Mn$_{0.5}$Fe$_2$O$_4$
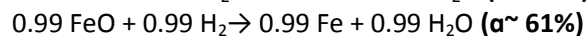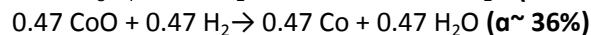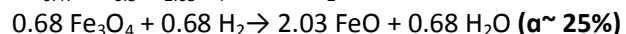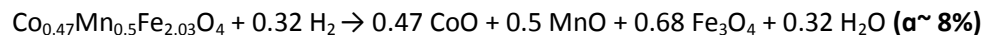
Co$_{0.47}$Mn$_{0.5}$Fe$_{2.03}$O$_4$ + 0.32 H$_2$ → 0.47 CoO + 0.5 MnO + 0.68 Fe$_3$O$_4$ + 0.32 H$_2$O **(α~ 8%)**

0.68 Fe$_3$O$_4$ + 0.68 H$_2$ → 2.03 FeO + 0.68 H$_2$O **(α~ 25%)**

0.47 CoO + 0.47 H$_2$ → 0.47 Co + 0.47 H$_2$O **(α~ 36%)**

0.99 FeO + 0.99 H$_2$ → 0.99 Fe + 0.99 H$_2$O **(α~ 61%)**

At the end of TPR1: incomplete reduction of FeO and MnO phases: Mn$_x$Fe$_y$O

→Mn$_{0.33}$Fe$_{0.67}$O

MnFe$_2$O$_4$

Mn$_{1.04}$Fe$_{1.96}$O$_4$ + 0.35 H$_2$ → 1.04 MnO + 0.65 Fe$_3$O$_4$ + 0.35 H$_2$O **(α~ 8%)**

0.65 Fe$_3$O$_4$ + 0.65 H$_2$ → 1.96 FeO + 0.65 H$_2$O **(α~ 25%)**

0.82 FeO + 0.82 H$_2$ → 0.82 Fe + 0.82 H$_2$O **(α~ 45%)**

At the end of TPR1: incomplete reduction of FeO and MnO phases:

Mn$_x$Fe$_y$O → Mn$_{0.48}$Fe$_{0.52}$O
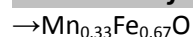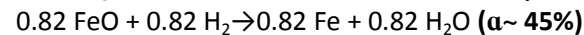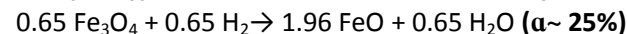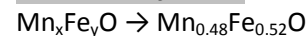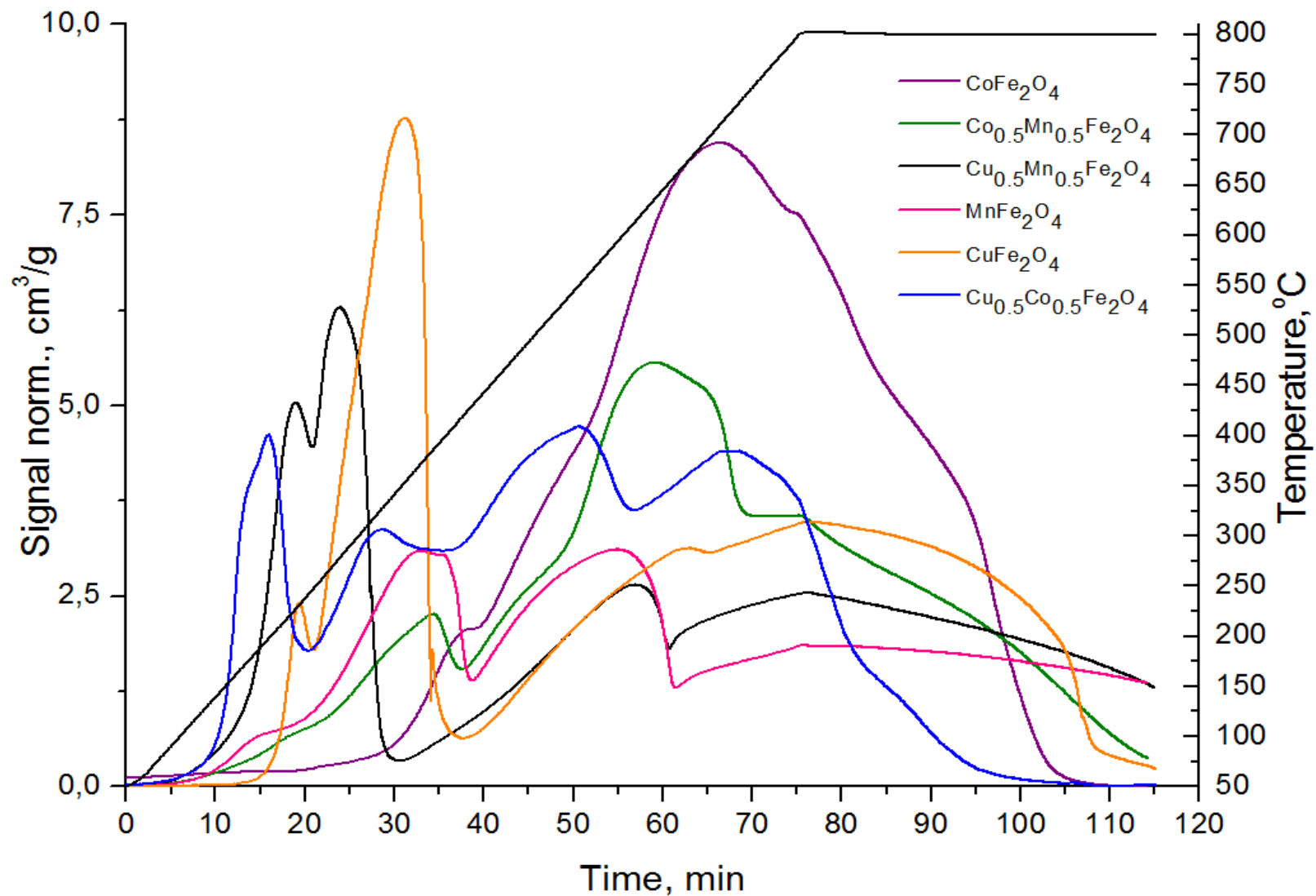
Figure 4-4. TPR profiles of MFe$_2$O$_4$ ferrites with temperature program from 50 to 800°C (+isotherm at T-800°C for 40 min)

TPR curves: α-vs-T

Different modifications in the composition of bare-Fe_3O_4 to MFe_2O_4 (M-Cu, Co, Ni, Mn, Mg, Ca, etc.) have been done by many research groups in order to change its redox properties. Moreover, the so called "promoting effect" of Cu^{2+} was also seen [116,117,74,118,], however a real role of copper ions and the reduction mechanism has not been clearly elucidated. Thus, the primary idea was to focus our study on a deep understanding of TPR profiles with a further data elaboration for possible clarification of MFe_2O_4 reduction mechanism.
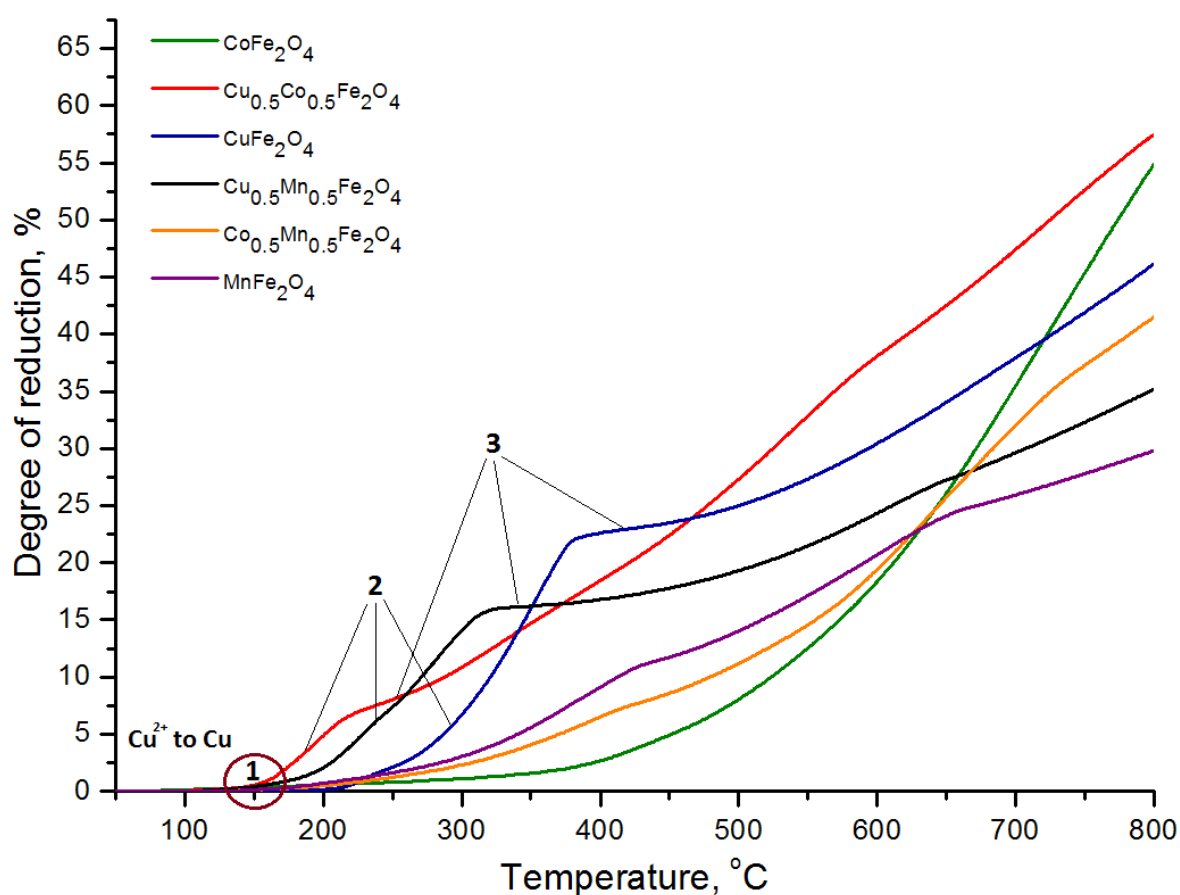
Figure 4-5. α vs T reduction curves of MFe_2O_4 ferrites

Conventionally, the shape of an (*α vs time)* isotherm can reveal information on the mechanism of solid state reactions[119]. And, according to A. Jones, the reduction of CuO produces an S-shape (sigmoidal) reduction isotherm familiar for a "nucleation and autocatalytic" reduction model, where the reduction consists of three distinct stages: 1. induction, 2. autocatalysis and 3. decreasing rate[120]. However, some oxides may be reduced via spontaneous nucleation over an entire surface which is usually characterized by a continuously decreasing rate. If the nucleation is very fast, the real formation of separated

and independent nuclei cannot be distinguished leading to a total coverage of the solid oxide particle with a thin layer of metallic product, and typical for $Mn_xO_y \rightarrow Mn$ redox system[121].Thus, we decided that the best depiction of the reduction models of MFe_2O_4 ferrites can be described being based on these two mechanisms.

Figure 4-5shows *α-versus-T* reduction curves of MFe_2O_4 samples. Increasing the temperature of the reduction markedly increased the reduction rate of all oxides regardless of the nature of incorporated metal M and this in turn can be justified by Arrhenius equation (exponential relation between K and T). However, looking at the reduction curves of Cu-incorporated ferrites a peculiar behavior is observed that cannot be explained only by an increase in the temperature. All three samples ($CuFe_2O_4$, $Cu_{0.5}Co_{0.5}Fe_2O_4$ and $Cu_{0.5}Mn_{0.5}Fe_2O_4$) produce the S-shaped (sigmoidal) reduction curve with a strong acceleration of the reduction rate above 160-200°C, which was associated with a self-catalyzed nucleation (autocatalysis). Apparently, nuclei catalyze further nuclei formation, due to branching of nuclei or to the catalytic role of the Cu metal in H_2dissociation.According to this, an effect of Cu^0 can be described as follows: Cu^0 formed in the early stage of the reduction ($Cu^{2+} \rightarrow Cu^{0*}$) is further catalyzing the reduction of a newly reformed Fe-enriched spinel (with generic formula - $M_{1-x}Fe_{(2+x)}O_4$). The reduction occurs on the basis of hydrogen spill over effect, where Cu^0 plays role of a catalyst which is needed to dissociate H_2 into 2H atoms. Essentially, hydrogen atoms would migrate from a hydrogen-rich (Cu^0) to a hydrogen-poor (spinel) surface (see Figure 4-6, A). On the other hand, we cannot ignore thermodynamic aspects of the following reaction; and from an enthalpy point of view (Table 4-3) the reduction of CuO to Cu^0 is an exothermal reaction with released energy of about 84 kj/mol$_{CuO}$ (**CuO+H$_2$=Cu+H$_2$O, ΔH$^0_{react}$=-84.53 kj/mol$_{CuO}$**). Using a heat equation (Q=C$_p$·m·ΔT) it is possible to calculate an approximate value of the temperature rise (T$_{rise}$= 768°C if 100% Cu^{2+} ions being reduced, however even if 50% of Cu^{2+} ions are reduced the T$_{increase}$ = 384°C, if 10% of Cu^{2+}T$_{increase}$=77°C, which is still very high). Moreover, we should take into consideration also the flowing gas mixture (5% of H_2 in Ar, *v*=30 ml/min), in that case the T$_{increase}$=118°C, when 100% of Cu^{2+} ions were reduced, or T$_{increase}$=12°C when only 10% of Cu^{2+} reduced. However, self-heating effects would result if too large amount of the sample was used. Thus, considering that experiments were carried

out under the small scale (with the sample mass of about 100 mg) and the self-heating effect in this case can be neglected.

Coming back to *α-versus-T* curves, the reduction of the $MnFe_2O_4$ and $Co_{0.5}Mn_{0.5}Fe_2O_4$ samples produces elongated curves without a strong acceleration of the reaction rate which led us to the idea of a different model, we called an "egg-shell" model (see Figure 4-6, B). Like, if the ferrite reduction goes through a total coverage of the solid oxide particle with a thin layer of newly formed product. Hence, the reduction of $MnFe_2O_4$ and $Co_{0.5}Mn_{0.5}Fe_2O_4$ ferrites can be better described by a spontaneous reduction over the entire surface which occurs immediately on the contact with hydrogen and lead to the expelling of Mn^{2+} cations out of the spinel structure with a formation of the new phases: a Fe-rich reformed spinel $(M_{1-x}Fe_{2+x}O_4)$ and a non-reducible layer of MnO oxide (since: $MnO \rightarrow Mn^0$, ε=1.18 eV)[106], like an "egg-shell" (or in the form of a thermodynamically stable oxide solid solution - Mn_xFe_yO, supported by ex-situ XRD study). This elucidate the elongated shape of the reduction curve, since the initially formed compact MnO/Mn_xFe_yO layer may act as a "shielding" layer, causing an aggravation of H_2 diffusion into the bulk leading to a starvation and a decrease of the total reduction rate of the core (reformed spinel $Mn_{1-x}Fe_{2+x}O_4$).

Table 4-3. Calculated values for ΔH^0_{react} and ΔG^0_{react}

REACTION	ΔH^0_{react}, kj/mol	ΔG^0_{react}, kj/mol
		T-298 K
$CuO+H_2=Cu+H_2O$	exothermic, ΔH^0_{react}=-84.53 kj/mol$_{CuO}$	-99.05
$Co_3O_4+H_2=3CoO+H_2O$	exothermic, ΔH^0_{react}=-45.63 kj/mol$_{Co3O4}$	-76.26
$CoO+H_2=Co+H_2O$	exothermic, ΔH^0_{react}=-3.89 kj/mol$_{CoO}$	-14.38
$Fe_2O_3+3H_2=2Fe+3H_2O$	endothermic, ΔH^0_{react}=+98.72kj/mol$_{Fe2O3}$	56.55
$3Fe_2O_3+H_2=2Fe_3O_4+H_2O$	exothermic, ΔH^0_{react}=-2.086 kj/mol$_{Fe2O3}$	-14.84
$Fe_3O_4+4H_2=3Fe+4H_2O$	endothermic, ΔH^0_{react}=+151.1kj/mol$_{Fe3O4}$	101.04

$Fe_3O_4+H_2=3FeO+H_2O$	endothermic, $\Delta H^0_{react}=+60.69$ kj/mol$_{Fe3O4}$	32.69
$FeO+H_2=Fe+H_2O$	endothermic, $\Delta H^0_{react}=+30.134$ kj/mol$_{FeO}$	22.79
$MnO+H_2=Mn+H_2O$	endothermic, $\Delta H^0_{react}=+143.39kj/mol_{MnO}$	134.33
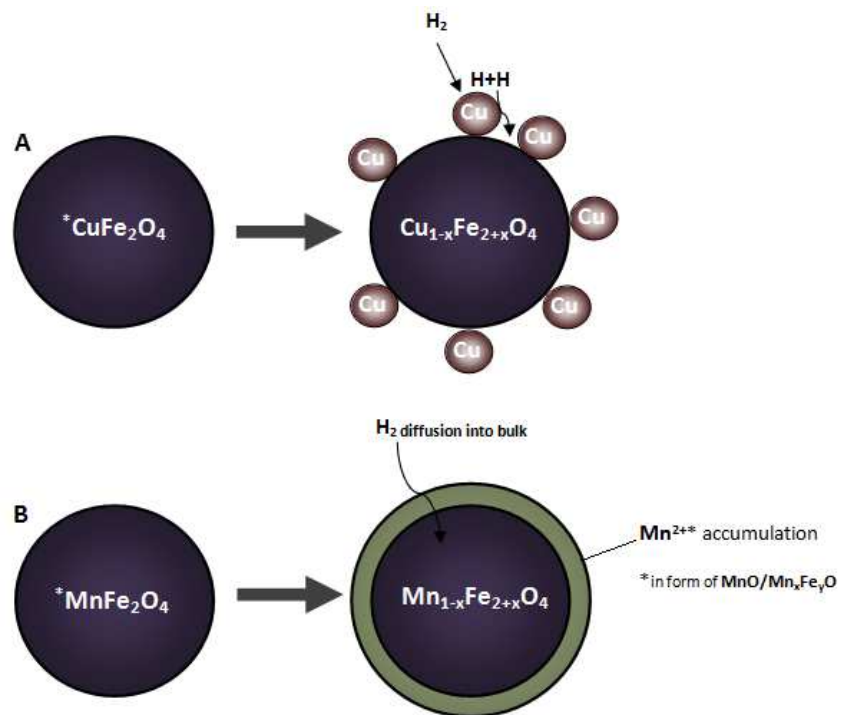
Figure 4-6. Schematic representation of H_2-reduction over: A-CuFe$_2$O$_4$, as "nucleation/autocatalytic" model and B-MnFe$_2$O$_4$, as an "egg-shell" model

CoFe$_2$O$_4$

Cu$_{0.5}$Co$_{0.5}$Fe$_2$O$_4$

CuFe$_2$O$_4$

Cu$_{0.5}$Mn$_{0.5}$Fe$_2$O$_4$
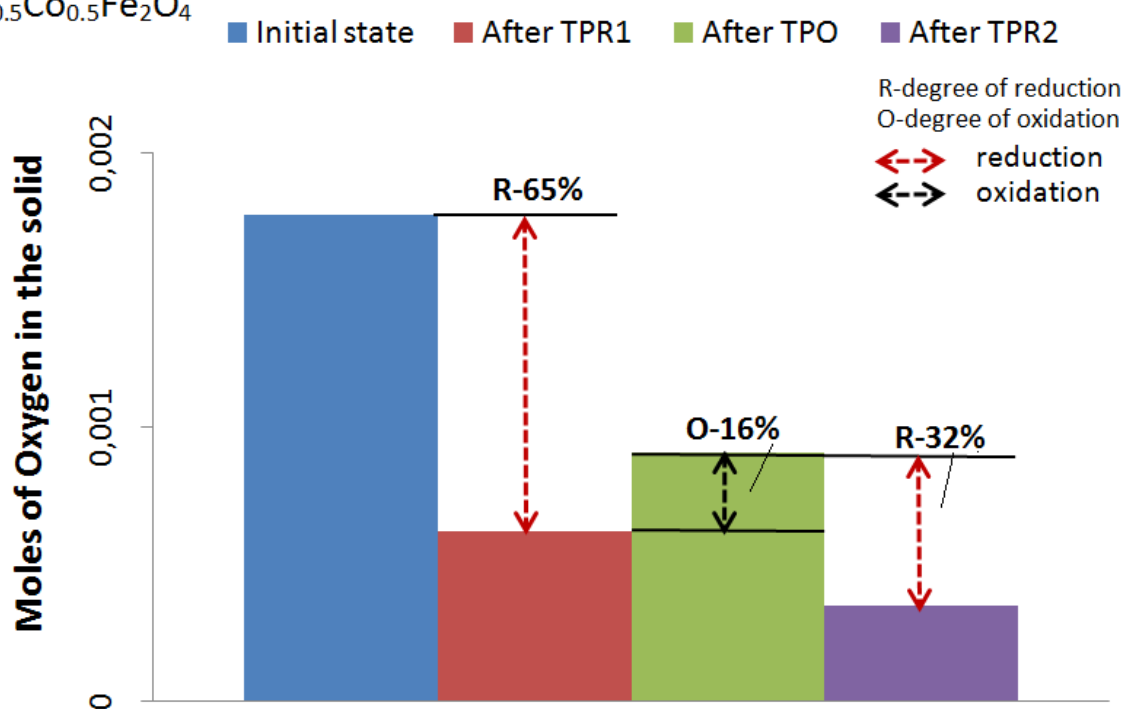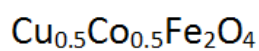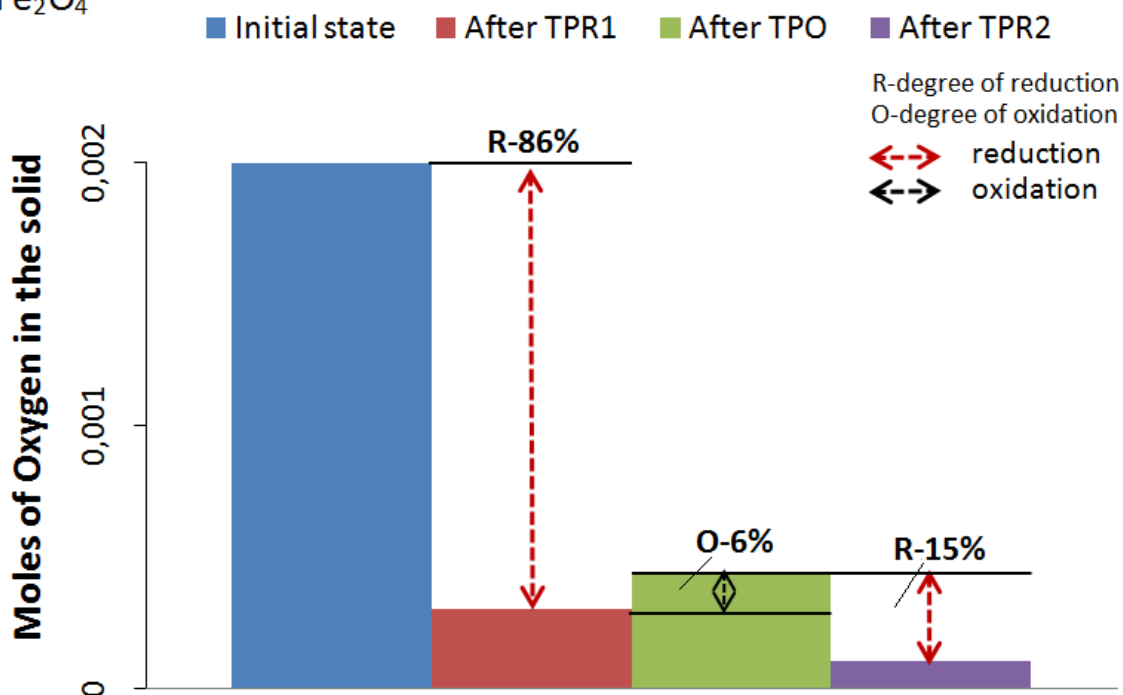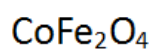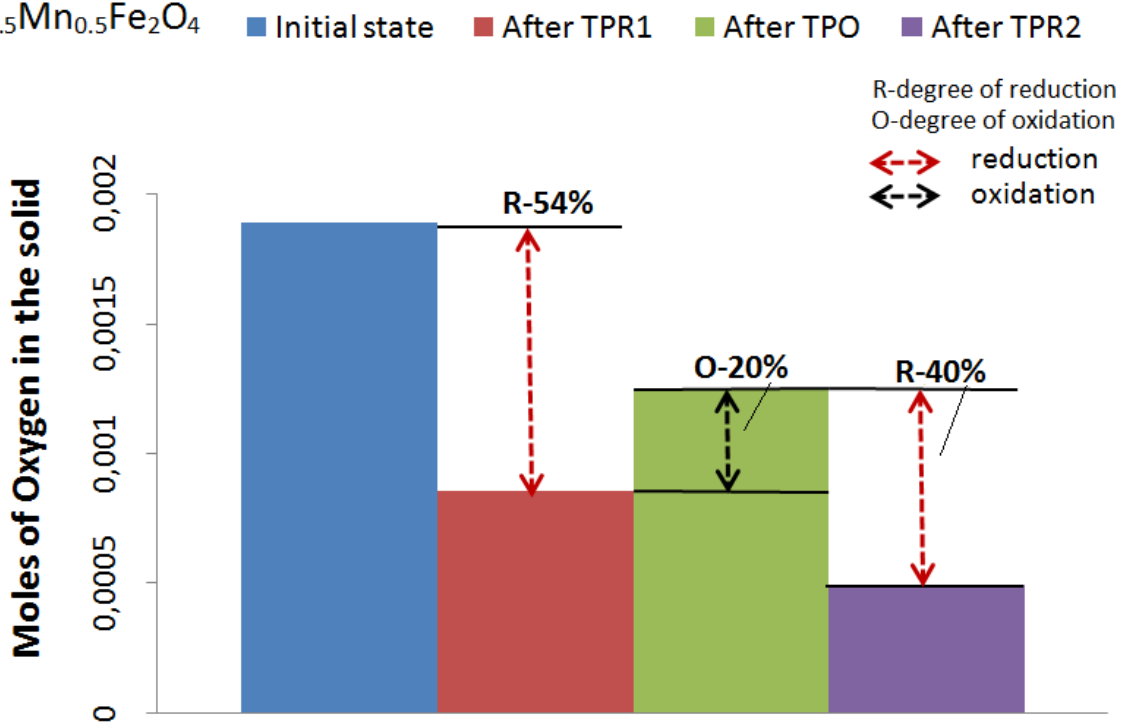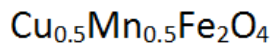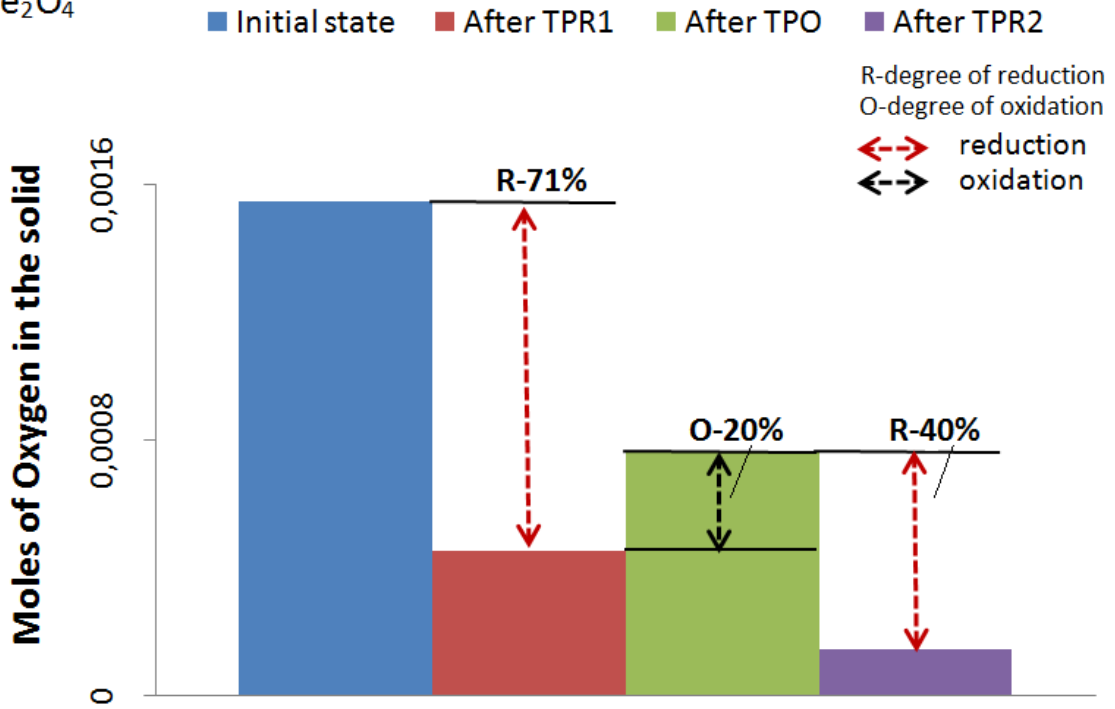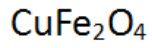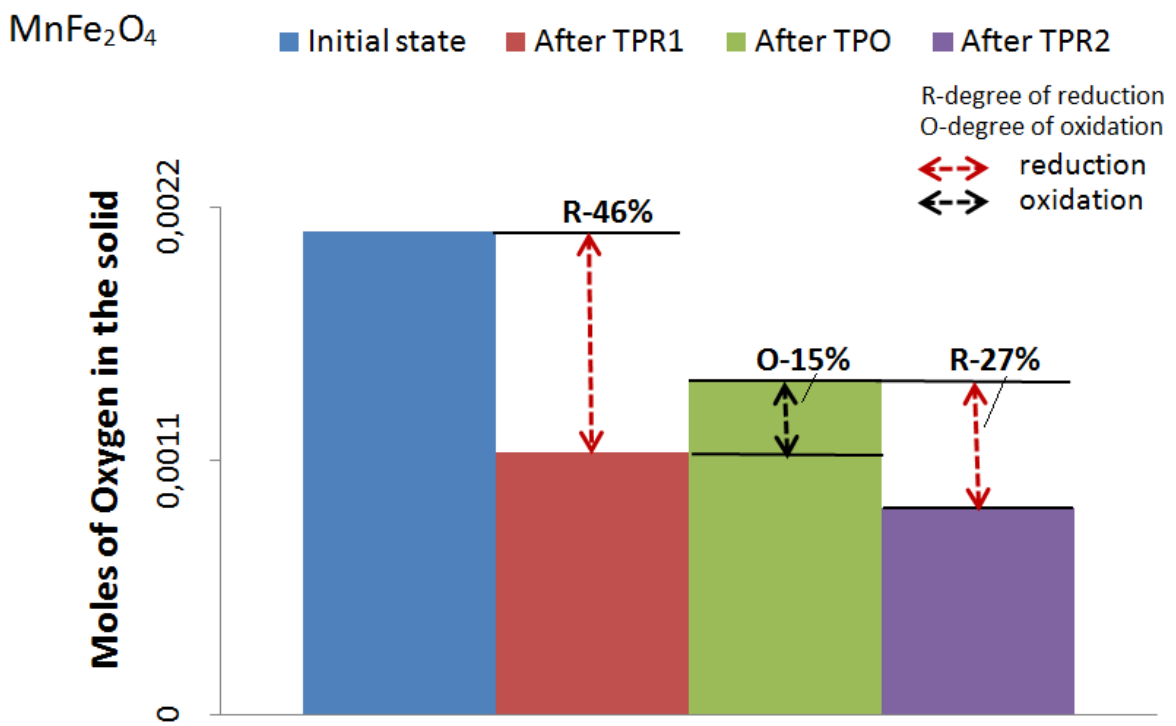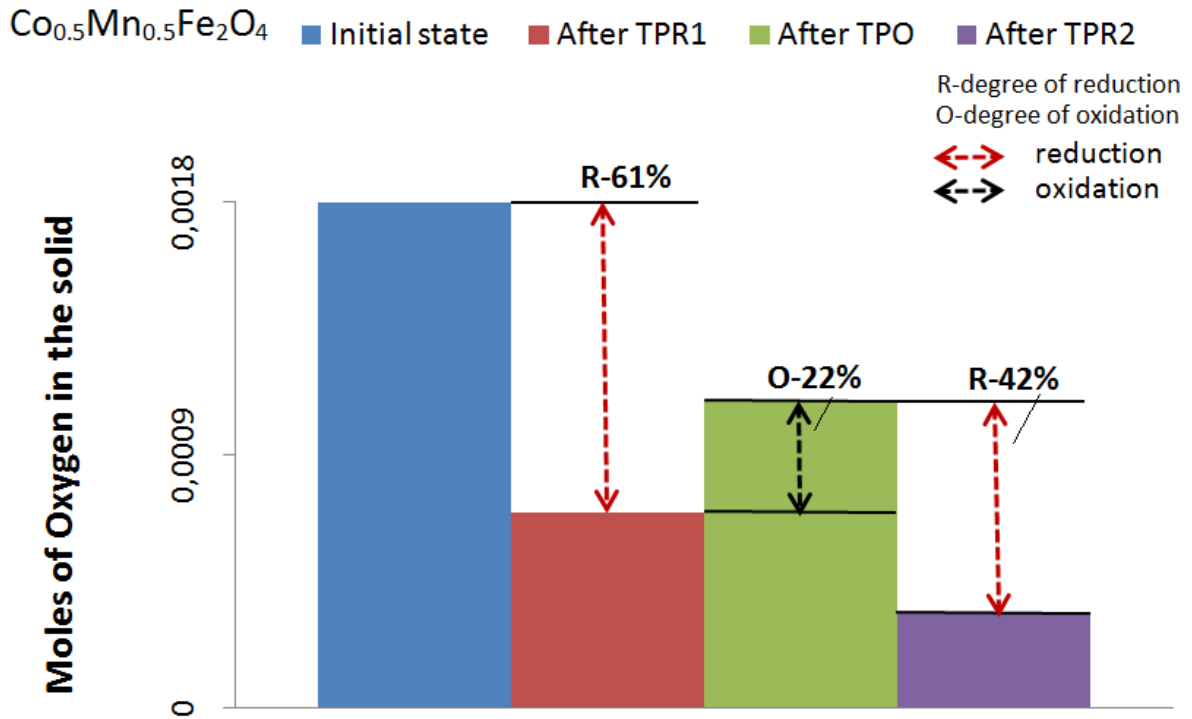
Figure 4-7. Reduction/oxidation evolution of MFe_2O_4 ferrites, derived from the results obtained during TPR1/TPO/TPR2 sequence

Table 4-4. Integrated values of consumed H_2/O_2 during TPR/O experiments

SAMPLE	Integrated values for H_2-/O_2, cm^3/g		
	TPR1	TPO	TPR2
$CoFe_2O_4$	357	24	63
$Cu_{0.5}Co_{0.5}Fe_2O_4$	267	66	130
$Co_{0.5}Mn_{0.5}Fe_2O_4$	258	93	176
$Cu_{0.5}Mn_{0.5}Fe_2O_4$	229	86	167
$CuFe_2O_4$	274	77	155
$MnFe_2O_4$	192	64	111

In addition to the conventional TPR measurements, discussed in Paragraph 4.4, MFe_2O_4 ferrospinels were tested in the TPR1-TPO-TPR2 sequence, which gave the important information on resulted interior redox properties of the binary/ternary complex systems.

Table 4-4 shows the integrated values of consumed H_2 and O_2 during TPR1/TPO/TPR2 experiments at 800°C (*note*: calculations are made based on the actual H_2/O_2 consumption with respect to the initially loaded mass, cm^3/g). In order to grasp the reason of the decreasing values for H_2 consumption during the second reduction (TPR2), see Table 4-4 , it was decided to calculate the actual degrees of reduction (TPR1)/oxidation (TPO)/reduction (TPR2) starting from initial moles of oxygen in the solid at the beginning of the experiment, as depicted in Figure 4-7 (*note:* an oxidation degree (O) was calculated starting from the experimentally obtained moles of consumed oxygen divided on the initial value, which assumed to be the max value whenever the material is being fully re-oxidized to its primary state – [($n_{Ox}^{TPO}/n_{Ox}^{TOT}$)·100]; whereas a reduction degree (R) during the TPR1/TPR2 experiments was calculated based on the amount of removed oxygen divided on its initial amount in a fresh sample – [(n_{Ox}^{TPR1} (or n_{Ox}^{TPR2})/n_{Ox}^{TOT})·100]. Considering the obtained results, several statements can be made:

TPR1:

- Co/Cu-incorporation leads to a higher reduction extent, i.e. is more attractive in terms of potentially higher reducibility: $CoFe_2O_4$ (R-86%), $CuFe_2O_4$ (R-65%) and

$Cu_{0.5}Co_{0.5}Fe_2O_4$ (R-71%); whereas, on the contrary, Mn-incorporation leads to a lower intrinsic reducibility of the resulted ferrites: $MnFe_2O_4$ (R-46%), $Co_{0.5}Mn_{0.5}Fe_2O_4$ (R-61%) and $Cu_{0.5}Mn_{0.5}Fe_2O_4$ (R-54%)

TPO:

- Mn/Cu-incorporation leads to a higher oxidation extent, i.e. is more attractive for the performing an easier re-oxidation: $MnFe_2O_4$ (O-15%), $Co_{0.5}Mn_{0.5}Fe_2O_4$ (O-22%), $Cu_{0.5}Mn_{0.5}Fe_2O_4$ (O-20%), $CuFe_2O_4$ (O-20%) and $Cu_{0.5}Co_{0.5}Fe_2O_4$ (O-16%); while Co-incorporation have an opposite effect: $CoFe_2O_4$ (O-6%)

TPR2:

- In connection with the previous two statements, derived from the TPR1 and TPO results: Co/Cu-incorporation enhances the reduction extent whereas Mn/Cu-incorporation enhances the oxidation extent implies that ternary ferrospinels, composed of Cu/Mn ($Cu_{0.5}Mn_{0.5}Fe_2O_4$), Co/Mn ($Co_{0.5}Mn_{0.5}Fe_2O_4$) or Cu/Co ($Cu_{0.5}Co_{0.5}Fe_2O_4$) together with the only Cu-incorporated sample - $CuFe_2O_4$, showed better results for the 2nd consecutive reduction (TPR2) with the values that are comparable to the ones obtained during the 1st reduction (TPR1): $Cu_{0.5}Mn_{0.5}Fe_2O_4$ (R-40%), $Co_{0.5}Mn_{0.5}Fe_2O_4$ (R-42%), $Cu_{0.5}Co_{0.5}Fe_2O_4$ (R-32%)and $CuFe_2O_4$ (R-40%).

To summarize: In view of the prospective to use M-ferrites as oxygen carrier materials, where the reduction as well as the oxidation degree are both important parameters that have a direct impact on the overall conversion and efficiency, utilization the material with equilibrated redox properties, such as $Cu_{0.5}Mn_{0.5}Fe_2O_4$, $Co_{0.5}Mn_{0.5}Fe_2O_4$, $Cu_{0.5}Co_{0.5}Fe_2O_4$ or $CuFe_2O_4$, can be more profitable for the large-scale applications.

4.5. Ex-situ XRD study of MFe_2O_4 ferrites

The discussion is focused on the deep understanding of the C_2H_5OH-reduction process of the MFe_2O_4 ferrites via stepwise reduction of the solids with the further XRD characterization including Rietveld refinement results.

Ex-situ XRD study of the reduced samples → ethanol reduction

The H_2-reduction of $Cu_{0.5}Mn_{0.5}Fe_2O_4$ and $Co_{0.5}Mn_{0.5}Fe_2O_4$ ferrites, discussed in the previous paragraph, has shown remarkable differences in the reaction models. The same idea was taken to explain the reduction of these samples with ethanol, which corresponds to the 1st step of the chemical-loop reforming process. The ex-situ study of XRD patterns, obtained after 1, 3, 5 and 20 min of ethanol exposure, was performed in order to justify this statement.

Essentially, a reduction cascade of the $MnFe_2O_4$ ferrite (Figure 4-8 and Figure 4-9) was chosen as a reference for the "egg-shell" model(Figure 4-14, B). The results, obtained after feeding ethanol for 1 min, reveal the appearance of a new Mn_xFe_yO oxide along with a remaining "reformed" spinel phase ($Mn_{1-x}Fe_{2-x}O_4$). Moreover, with increasing the reduction time from 1 to 20 min the relative amount of the spinel phase continued to decrease (from 92 to 67 %$_w$) whereas that of the Mn_xFe_yO increased (from 8 to 33 %$_w$) without an appearance of the other phases. This apparently shows that the reduction of the $MnFe_2O_4$goes through the formation of Mn_xFe_yO phase, which is an important proof of the previously discussed TPR results where we proposed the reduction mechanism which goes through the formation of hardly reducible and thermodynamically stable layer of Mn_xFe_yO oxide.

3 min ^{red}
$MnFe_2O_4$

Spinel 82.29%
Mn_xFe_yO 17.71%

Mn_xFe_yO

5 min ^{red}
$MnFe_2O_4$

Spinel 76.94%
Mn_xFe_yO 23.06%

Mn_xFe_yO

20 min ^{red}
$MnFe_2O_4$

Spinel 67.13%
Mn_xFe_yO 32.87%

Mn_xFe_yO
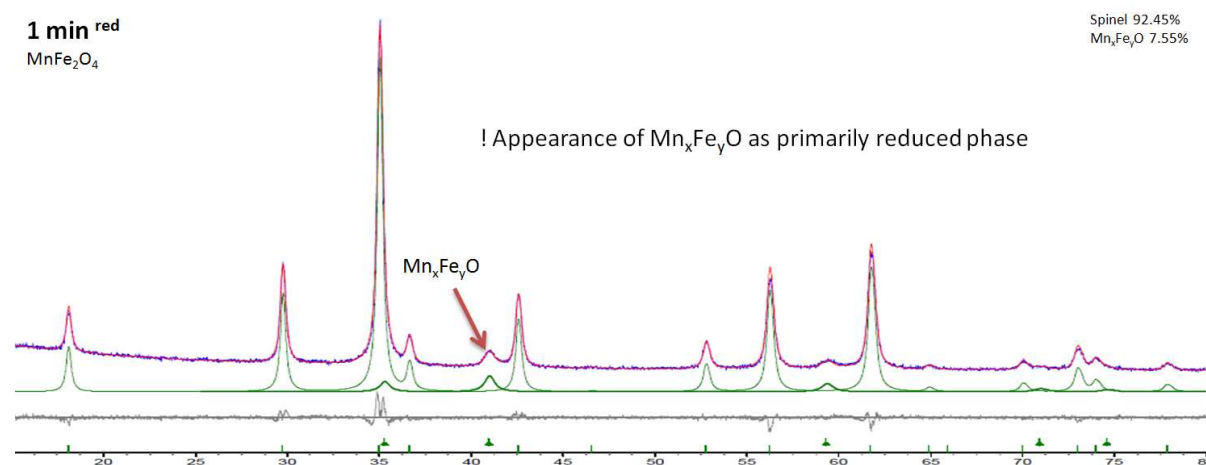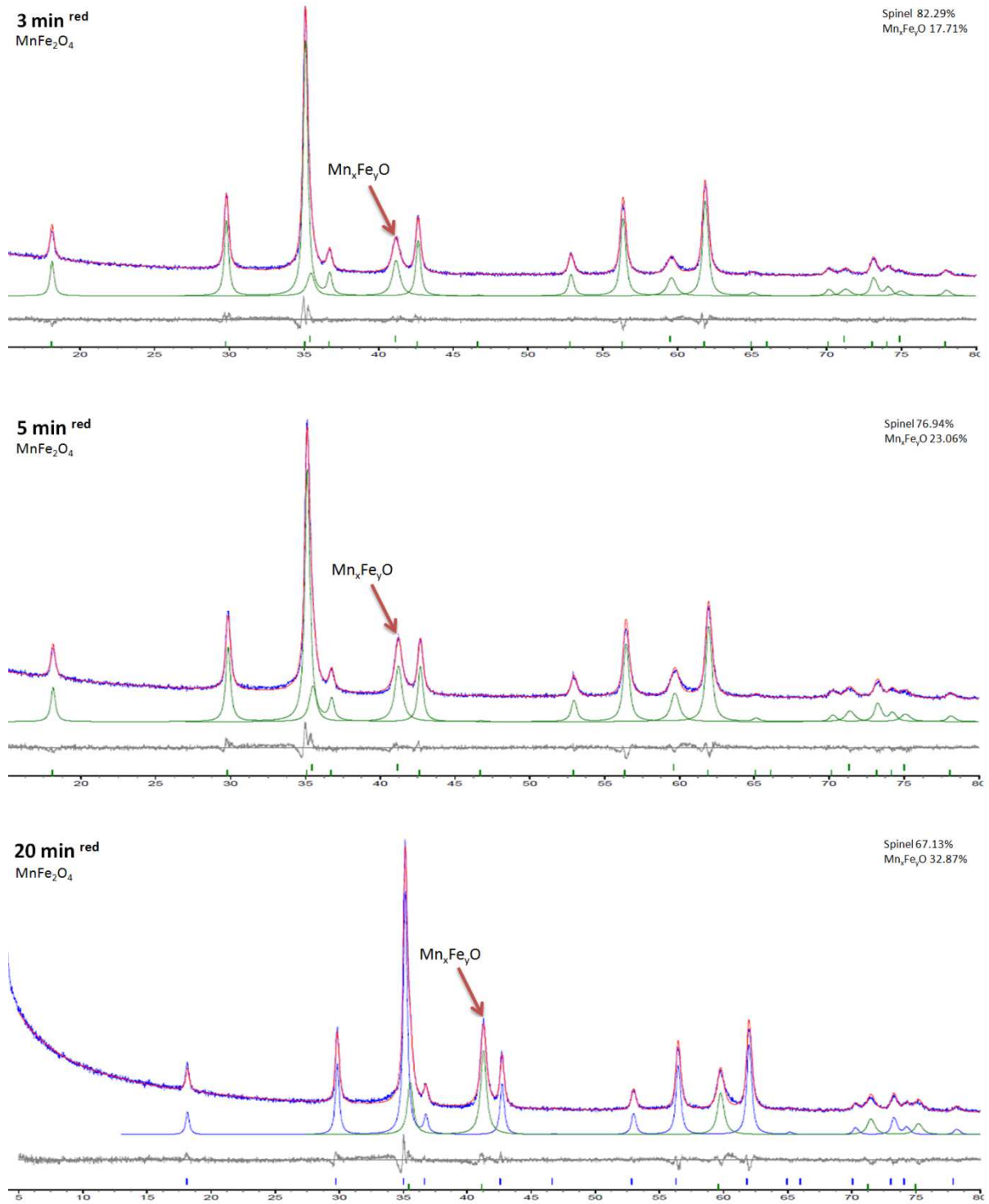
Figure 4-8. Stepwise (1, 3, 5 and 20 min) reduction of MnFe$_2$O$_4$
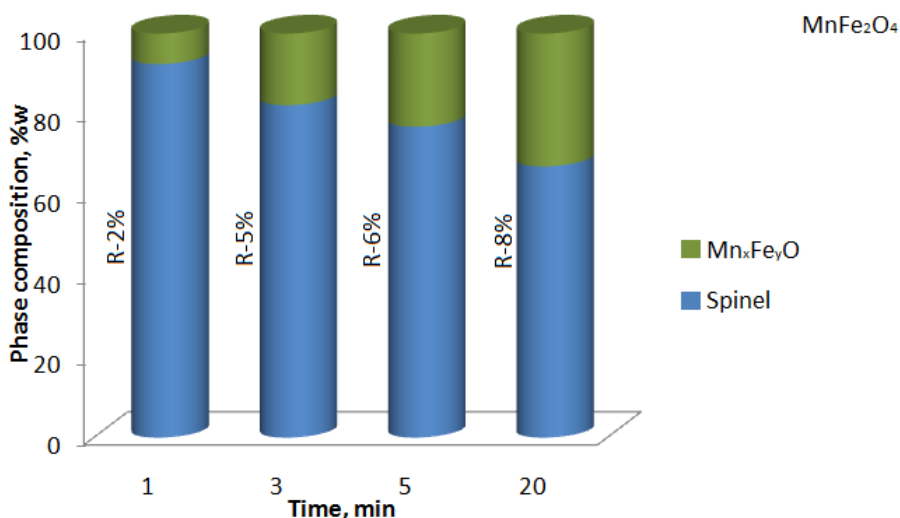
Figure 4-9. The evolution of phases during the MnFe$_2$O$_4$ stepwise reduction; R – reduction extent, %

The stepwise reduction of Cu$_{0.5}$Mn$_{0.5}$Fe$_2$O$_4$ (Figure 4-10 and Figure 4-11) clearly indicates that a primarily formed phase during the 1stmin of ethanol exposure was Cu^0 (with app. 11%$_w$). Increasing the reaction time to 3 min resulted in the formation of the second reduced phase – an oxide solid solution Mn$_x$Fe$_y$O, with app. 12%$_w$. Subsequent increase of the reduction time to 5 min led to a decrease of the spinel relative amount to 63%$_w$ whereas the one of Mn$_x$Fe$_y$O increased to 25%$_w$,while Cu^0 phase remained practically unchanged, app. 12%.Further step up in the reduction time (up to 20 min) resulted in the formation of strongly reduced species like iron carbides (Fe$_5$C$_2$ and Fe$_3$C), with total amount of 55%$_w$.On this basis, we may point out that the reduction of Cu$_{0.5}$Mn$_{0.5}$Fe$_2$O$_4$ at first proceeds with the formation of Cu^0 and iron-rich reformed spinel (Cu$_{0.5-x}$Mn$_{0.5}$Fe$_{2+x}$O$_4$), where Cu^0 may play its role as a catalyst for the deeper reduction with a formation of Mn$_x$Fe$_y$O and Fe-carbides, as also been supported by TPR study.

1 min ^{red}
$Cu_{0.5}Mn_{0.5}Fe_2O_4$

Spinel 89.15%
$Cu_{0.99}Fe_{0.01}$ 10.85%

! Appearance of Cu^0 as primarily reduced phase

Cu^0
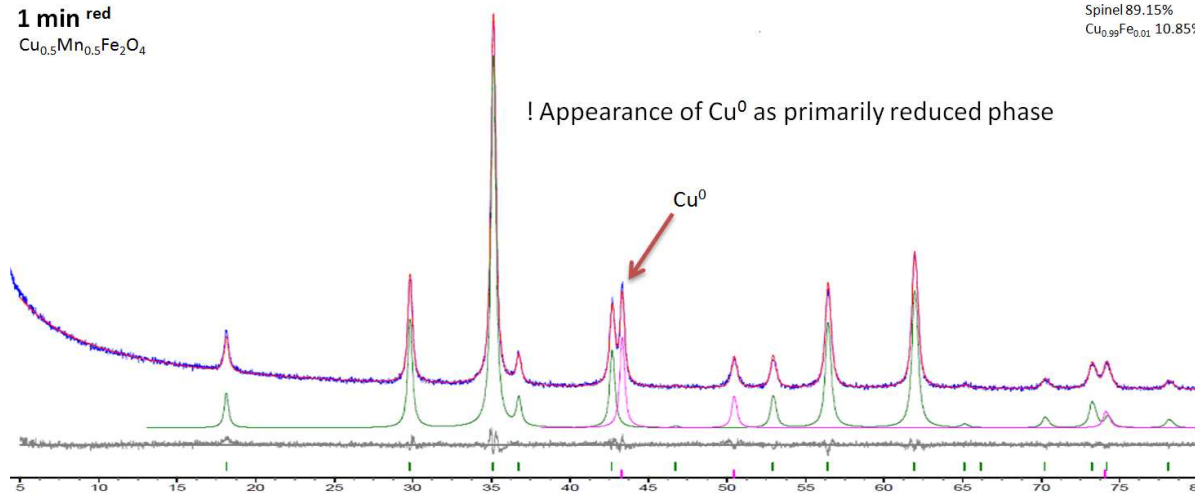
3 min ^{red}
$Cu_{0.5}Mn_{0.5}Fe_2O_4$

Spinel 76.10%
$Cu_{0.99}Fe_{0.01}$ 11.71%
Mn_xFe_yO 12.19 %

Mn_xFe_yO
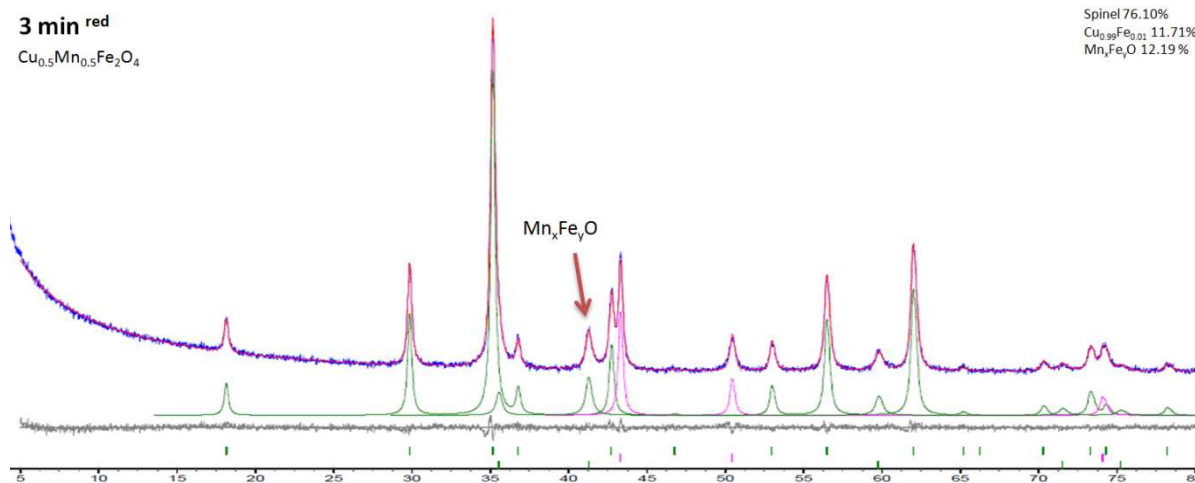
5 min ^{red}
$Cu_{0.5}Mn_{0.5}Fe_2O_4$

Spinel 63.41%
$Cu_{0.99}Fe_{0.01}$ 11.82%
Mn_xFe_yO 24.78 %

Mn_xFe_yO Cu^0
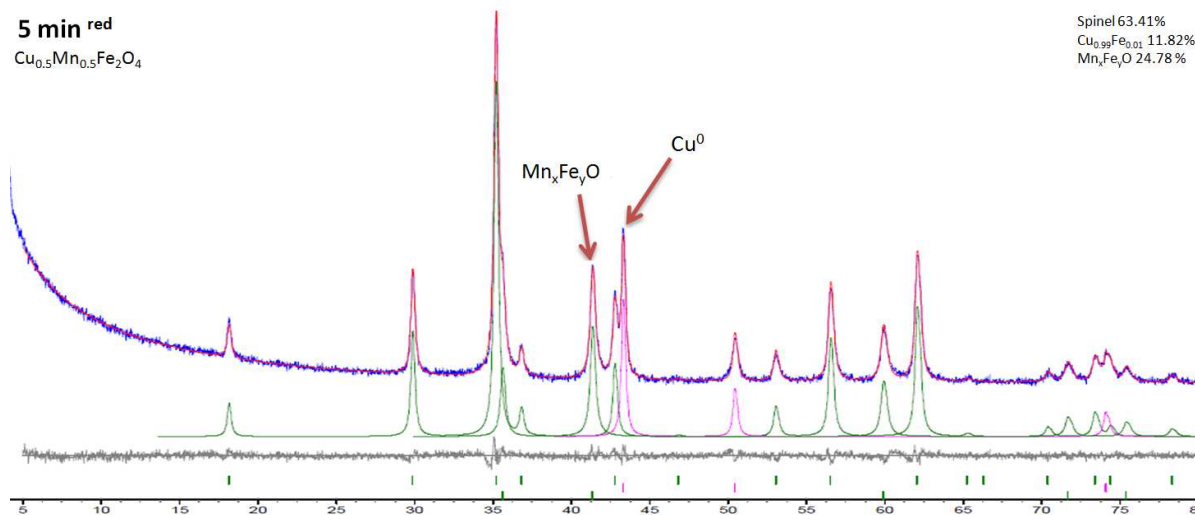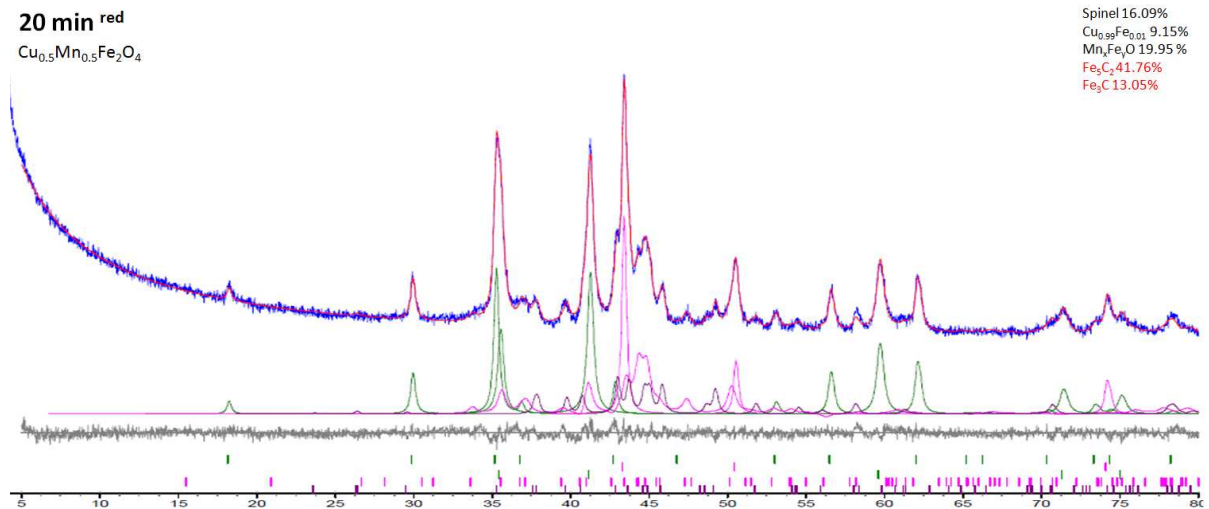
Figure 4-10. Stepwise (1, 3, 5 and 20 min) reduction of $Cu_{0.5}Mn_{0.5}Fe_2O_4$
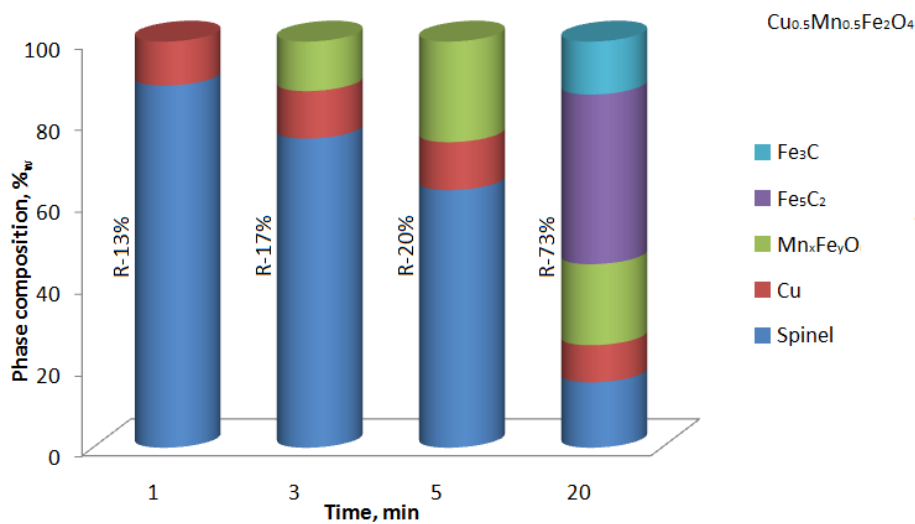
Figure 4-11. The evolution of phases during the $Cu_{0.5}Mn_{0.5}Fe_2O_4$ stepwise reduction; R – reduction extent, %

The reduction cascade of the $Co_{0.5}Mn_{0.5}Fe_2O_4$ ferrite is shown in Figure 4-12 and Figure 4-13. It is worth noting, that incorporation of Co-cations may stabilize iron in the ferric state in an even higher proportion, exceeding the nominal 1:2 ratio[74]; this in turn determines the reduction mechanism and, as a consequence, phases which are formed during the reduction step. From the obtained results, the reduction of $Co_{0.5}Mn_{0.5}Fe_2O_4$ have the same nature as the one of $MnFe_2O_4$; which primarily gives rise to app. 15%$_w$ of Mn_xFe_yO oxide and 85%$_w$ of Fe-enriched spinel with its further evolution to 42 and 58 %$_w$, respectively. The formation of Mn_xFe_yO acts as a "shielding" layer and prevents a deep reduction of the following ferrite. This also can explain such high difference in the reduction degree (α) between

$Co_{0.5}Mn_{0.5}Fe_2O_4$ (10%) and $Cu_{0.5}Mn_{0.5}Fe_2O_4$ (73%) whereas samples without Mn-incorporation showed the same α: $CoFe_2O_4$ (82%) and $CuFe_2O_4$ (82%) (Figure 4-15).

1 min ^{red}
$Co_{0.5}Mn_{0.5}Fe_2O_4$

Spinel 84.88%
Mn_xFe_yO 15.12 %

! Appearance of Mn_xFe_yO as primarily reduced phase

Mn_xFe_yO

3 min ^{red}
$Co_{0.5}Mn_{0.5}Fe_2O_4$

Spinel 73.38%
Mn_xFe_yO 26.62%

Mn_xFe_yO

5 min ^{red}
$Co_{0.5}Mn_{0.5}Fe_2O_4$

Spinel 68.65%
Mn_xFe_yO 31.35%

Mn_xFe_yO

20 min **red**
$Co_{0.5}Mn_{0.5}Fe_2O_4$

Spinel 57.69%
Mn_xFe_yO 42.31%

Mn_xFe_yO
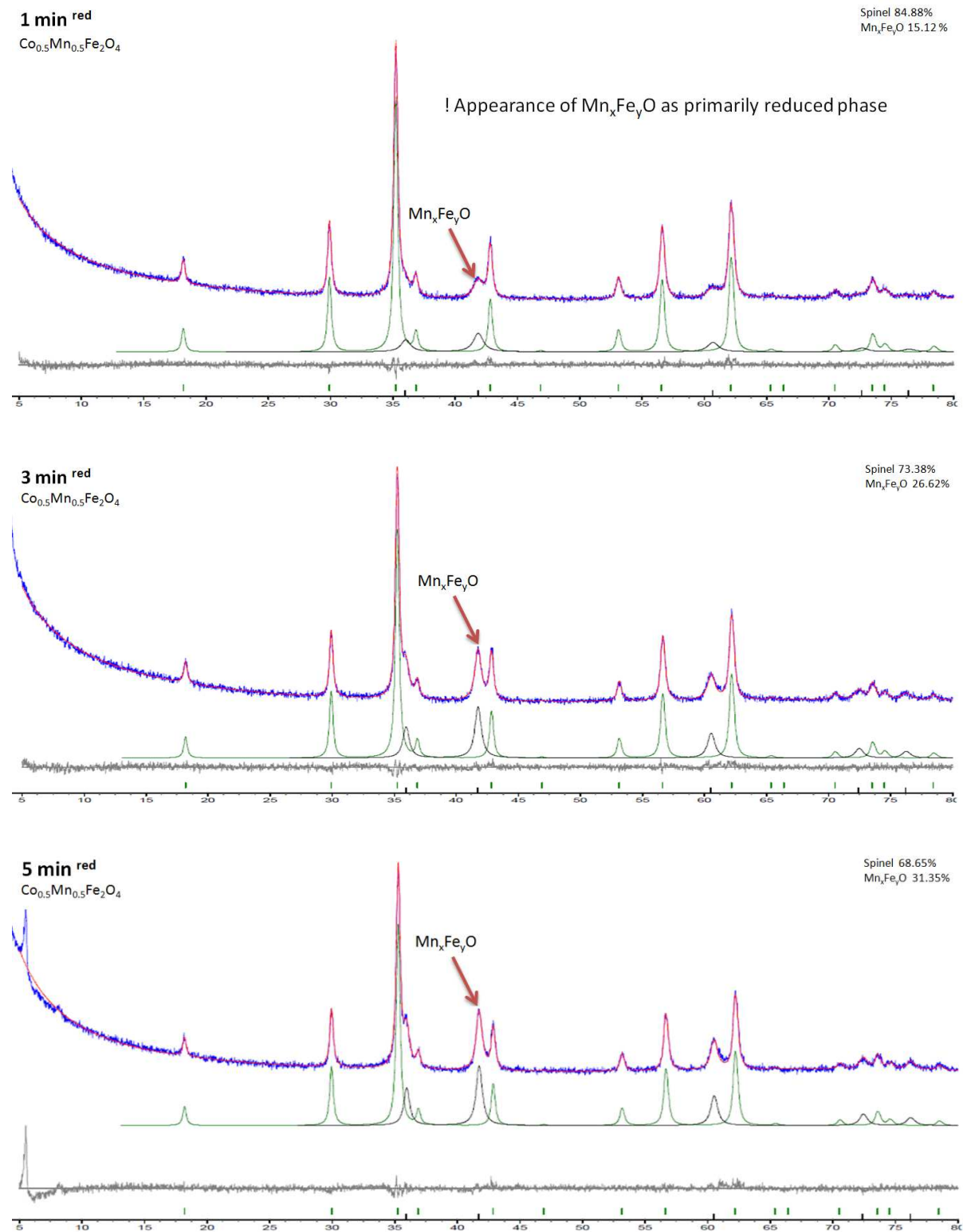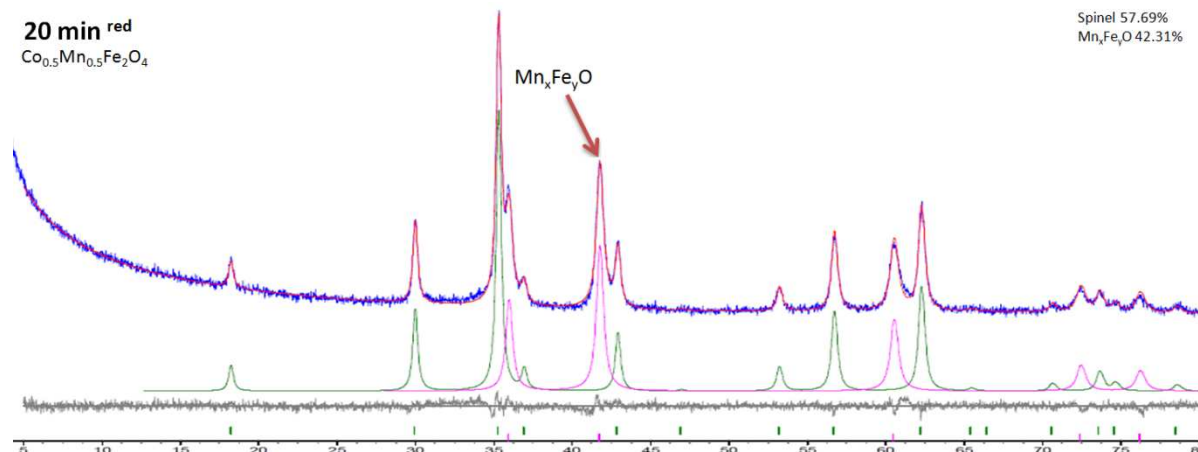
Figure 4-12. Stepwise (1, 3, 5 and 20 min) reduction of $Co_{0.5}Mn_{0.5}Fe_2O_4$

$Co_{0.5}Mn_{0.5}Fe_2O_4$

- Mn_xFe_yO
- Spinel
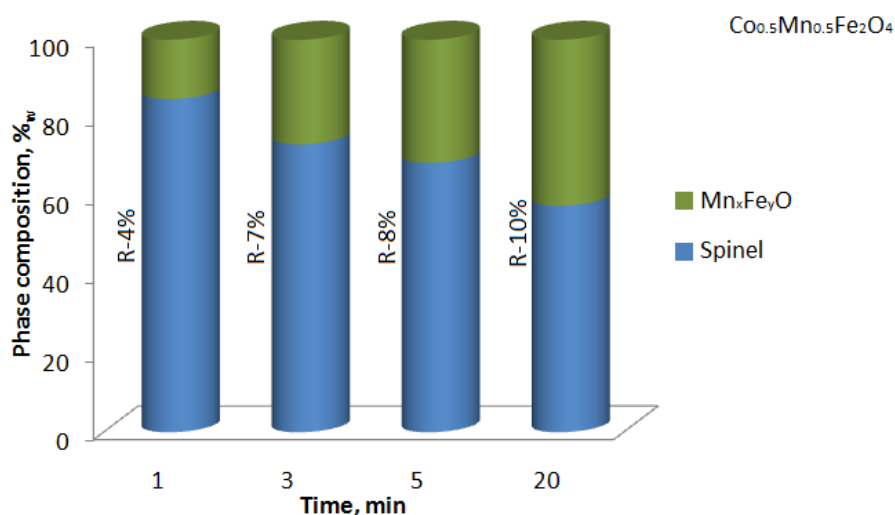
Figure 4-13. The evolution of phases during the $Co_{0.5}Mn_{0.5}Fe_2O_4$ stepwise reduction; R – reduction extent, %

Figure 4-15 and Table 4-5summarize the results on the Rietveld refinement for all MFe_2O_4 samples after ethanol reduction within 20 min. By looking at the reduction degree values, an introduction of Cu^{2+} ions into the Co/Fe system shows its strong promoting effect on the reduction of $Cu_{0.5}Co_{0.5}Fe_2O_4$ (α=100%), caused by a synergetic effect of Cu-Co couple (while by itself the reduction degree of $CuFe_2O_4$ and $CoFe_2O_4$ is equal to 82%). On the contrary, even though the highest surface area was shown by $MnFe_2O_4$,$Co_{0.5}Mn_{0.5}Fe_2O_4$and $Cu_{0.5}Mn_{0.5}Fe_2O_4$catalysts (SSA values of the fresh samples reported in Table 4-2), the Mn-incorporation illustrates an opposite inhibiting effect on the MFe_2O_4-reduction, causing its drop from 82% ($CoFe_2O_4$) to 10% ($Co_{0.5}Mn_{0.5}Fe_2O_4$) and from 82% ($CuFe_2O_4$) to 73% ($Cu_{0.5}Mn_{0.5}Fe_2O_4$). This suggests that the difference in the reducibility of the resulted M-

modified ferrospinels is related to the nature of the M-incorporated cation and its intrinsic reactivity.
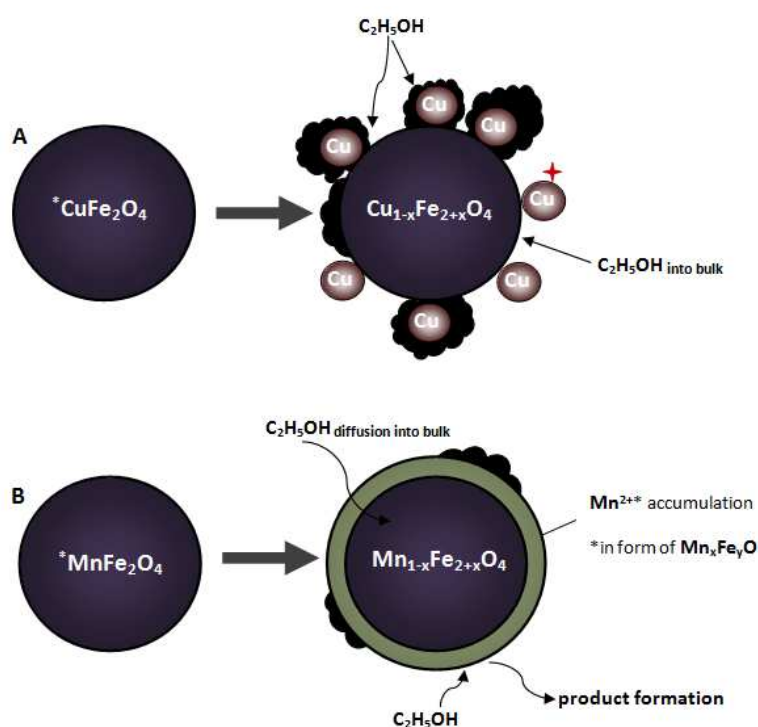
Figure 4-14. Schematic representation of C$_2$H$_5$OH-reduction over: A-CuFe$_2$O$_4$, as "nucleation/autocatalytic" model and B-MnFe$_2$O$_4$, as an "egg-shell" model

Table 4-5. Rietveld refinement data of MFe$_2$O$_4$ ferrites after 20 min reduction with ethanol

CATALYST	Degree of reduction (α), % (*from RV)	Phase composition after 20 min ethOH
MnFe$_2$O$_4$	8%	SPINEL – 67.16%$_w$ Mn$_x$Fe$_y$O – 32.84%$_w$
Cu$_{0.5}$Mn$_{0.5}$Fe$_2$O$_4$	73%	SPINEL – 16.09%$_w$ Mn$_x$Fe$_y$O – 19.95%$_w$ Fe$_5$C$_2$ – 41.76%$_w$ Fe$_3$C – 13.05%$_w$ Cu – 9.15%$_w$

$Co_{0.5}Mn_{0.5}Fe_2O_4$	10%	SPINEL – 57.69%$_w$
		Mn_xFe_yO – 42.31%$_w$
$CuFe_2O_4$	82%	Cu – 20.61%$_w$
		Fe_5C_2 – 29.45%$_w$
		Fe_3C – 22.27%$_w$
		SPINEL – 22.92%$_w$
		Fe – 4.75%$_w$
$CoFe_2O_4$	82%	$CoFe_{alloy}$ – 54.03%$_w$
		SPINEL – 22.65%$_w$
		Fe_5C_2 – 17.34%$_w$
		$FeC_{0.045}$ – 5.98%$_w$
$Cu_{0.5}Co_{0.5}Fe_2O_4$	100%	Cu – 12.34%$_w$
		Fe_5C_2 – 40.08%$_w$
		Fe_3C – 30.87%$_w$
		$CoFe_{alloy}$ – 16.71%$_w$
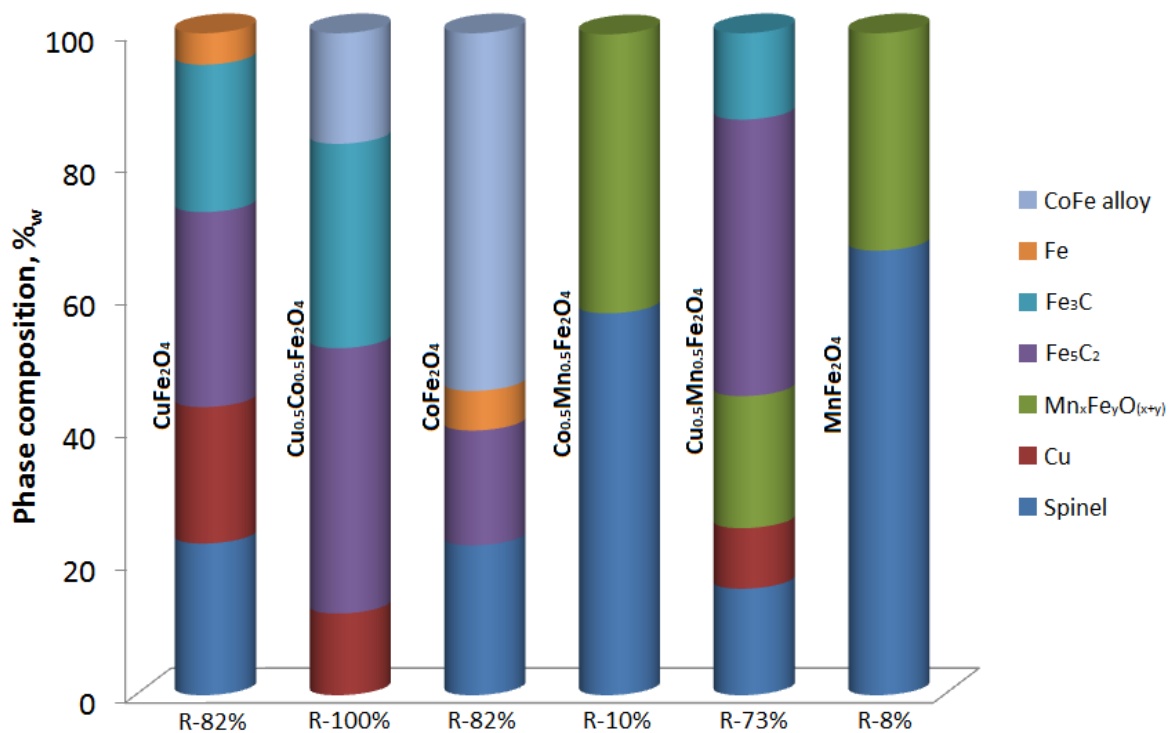
Figure 4-15. The evolution of phases during the MFe_2O_4 stepwise reduction; R – reduction extent, %

4.6. Ex-situ Mössbauer study

$Cu_{0.5}Co_{0.5}Fe_2O_4$ 20 min ethOH
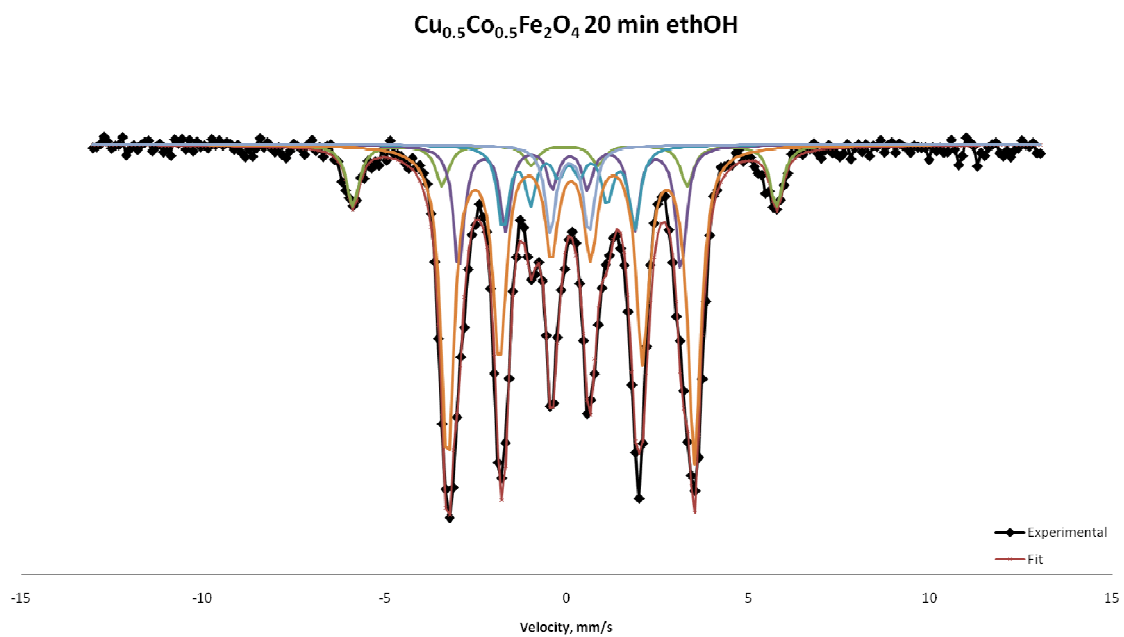
CuFe$_2$O$_4$ 20 min ethOH
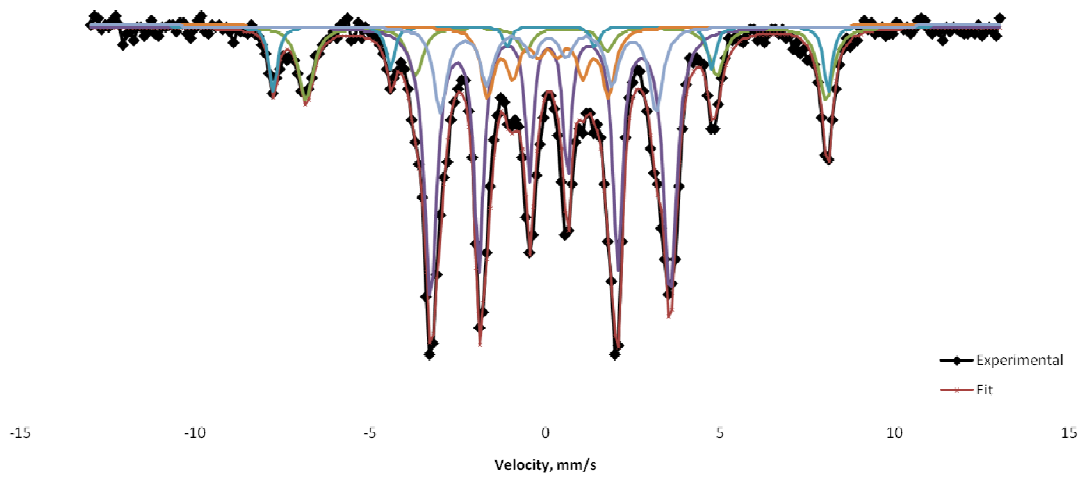
CoFe$_2$O$_4$ 20 min ethOH
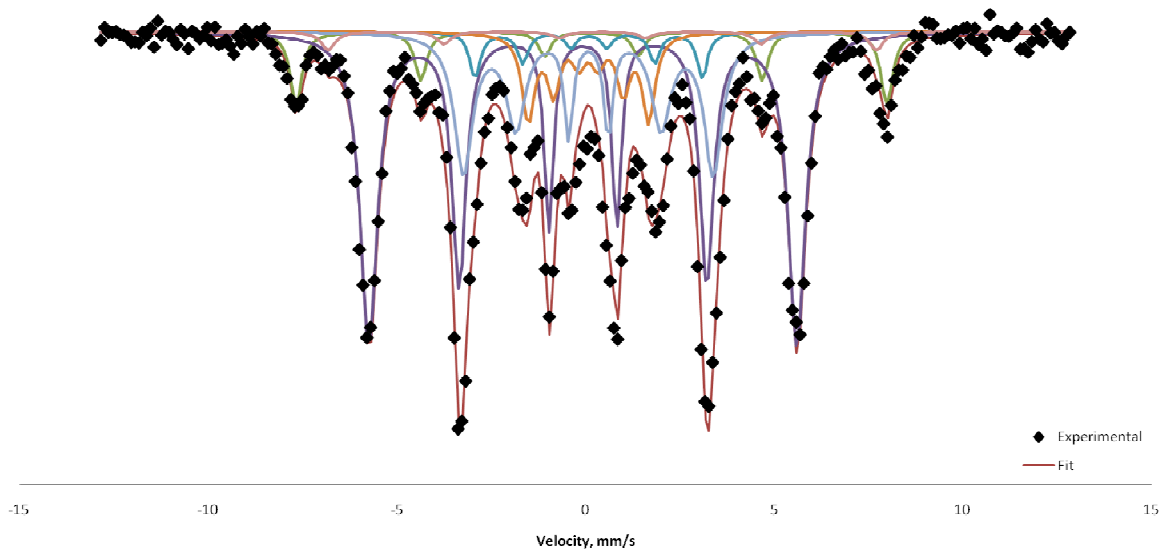
Cu$_{0.5}$Mn$_{0.5}$Fe$_2$O$_4$ 20 min ethOH
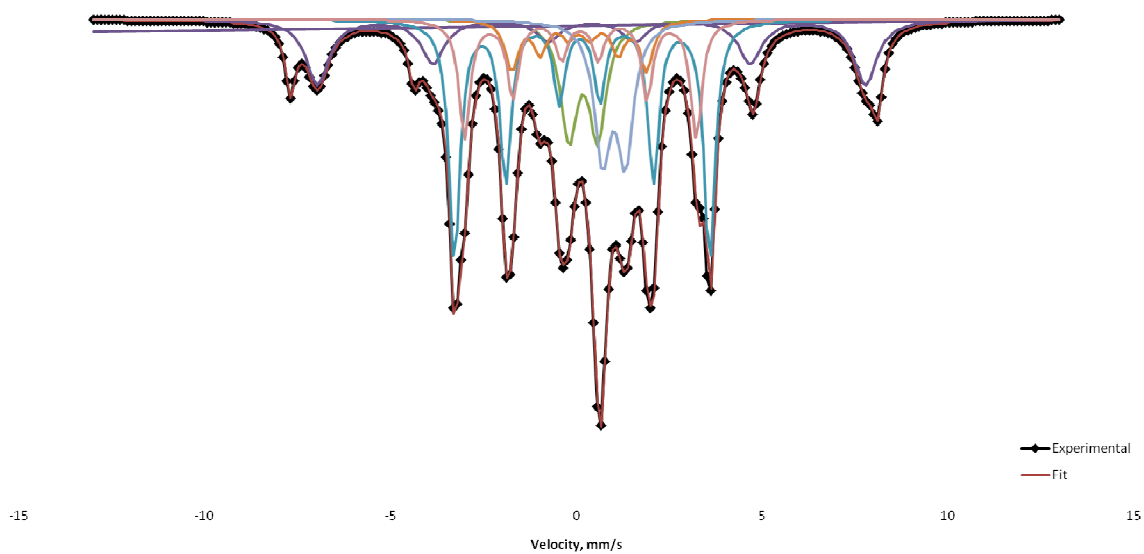
Co$_{0.5}$Mn$_{0.5}$Fe$_2$O$_4$ 20 min ethOH
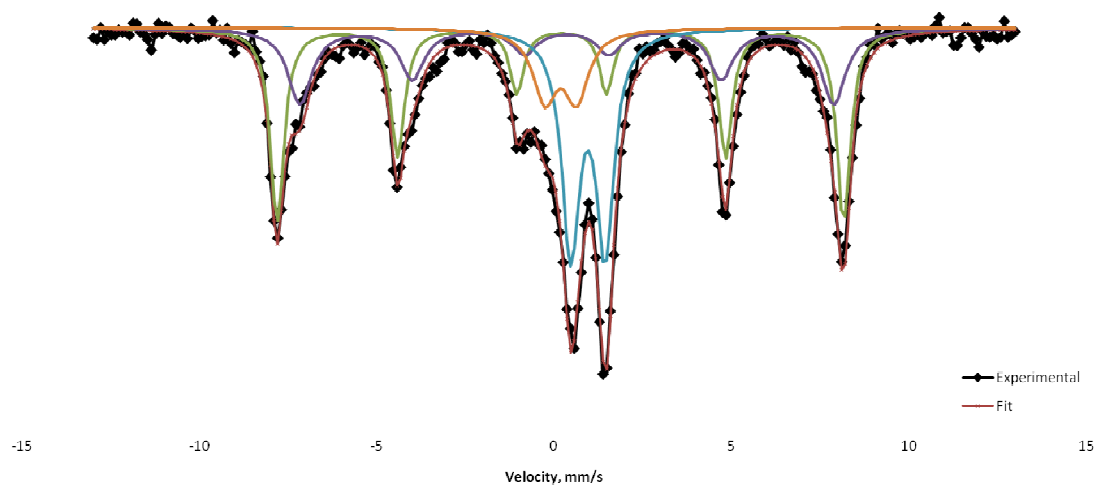
MnFe₂O₄ 20 min ethOH
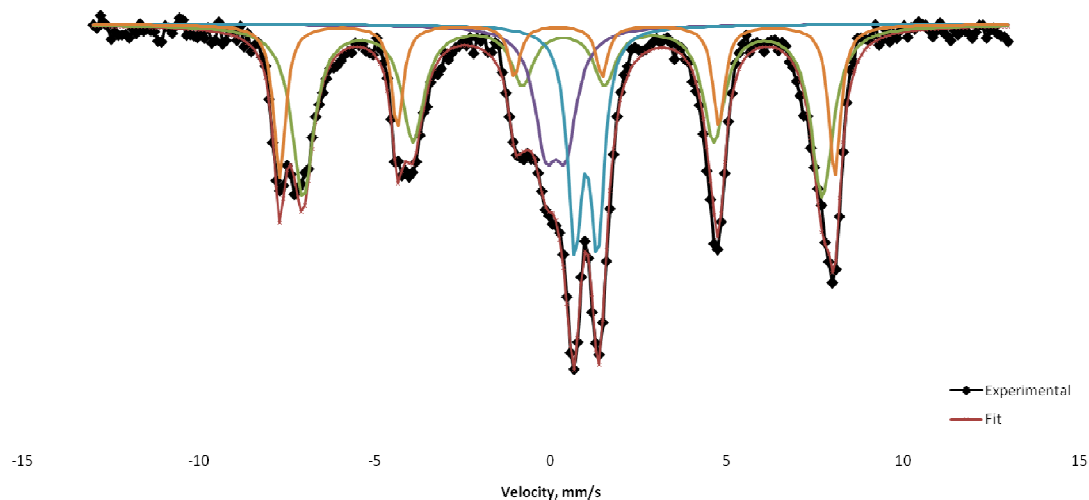
Figure 4-16. ⁵⁷Fe Mössbauer absorption spectra of the MFe₂O₄ ferrites recorded at 25 °C after 20 min C₂H₅OH-reduction at 450°C; solid lines are derived from the least-square fits

Mössbauer spectra on the MFe_2O_4 ferrites reduced with ethanol at 450°C for 20 min have been recorded in order to support the statements made on the basis of the ex-situ XRD studies and to gain new quantitative and compositional information (Figure 4-16). Experimental data were fitted using Lorentzian functions and the hyperfine parameters derived from the fittings are listed in Table 4-6.

The spectrum of $Cu_{0.5}Co_{0.5}Fe_2O_4$ ferrite (with α~100%) was fitted with 4 sextets and one doublet. The first sextet (δ-0.04 mm/s, H-35.9 T and Rel.In.-10%$_{at}$) was attributed to Fe^0 in the $CoFe_{alloy}$ phase, which was also detected by XRD. The other 3 sextets correspond to the two iron carbides (Fe_3C-cementite and Fe_5C_2-Hagg carbide), formed as the main phases (84%$_{at}$) during the reduction process. The best fit of the experimental spectrum was obtained with two sextets for Fe_5C_2 (δ-0.19 mm/s, H-18.9 T and δ-0.17 mm/s, H-11.2 T) and one shared sextet (δ-0.21 mm/s, H-21.0 T) for $Fe_5C_2+Fe_3C$ components. The obtained parameters of the corresponding sextets are in a good agreement with those reported literature [122–124].The doublet (δ 0.18 mm/s; Δ 1.05 mm/s) representing just6%$_{at}$ of the total spectrum, was ascribed to the presence of Fe^{3+} phase in the form of carburized Fe oxide (or Co/Fe oxide) resulting from the incomplete transformation of the ferrite (it should be recall

that X-ray diffraction is not extremely sensitive and up to 5% of the remained/formed phase could not be detected).

The experimental spectrum of $CuFe_2O_4$ ferrite (with $\alpha \sim 82\%$) was fitted with 5 sextets. Spinel component ($24\%_{at}$) with generic formula: $Cu_{(1-x)}Fe_{(2+x)}O_4$ composed of 2 sextets with the corresponding distribution of Fe-cations in between T_d and O_h sites: IS-0.25 mm/s, CH-49 T and δ-0.67 mm/s, H-45.9 T, respectively. Another 3 sextets are similar to those discussed above and were attributed to the existence of a relatively high amount of Fe_xC_y phases ($Fe_3C+Fe_5C_2 \sim 76\%_{at}$).

Mössbauer spectrum of $CoFe_2O_4$ sample (with $\alpha \sim 82\%$) was fitted with 6 sextets. The first two sextets (Fe in T_d sites: δ-0.25 mm/s and H-48.4 T; Fe in O_h sites: δ-0.55 mm/s and H-44.9 T) represent a remained spinel component – $Co_{1-x}Fe_{2+x}O_4$ ($10\%_{at}$) resulted from the incomplete reduction, as supported by ex-situ XRD study. The third sextet (δ-0.02 mm/s and H-35.0 T) with a relatively high contribution to the total spectrum ($51\%_{at}$) was attributed to Fe^0 and should correspond to $CoFe_{alloy}$ and $FeC_{0.045}$ phases, see Table 4-6. The three remained sextets were assigned to Hagg-carbide (Fe_5C_2), representing $39\%_{at}$ with the following hyperfine parameters: δ-0.17 mm/s and H-20.5 T, δ-0.18 mm/s and H-18.5 T, δ-0.17 mm/s and H-9.8 T, which corresponds to the three types of Fe in the unit cell of Fe_5C_2[122].

Experimental data of the $Cu_{0.5}Mn_{0.5}Fe_2O_4$ sample (with $\alpha \sim 73\%$) were fitted with 5 sextets and 2 doublets. Spinel component ($24\%_{at}$) composed of 2 sextets: Fe in T_d sites with δ-0.30 mm/s and H-48.8 T; Fe in O_h sites with δ-0.49 mm/s and H-45.6 T. Another 3 sextets are similar to those discussed above and were attributed to the existence of a relatively high amount of Fe_xC_y phases ($Fe_3C+Fe_5C_2 \sim 53\%_{at}$). Remaining two doublets which represent ferric (Fe^{3+} as $11\%_{at}$) and ferrous (Fe^{2+} as $12\%_{at}$) iron oxides characterized by an δ:Fe^{3+}- 0.28 mm/s; Fe^{2+}- 1.10 mm/s and a Δ: Fe^{3+}- 0.78 mm/s; Fe^{2+}- 0.62 mm/s and were attributed to the presence of the Mn_xFe_yO oxide solid solution (a small amount of Fe^{3+} in FeO (is generally present in FeO) was also seen by Johnson[125]). Eventually, the obtained results support the ex-situ XRD study and a lower α-value obtained over $Cu_{0.5}Mn_{0.5}Fe_2O_4$ sample in comparison to $CuFe_2O_4$ and $CoFe_2O_4$ ones, which in turn explained by the direct effect of Mn-incorporation, leading to the formation scarcely reducible phase - Mn_xFe_yO).

Mössbauer spectroscopy results on the $Co_{0.5}Mn_{0.5}Fe_2O_4$ (with $\alpha \sim 10\%$) and $MnFe_2O_4$ (with $\alpha \sim 8\%$) ferrites once again confirmed the apparent differences observed between the Mn, Mn/Co- and Co, Cu, Cu/Co, Cu/Mn-incorporated samples. Corresponding spectra were all fitted with 2 sextets and 2 doublets. Two sextets were used to fit the remained spinel component (in the form of $M_{1-x}Fe_{2+x}O_4$): $Co_{0.5}Mn_{0.5}Fe_2O_4$ with $65\%_{at}$ (Fe in Td sites: δ-0.29 mm/s, H-49.3 T; Fe in Oh sites: δ-0.45 mm/s, H-46.5 T) and $MnFe_2O_4$ with $68\%_{at}$ (Fe in Td sites: δ-0.28 mm/s, H-48.7 T; Fe in Oh sites: δ-0.44 mm/s, H-45.6 T). The two doublets ($Co_{0.5}Mn_{0.5}Fe_2O_4$: δ-0.28 mm/s, Δ-0.87 mm/s and δ-1.04 mm/s, Δ-0.97 mm/s; $MnFe_2O_4$: δ-0.23 mm/s, Δ-0.57 mm/s and δ-1.09 mm/s, Δ-0.64 mm/s) were attributed to the same ferric (Fe^{3+}) and ferrous (Fe^{2+}) iron oxides, respectively, as detected in $Cu_{0.5}Mn_{0.5}Fe_2O_4$ sample. From the obtained results, it is clear that the reduction of $Co_{0.5}Mn_{0.5}Fe_2O_4$ and $MnFe_2O_4$ samples is of the same nature and follows a proposed "egg-shell" model, with only the formation of two new phases: a Fe-rich reformed spinel ($M_{1-x}Fe_{2+x}O_4$) and a thermodynamically stable hardly reducible layer of Mn_xFe_yO oxide solid solution. These results are in agreement with those of TPR and ex-situ XRD studies.

Table 4-6. Hyperfine parameters derived from the fittings of the ^{57}Fe Mössbauer absorption spectra over MFe_2O_4 ferrites after 20 min C_2H_5OH-reduction at 450°C

Compound	δ (mm/s)	Δ (mm/s)	H (T)	Rel. Int. (%)	Phase attribution
	0.25	-0.00	49.0$_{Td}$	8	spinel
$CuFe_2O_4$	0.67	-0.00	45.9$_{Oh}$	16	
after 20 min reduction	0.20	-0.00	21.1	48	$Fe_5C_2 + Fe_3C$
	0.17	-0.00	10.7	12	Fe_5C_2
	0.19	-0.00	19.1	16	Fe_5C_2
	0.04	0.00	35.9	10	Fe^0 (alloy)
$Cu_{0.5}Co_{0.5}Fe_2O_4$	0.19	0.00	18.9	17	Fe_5C_2
after 20 min reduction	0.17	0.00	11.2	13	$Fe5C_2$
	0.21	0.00	21.0	54	$Fe_5C_2 + Fe_3C$
	0.18	1.05	-	6	Fe^{3+}

$CoFe_2O_4$	0.25	0.00	48.4_{Td}	7	spinel
after 20 min reduction	0.55	0.00	44.9_{Oh}	3	
	0.02	0.00	35.0	51	Fe^0 (alloy)
	0.17	0.00	20.5	23	Fe_5C_2
	0.18	0.00	18.5	6	Fe_5C_2
	0.17	0.00	9.8	10	Fe_5C_2
$Cu_{0.5}Mn_{0.5}Fe_2O_4$	0.30	0.00	48.8	7	spinel
after 20 min reduction	0.49	0.00	45.6	17	
	0.21	0.00	21.2	33	$Fe_5C_2 + Fe_3C$
	0.16	0.00	11.3	7	Fe_5C_2
	0.19	0.00	19.2	13	Fe_5C_2
	0.28	0.78	-	11	Fe^{3+}
	1.10	0.62	-	12	Fe^{2+}
$Co_{0.5}Mn_{0.5}Fe_2O_4$	0.29	0.00	49.3_{Td}	37	spinel
after 20 min reduction	0.45	0.00	46.5_{Oh}	25	
	0.28	0.87	-	11	Fe^{3+}
	1.04	0.97	-	27	Fe^{2+}
$MnFe_2O_4$	0.44	0.00	45.6_{Oh}	46	spinel
after 20 min reduction	0.28	0.00	48.7_{Td}	22	
	0.23	0.57	-	14	Fe^{3+}
	1.09	0.64	-	18	Fe^{2+}

4.7. Reactivity tests and characterization of the cycled materials

This chapter contains a further discussion on the redox properties of MFe_2O_4 ferrites and its usage as looping materials (LM) in the ethanol chemical-loop reforming (CLR), which consists of 2 steps: 1st step - reduction of LM^{fresh} with ethanol at T-450°C; 2nd - re-oxidation of LM^{red} with water steam. The choice of reaction conditions and cycling time was adopted according to the study of Cocchi (reducing agent: methanol, T_{red} – 300 and 420°C/T_{re-ox} – 420°C, looping materials: Fe_3O_4, $CoFe_2O_4$ and $NiFe_2O_4$)[100] and Trevisanut (reducing agent: ethanol, T_{red}– 400 and 450°C/T_{re-ox} – 450°C, looping materials: Fe_3O_4, $CoFe_2O_4$ and $NiFe_2O_4$)[101]. Important to note, that the essential aim of the reduction step was to maximize the reduction extent with a minimum deactivation (an effect of coke accumulation and incomplete M^0 re-oxidation) of the looping material along with an improving of its cycling

stability. Hence, previously obtained results suggested the best reaction conditions to be as follows: 1st step – ethanol reduction at T_{red}-450°C and 2nd step – water re-oxidation at T_{re-ox}-450°C. Cycling time was chosen on the same basis with the final optimum duration of both steps as 20 min per each cycle. Moreover, the composition of MFe_2O_4 ferrospinels was also varied in between Co, Mn, Cu and its combination Cu/Co, Cu/Mn and Co/Mn. The aim of the following modifications was to pursue a better performance (like a _cycling stability ($Y^{int}(H_2))=f(cycles)=const$_) of the M-incorporated ferrites in comparison to a pristine Fe_3O_4, as a primarily accepted LM for the CLR, proposed first by Nakamura.

In addition, as reported by Trevisanut[101], it is impossible to avoid a coke deposition in the anaerobic reduction conditions, which accumulates after each complete cycle leading to an inevitable deactivation. This in turn led us to an idea of the "modified ethanol CLR", which now consists of 3 steps: 1st step - reduction of LM^{fresh} with ethanol at T-450°C; 2nd- re-oxidation of LM^{red} with water steam; 3rd step - regeneration of coked LM^{re-ox} with air at T-450°C. The obtained results are compared to a conventional 2 steps CLR process.

1st step: 20 min reduction with ethanol
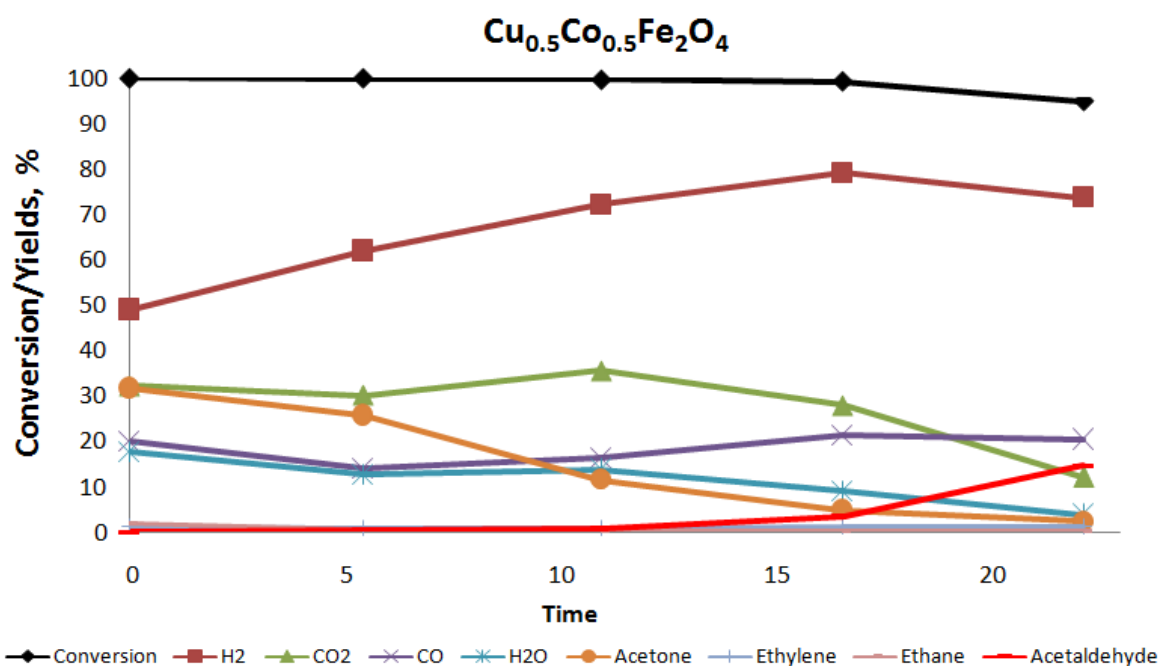
Figure 4-17. Conversion and Yields to the main products obtained for $Cu_{0.5}Co_{0.5}Fe_2O_4$ during the 20 min cycling at T-450°C

Figure 4-17, Figure 4-19 to Figure 4-23 show conversion and yields for the main products (yield >5%), obtained during the ethanol reduction step performed at 450°C for 20 min. The general statement which can be applied to all the MFe_2O_4 (as LM): the amount of each product is greatly affected by the degree of metal oxide reduction. Thus, $Cu_{0.5}Co_{0.5}Fe_2O_4$ ferrite (Figure 4-17) starting from the first minutes of the reaction showed 100% of conversion followed by its decrease down to 95%, while the extent of a spinel reduction increased from 0 to 100 % (see Table 4-5). One of the main products of ethanol conversion was hydrogen, with an initial yield of about 50%, which increased up to 74%. The sim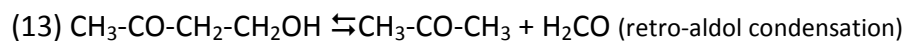ilar trend, as the one for hydrogen, was observed for CO with its max yield about 20%. Looking at CO_2 and H_2O profiles, one may notice a similar decreasing trend (starting yields: CO_2-32% and H_2O-18%, final yields: CO_2-12% and H_2O-4%). Thus, taking into account the elaborated results, we suggest that the main reactions during spinel reduction involved the partial and total oxidation of ethanol:

(1) $C_2H_5OH + MeO_x \rightarrow 2\ CO + 3\ H_2 + MeO_{(x-1)}$

(2) $C_2H_5OH + 3\ MeO_x \rightarrow 2\ CO_2 + 3\ H_2 + 3\ MeO_{(x-1)}$

(3) $C_2H_5OH + 6\ MeO_x \rightarrow 2\ CO_2 + 3\ H_2O + 6\ MeO_{(x-1)}$

In addition, the formation of water involves several possible reactions:

(4) $H_2 + MeO \rightarrow H_2O + Me$

(5) $C_2H_5OH \rightarrow 2\ C + 2\ H_2 + H_2O$
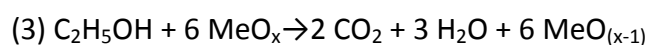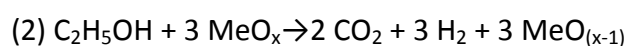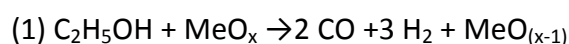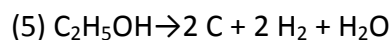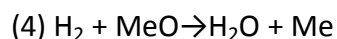
Acetone formation, which declined with time from 32 to 2%, as reported previously[126], can be a result of an aldol condensation of the intermediately formed acetaldehyde, with further isomerization of the aldol into hydroxyketone followed by a reverse reaction to form acetone and formaldehyde (converted into CO and H_2). Either, as recently proposed by Rodrigues et al., by ketonization of carboxylates (acetates) which are obtained by dehydrogenation of this alcohol followed by oxidation[127]. In fact, the formation of acetates over $Cu_{0.6-x}Mn_xFe_{2.4}O_y$ and $Co_{0.6-x}Mn_xFe_{2.4}O_y$ samples was confirmed by DRIFTS study [106].

Increasing yields for an acetaldehyde (from 1 to 15%) over the continuously reducing sample indicates that dehydrogenation/deoxyhydrogenation of ethanol also occurred:
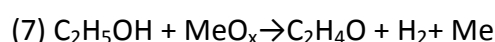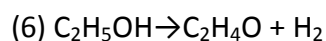
(6) $C_2H_5OH \rightarrow C_2H_4O + H_2$

(7) $C_2H_5OH + MeO_x \rightarrow C_2H_4O + H_2 + Me$

Coke and heavy compounds (mainly aromatics) are formed at the very beginning of the reaction time (~1%), with a progressive increase in yield to 39%. The generation of coke was likely due to the dehydrogenation and total deoxygenation of ethanol:

(8) $C_2H_5OH \rightarrow C + CO + 3\ H_2$

(9) $C_2H_5OH \rightarrow 2\ C + H_2O + 2\ H_2$
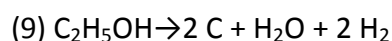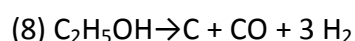
Moreover, a disproportionation of CO (Boudouard reaction) can also lead to the coke deposition:

(10) $2\ CO \rightarrow CO_2 + C$
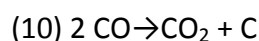
Several heavy compounds, with 4 and more C atoms, were also detected during the reduction step (Figure 4-17):

- Butenes
- Benzene
- 2-Pentanone

- 4-Penten-2-one and isomers
- Xylenes
- C_8 and C_9 aromatics
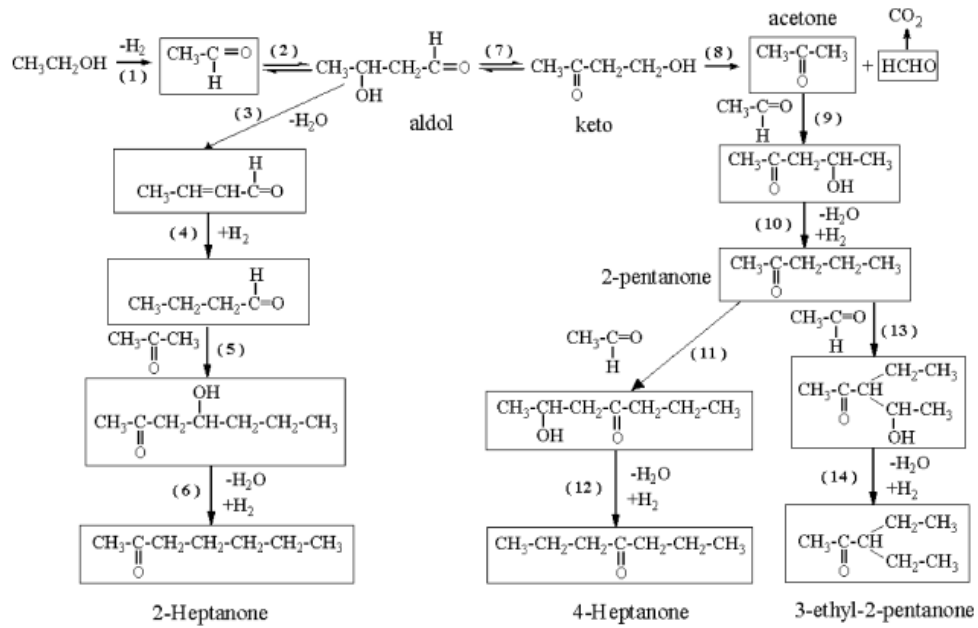
Figure 4-18. General scheme of pentanones/heptanones formation starting from ethanol[128]
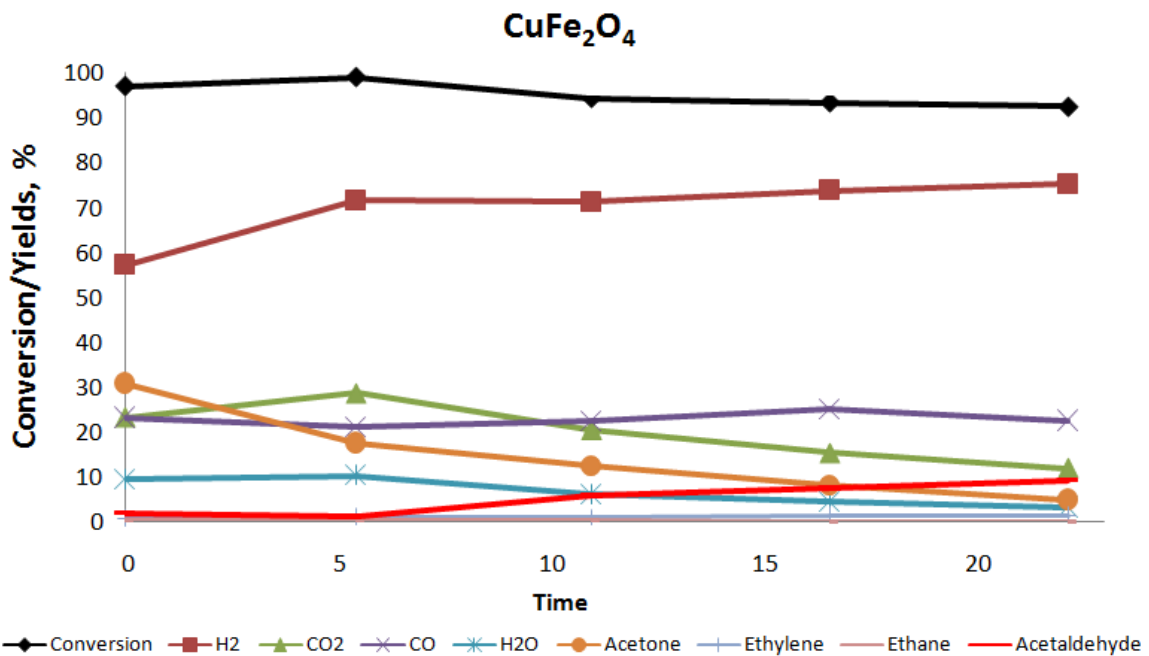
Figure 4-19. Conversion and Yields to the main products obtained for $CuFe_2O_4$ during the 20 min cycling at T-450°C

Looking at the conversion and yields evolution over $CuFe_2O_4$ ferrite (Figure 4-19), the results demonstrate similar trends in the products distribution and, as a consequence, similar

reduction paths which involve the same set of reactions (eq. 1 to 10). The reduction of $CuFe_2O_4$ sample started with 95 % of ethanol conversion which approached to 92% after 20 min of reduction time, while degree of reduction reached 82%. As for the previously discussed ferrite, hydrogen was one of the main products of the ethanol conversion, with the following increasing trend: from 57 to 75%. However, H_2O and CO_2 have decreasing trends from 9 to 3% and 23 to 12%, respectively. This may indicate that the total oxidation is more favourable at the beginning of the reduction process (eq.3) over a less reduced material. Acetaldehyde was observed only after 5 min of *tos* (time-on-stream) with the increasing trend from 2 to 9%, eq. 6 and 7. Acetone was formed at the beginning with the yield of 31% and then its amount decreased to 5%. The overall reactions for the formation of acetone via aldol condensation may be expressed as follows:

(11) $2\ CH_3CHO \leftrightarrows CH_3\text{-}CH(OH)\text{-}CH_2\text{-}CHO$ (aldol condensation)

(12) $CH_3\text{-}CH(OH)\text{-}CH_2\text{-}CHO \leftrightarrows CH_3\text{-}CO\text{-}CH_2\text{-}CH_2OH$ (intramolecular disproportion-isomerization)

(13) $CH_3\text{-}CO\text{-}CH_2\text{-}CH_2OH \leftrightarrows CH_3\text{-}CO\text{-}CH_3 + H_2CO$ (retro-aldol condensation)

(14) $H_2CO \rightarrow CO + H_2$ (decomposition of formaldehyde)
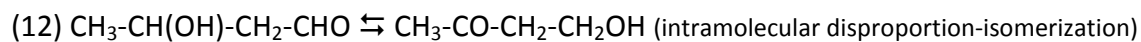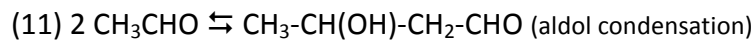
or via ketonization from the acetates bounded to the surface:

(15) $2CH_3COOH \rightarrow CH_3COCH_3 + CO_2 + H_2O$ (via ketonization)
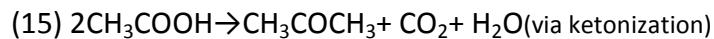
Coke and heavy compounds (mainly aromatics) are also formed with the comparably high yield as for the $Cu_{0.5}Co_{0.5}Fe_2O_4$ sample (increasing from 7 to 38%).
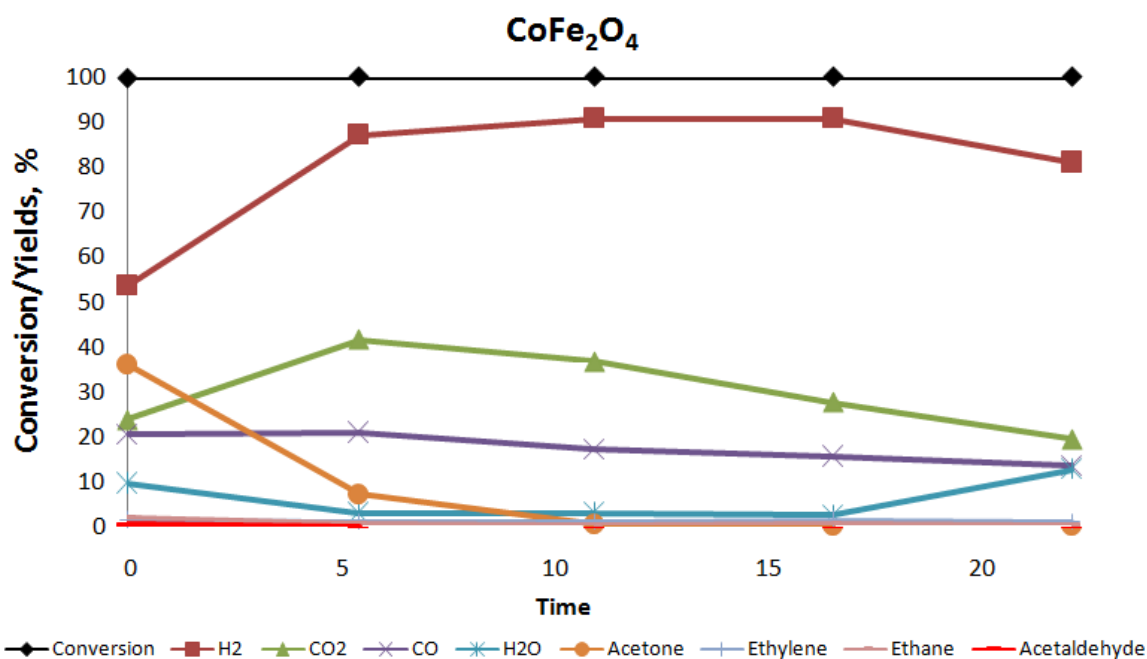
Figure 4-20. Conversion and Yields to the main products obtained for CoFe$_2$O$_4$ during the 20 min cycling at T-450°C

Results obtained with the CoFe$_2$O$_4$ ferrite are very similar to those obtained with the Cu$_{0.5}$Co$_{0.5}$Fe$_2$O$_4$ and CoFe$_2$O$_4$ samples (Figure 4-20, eq.1-15). The conversion, starting from the beginning, reached its max (app. 100%) and was stable during the reduction time, yielding to 82% of the material reduction. The formation of CO$_x$ and H$_2$O, H$_2$ as the main products led to the same conclusion on the prevailing reactions of the total and partial ethanol oxidation (eq. 1-3). The main difference between the previous two samples was observed in the amount of produced acetaldehyde (in this case the yield is very small, ≤1% during all 20 min of *tos*) and coke+HC (increased from 4 to 60%).
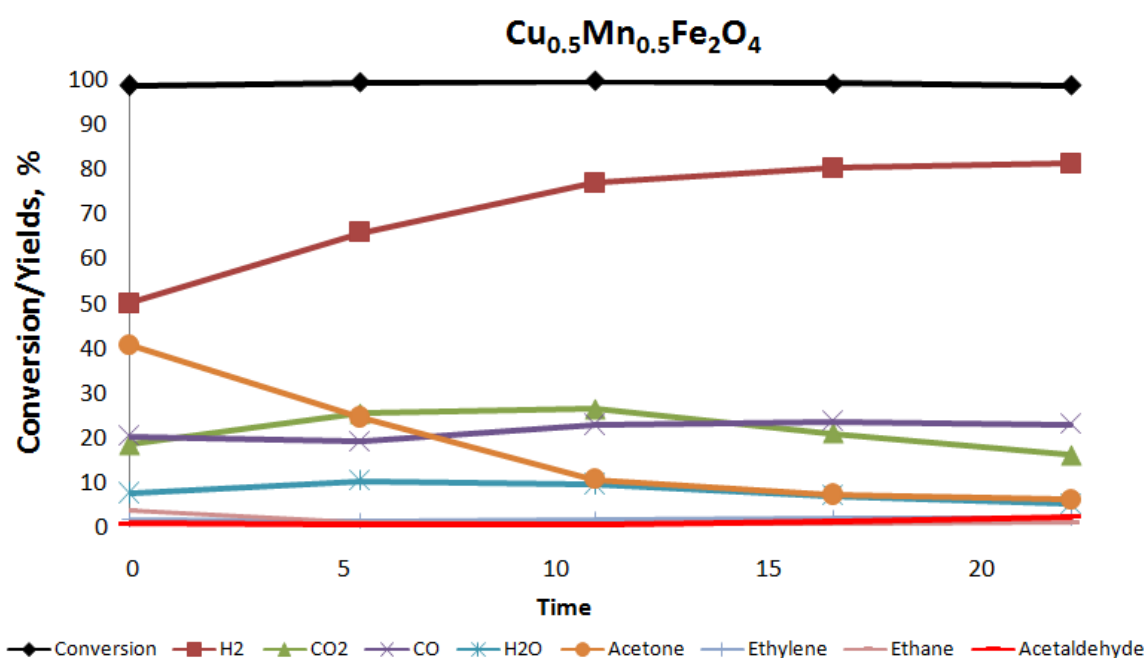
Figure 4-21. Conversion and Yields to the main products obtained for $Cu_{0.5}Mn_{0.5}Fe_2O_4$ during the 20 min cycling at T-450°C

The conversion and yields during the reduction of the $Cu_{0.5}Mn_{0.5}Fe_2O_4$ ferrite are shown in Figure 4-21. An addition of Mn-cations into Cu/Fe system just slightly affected the catalytic performance of the resulted material (in comparison to Cu/Fe system – $CuFe_2O_4$). Thus, during 20 min of *tos* the sample was reduced just about 73%; the conversion starting from the very beginning approached to 99% and was stable till the end of the reduction step. The formation of products (eq. 1-15) showed the following trend distributions: H_2 increased from 50 to 81%, CO_2 varying from 18 to 16% (with the max value of 26%), CO decreased from 20 to 13%, H_2O decreased from 9 to 2%, acetone decreased from 36 to 1% and acetaldehyde was detected just in traces.
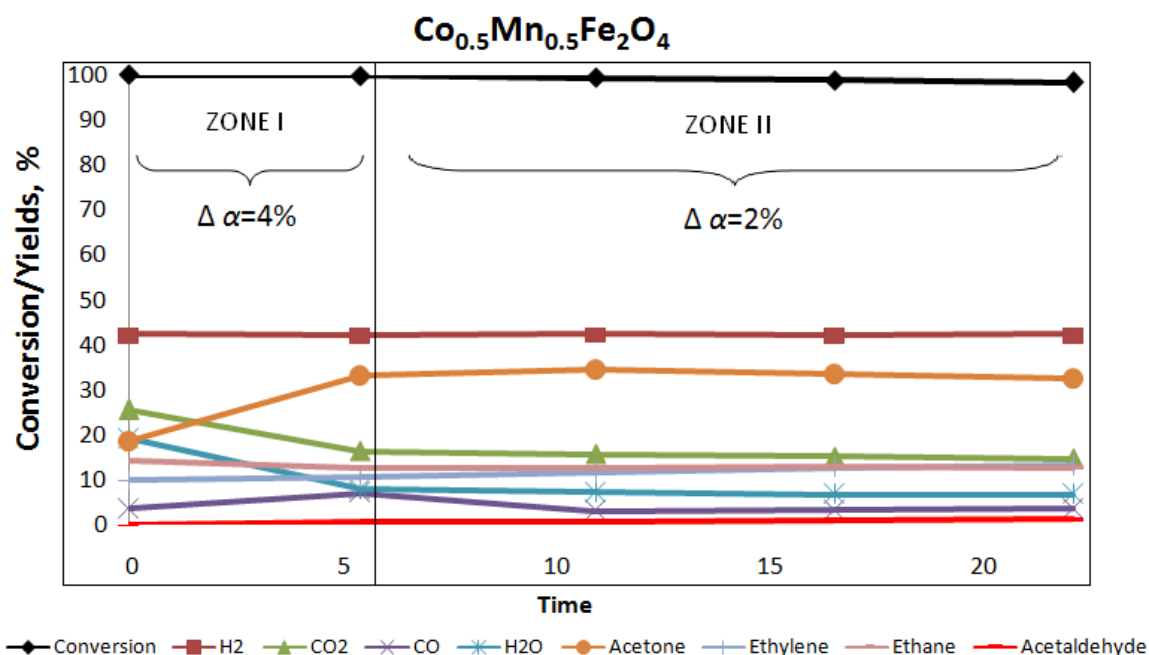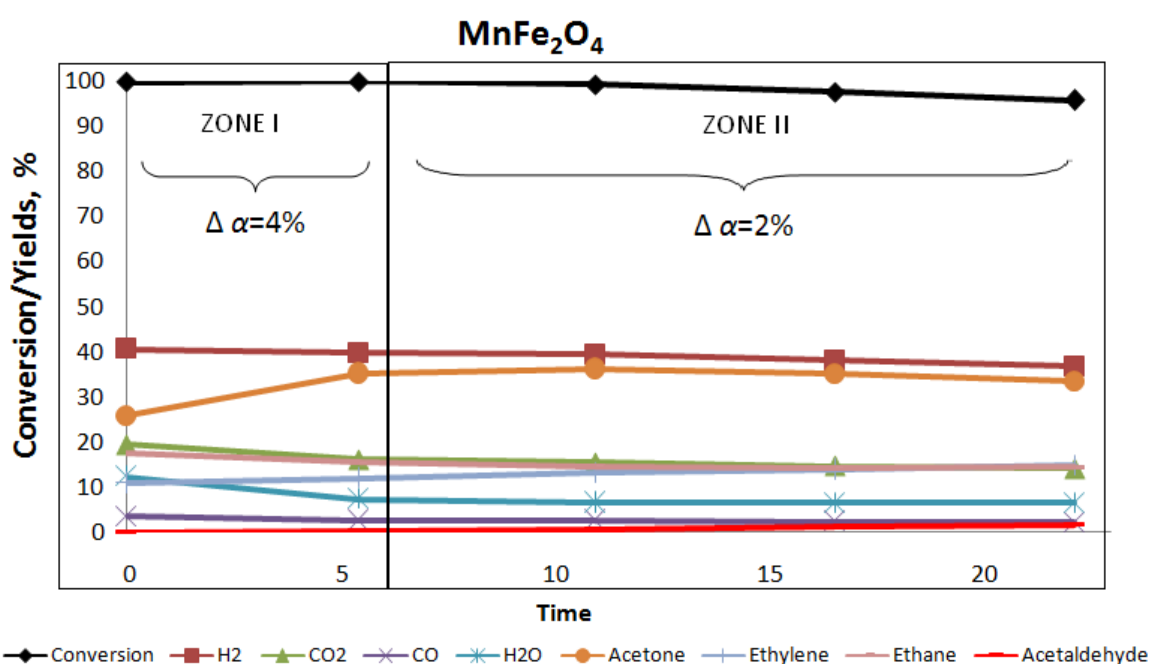
Figure 4-22. Conversion and Yields to the main products obtained for $Co_{0.5}Mn_{0.5}Fe_2O_4$ during the 20 min cycling at T-450°C

Figure 4-22 and Figure 4-23show the conversion of ethanol and the yields to the various products obtained over $MnFe_2O_4$ and $Co_{0.5}Mn_{0.5}Fe_2O_4$ ferrites. The data demonstrate an apparent difference in the reducibility and the "catalytic activity" of these ferrites in comparison to the four previously discussed samples. Specifically, we could distinguish two different zones, during which the spinel first underwent a progressive reduction followed by "pseudo-steady-state". Taking into account the ex-situ XRD study of the $MnFe_2O_4$ and $Co_{0.5}Mn_{0.5}Fe_2O_4$ ferrites performed at different reduction stages (1, 3, 5 and 20 min of *tos*), the formation of just two phases Mn_xFe_yO and $Mn_{1-x}Fe_{2+x}O_4$ helped us to explain their peculiar behavior.

Looking first at the $Co_{0.5}Mn_{0.5}Fe_2O_4$ graph (Figure 4-22), the conversion of ethanol during 20 min of *tos* slightly decreased from 100 to 98%, giving its max reduction degree of just 10% (while by itself $CoFe_2O_4$during the same 20 min of *tos* was almost completely reduced – 82%). At the same time, the conversion of ethanol over $MnFe_2O_4$ decreased from 100 to 96% (Figure 4-23).The evolution of the product yields over these two samples showed the same time depending trend variations, viz. in approximately 5 min (**zone I**) the yields to all the products varied the most, while the reduction degree approached to 6 % for $MnFe_2O_4$ and 8% for $Co_{0.5}Mn_{0.5}Fe_2O_4$ (corresponds to the reduction speed of 0.8 %/min). Thereafter a

zone II started (from 5 to 20 min of tos, Δt=15 min), where all the yields were stable in time without any big changes, while the total reduction extent reached 8% for $MnFe_2O_4$ and 10% for $Co_{0.5}Mn_{0.5}Fe_2O_4$ (corresponds to Δα=2% and the reduction speed of 0.13%/min). In comparison to Co, Cu, Cu/Co and Cu/Mn ferrites, the reduction of $MnFe_2O_4$ and $Co_{0.5}Mn_{0.5}Fe_2O_4$ samples demonstrates different trends in the products distribution. Namely ethane, ethylene and acetone were formed continuously within 20 min of *tos* with much higher yields of about 14, 15 and 39% for $MnFe_2O_4$/12, 13 and 33% for $Co_{0.5}Mn_{0.5}Fe_2O_4$, respectively:

Figure 4-23. Conversion and Yields to the main products obtained for $MnFe_2O_4$ during the 20 min cycling at T-450°C

(16) $2 \, C_2H_5OH \rightarrow CH_3CH_3 + CH_3CHO + H_2O$

(17) $C_2H_5OH \rightarrow C_2H_4 + H_2O$

(18) $C_2H_4 \rightarrow 2 \, C + 2 \, H_2$
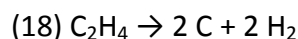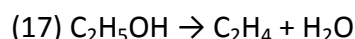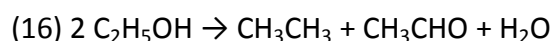
According to the TPR and ex-situ XRD results (discussed previously), the reduction of the following samples is described by a spontaneous reduction over the entire surface which occurs immediately on the contact with the reducing stream and leads to the expelling of Mn^{2+} cations out of the spinel structure. The formation of new phases resembles more to a core-shell catalytic system, comprised of Fe-enriched spinel core ($Mn_{1-x}Fe_{2+x}O_4$) covered with a Mn_xFe_yO shell ($Mn_{1-x}Fe_{2+x}O_4@Mn_xFe_yO$). According to this, a significant slowdown of

the reduction speed from 0.8 to 0.13%/min was attributed to an accumulation of Mn_xFe_yO phase, which has a high thermodynamic stability and as a consequence ascarce attitude towards the reduction to the metallic component, where the further diffusion of the reducing stream into the bulk (core) may be more problematic. Moreover, the "core@shell" model may also explain the formation of acetone directly from the ethanol via ketonization of acetates (eq.15), where the formed shell of Mn_xFe_yO acts as a catalyst while $Mn_{1-x}Fe_{2+x}O_4$ core delivers oxygen (O_L) to restore the pre-reduced shell. It is worth noting, that DRIFTS study performed earlier over $Co_{0.6-x}Mn_xFe_{2.4}O_y$[106] ferrospinels confirmed the formation of acetates and carbonates as important surface intermediates. Moreover, only in the case of $Mn_{0.6}Fe_{2.4}O_y$ sample there was no evidence of the acetate species to be transformed into carbonates one, which may also justify the high acetone yields over $Mn_{0.6}Fe_{2.4}O_y$ as well as for $MnFe_2O_4$ and $Co_{0.5}Mn_{0.5}Fe_2O_4$ samples.

Coke and heavy compounds were formed in a much smaller amount $MnFe_2O_4$ (from 16 to 8%) and $Co_{0.5}Mn_{0.5}Fe_2O_4$ (from 21 to 12 %); the total integrated yields to coke for all MFe_2O_4 ferrites are plotted in Figure 4-24(see also CHNS analysis).
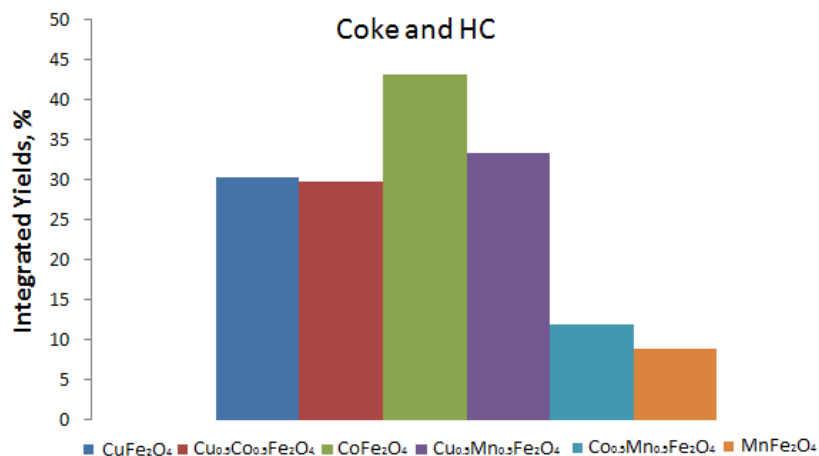
Figure 4-24. Integrated yields of coke and heavy compounds formed within 20 min over MFe₂O₄ ferrites

Determination of carbon content (CHNS analysis): after 1ˢᵗ reduction step with ethanol

In order to evaluate the amount of coke formed during the reduction step with ethanol (within 20 min), an elemental analysis (CHNS) on the different materials was carried out. Table 4-7summarizes the results of CHNS analysis over MFe_2O_4 ferrospinels. According to the obtained results, the highest amount of coke accumulated during the ethanol reduction

was detected over $Cu_{0.5}Co_{0.5}Fe_2O_4$ and $CoFe_2O_4$ samples and it declines in the following order: $Cu_{0.5}Co_{0.5}Fe_2O_4 > CoFe_2O_4 > CuFe_2O_4 > Cu_{0.5}Mn_{0.5}Fe_2O_4 > Co_{0.5}Mn_{0.5}Fe_2O_4 > MnFe_2O_4$.

Table 4-7. CHNS results over MFe2O4 ferrites after 20 min reduction

Sample	$C_{w\%}$ (after 20 min reduction)
$CuFe_2O_4$	6.9
$Cu_{0.5}Co_{0.5}Fe_2O_4$	16.3
$CoFe_2O_4$	11.6
$Co_{0.5}Mn_{0.5}Fe_2O_4$	1.5
$Cu_{0.5}Mn_{0.5}Fe_2O_4$	6.1
$MnFe_2O_4$	1.7

2nd step: 20 min re-oxidation with water
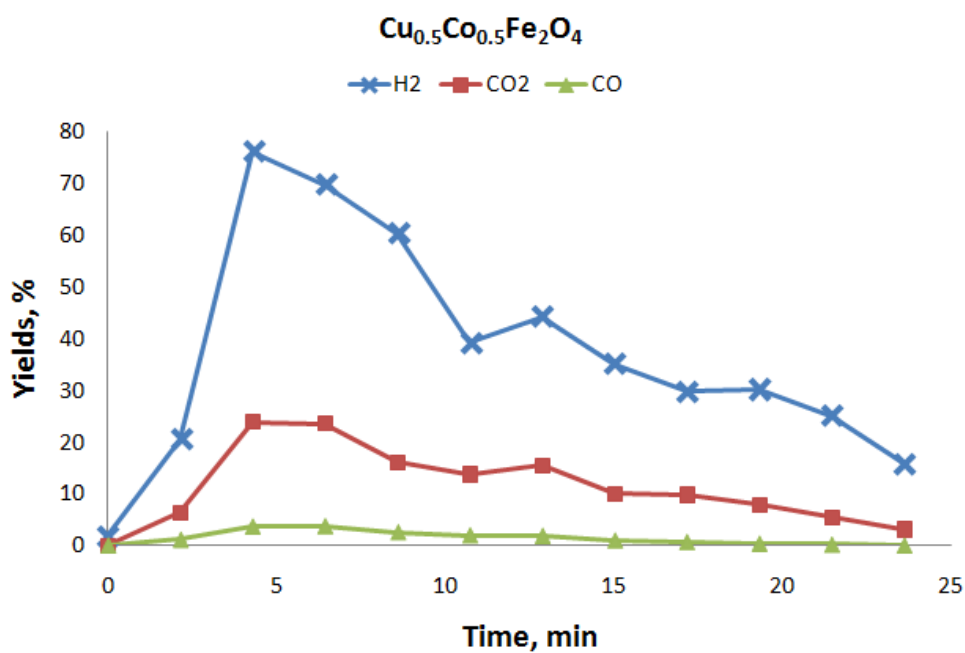
Figure 4-25. Yields to H_2 and CO_x obtained for $Cu_{0.5}Co_{0.5}Fe_2O_4$ during the re-oxidation step at T-450°C within 20 min of tos
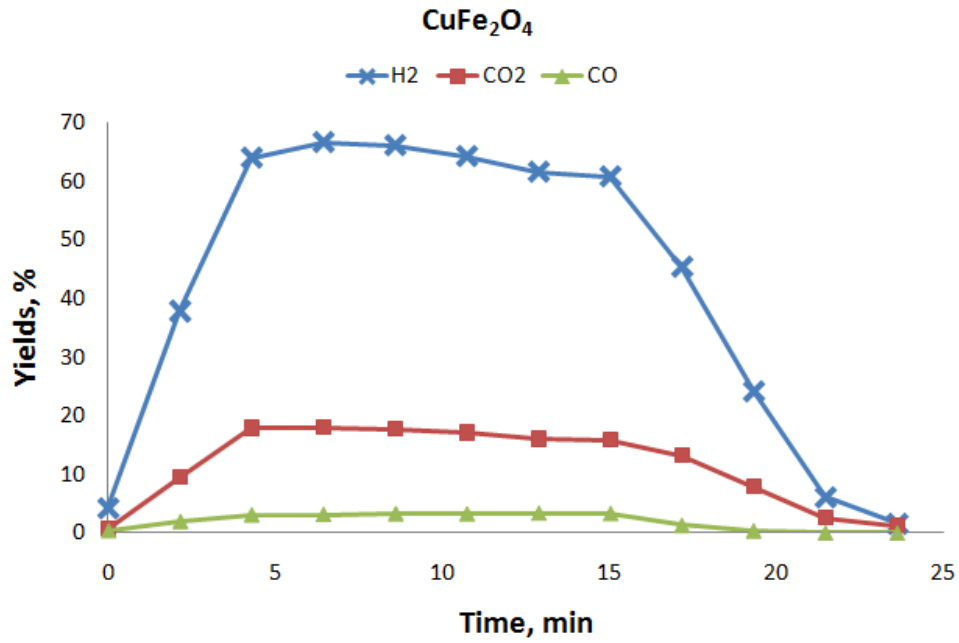
Figure 4-26. Yields to H$_2$ and CO$_x$ obtained for CuFe$_2$O$_4$ during the re-oxidation step at T-450°C within 20 min of tos
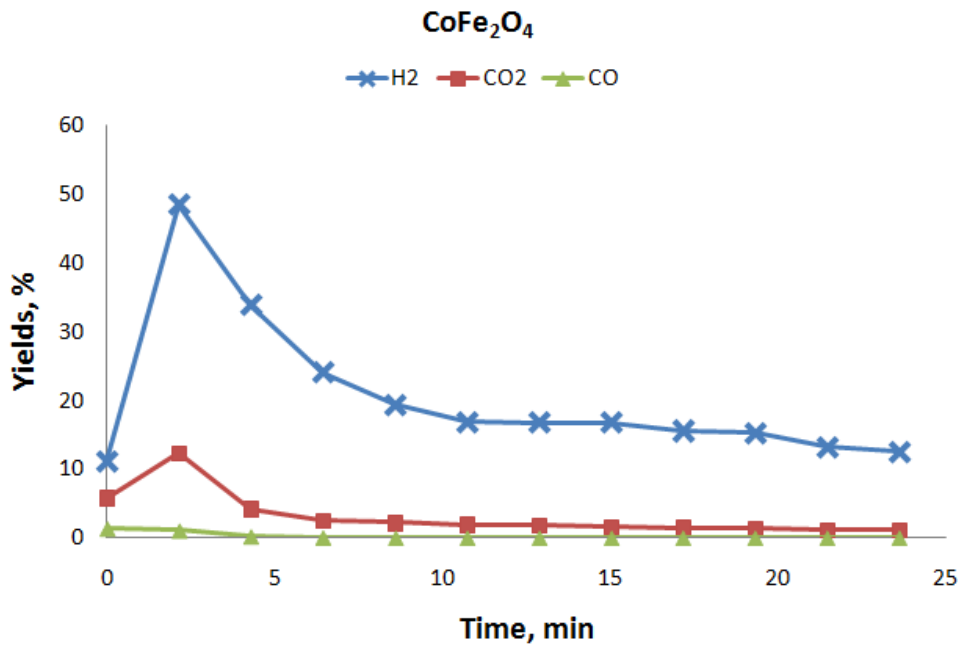
Figure 4-27. Yields to H$_2$ and CO$_x$ obtained for CoFe$_2$O$_4$ during the re-oxidation step at T-450°C within 20 min of tos
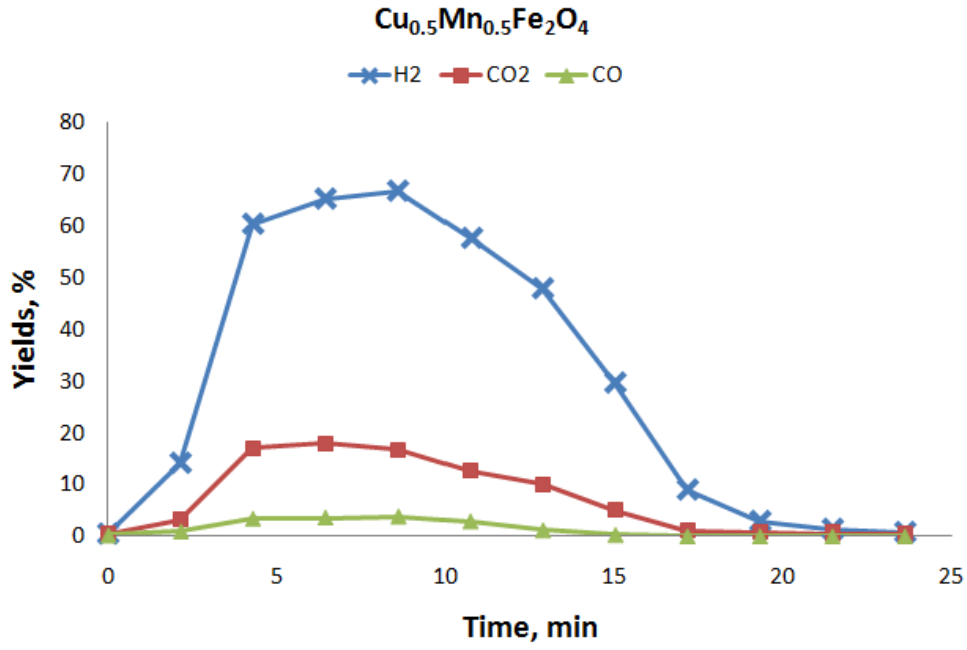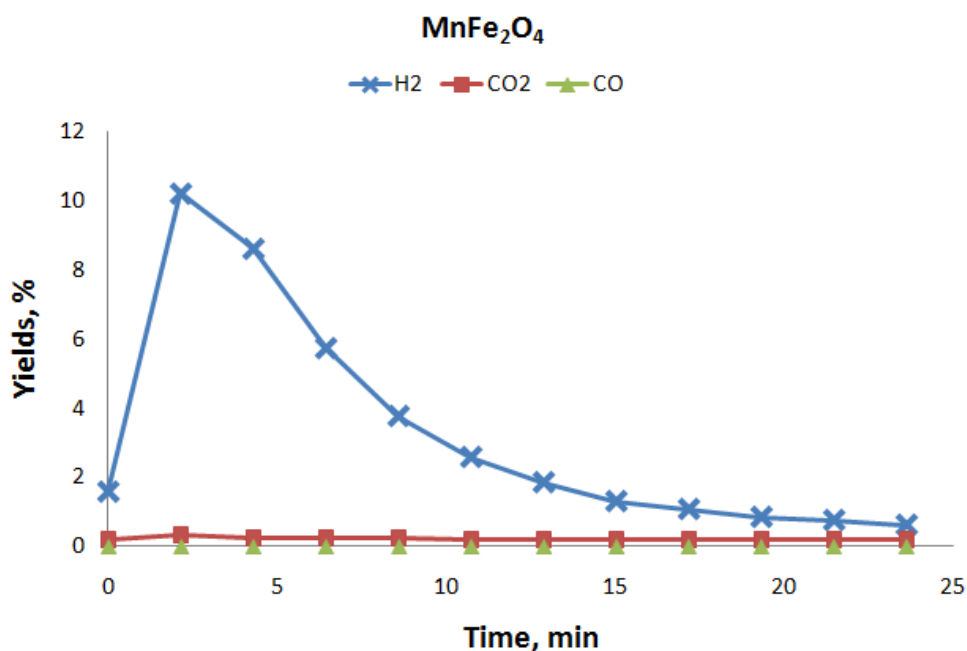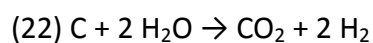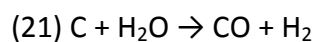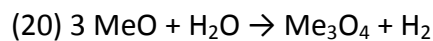
Figure 4-28. Yields to H$_2$ and CO$_x$ obtained for Cu$_{0.5}$Mn$_{0.5}$Fe$_2$O$_4$ during the re-oxidation step at T-450°C within 20 min of tos
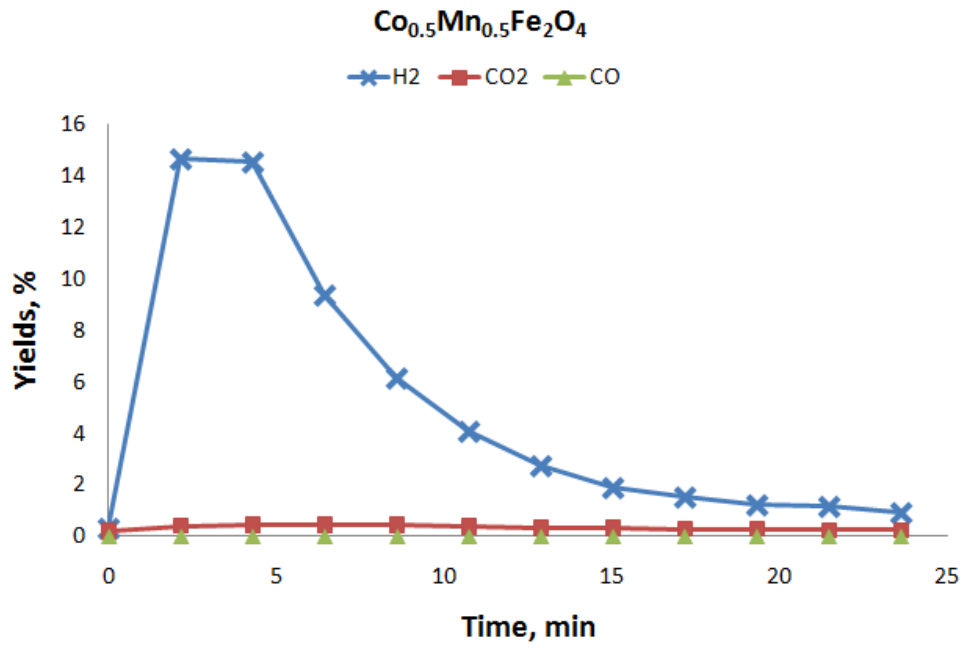
Figure 4-29. Yields to H$_2$ and CO$_x$ obtained for Co$_{0.5}$Mn$_{0.5}$Fe$_2$O$_4$ during the re-oxidation step at T-450°C within 20 min of tos

Figure 4-30. Yields to H_2 and CO_x obtained for $MnFe_2O_4$ during the re-oxidation step at T-450°C within 20 min of tos

After the 1st step with ethanol, the reduced material was then re-oxidized with water steam at 450°C during the same *tos* of 20 min, which corresponds to the 2nd step of the CLR process. The out flowing gas mixture was first passed through a water trap, in order to avoid a high-water concentration which could be pernicious for the micro-GC columns. The GC method, created to quantify all the compounds present in the gas mixture, allowed us to carry out an analysis every1.5 min. The reactions conditions described in Paragraph 2.11.

Figure 4-25 to Figure 4-30 report the yields to H_2, CO_2 and CO versus time (yields have been calculated based on the H (for H_2) or O (CO_x) content in products, with respect to the water fed – described in Paragraph 2.11.), whereas Figure 4-31compares the overall integrated yields to H_2, CO and CO_2 formed during 20 min over MFe_2O_4 ferrites. It is important to notice, that the increasing trends (within 0-5 min) shown in the Figure 4-25 to Figure 4-30most probably arise from the following fact: the stream, containing unconverted steam and products, needs a few minutes to reach the catalyst and then the on-line GC instrument after the start-up of the reaction. A common feature, which observed for almost all the samples, was a complete re-oxidation of the material in the chosen timeframe of 20 min (excluding only $CoFe_2O_4$ and $Cu_{0.5}Co_{0.5}Fe_2O_4$ samples, where the H_2-yield was still decreasing indicating an incomplete re-oxidation).

The highest hydrogen yields were detected for all three samples which contain Cu-cations as one of the incorporated metals: $CuFe_2O_4$ (52%), $Cu_{0.5}Co_{0.5}Fe_2O_4$ (47%), and $Cu_{0.5}Mn_{0.5}Fe_2O_4$ (37%); whereas a lower amount of hydrogen produced during the re-oxidation process, was obtained over Co, Mn and Mn/Co-incorporated samples: $CoFe_2O_4$ (24%), $Co_{0.5}Mn_{0.5}Fe_{2.4}O_y$ (6%) and $MnFe_2O_4$ (4%). These data lie in parallel with the previously discussed results and can be explained, taking into account the values of the reduction extent (α), calculated on the basis of Rietveld refinement; the increasing order of α: $Cu_{0.5}Co_{0.5}Fe_2O_4$-100%> $CuFe_2O_4$=$CoFe_2O_4$-82%> $Cu_{0.5}Mn_{0.5}Fe_2O_4$-73%> $Co_{0.5}Mn_{0.5}Fe_2O_4$-10%> $MnFe_2O_4$-8%, corresponds quite well to the increasing order for H_2-yields: $CuFe_2O_4$-52%> $Cu_{0.5}Co_{0.5}Fe_2O_4$-47%> $Cu_{0.5}Mn_{0.5}Fe_2O_4$-37%> $CoFe_2O_4$ (24%)> $Co_{0.5}Mn_{0.5}Fe_2O_4$-6%>$MnFe_2O_4$-4%, with the exception of only two catalysts - $CoFe_2O_4$ and $Cu_{0.5}Co_{0.5}Fe_2O_4$ which indeed was expected since the re-oxidation never reached the end.

Apart of the produced hydrogen, the common feature for all the samples was the formation of CO_x (CO_2 and CO) during the re-oxidation step (Figure 4-25 to Figure 4-31), because of the gasification of carbonaceous residues, previously formed during the reduction step. The main reactions occur during the re-oxidation process are defined as following:

(19) $Me + H_2O \rightarrow MeO + H_2$

(20) $3\ MeO + H_2O \rightarrow Me_3O_4 + H_2$

(21) $C + H_2O \rightarrow CO + H_2$

(22) $C + 2\ H_2O \rightarrow CO_2 + 2\ H_2$
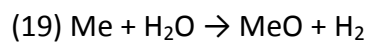
The formation of CO_x was observed with all MFe_2O_4 ferrites, thoughthe total amount of CO_2+CO was significantly different. According to the obtained results, Mn-containing catalysts produced less CO_x which resulted from a lower amount of deposited carbon during the reduction step, this results agreed with the calculated values of Coke+HC and CHNS analysis (Table 4-7).
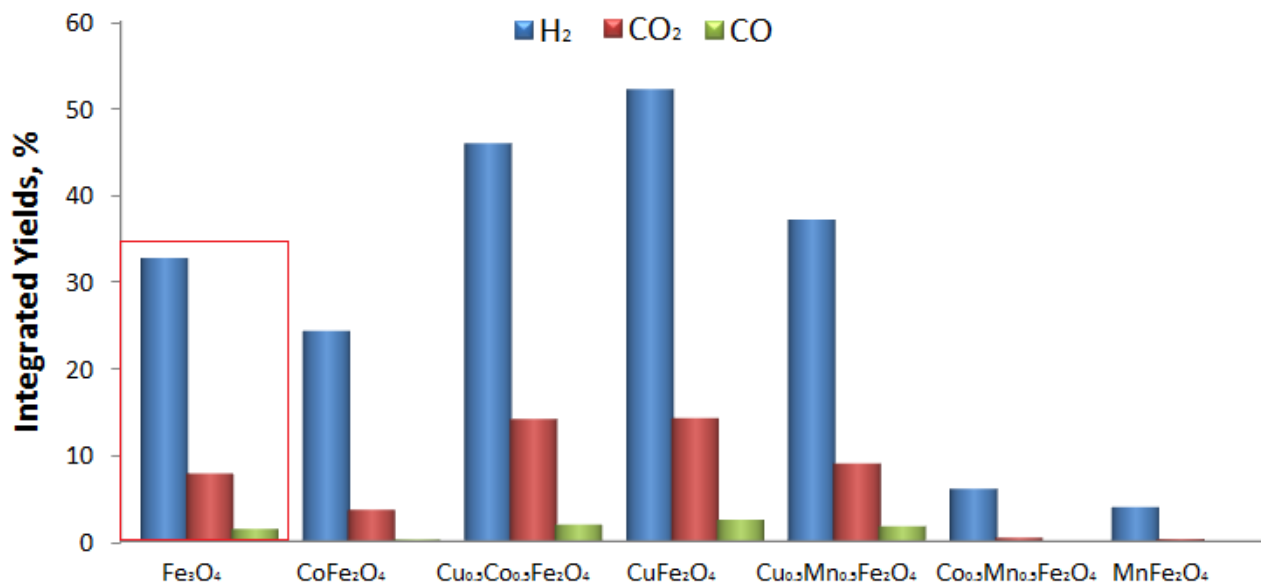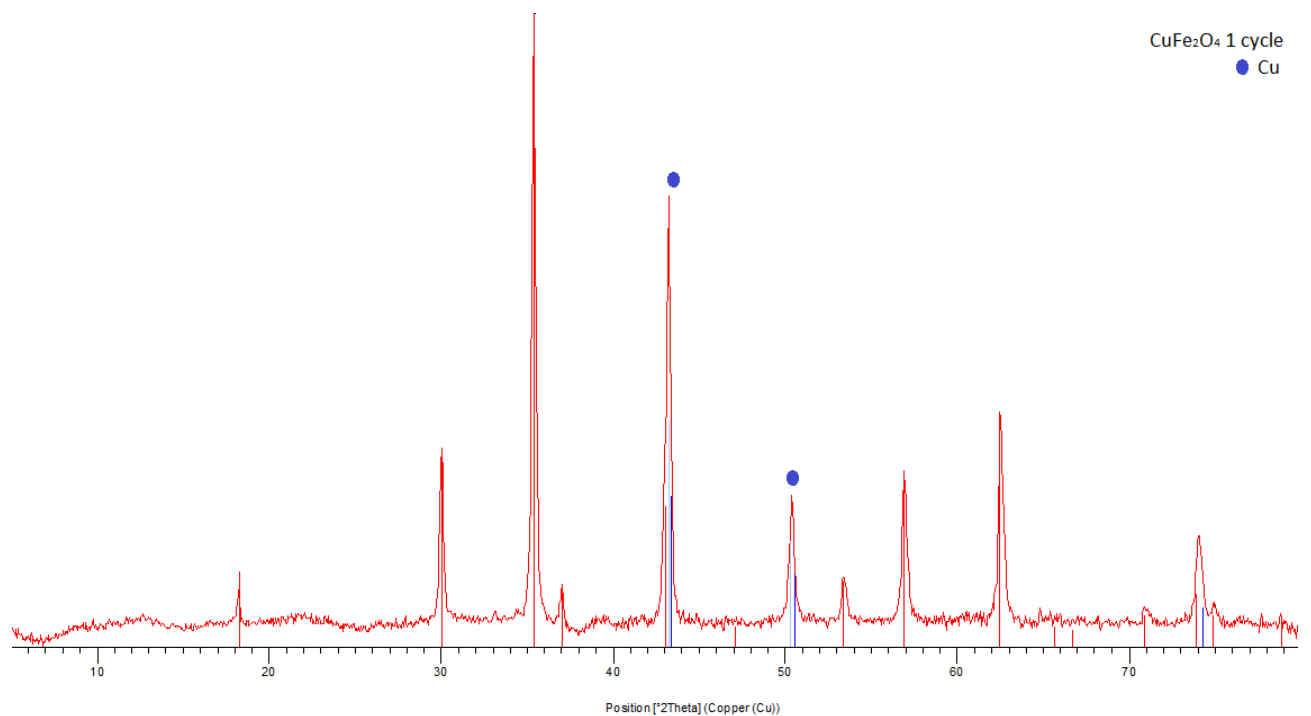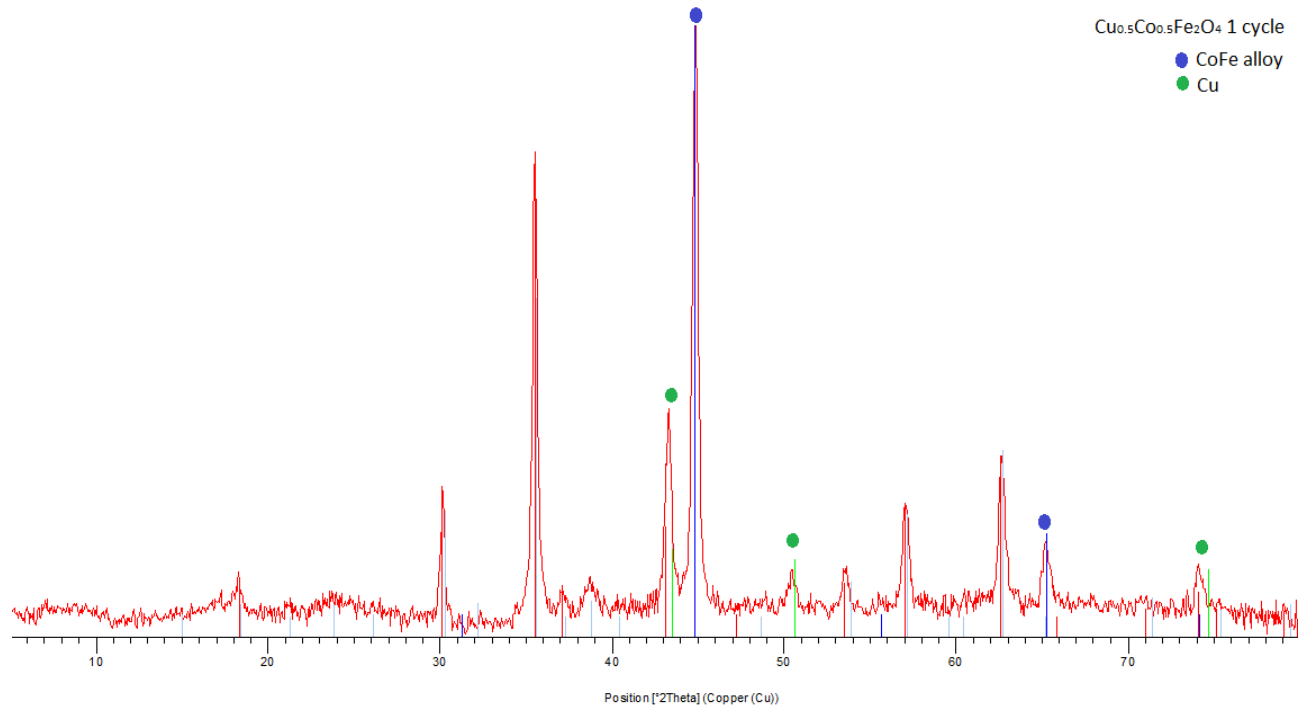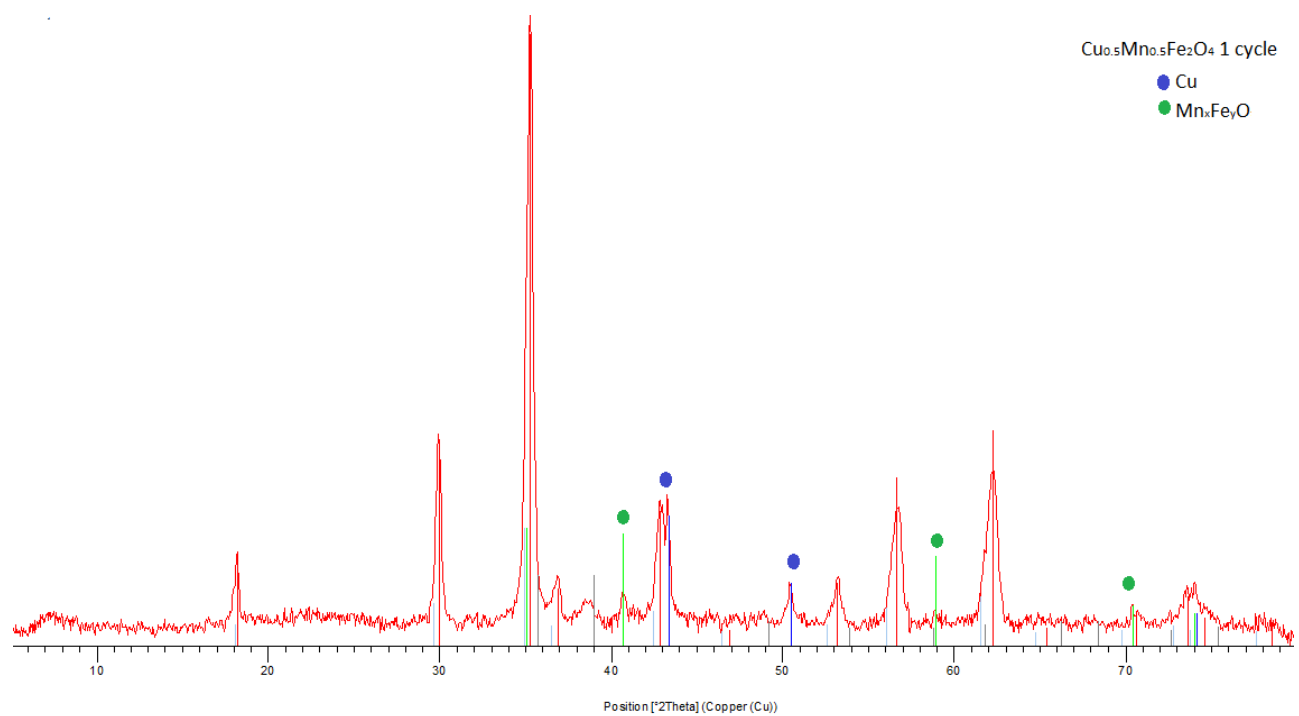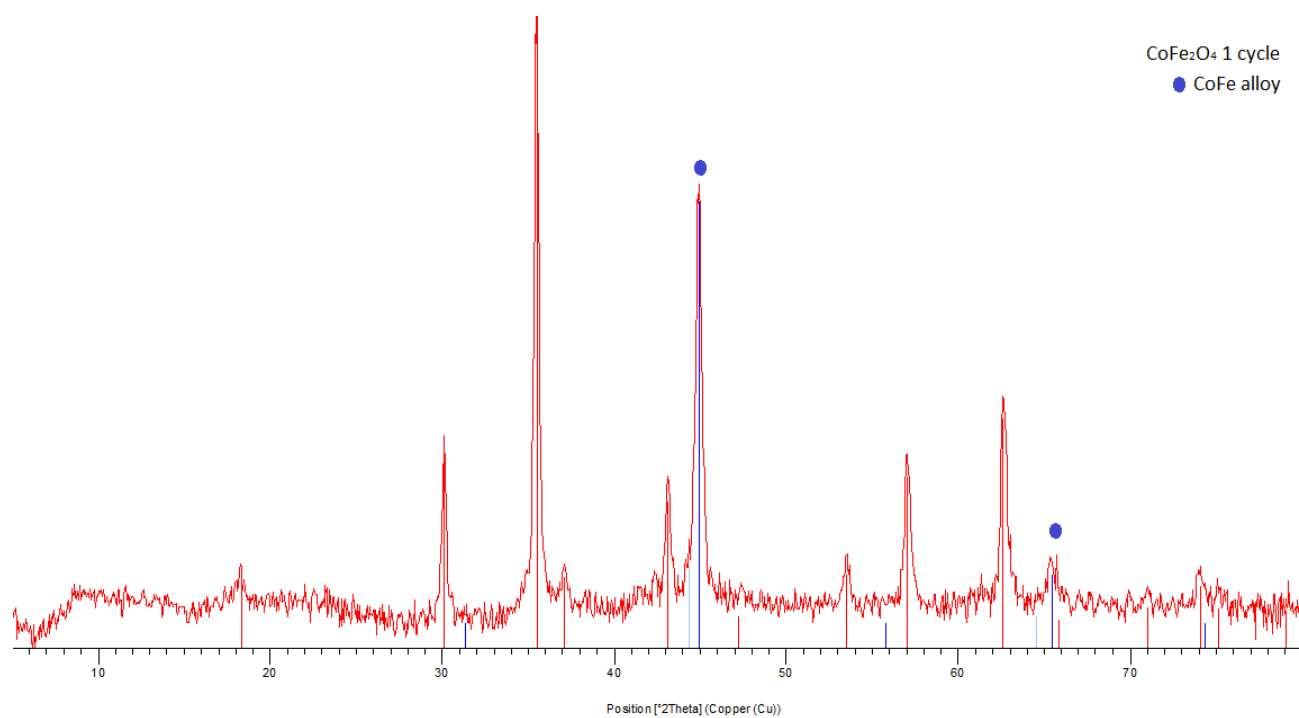
Figure 4-31. Integrated yields for H_2 and CO_x formed during the re-oxidation step with H_2O at 450^oC

It is worth noting, that the initial reason for altering composition of the original looping material-Fe_3O_4 was to achieve a better efficiency and a cycling stability, which was defined as the main drawback by Trevisanut et al[101]. From the Figure 4-31 one may notice that pristine Fe_3O_4 by itself is a reasonably efficient LM with the H_2-yield of 33%, although it turned out that Cu-incorporated samples surpassed the overall yield to H_2. From this point, we decided to compare the cycling stability of Fe_3O_4 with $CuFe_2O_4$ (52%) and $Cu_{0.5}Co_{0.5}Fe_2O_4$ (47%) samples, which gave the max yields to hydrogen(see Paragraph 4.9).

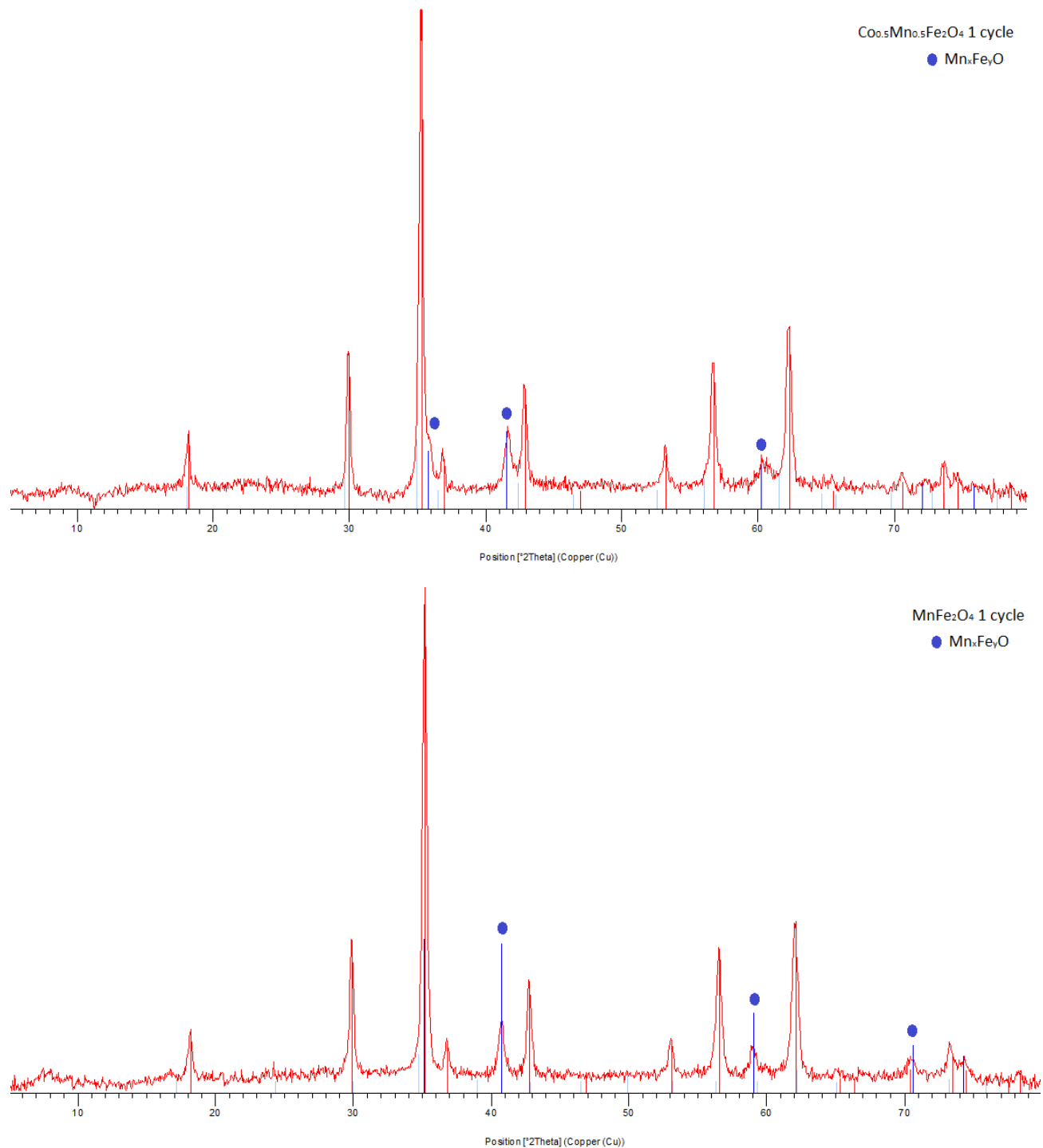**Ex-situ XRD results: "2 step CLR" – 1 complete cycle (20 min red/20 min re-ox)**

CoFe$_2$O$_4$ 1 cycle
● CoFe alloy

Position [°2Theta] (Copper (Cu))

Cu$_{0.5}$Mn$_{0.5}$Fe$_2$O$_4$ 1 cycle
● Cu
● Mn$_x$Fe$_y$O

Position [°2Theta] (Copper (Cu))

Figure 4-32. XRD patterns after 1 complete cycle of the "2 steps CLR" performed on MFe$_2$O$_4$ ferrites

One of the key points to obtain an efficient CLR process lies in the use of potentially stable (the ability to reform a spinel phase after each complete cycle with minimum segregation) and highly active (with no significant loss in the redox performance with cycling) materials. By mean of the ex-situ XRD study, performed on the used MFe$_2$O$_4$ materials, identification of the reformed phases after 1 complete cycle reveals important information on the stability

---

of the spinel phase itself and a relevance of the use of only H_2O steam to restore the original state of the looping material.

Figure 4-32 shows the XRD results taken on the cycled samples after 1 complete cycle. It can be seen, that all tested materials underwent some morphological changes and were significantly affected by sintered temperature (narrowing of the XRD patterns), segregation (presence of M and MO phases in addition the spinel one).

Performing the 2nd re-oxidation step with water steam at 450°C led to the formation of the following phases: _$Cu_{0.5}Co_{0.5}Fe_2O_4$_ (reformed spinel, CoFe alloy and metallic Cu^0), _$CuFe_2O_4$_ (reformed spinel and metallic Cu^0), _$CoFe_2O_4$_ (reformed spinel and CoFe alloy), _$Cu_{0.5}Mn_{0.5}Fe_2O_4$_ (reformed spinel, metallic Cu^0 and Mn_xFe_yO), _$Co_{0.5}Mn_{0.5}Fe_2O_4$_ (reformed spinel and Mn_xFe_yO) and _$MnFe_2O_4$_ (reformed spinel and Mn_xFe_yO). The following results indicate that all of the looping materials were affected by segregation phenomena in addition to the sintering one. Nevertheless, the presence of the reformed spinel phase (a main 100% reflection of (311) plane at 35.5° 2θ) in all re-oxidized MFe_2O_4 samples indicate the possibility to partly re-obtain the original state of the looping material. However, the evidence of the incomplete re-oxidation of the metallic component - M^0 (mainly as CoFe alloy and Cu^0) to M^{n+} indicated that the use of H_2O steam as the only oxidant at T-450°C was insufficient. One of the possible solutions to overcome this problem is to add the 3rd step (O_2-feeding to complete re-oxidation and to clean the looping material from the remained coke), discussed in the next paragraph.

4.8. Characterization of cycled looping materials: 3 steps CLR - 1 complete cycle (20 min red/20 min re-ox/30 min air)

XRD and BET results after 1 complete cycle

The structure of the materials after 1 complete cycle in the "3 step CLR" with air regeneration is defined from XRD patterns (Figure 4-33). Resulted patterns confirm the formation of the spinel oxide, as the main phase for all the regenerated samples. Using Rietveld refinement we managed to quantify the amount of the supplementary phases formed during the regeneration step with air: $Cu_{0.5}Co_{0.5}Fe_2O_4$ (spinel-98,52% and CuO-1.48%), $CuFe_2O_4$ (spinel-80,44% and CuO-19,56%, note that the starting material contained

21% of CuO), $CoFe_2O_4$ (spinel-83,36% and Co_3O_4-16,64%), $Cu_{0.5}Mn_{0.5}Fe_2O_4$ (spinel- 100%), $Co_{0.5}Mn_{0.5}Fe_2O_4$ (spinel-100%) and $MnFe_2O_4$ (no RV refinement was done, however the small intensity reflection from MnO_2 in addition to the spinel phase was observed).

In the Table 4-8are listed results for SSA, crystallite size (calculated by Scherrer eq.) and particle size (calculations are based on N_2 adsorption (BET) data) of fresh and regenerated samples. Apparent increase of the crystallite/particle size (as a consequence decrease of the SSA) observed for all MFe_2O_4 ferrites is a result of the sintering temperature effect.
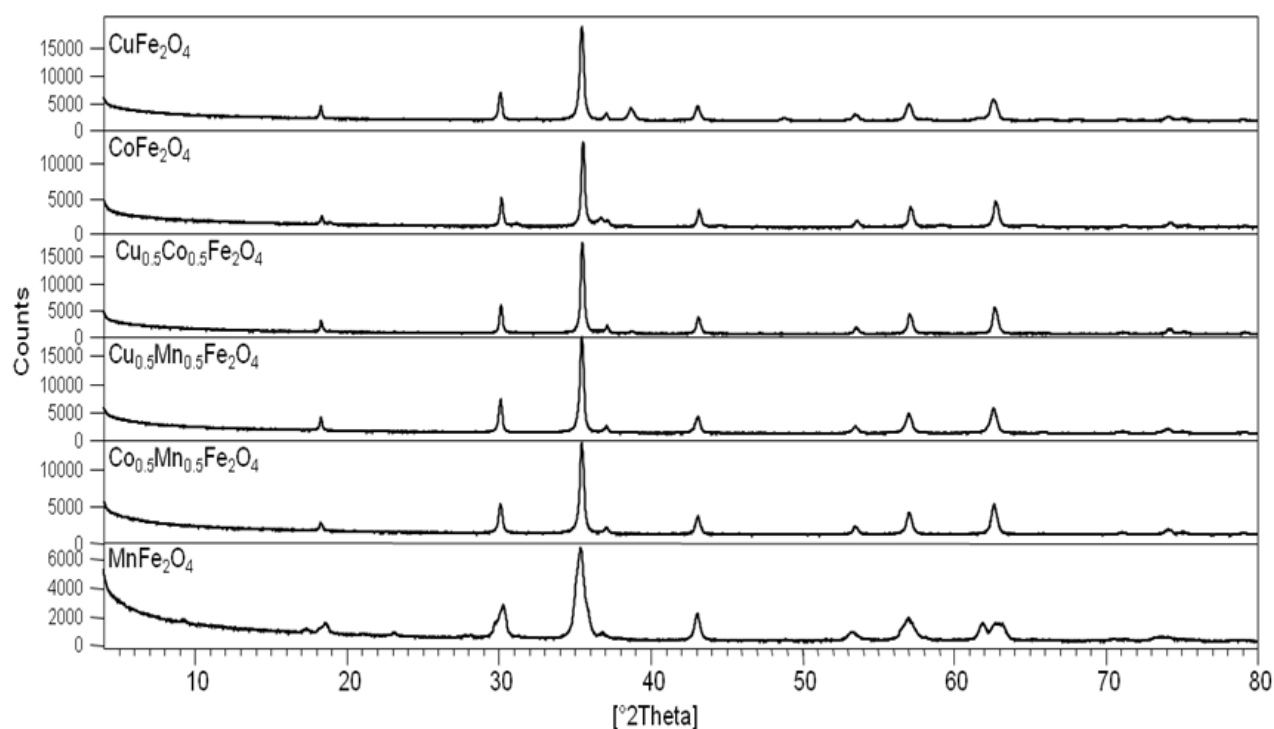
Figure 4-33. XRD results after 1 complete cycle in the "3 steps CLR"

Table 4-8. Specific surface area (SSA) and crystallite/particle size results

Sample name	SSA $_{fresh}$, m²/g	SSA $_{reg}$, m²/g	Crystallite size (Scherrer eq.) $_{fresh}$, nm	Crystallite size (Scherrer eq.) $_{reg}$, nm	Particle size (d_{BET}) $_{fresh}$, nm	Particle size (d_{BET}) $_{reg}$, nm
$CuFe_2O_4$	60	12	7.2 (22)*	34.6 (18.6)*	18.3	91.3
$Cu_{0.5}Co_{0.5}Fe_2O_4$	67	17	10.9	35^m	16.5	65.1
$CoFe_2O_4$	69	29	12.0	32^m	16.2	38.5

Co$_{0.5}$Mn$_{0.5}$Fe$_2$O$_4$	141	30	3.5	31.2^m	8.0	37.6
Cu$_{0.5}$Mn$_{0.5}$Fe$_2$O$_4$	112	14	-	27.7^m	10.0	79.7
MnFe$_2$O$_4$	165	26	-	17.1^m	6.9	43.7

***CuO phase**

^{m}**-medium value (at app.30.1 and 62.5 2θ)**

Determination of carbon content (CHNS analysis) after 1 complete cycle

One of the reasons that the looping material undergoes deactivation is related to the coke deposition and its further accumulation during cycling using conventional "2 steps CLR". From that point it was important to overcome it using modified process, so called "3 steps CLR". Table 4-9summarizes the results of CHNS analysis over MFe$_2$O$_4$ ferrospinels.The amount of remained carbon after carrying the 3rd step with air was neglectable, leading us to the conclusion that an addition of the 3rd step to the conventional process has its beneficial effect on the coke removal in addition to the possibility to restore the original state of the looping material which confirmed previously by XRD results.

Table 4-9. CHNS results over MFe$_2$O$_4$ ferrites after 1 complete cycle in the "3 steps CLR" process

Sample	C$_{w\%}$ (after regeneration)
CuFe$_2$O$_4$	**0.01**
Cu$_{0.5}$Co$_{0.5}$Fe$_2$O$_4$	**0.02**
CoFe$_2$O$_4$	**0.14**
Co$_{0.5}$Mn$_{0.5}$Fe$_2$O$_4$	**0**
Cu$_{0.5}$Mn$_{0.5}$Fe$_2$O$_4$	**0**
MnFe$_2$O$_4$	**0.11**

4.9. 2 steps CLR vs 3 steps CLR: cycling of looping materials (3 cycles·20 min)

Fe₃O₄ 3 cycles (2 step CLR)

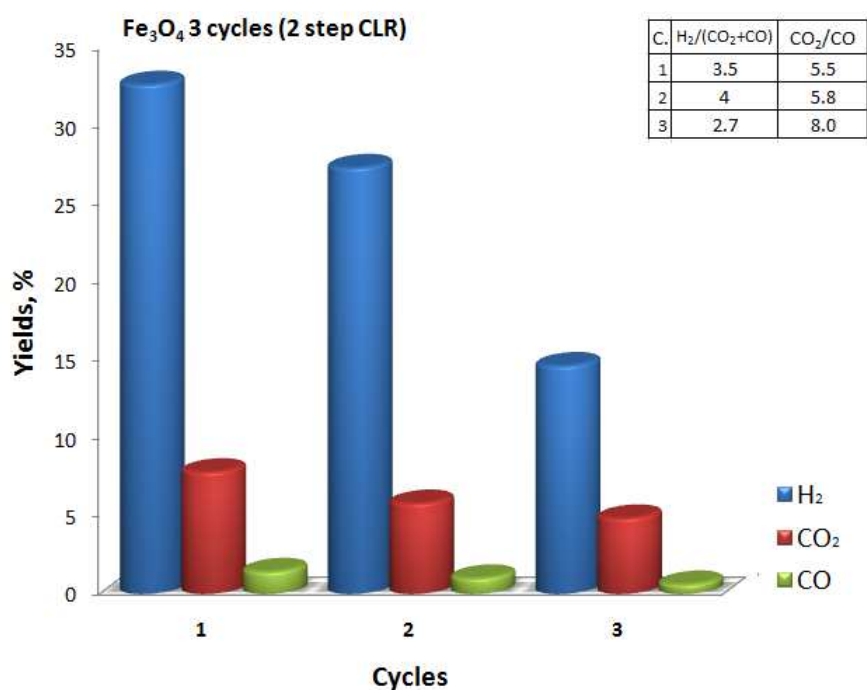| C.	$H_2/(CO_2+CO)$	CO_2/CO
1	3.5	5.5
2	4	5.8
3	2.7	8.0

Figure 4-34. Yields to H_2 and CO_x obtained for Fe_3O_4 during the re-oxidation step at T-450°C within 3 cycles·20 min in the "2 steps CLR" process
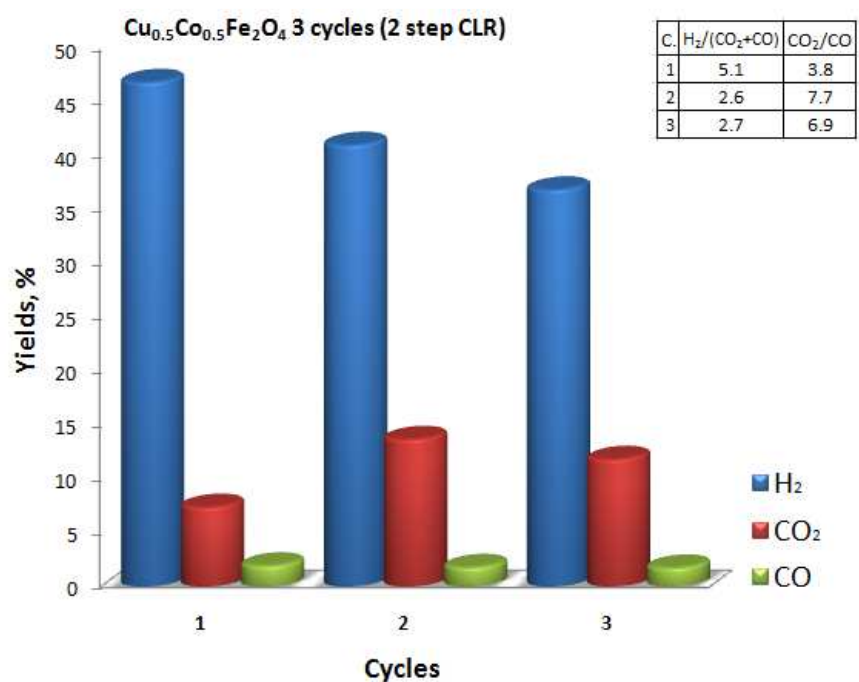
$Cu_{0.5}Co_{0.5}Fe_2O_4$ 3 cycles (2 step CLR)

C.	$H_2/(CO_2+CO)$	CO_2/CO
1	5.1	3.8
2	2.6	7.7
3	2.7	6.9

Figure 4-35. Yields to H_2 and CO_x obtained for $Cu_{0.5}Co_{0.5}Fe_2O_4$ during the re-oxidation step at T-450°C within 3 cycles·20 min for each step (equal to the total *tos* of 60 min for the first step) in the "2 steps CLR" process
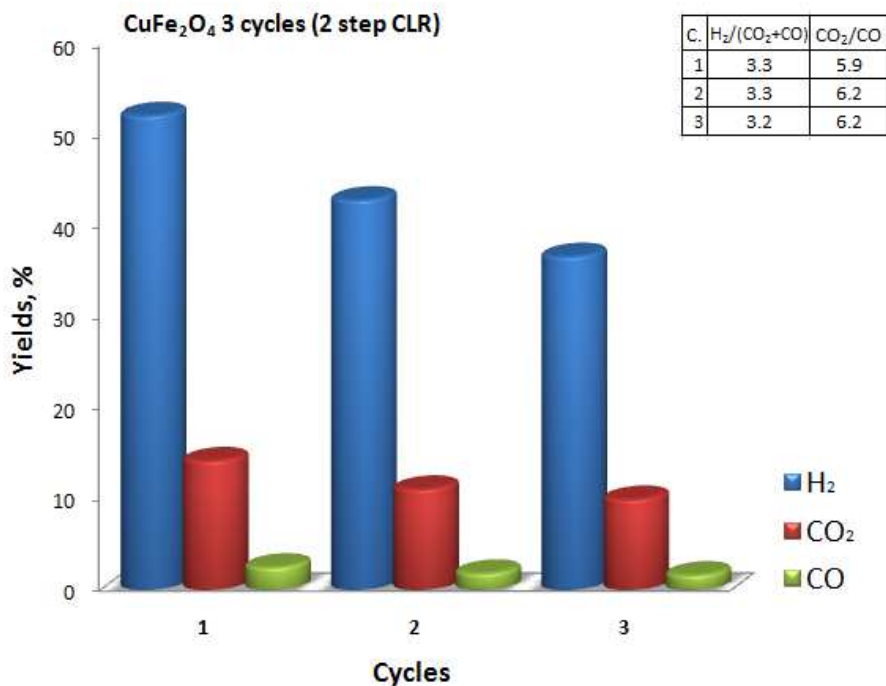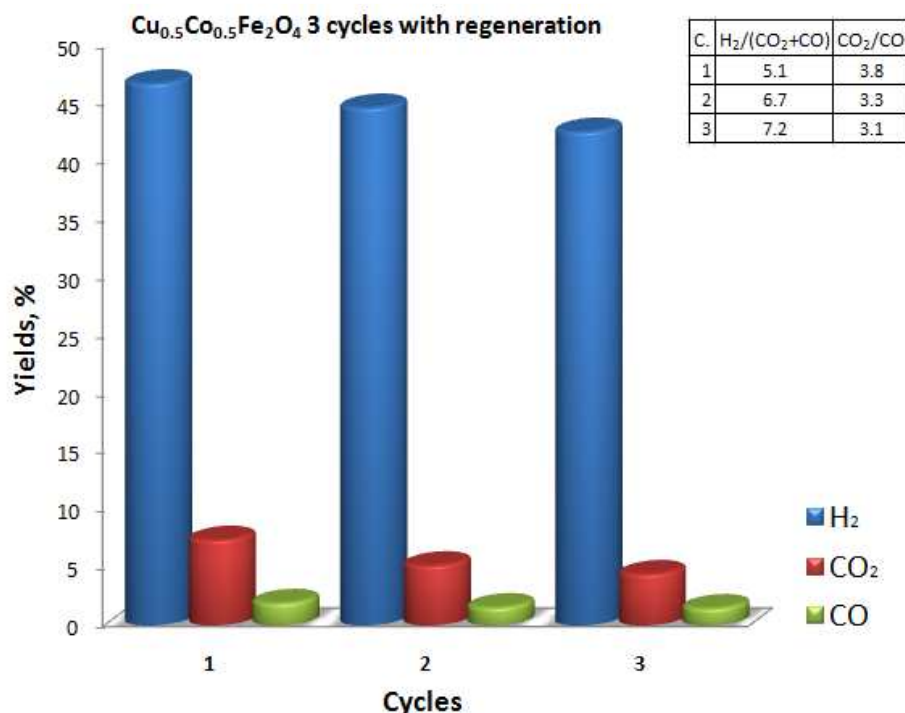
Figure 4-36. Yields to H_2 and CO_x obtained for CuFe$_2$O$_4$ during the re-oxidation step at T-450°C within 3 cycles·20 min for each step (equal to the total *tos* of 60 min for the first step) in the "2 steps CLR" process

Figure 4-34 to Figure 4-36 show integrated values for the produced H_2 and CO_x obtained during the 3 complete 2-steps CLR cycles of 20 min for each step (equal to the total *tos* of 60 min for the first step), where bare-Fe$_3$O$_4$ was taken as a reference. From the results it is clear, that both M modified samples (Cu$_{0.5}$Co$_{0.5}$Fe$_2$O$_4$ and CuFe$_2$O$_4$) and Fe$_3$O$_4$ exhibited a decrease in the total amount of produced H_2 with each performed cycle, however magnetite showed the most extreme decreasing trend: Cu$_{0.5}$Co$_{0.5}$Fe$_2$O$_4$ – 1st (47%), 2nd (41%) and 3rd (36%); CuFe$_2$O$_4$ – 1st(52%), 2nd (43%) and 3rd (36%); Fe$_3$O$_4$ – 1st (33%), 2nd (27%) and 3rd (15%). Moreover, the ratio between moles of produced H_2 and CO+CO$_2$ indicates that selectivity to H_2 is continuously declining whereas the CO_x amount is growing which also specifies in a higher contribution of the coke gasification reactions to the total amount of produced hydrogen.

Thus, the obtained results confirm a previously made statement that the looping material tends to deactivate and its nature derives from the following: 1. deep modification of the starting material via sintering and segregation phenomena; 2. continuous "coking" of the material with each performed cycle due to impossibility to achieve a total removal of it in the conventional 2 steps CLR process; 3. incomplete re-oxidation of the metallic component (M^0) using just H_2O as an oxidant (supported by XRD and CHNS results).

Such conclusions incited us to make changes to the 2 steps CLR process, using instead 3 steps "modified ethanol CLR", which consists of: 1st step - reduction of LM^{fresh} with ethanol at T-450°C; 2nd- re-oxidation of LM^{red} with water steam; 3rd step - regeneration of coked LM^{re-ox} with air at T-450°C.

Figure 4-37 and Figure 4-38report the results obtained with $Cu_{0.5}Co_{0.5}Fe_2O_4$ and $CuFe_2O_4$ ferrites in the "3 steps CLR" process (with the regeneration in air); materials were selected on the basis of the higher H_2 production, as already has been mentioned. The plotted results indicate that the amount of produced hydrogen during the 1st cycle was almost identical to its amount during the 2nd and the 3rd cycle: $Cu_{0.5}Co_{0.5}Fe_2O_4$ – 1st (47%), 2nd (45%) and 3rd (44%); $CuFe_2O_4$ – 1st (52%), 2nd (54%) and 3rd (53%). Whereas, the ratio $H_2/CO+CO_2$ and CO_2/CO during 3 consecutive cycles remains practically unchanged indicating that the selectivity to H_2 is constant with no additional contribution of H_2 produced due to the gasification of coke. This in turn shows that the modified "3 steps CLR" process shows an improved cycling stability of the looping materials in comparison to the conventional "2 steps CLR".

Figure 4-37. Yields to H_2 and CO_x obtained for $Cu_{0.5}Co_{0.5}Fe_2O_4$ during the re-oxidation step at T-450°C within 3 cycles·20 min for each step (equal to the total *tos* of 60 min for the first step) in the "3 steps CLR" process
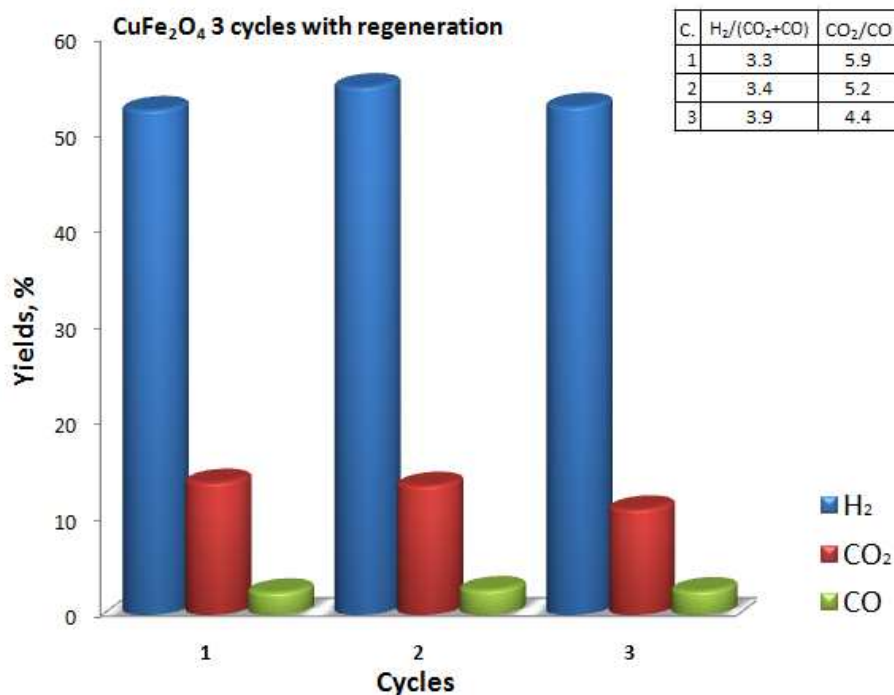
Figure 4-38. Yields to H_2 and CO_x obtained for $Cu_{0.5}Co_{0.5}Fe_2O_4$ during the re-oxidation step at T-450°C within 3 cycles·20 min for each step (equal to the total *tos* of 60 min for the first step) in the "3 steps CLR" process

Ex-situ XRD study: 2 steps CLR vs 3 steps CLR: cycling of looping materials (3 cycles·20 min)

In order to understand the main difference between the "2 steps CLR" and "3 steps CLR" processes, ex-situ XRD study was carried out on the cycled materials (Figure 4-39 to Figure 4-42).Performed 3 complete cycles of the "2 steps CLR" at 450°C led to the formation of the following phases: $\underline{Cu_{0.5}Co_{0.5}Fe_2O_4}$ (reformed spinel, CoFe alloy, metallic Cu^0 and alpha Fe^0) and $\underline{CuFe_2O_4}$ (reformed spinel and metallic Cu^0). Recalling previously discussed XRD results after 1 complete cycle the phases were detected as follows: $\underline{Cu_{0.5}Co_{0.5}Fe_2O_4}$ (reformed spinel, CoFe alloy and metallic Cu^0) and $\underline{CuFe_2O_4}$ (reformed spinel and metallic Cu^0 with much lower intensity peak). Thus, the deactivation of the looping material together with the decreasing yield to H_2 first of all can be attributed to the incomplete re-oxidation of the metallic component (M^0) which tends to accumulate in its higher amount with each subsequent cycle resulting in the less and less available MFe_2O_4/MO form to be further reduced.

Looking at the same 3 complete cycles in the "3 steps CLR" process at 450°C the detected phases were identified as follows: $\underline{Cu_{0.5}Co_{0.5}Fe_2O_4}$ (reformed spinel) and $\underline{CuFe_2O_4}$ (reformed

spinel and CuO) which appears to be exactly the same phases of the primary starting materials. And as the matter of fact, it can explain the improved stability of the looping material by adding the 3rd regeneration step (with air).
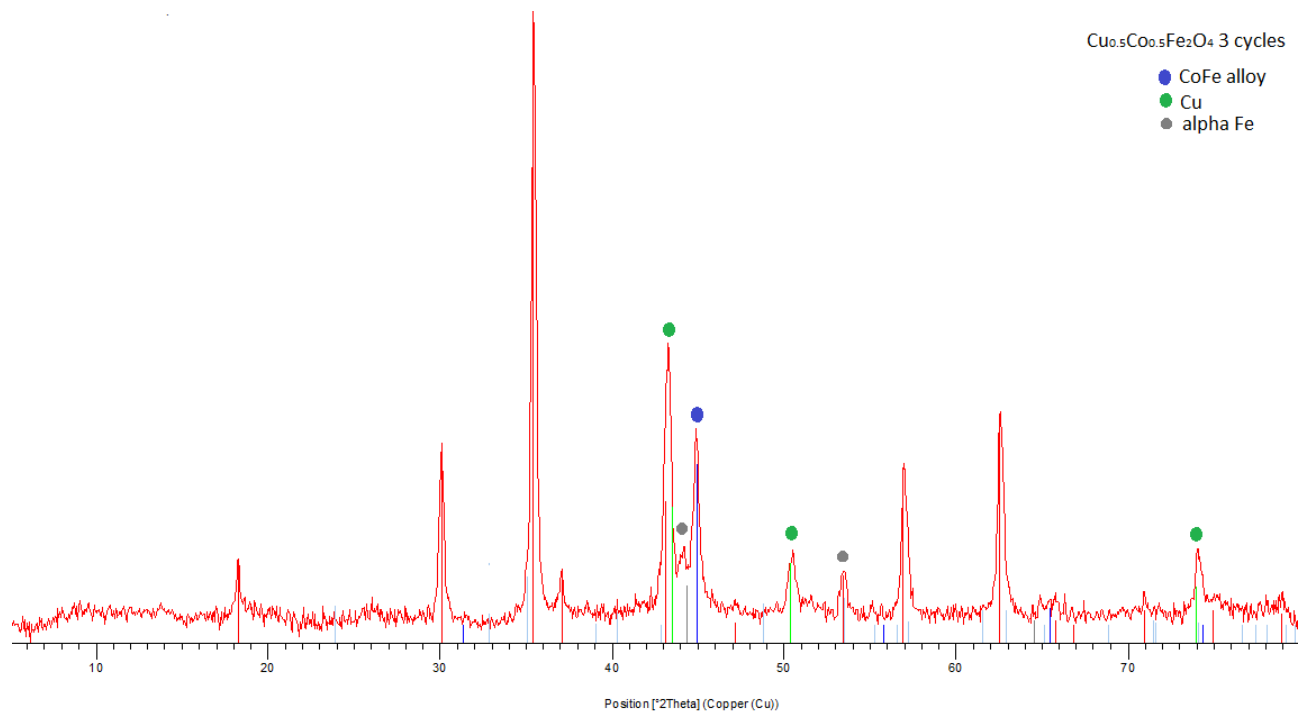

Figure 4-39. XRD patterns for Cu$_{0.5}$Co$_{0.5}$Fe$_2$O$_4$ ferrite taken after 3 complete cycles during the "2 steps CLR" process
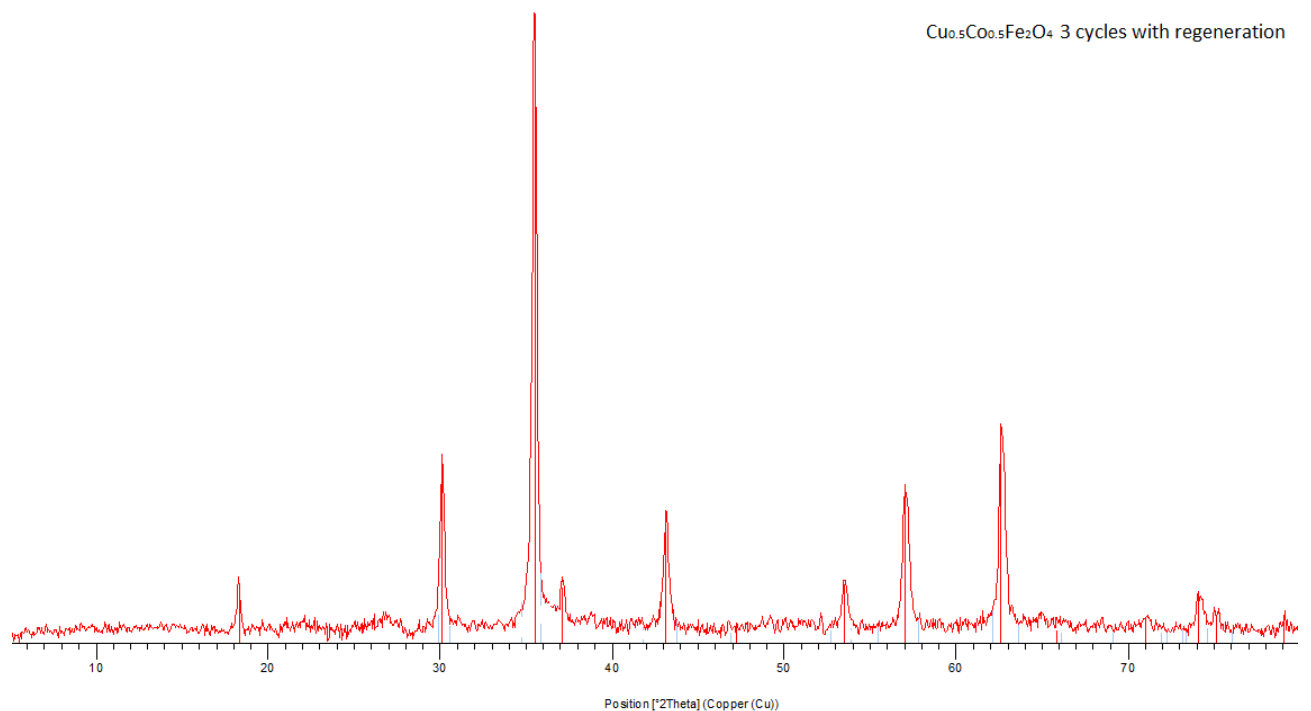

Figure 4-40. XRD patterns for Cu$_{0.5}$Co$_{0.5}$Fe$_2$O$_4$ ferrite taken after 3 complete cycles during the "3 steps CLR" process
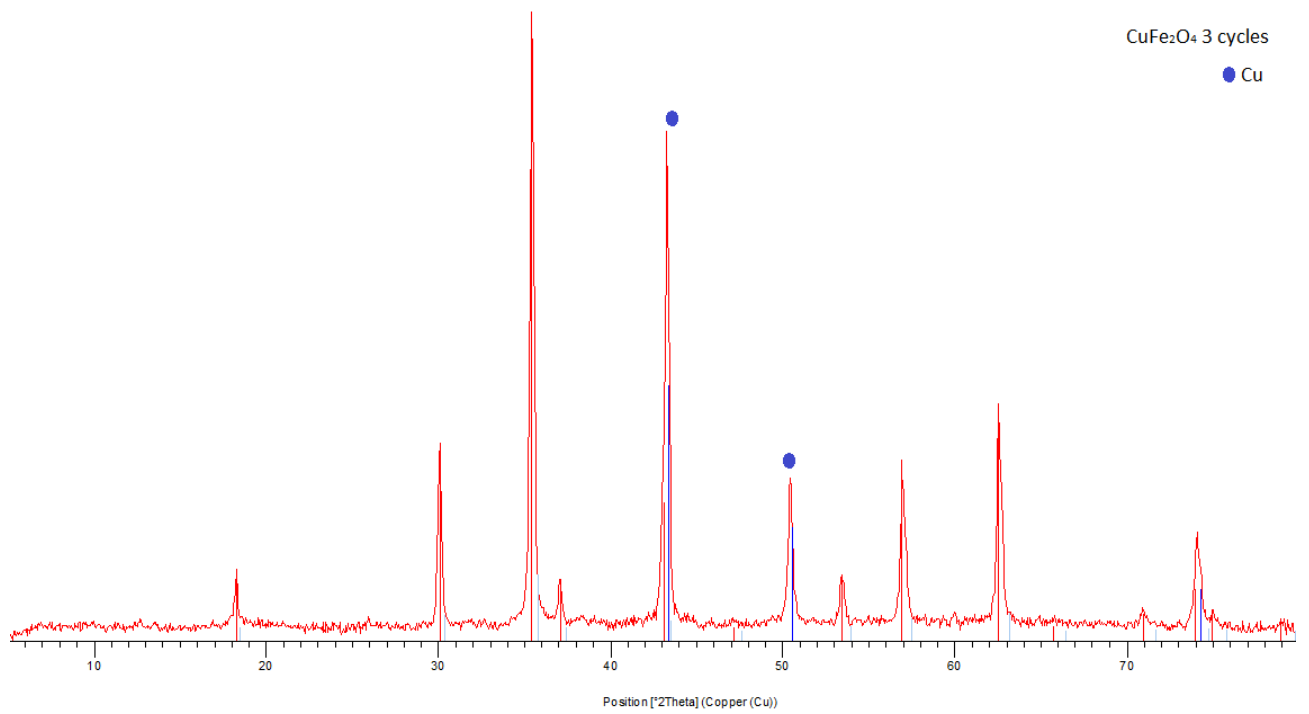
Figure 4-41. XRD patterns for CuFe$_2$O$_4$ferrite taken after 3 complete cycles during the "2 steps CLR" process
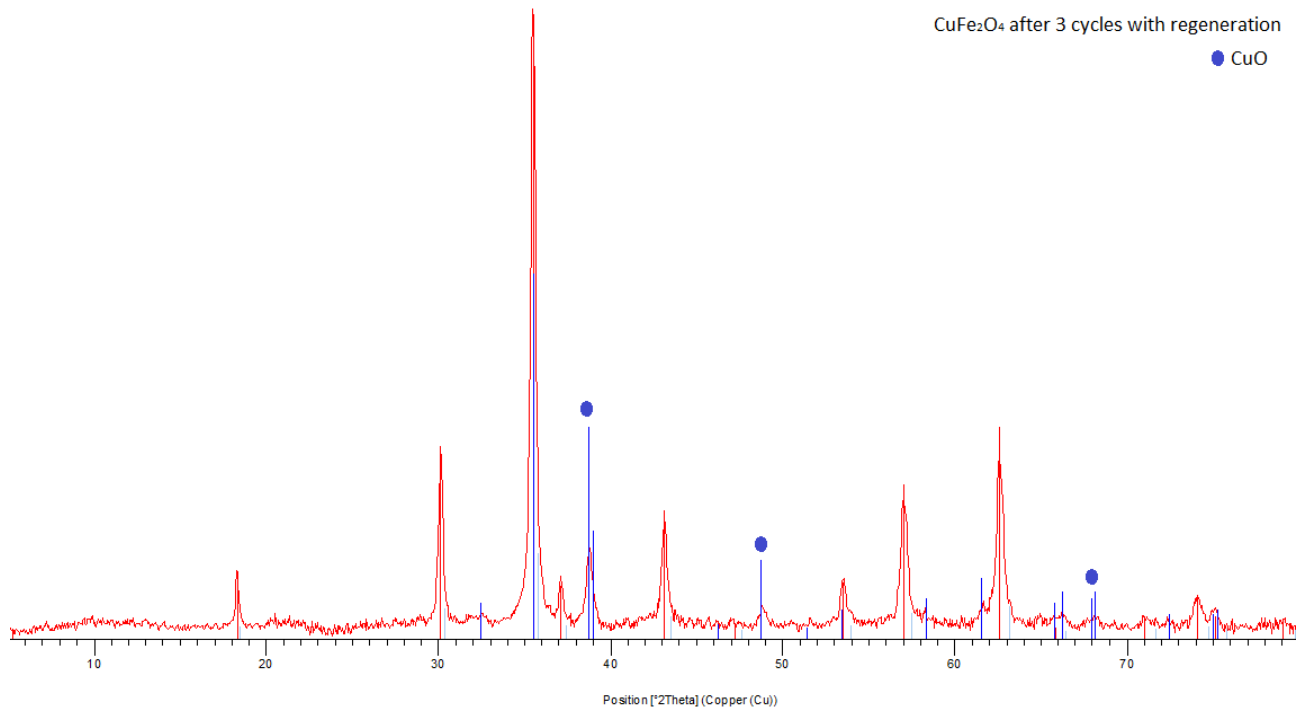
Figure 4-42. XRD patterns for CuFe$_2$O$_4$ferrite taken after 3 complete cycles during the "3 steps CLR" process

4.10. Conclusions on the study of MFe₂O₄ ferrospinels

This part of the work is focused on the study of TYPE I – MFe_2O_4 ferrospinels as O^{2-}/electrons carriers, where the composition was varied in between transition metals: Co, Mn, Cu and their combinations: Cu/Co, Cu/Mn, Co/Mn. Particular interest represented a deep study of the H_2/C_2H_5OH-reduction profiles in order to understand the main difference in the reducibility among the samples and its nature. On the basis of TPR studies, all Cu-incorporated samples $CuFe_2O_4$, $Cu_{0.5}Co_{0.5}Fe_2O_4$ and $Cu_{0.5}Mn_{0.5}Fe_2O_4$ were proposed to reduce via so called "autocatalytic" model, where the primarily formed Cu^0nucleus ($Cu^{2+} \rightarrow Cu^{0*}$) is further catalyzing the reduction of a newly reformed Fe-enriched spinel (with generic formula - $M_{1-x}Fe_{(2+x)}O_4$). The reduction occurs on the basis of hydrogen spill over effect, where Cu^0 plays the role of a catalyst which is needed to dissociate H_2 into 2H atoms. Whereas, the reduction of $MnFe_2O_4$ and $Co_{0.5}Mn_{0.5}Fe_2O_4$ ferrites appeared to be more complicated and was described by a spontaneous reduction over the entire surface which occurs immediately on the contact with hydrogen and lead to the expelling of Mn^{2+} cations out of the spinel structure with a formation of the new phases: a Fe-rich reformed spinel ($M_{1-x}Fe_{2+x}O_4$)and a hardly-reducible layer of Mn_xFe_yO oxide solid solution, like an "egg-shell".

Using ex-situ XRD approach, we followed C_2H_5OH-reduction of the $MnFe_2O_4$, $Co_{0.5}Mn_{0.5}Fe_2O_4$ and $Cu_{0.5}Mn_{0.5}Fe_2O_4$ ferrites which corresponds to the 1st step of the chemical-loop reforming process. For $MnFe_2O_4$ and $Co_{0.5}Mn_{0.5}Fe_2O_4$ ferrites, the data clearly indicated that after feeding ethanol for 1 min the formation of a new Mn_xFe_yOphase was observed. With increasing the reduction time from 1 to 20 min the spinel relative amount continued decreasing whereas that of the Mn_xFe_yO increased without the appearance of other phases, which is an important proof of the "egg-shell" reduction model. Instead, the stepwise reduction of $Cu_{0.5}Mn_{0.5}Fe_2O_4$ clearly indicated that a primarily formed phase during the 1st min of ethanol exposure was Cu^0, and the further increase of the reaction time led to a deeper reduction with the formation of Fe-carbides, thus pointing out to the "autocatalytic" reduction model. Besides, the introduction of Cu^{2+} ions into the Co/Fe system showed its strong promoting effect on the reduction of $Cu_{0.5}Co_{0.5}Fe_2O_4$ (α=100%), caused by a synergetic effect of Cu-Co couple (while by itself the reduction degree of $CuFe_2O_4$ and $CoFe_2O_4$ is equal to 82%).

Moreover, all of the MFe_2O_4 ferrites were tested as looping materials in the "2 steps CLR" process. The obtained results showed that $CuFe_2O_4$, $Cu_{0.5}Co_{0.5}Fe_2O_4$, $Cu_{0.5}Mn_{0.5}Fe_2O_4$ and $CoFe_2O_4$ within 20 min of ethanol reduction reached almost complete reduction, and as a consequence the higher yields to H_2 produced during the re-oxidation step with steam. However, with each performed cycle the material tends to deactivate as the result of: 1. deep modification of the starting material via sintering and segregation phenomena; 2. continuous "coking" of the material with each performed cycle due to impossibility to achieve a total removal of it in the conventional CLR process; 3. incomplete re-oxidation of the metallic component (M^0) using just H_2O as an oxidant. On the other hand, modifying the conventional 2 steps process by adding the 3rd step with air helped us to overcome these problems.

5. RESULTS AND DISCUSSION, PART II: TYPE II SPINELS ($M_{0.6}Fe_{2.4}O_y$)

Bulk characterization of fresh materials

The section includes a discussion of the results obtained from several characterization techniques over fresh $M_{0.6}Fe_{2.4}O_y$ (M-Co, Cu, Mn) samples: EDX analysis, XRD, N_2 adsorption, Raman Spectroscopy, TPR/TPO used to study bulk properties of freshly prepared ferrospinels, which maintain their importance being the nature of surface sites determined by those properties.

5.1. Energy dispersive spectroscopy (EDX)

EDX is an addition characterization technique used for the elemental analysis or chemical characterization of the samples (the overall analytical accuracy is app. ± 2%). In the Table 5-1are shown theoretical and measured ratios between Fe/M (M-foreign metal: Co, Cu, Mn). In all the cases the real ratio of Fe/M is slightly different from the expected one. This difference can first of all come from a weighing error and an incomplete pouring of the metal precursor solutions or to the slight hydration of the samples powders. Moreover, according to EDX analysis there is also a presence of Na < 1‰$_w$ (as a residual which comes from the synthesis procedure).

Table 5-1. Results of EDX analysis

SAMPLE	Theoretical ratio, *Fe/M*	Measured ratio, *Fe/M*
$Co_{0.6}Fe_{2.4}O_y$	Fe/Co - 4/1	Fe/Co - 3.69/1
$Co_{0.54}Mn_{0.06}Fe_{2.4}O_y$	Fe/Co - 4.4/1	Fe/Co - 4.65/1
	Fe/Mn - 40/1	Fe/Mn - 37.24/1
$Co_{0.3}Mn_{0.3}Fe_{2.4}O_y$	Fe/Co - 8/1	Fe/Co - 7.32/1
	Fe/Mn - 8/1	Fe/Mn - 7.76/1
$Mn_{0.6}Fe_{2.4}O_y$	Fe/Mn - 4/1	Fe/Mn - 3.76/1
$Cu_{0.3}Mn_{0.3}Fe_{2.4}O_y$	Fe/Cu - 8/1	Fe/Cu - 8.93/1

	Fe/Mn - 8/1	Fe/Mn - 7.62/1
$Cu_{0.6}Fe_{2.4}O_y$	Fe/Cu - 4/1	Fe/Cu - 4.47/1

5.2. XRD and N_2 adsorption
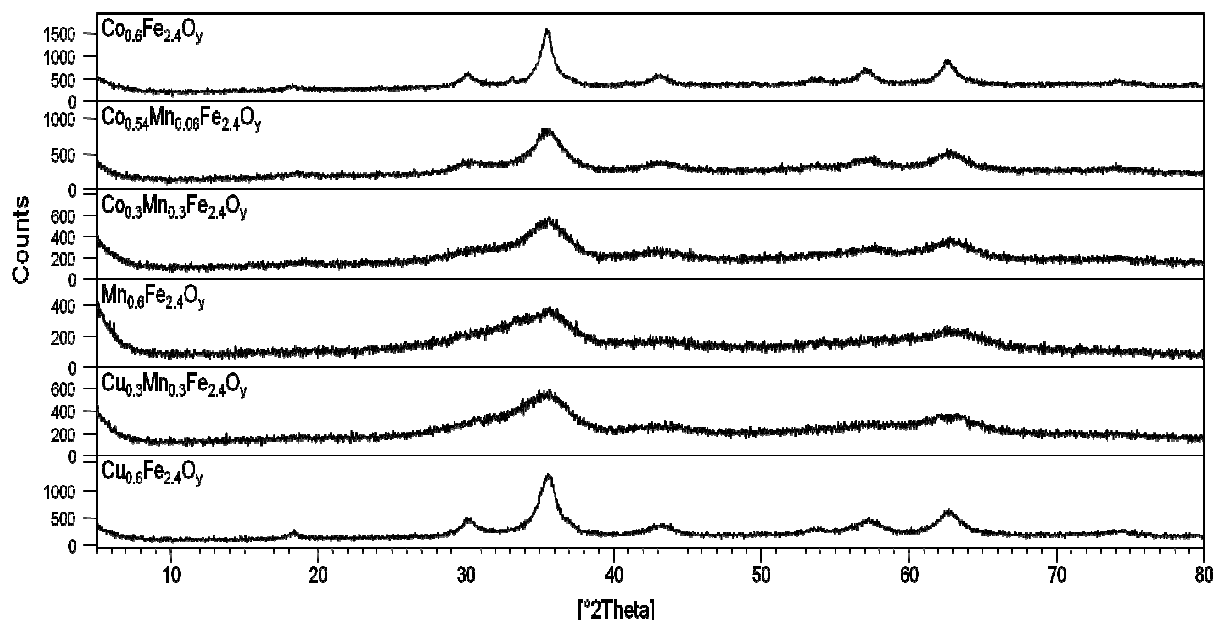
Figure 5-1. XRD patterns of $M_{0.6}Fe_{2.4}O_y$ ferrites calcined at 450 °C

XRD patterns of the fresh materials calcined at 450°C (for 8 h) are shown in Figure 5-1. Based on the obtained results a following conclusion can be stated: all $M_{0.6}Fe_{2.4}O_y$ ferrites display a spinel-like phase of magnetite (Fe_3O_4) [129,103] with its characteristic diffraction peaks (the main peak – hkl (311) with 100% intensity at app. 35.5° 2theta). However, a significant broadening of the diffraction patters observed for Mn-modified samples (Figure 5-1, see $Mn_{0.6}Fe_{2.4}O_y$, $Cu_{0.3}Mn_{0.3}Fe_{2.4}O_y$, $Co_{0.3}Mn_{0.3}Fe_{2.4}O_y$ and $Co_{0.54}Mn_{0.06}Fe_{2.4}O_y$) which first of all can be attributed to a decrease in a particle size/-crystallite size or as a fact of a lower crystallinity[7]. Crystallite size of the following samples was calculated using Scherrer equation, results are listed in the Table 5-2 (values are obtained for (440) plane at app.62.5° 2theta).

Table 5-2. Surface area results for $M_{0.6}Fe_{2.4}O_y$ ferrites

SAMPLE	SSA, m^2/g	Particle size d_{BET}, nm	Crystallite size (Scherrer eq.), nm
$Co_{0.6}Fe_{2.4}O_y$	71	16	7
$Co_{0.54}Mn_{0.06}Fe_{2.4}O_y$	88	13	4
$Co_{0.3}Mn_{0.3}Fe_{2.4}O_y$	138	8	3
$Mn_{0.6}Fe_{2.4}O_y$	157	7	-
$Cu_{0.3}Mn_{0.3}Fe_{2.4}O_y$	131	9	-
$Cu_{0.6}Fe_{2.4}O_y$	72	15	5

Further characterization such as N_2 adsorption (BET) has shown that all the Mn-ferrospinels possess apparent differences in specific surface area (SSA). The highest SSA is shown by $Mn_{0.6}Fe_{2.4}O_y$, and this value declines with an increase of Co- and Cu-content. This indicates the presence of smaller particles, which is also in a good agreement with previously discussed XRD results. A further confirmation was obtained from the average particle size (Table 5-2), which can be calculated from the SSA results making some assumption about the particle shape (the particles are spherical and non-porous)[130].

5.3. Raman Spectroscopy

The crystallographic structure of spinel oxides group is formed by a nearly closed-packed face centered cubic (**fcc**) of anions with two unequivalent sites for cations, which differ in oxygen coordination[89]. In the **normal spinel**, the A cations (divalent) occupy all the tetrahedral sites, and the B cations (trivalent) fill the octahedral sites. In **inverse spinel**, the B cations occupy the tetrahedral sites, and the octahedral sites contains a mixture of B and A cations[89,91]. The preference of the individual ions for the two types of lattice sites is determined by: the ionic radii of the specific ions; the size of the interstices; temperature; the orbital preference for specific coordination.
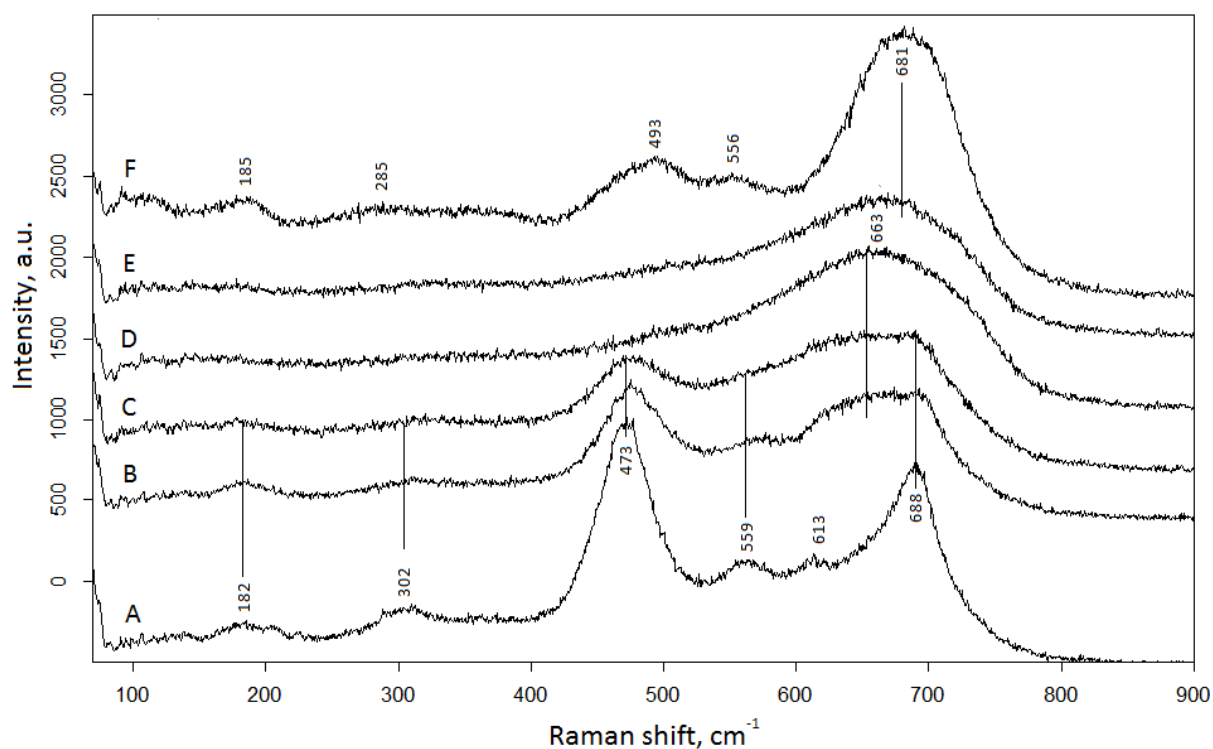
Figure 5-2. Raman spectra of M-modified ferrites: A- $Co_{0.6}Fe_{2.4}O_Y$, B-$Co_{0.54}Mn_{0.06}Fe_{2.4}O_Y$, C-$Co_{0.3}Mn_{0.3}Fe_{2.4}O_Y$, D-$Mn_{0.6}Fe_{2.4}O_Y$, E-$Cu_{0.3}Mn_{0.3}Fe_{2.4}O_Y$ and F-$Cu_{0.6}Fe_{2.4}O_Y$
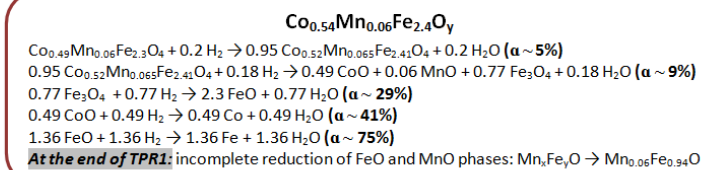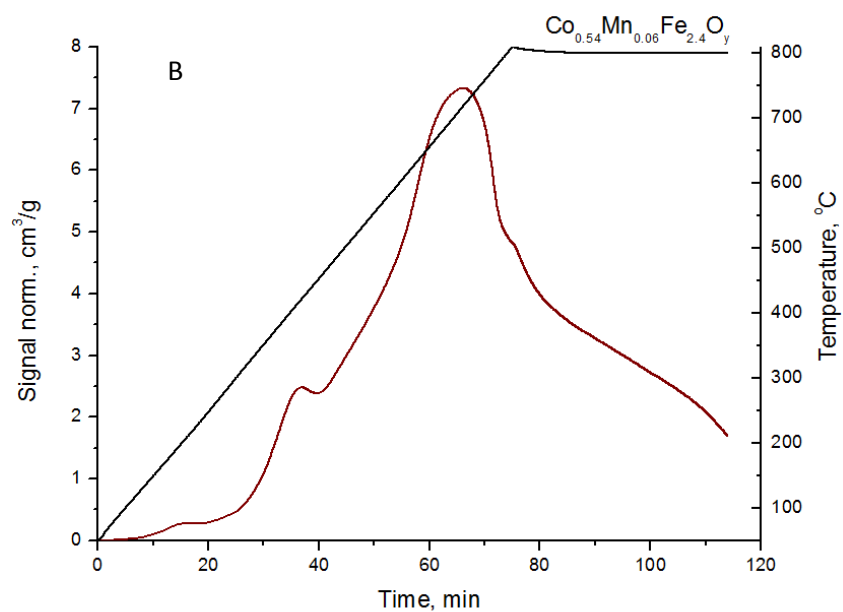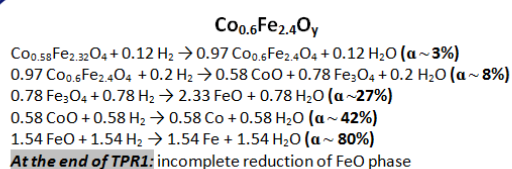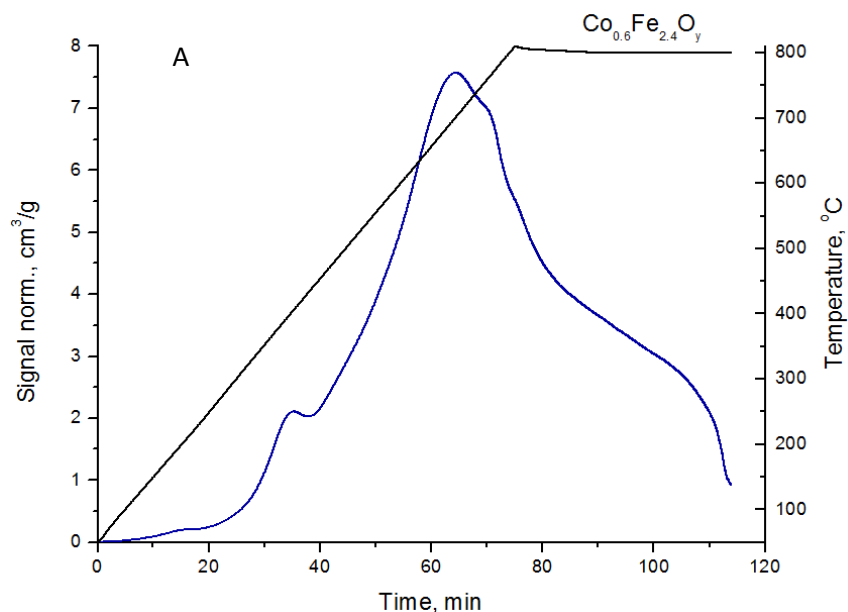
Many of the ferrites exhibit inversion of the cations between the tetrahedral and octahedral sites. Normally, Fe_3O_4 and $CoFe_2O_4$ are completely inverse spinels. Raman spectra of these inverse spinels is more complicated and show additional Raman-active modes over the five predicted by group theory [90]. Unlike the other ferrites $MnFe_2O_4$ is a normal spinel [110]. However, nanostructured powders of various synthesis and treatment methods have exhibited differing degrees of inversion. Thus, the nature of the substituted ions, charges and their distribution among the O_h and T_d sites of the ferrospinels affect their catalytic properties. Substitution of 'Fe' centers with other transition/non-transition/inner-transition metals leads to the formation of an inverse/normal, either mixed spinels with different degree of inversion. In spite of this, such an introduction may strongly modify the redox properties of the resultant ferrites.
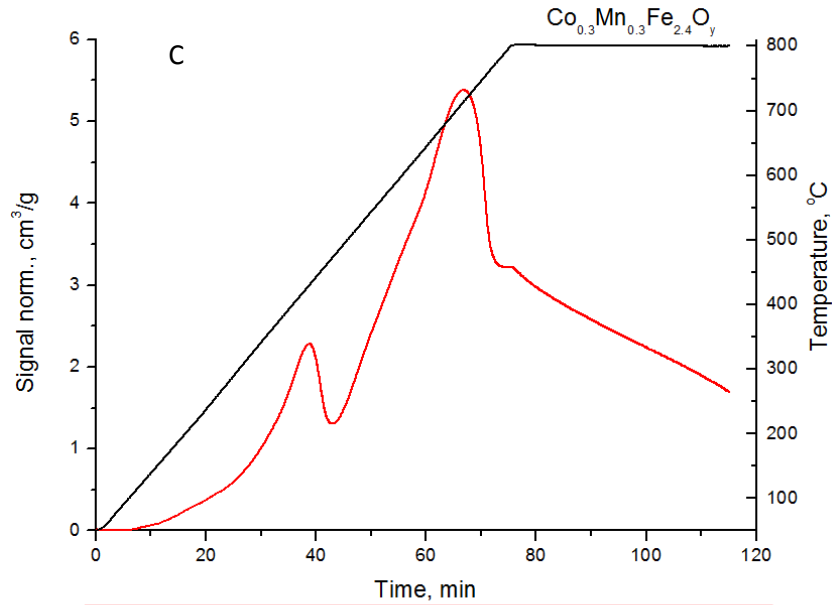
Raman features of ferrites are samples specific, depending on non-stoichiometry, cation distribution, defects, and also on the experimental conditions. According to the literature, there are five predicted Raman active modes: A_{1g}, E_g, and three T_{2g} modes (E_g, E_g, $^3T_{2g}$). Additional modes may appear in vibrational spectra due to local distortions of the crystal
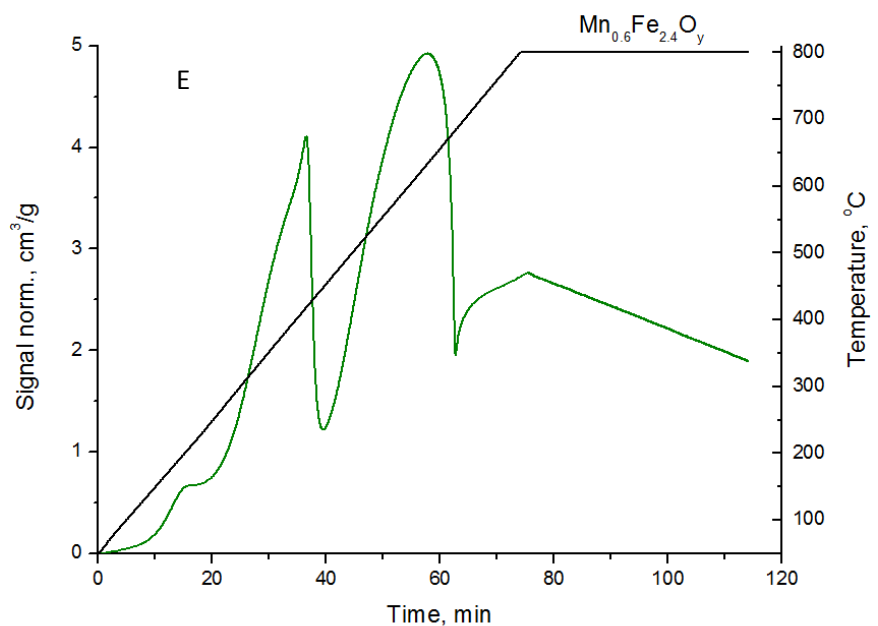
lattice. These defects do not affect the long-range ordering of the system, and are often cannot be detected by x-ray diffraction [108,131].

Figure 5-2 shows the Raman spectra obtained over TYPE II ferrites with a nominal composition of $M^1_{0.6-x}M^2_xFe_{2.4}O_y$ (where M^1 = Co/Cu and M^2 = Mn). The spectrum A - $Co_{0.6}Fe_{2.4}O_y$ reveals 6 vibration modes: 5 predicted by the literature and an additional one caused by the local distortions in the lattice. With increasing the Mn-contain the shape of the most intensive band A_{1g} at 688 cm^{-1} which corresponds to the Fe-O symmetric stretching in tetrahedron become more broad for $Co_{0.54}Mn_{0.06}Fe_{2.4}O_y$ and each peak can be presented like a doublet. A higher intensity mode A_{1g} (~688 cm^{-1}) for mixed Mn-Co- and only Co- iron-rich ferrites has a shoulder at lower frequency (~613 cm^{-1}), which is caused by disorder effects of M^{2+} and Fe^{3+} over the Td and Oh sites[109]. However, the spectra of $Mn_{0.6}Fe_{2.4}O_y$ and $Cu_{0.3}Mn_{0.3}Fe_{2.4}O_y$ possess completely different vibration modes, a broad band at ~663 cm^{-1} which can be an overlap of Fe^{3+}/Mn^{2+} in the tetrahedral sites have hardly visible doublet structure and no lower frequency shoulder can be seen. As a result, according to the following substitution mechanism, where Mn^{2+} ions partly replace Fe^{3+} ions in the Td sites thus changing the degree of inversion towards the formation of the normal spinel[110]. The resulting spectrum of $Mn_{0.6}Fe_{2.4}O_y$ is in agreement with previous reports.[111] The low intensity of the peaks and partial energy shifts can be related also to a high defectivity[107] and a low crystallinity as confirmed by XRD. It should be emphasized that Co^{2+} was previously found to increase the hyperfine field of the B sublattice over a similar composition range. Thus, the presence of an inversion center in the centrosymmetrical space group Fd3m implies mutual exclusion of Raman and IR activities for the same vibrational mode. Furthermore, the bands in IR and Raman spectroscopy are sensitive to coordination geometry and oxidation states.
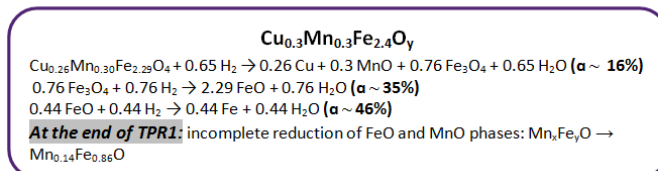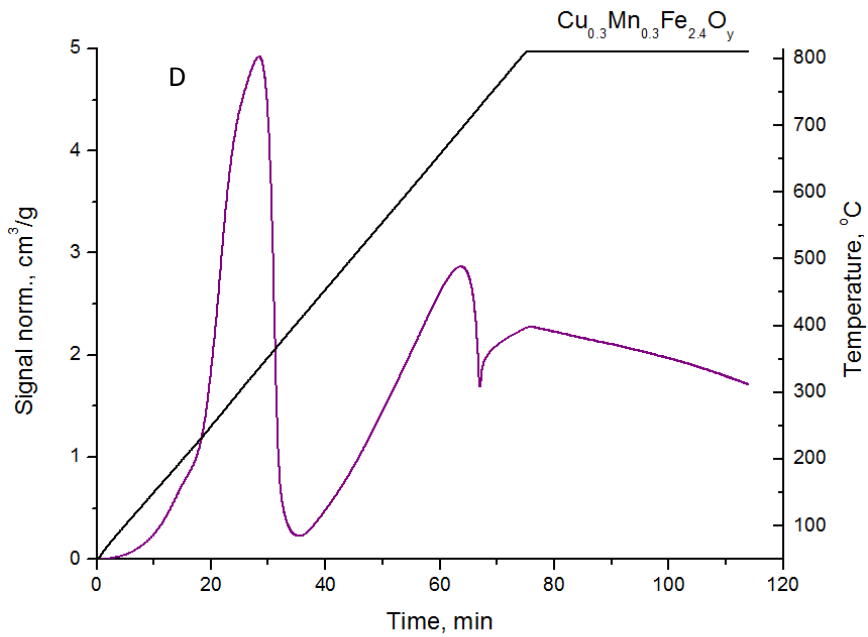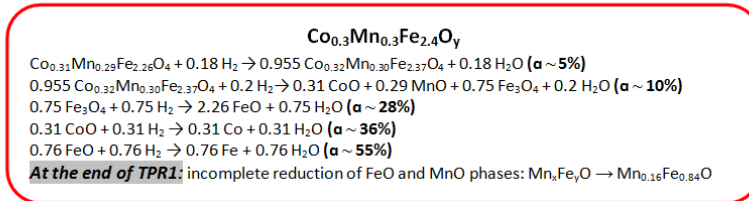
$Co_{0.6}Fe_{2.4}O_y$

$Co_{0.6}Fe_{2.4}O_y$
$Co_{0.58}Fe_{2.32}O_4 + 0.12\,H_2 \rightarrow 0.97\,Co_{0.6}Fe_{2.4}O_4 + 0.12\,H_2O\,(\alpha \sim 3\%)$
$0.97\,Co_{0.6}Fe_{2.4}O_4 + 0.2\,H_2 \rightarrow 0.58\,CoO + 0.78\,Fe_3O_4 + 0.2\,H_2O\,(\alpha \sim 8\%)$
$0.78\,Fe_3O_4 + 0.78\,H_2 \rightarrow 2.33\,FeO + 0.78\,H_2O\,(\alpha \sim 27\%)$
$0.58\,CoO + 0.58\,H_2 \rightarrow 0.58\,Co + 0.58\,H_2O\,(\alpha \sim 42\%)$
$1.54\,FeO + 1.54\,H_2 \rightarrow 1.54\,Fe + 1.54\,H_2O\,(\alpha \sim 80\%)$
At the end of TPR1: incomplete reduction of FeO phase

$Co_{0.54}Mn_{0.06}Fe_{2.4}O_y$

$Co_{0.54}Mn_{0.06}Fe_{2.4}O_y$
$Co_{0.49}Mn_{0.06}Fe_{2.3}O_4 + 0.2\,H_2 \rightarrow 0.95\,Co_{0.52}Mn_{0.065}Fe_{2.41}O_4 + 0.2\,H_2O\,(\alpha \sim 5\%)$
$0.95\,Co_{0.52}Mn_{0.065}Fe_{2.41}O_4 + 0.18\,H_2 \rightarrow 0.49\,CoO + 0.06\,MnO + 0.77\,Fe_3O_4 + 0.18\,H_2O\,(\alpha \sim 9\%)$
$0.77\,Fe_3O_4 + 0.77\,H_2 \rightarrow 2.3\,FeO + 0.77\,H_2O\,(\alpha \sim 29\%)$
$0.49\,CoO + 0.49\,H_2 \rightarrow 0.49\,Co + 0.49\,H_2O\,(\alpha \sim 41\%)$
$1.36\,FeO + 1.36\,H_2 \rightarrow 1.36\,Fe + 1.36\,H_2O\,(\alpha \sim 75\%)$
At the end of TPR1: incomplete reduction of FeO and MnO phases: $Mn_xFe_yO \rightarrow Mn_{0.06}Fe_{0.94}O$

Co$_{0.3}$Mn$_{0.3}$Fe$_{2.4}$O$_y$

Co$_{0.31}$Mn$_{0.29}$Fe$_{2.26}$O$_4$ + 0.18 H$_2$ → 0.955 Co$_{0.32}$Mn$_{0.30}$Fe$_{2.37}$O$_4$ + 0.18 H$_2$O **(α ∼ 5%)**
0.955 Co$_{0.32}$Mn$_{0.30}$Fe$_{2.37}$O$_4$ + 0.2 H$_2$ → 0.31 CoO + 0.29 MnO + 0.75 Fe$_3$O$_4$ + 0.2 H$_2$O **(α ∼ 10%)**
0.75 Fe$_3$O$_4$ + 0.75 H$_2$ → 2.26 FeO + 0.75 H$_2$O **(α ∼ 28%)**
0.31 CoO + 0.31 H$_2$ → 0.31 Co + 0.31 H$_2$O **(α ∼ 36%)**
0.76 FeO + 0.76 H$_2$ → 0.76 Fe + 0.76 H$_2$O **(α ∼ 55%)**
At the end of TPR1: incomplete reduction of FeO and MnO phases: Mn$_x$Fe$_y$O → Mn$_{0.16}$Fe$_{0.84}$O

Cu$_{0.3}$Mn$_{0.3}$Fe$_{2.4}$O$_y$

Cu$_{0.26}$Mn$_{0.30}$Fe$_{2.29}$O$_4$ + 0.65 H$_2$ → 0.26 Cu + 0.3 MnO + 0.76 Fe$_3$O$_4$ + 0.65 H$_2$O **(α ∼ 16%)**
0.76 Fe$_3$O$_4$ + 0.76 H$_2$ → 2.29 FeO + 0.76 H$_2$O **(α ∼ 35%)**
0.44 FeO + 0.44 H$_2$ → 0.44 Fe + 0.44 H$_2$O **(α ∼ 46%)**
At the end of TPR1: incomplete reduction of FeO and MnO phases: Mn$_x$Fe$_y$O →
Mn$_{0.14}$Fe$_{0.86}$O

Figure 5-3. TPR profiles of $M_{0.6}Fe_{2.4}O_y$ ferrospinels including the box with reduction passages*

*data on the reduction passages were made based on the following: initial composition, reduction potentials of corresponding redox couples and amount of consumed H_2.

Temperature-programmed reduction (TPR) measurements were performed to investigate the role of different metals on the reducibility of M-modified ferrites, denoted as TYPE II ferrospinels with a generic formula of $M_{0.6}Fe_{2.4}O_y$. As discussed previously, (*note*: see PART I of the discussion, Paragraph 4) the acquired data were elaborated based on the amount of consumed hydrogen considering the nature of the incorporated metals. Being guided by the results obtained over TYPE I ferrospinels (MFe_2O_4), the TPR profiles of TYPE II samples ($M_{0.6}Fe_{2.4}O_y$) follow the same reduction scheme (as depicted in Figure 4-3) and can be conditionally divided into two parts: the reduction of iron oxide to metallic iron and the reduction of incorporated foreign metal oxide to its metallic component. As it was seen previously, the reduction temperature of '$Fe_3O_4 \rightarrow FeO \rightarrow Fe$' passage and completeness of the process itself strongly depends on the nature of a present foreign metal M (M=Co, Cu, Mn) that also follows from observed differences in the initiation of the reduction process and the total amount of consumed hydrogen (Figure 5-3 and Figure 5-5). The low-T reduction shoulder at ~200∘C, which accounts for ~5% of the total reduction, was experimentally observed for the Co, Co/Mn and Mn-incorporated sample and attributed to the reduction of $M_{0.57}Fe_{2.28}O_4$ to $M_{0.6}Fe_{2.4}O_4$ due to the presence of cation vacancies in the highly defective materials (*note:* presence of only Fe^{3+} cations in the fresh samples was confirmed by Mössbauer experiments → the values of IS (δ) lie in a typical range for Fe^{3+} species: 0.31-0.35 mm/s). Further reduction of $Co_{0.6}Fe_{2.4}O_y{}^{(A)}$, $Co_{0.54}Mn_{0.06}Fe_{2.4}O_y{}^{(B)}$, $Co_{0.3}Mn_{0.3}Fe_{2.4}O_y{}^{(C)}$ and $Mn_{0.6}Fe_{2.4}O_y{}^{(D)}$ samples follows the same stages as for Co-, Co/Mn- and Mn-incorporated TYPE I ferrospinels (see the pass II, illustrated in Figure 4-3); where the first small peak at ~400°C was attributed to the primary spinel reduction with a stepwise formation of CoO and Fe_3O_4 (or CoO, MnO and Fe_3O_4) phases (which corresponds to α~8%), whereas in only Mn-incorporated ferrite, $Mn_{0.6}Fe_{2.4}O_y$, this step starts at lower temperature of ~380°C (*note*: $Mn_{0.6}Fe_{2.4}O_4 + 0.2 H_2 \rightarrow 0.6 MnO + 0.8 Fe_3O_4 + 0.2 H_2O$). However, the Co-containing samples reached significantly higher reduction extents (α~80$^{(A)}$, 75$^{(B)}$ and 55$^{(C)}$%) in comparison to the Mn-containing sample (α~58$^{(D)}$%); and it was again attributed to the formation of the scarcely reducible phase of MnO (or in the form of wustite-like Mn_xFe_yO oxide). Looking at the TPR profiles of $Cu_{0.6}Fe_{2.4}O_y{}^{(E)}$ and $Cu_{0.3}Mn_{0.3}Fe_{2.4}O_y{}^{(F)}$ ferrites, the first peak at ~ 350°C was attributed to the primary stepwise spinel reduction with the final formation of $Cu^{0(E)}/Cu^0 + MnO^{(F)}$ and Fe_3O_4 phases (which accounts for α~23$^{(E)}$/16$^{(F)}$%), following the pass I$^{(E)}$/III$^{(F)}$ (Figure 4-3); the further reduction of $Fe_3O_4 \rightarrow$ FeO and FeO $\rightarrow$

Fe^0_{incom} appears at higher temperatures with the total reduction extent of ~52[E]/46[F]%. As explained previously for the Co/Mn-and Mn-incorporated ferrospinels, the reduction of $MnO \rightarrow Mn^0$(-1.18 eV)[106] can occur only at very extreme temperatures (see ΔG^0_{react}, Table 4-3) which, in turn, leads to the formation of the scarcely reducible phase of MnO/Mn_xFe_yO. Summarizing the TPR results over TYPE I/II ferrospinels, a general reduction path for the $M_{0.6}Fe_{2.4}O_y$ samples was illustrated as follows:

I. $M^1_{0.6}Fe_{2.4}O_y \rightarrow 0.6\ M^1O + 0.8\ Fe_3O_4$

$M^2_{0.6}Fe_{2.4}O_y \rightarrow 0.6\ M^2 + 0.8\ Fe_3O_4$

$M^3_{0.6}Fe_{2.4}O_y \rightarrow 0.6\ M^3O + 0.8\ Fe_3O_4$

II. $Fe_3O_4 \rightarrow FeO$

III. $M^1O \rightarrow M^1$

IV. $FeO \rightarrow Fe$

V. $M^3O \nrightarrow$
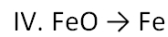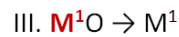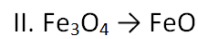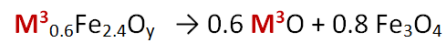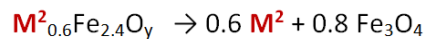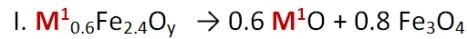
where M^1 – Co, M^2 – Cu and M^3 – Mn

Figure 5-4. General scheme for $M_{0.6}Fe_{2.4}O_y$ reduction
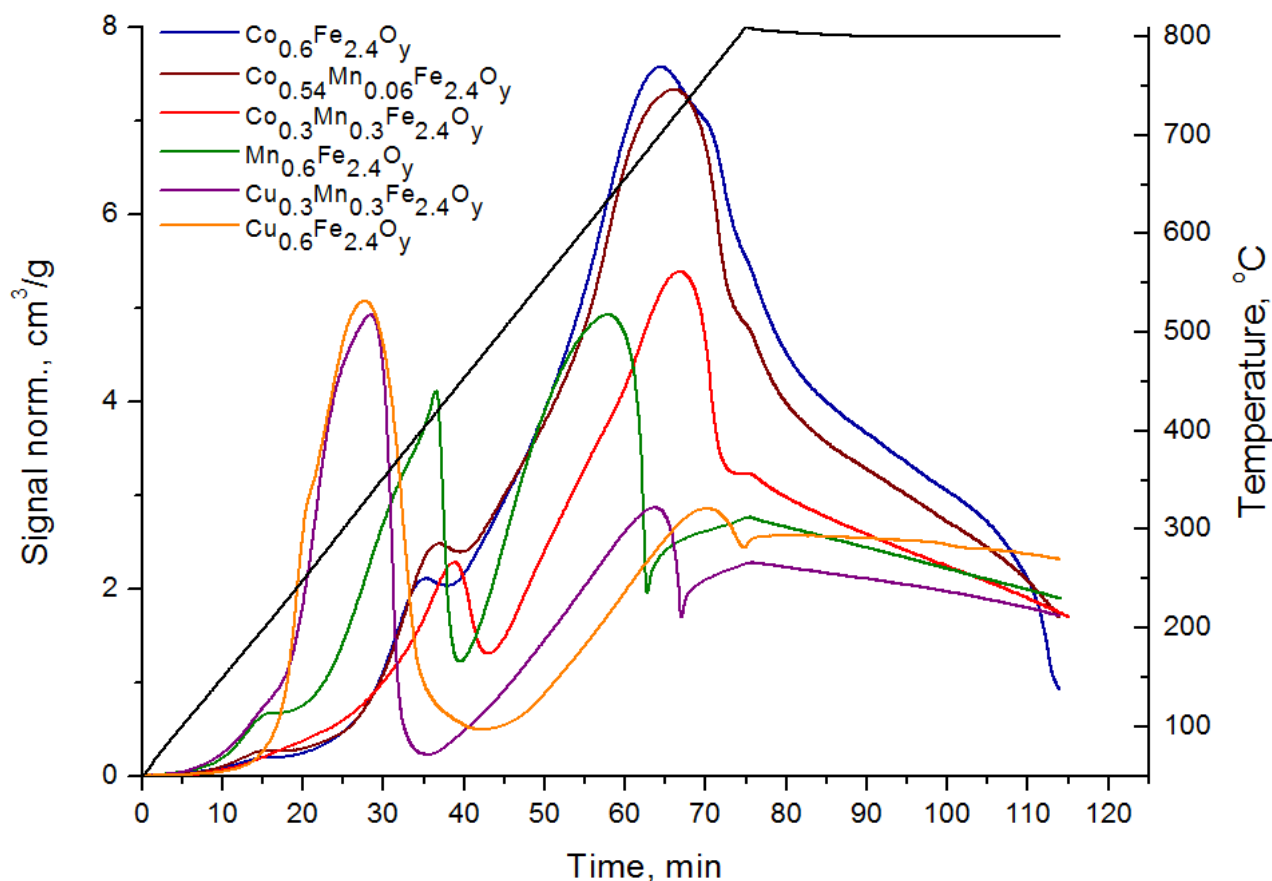
Figure 5-5. TPR profiles for $M_{0.6}Fe_{2.4}O_y$ ferrospinels

5.5. Ferrospinels TYPE II: study of $Co_{0.6-x}Mn_xFe_{2.4}O_y$ system

This section is focused on the study of $Co_{0.6-x}Mn_xFe_{2.4}O_y$ mixed ferrites as potentially new oxygen carrier materials for chemical-loop reforming process. The new materials were tested in terms of both redox properties (Paragraph 5.4) and catalytic activity to generate hydrogen by oxidation with steam, after a reductive step carried out with ethanol. In addition, the section includes in-situ DRIFTS and in-situ XPS studies that allowed to extract information at molecular level and to follow surface changes within the reduction/re-oxidation processes during ethanol chemical-loop reforming.
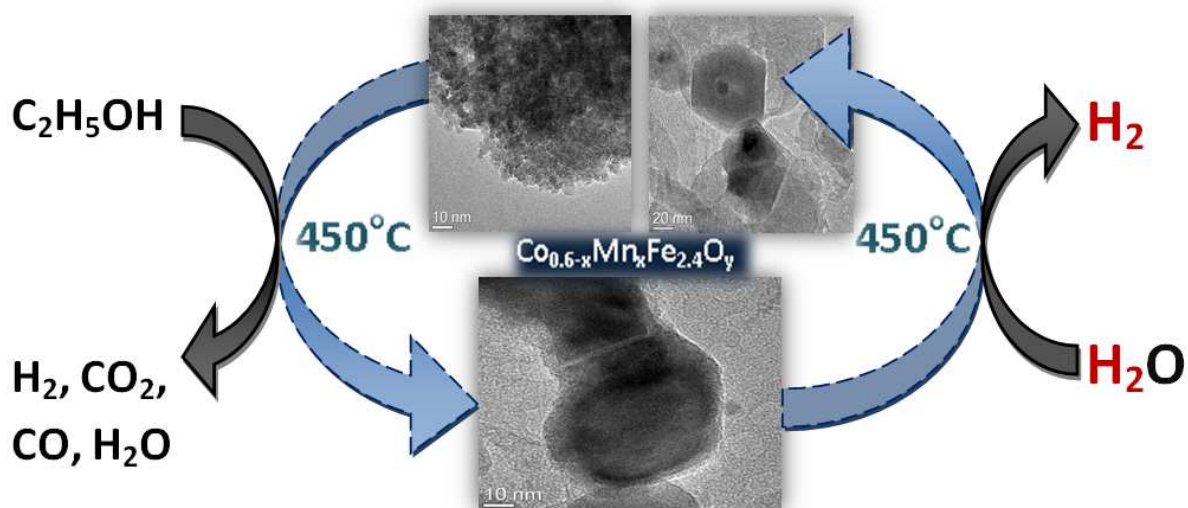
5.6.   Surface characterization: in-situ DRIFTS experiments
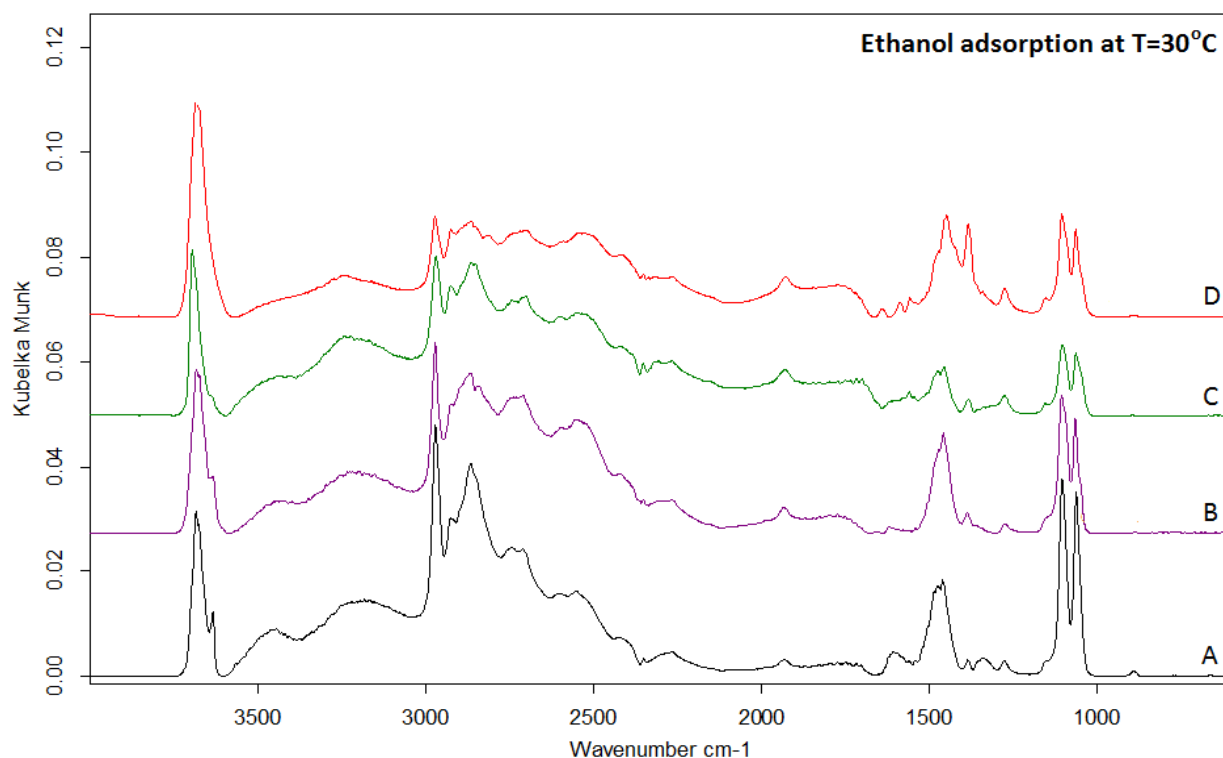
Figure 5-6. DRIFTS spectra: (A)-$Co_{0.6}Fe_{2.4}O_Y$, (B)-$Co_{0.54}Mn_{0.06}Fe_{2.4}O_Y$, (C)-$Co_{0.3}Mn_{0.3}Fe_{2.4}O_Y$ and (D)-$Mn_{0.6}Fe_{2.4}O_Y$

The adsorption of alcohols over metal oxides can lead to different kind of adsorbed species depending on the surface properties of the material under study. According to the literature, ethanol adsorbs on the surface mainly as an ethoxide, formed from the scission of the O-H bond.[95–99] However, the species formed with increasing temperatures are more related to the surface chemistry of each compound.[94] Figure 5-6 shows spectra of adsorbed

ethanol at RT over the four samples. Ethoxy bands (dissociative adsorption) can be observed at 1057 and 1103 cm^{-1} for the C-O/C-C stretching modes together with the bands of the undissociated ethanol (at 1383 cm^{-1} and 1274 cm^{-1} for $CH_3\delta$ and $OH\delta$, respectively).[94,132] The complex absorption in the 2800-2400 cm^{-1} region is probably due to a Fermi resonance of the overtone of the $OH\delta$ vibration mode with the CH- stretching modes at 2971, 2929, and 2863 cm^{-1} ($CH_{3(as)}$, $CH_{2(as)}$ and $CH_{3(s)}$ modes of the ethoxide species).[97,94] Figure 5-6(A-C) show a strong band at 3252 cm^{-1} that may be assigned to the OH stretching of ethanol H-bonded to the surface, which also was observed over the stoichiometric $CoFe_2O_4$ferrospinel in our previous paper.[94] The sharp band at 3681 cm^{-1} together with a shoulder at 3635 cm^{-1} is assigned to the –OH stretching vibration of chemisorbed undissociated ethanol over surface Lewis acid sites (M^{n+}).[133–135] The shoulder at lower frequency may indicate the presence of different active sites on the materials. However, with increasing the Mn-contain the shoulder decreases in intensity and only for $Mn_{0.6}Fe_{2.4}O_y$ it completely disappears. This effect was already seen by Raman spectroscopic measurements, described above (Paragraph 5.6).
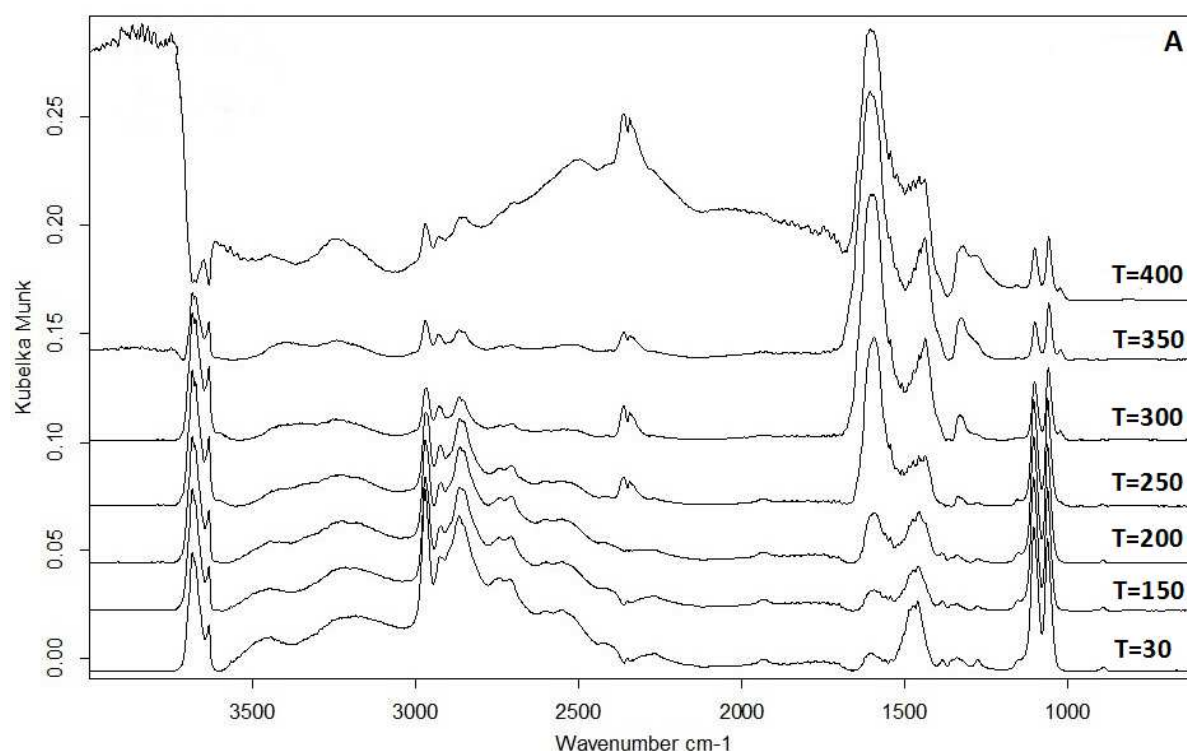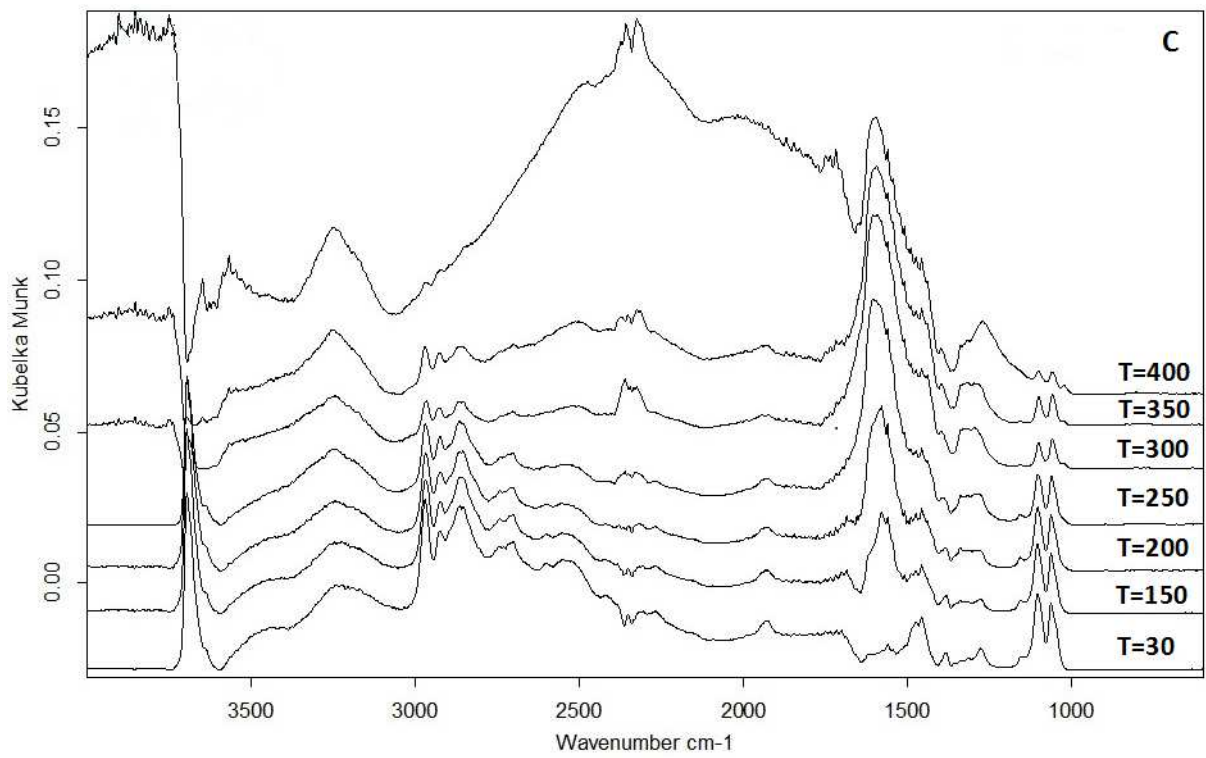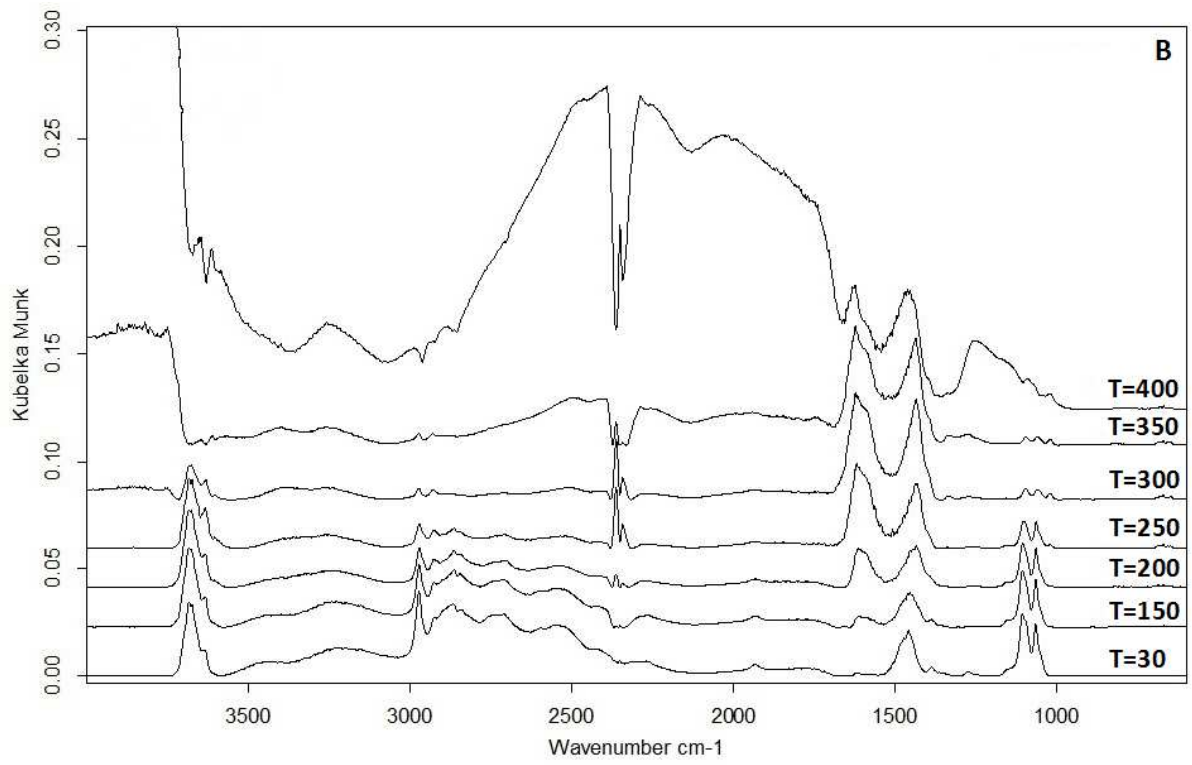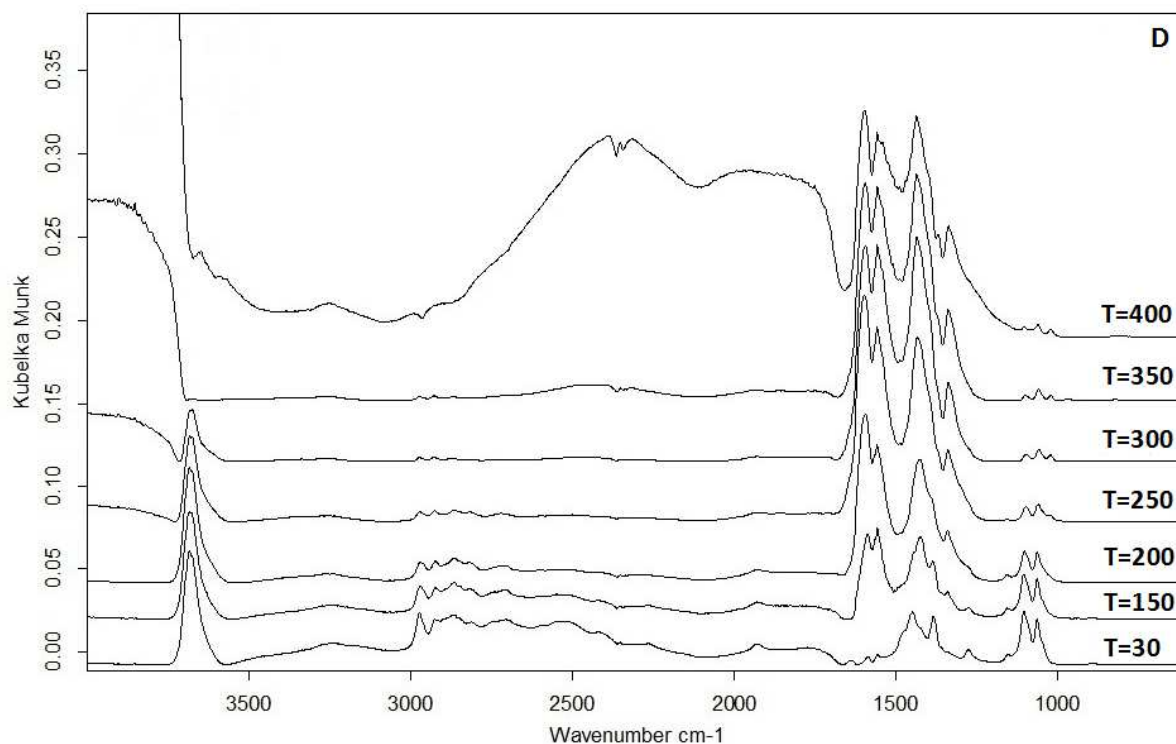
Figure 5-7. DRIFTS spectra: (A)-$Co_{0.6}Fe_{2.4}O_y$, (B)-$Co_{0.54}Mn_{0.06}Fe_{2.4}O_y$, (C)-$Co_{0.3}Mn_{0.3}Fe_{2.4}O_y$ and (D)-$Mn_{0.6}Fe_{2.4}O_y$

Some remarkable differences between the DRIFTS spectra of samples are observed when the temperature is increased (Figure 5-7); acetate bands appear (at 1334, 1439, 1590 cm^{-1} for the CH3 δ, (OCOv(s), and OCOv(as) vibrations, respectively). The increasing in intensity and broadening of the band at 1590 cm^{-1} (at 250°C) also indicates the formation of carbonate species.[136] These species could further produce CO_2, which is detected as the doublet at the 2358-2338 cm^{-1} region and corresponds to adsorbed and/or gaseous CO_2 rotation vibration P and R bands.[137] The DRIFT spectra obtained on $Mn_{0.6}Fe_{2.4}O_4$ (Figure 5-7-D), also exhibit the bands for acetate species, formed by the reaction of ethoxy species with surface oxygen (1598, 1555, 1433 and 1334 cm^{-1}).[98,138] When the temperature is increased (up to 400°C) the intensity of the bands corresponding to ethoxy species is reduced, whereas the bands associated with acetate species (strongly bounded to the surface) remain almost unchanged. However, the main difference between the spectra of $Mn_{0.6}Fe_{2.4}O_y$ and of other Co- and Co-Mn ferrospinels spectra lies in the absence of the bands associated with carbonate species; the band of the adsorbed CO_2 was not observed as well. Thus, the results may indicate that Co and Co-Mn-modified systems were more reactive than the Mn ferrospinel. This is also followed by the presence of a broad absorbed

feature in the 3000-1800 cm^{-1} region, which is attributed to the electronic absorption of the partially reduced sample.[94,139]

In summary, the redox properties of M-modified ferrospinels and hence their catalytic activity in the chemical-loop reforming of ethanol are strongly influenced by the nature of M and by the M^{n+} distribution among the Oh and Td sites in the crystal lattice. The main differences between the four spinels studied are the following: the incorporation of only Co leads to the formation mainly of an inverse spinel, however the addition of Mn resulted in the substitution of Td coordinated Fe^{3+} ions with Mn^{2+} and, as a consequence, the formation of new type of active sites. The reduction of M-modified ferrospinels appears to be a complex process due to the presence of various reduced forms of Fe oxides together with oxides of substituted metal ions (Co_xO_y and Mn_xO_y). Besides, it was observed that incorporation of Co-Mn metal cations into magnetite structure affects its reducibility, which directly depends on the nature of the incorporated metal cation. In particular, the Co-Mn system presents a cooperative influence on each other's reduction profiles. Moreover, during the ethanol anaerobic decomposition/oxidation step over Co and mixed Co-Mn ferrospinels, acetates and carbonates appeared to be important surface intermediates and in the case of the only Mn containing catalyst, there was no evidence for the carbonates formation.

5.7. Surface characterization: in-situ XPS study
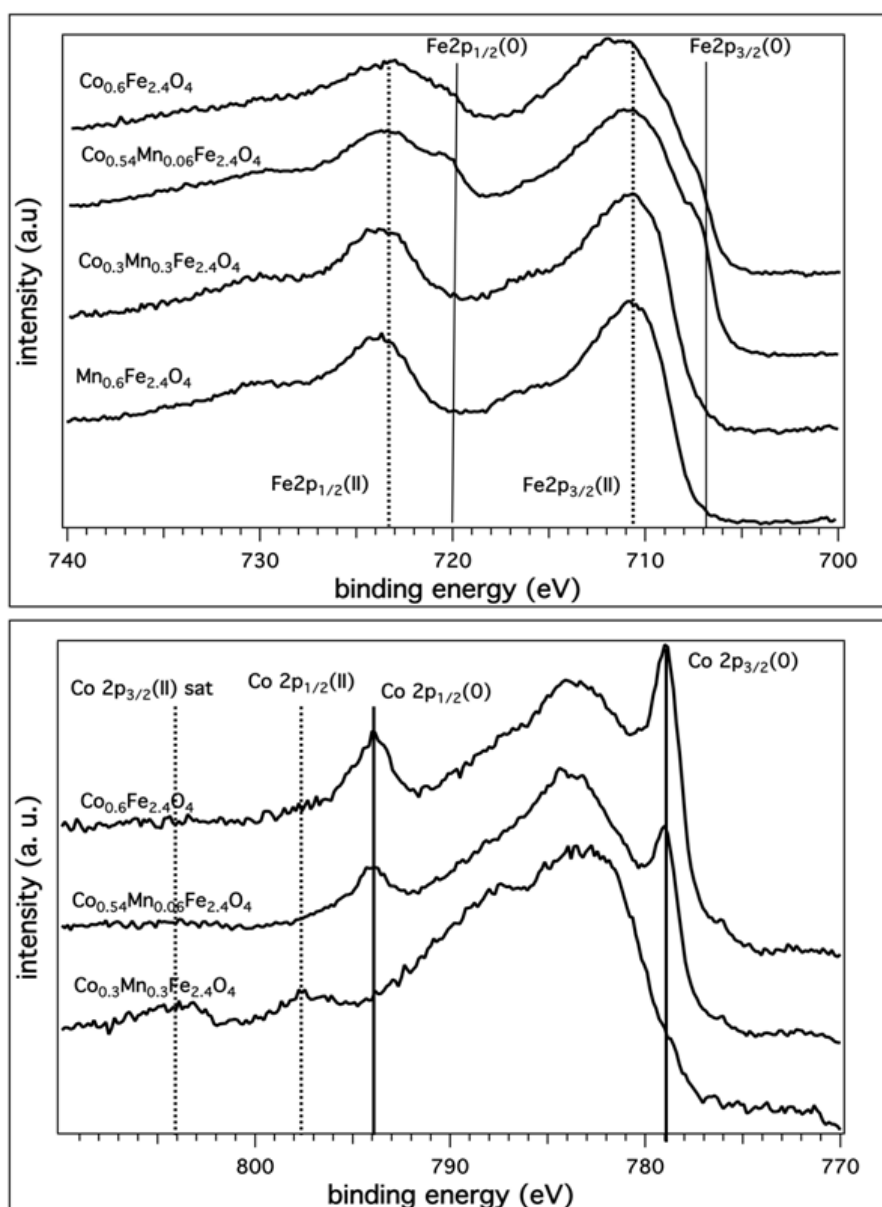
Figure 5-8. (top) Fe 2p and (bottom) Co 2p photoemission spectra after the exposure to ethanol at 450°C for 80 minutes

In order to study the kinetics of the reduction and re-oxidation processes that take place on the catalytic surface, *in-situ* XPS measurements were performed. In particular, by monitoring the changes occurred in the photoemission spectra of Fe2p, Co2p and Mn2p, during ethanol (5×10^{-6} mbar at 450°C) and water (2×10^{-4} mbar at 450°C) exposure, it was possible to determine the role played by each component of the Co/Mn-modified ferrospinels on the surface chemistry.

Let us first concentrate on the changes in the XPS data after the sample annealing at 450°C in UHV. As an example, in Figure 5-9 we compare the spectra of $Co_{0.3}Mn_{0.3}Fe_{2.4}O_y$ as

received and after annealing: a significant decrease of the FWHM in the O 1s spectrum and a small shift of Fe2p and Mn2p peaks lower binding energy (BE) values are clearly observed, which indicate a surface modification occurred after elimination of the adsorbed hydroxyl (OH-) groups or/and water molecules, and the reduction of highly oxidized metal species (e.g. Fe_2O_3 to Fe_3O_4 formation). In any case, the spectra obtained after this UHV annealing are taken as a reference for the subsequent chemical changes induced by the chemical treatments.

The chemical composition determined by photoemission and the spectral fingerprints observed confirm the presence of M-modified ferrospinels whose stoichiometric ratio is in agreement with the nominal ratio of the synthesis protocol.

The samples were exposed to an increasing amount of ethanol and the evolution of the main core level spectra (see Figure 5-10 - Figure 5-13), was measured observing clear differences in the surface composition as a function of the presence of different M.

Starting from the very beginning of ethanol feeding, the reduction of iron from Fe^{3+} to Fe^{2+} was observed for all tested samples, which is evidenced by the decrease of the intensity of the Fe 2p peak in conjunction with the energy shift of Fe 2$p_{3/2}$ satellite from 8 eV (typical for Fe^{3+}) to 5 eV , which can be ascribed to oxides with a lower valence.[140,141]

In the case of prolonged ethanol exposure, the appearance of a further component at 707.0 eV indicates the formation of a metal component. Such a phenomenon is strongly dependent on the actual composition of the corresponding sample, and especially on the Co/Mn ratio. As shown in Figure 5-8, it was found that Co(II)-incorporation effectively improves the reducibility of the catalyst, whereas addition of Mn has an opposite effect. This effect is once again confirmed by the previously described TPR and DRIFTS results (Paragraphs 5.4 and 5.6 respectively). Moreover, $Co_{0.54}Mn_{0.06}Fe_{2.4}O_y$ showed a stronger reduction in comparison to the sample without Mn ($Co_{0.6}Fe_{2.4}O_y$ - Figure 5-8). This behavior can be explained by the size effect induced by the presence of Mn (with increasing of Mn-content the specific surface area also increased (Paragraph 5.2). In the $Co_{0.3}Mn_{0.3}Fe_{2.4}O_y$ferrospinel within 80 min of reduction by ethanol, a peak corresponding to the formation of an iron metal phase was not detected and it was seen only after 120 min of ethanol feeding (see Figure 5-11). This resilience towards the reduction was observed also for $Mn_{0.6}Fe_{2.4}O_y$, whose reduction behavior is very similar (see Figure 5-10).

Moreover, we could observe changes in the line shape of Mn 2p only after the annealing in UHV at 450°C (due to desorption of surface OH- groups and/or water molecules), whereas afterwards spectra remained unchanged, despite the iron and cobalt underwent substantial reduction.

It has been already mentioned that Co boosts the reduction of ferrospinels; however it is interesting to compare the tendency toward the reduction of Co vs Fe. The photoemission peak of Co 2p overlaps with Fe Auger peak, which complicates its analysis, nevertheless some qualitative information can be obtained. Cobalt is present as Co^{2+} and therefore no more reduced species can be formed, but the metal. As a matter of fact in the Co 2p photoemission line it can be observed a progressive disappearance of the Co^{2+} $2p_{1/2}$ peaks (795.5 eV) and its satellite in favour of the formation of a metal component (793.3 eV). Metal components of Fe and Co were observed almost at the same time, however it can be noted that cobalt was fully reduced to metal in the case $Co_{0.6}Fe_{2.4}O_y$ and $Co_{0.54}Mn_{0.06}Fe_{2.4}O_y$ whereas the reduction of iron species to metallic iron was only partial (Figure 5-8).

In the case of relatively large Mn-content ($Co_{0.3}Mn_{0.3}Fe_{2.4}O_y$), Co cations are not reduced immediately, but a relevant oxidized component can be observed in standard conditions (80 min of ethanol feeding), whereas only after 120 min is fully reduced. It is also interesting to note that such reaction seems to be autocatalytic; actually in the stage from 80 to 120 min there is a fast increase in the reduced components with the formation of metallic phases. These experiments suggest that when Mn is present in large amount there is a substantial depression of reduction. This indicates that the synthesized ferrospinel are homogeneous and not a physical mixture of $Co_{0.6}Fe_{2.4}O_y$ and $Mn_{0.6}Fe_{2.4}O_y$. Moreover, the chemical activity of the M-modified ferrospinels is ruled in a complex way by the sum of the effects due to the two incorporated metals.

To summarize the picture emerging from the XPS investigation we can propose that the reduction process involves the fast formation of a reduced oxide with a satellite at 5 eV and afterwards the nucleation of iron metal. This shift of the satellite can be qualitatively associated with the reduction of Fe^{3+} to Fe^{2+} which from the structural point of view corresponds to the reduction to wustite, and only afterwards this latter is progressively reduced to metal iron.

The formation of the metal phase seems to be a rather slow process and requires a significant induction period whereas the first reduction from Fe^{3+} to Fe^{2+} is quite fast in the used conditions.
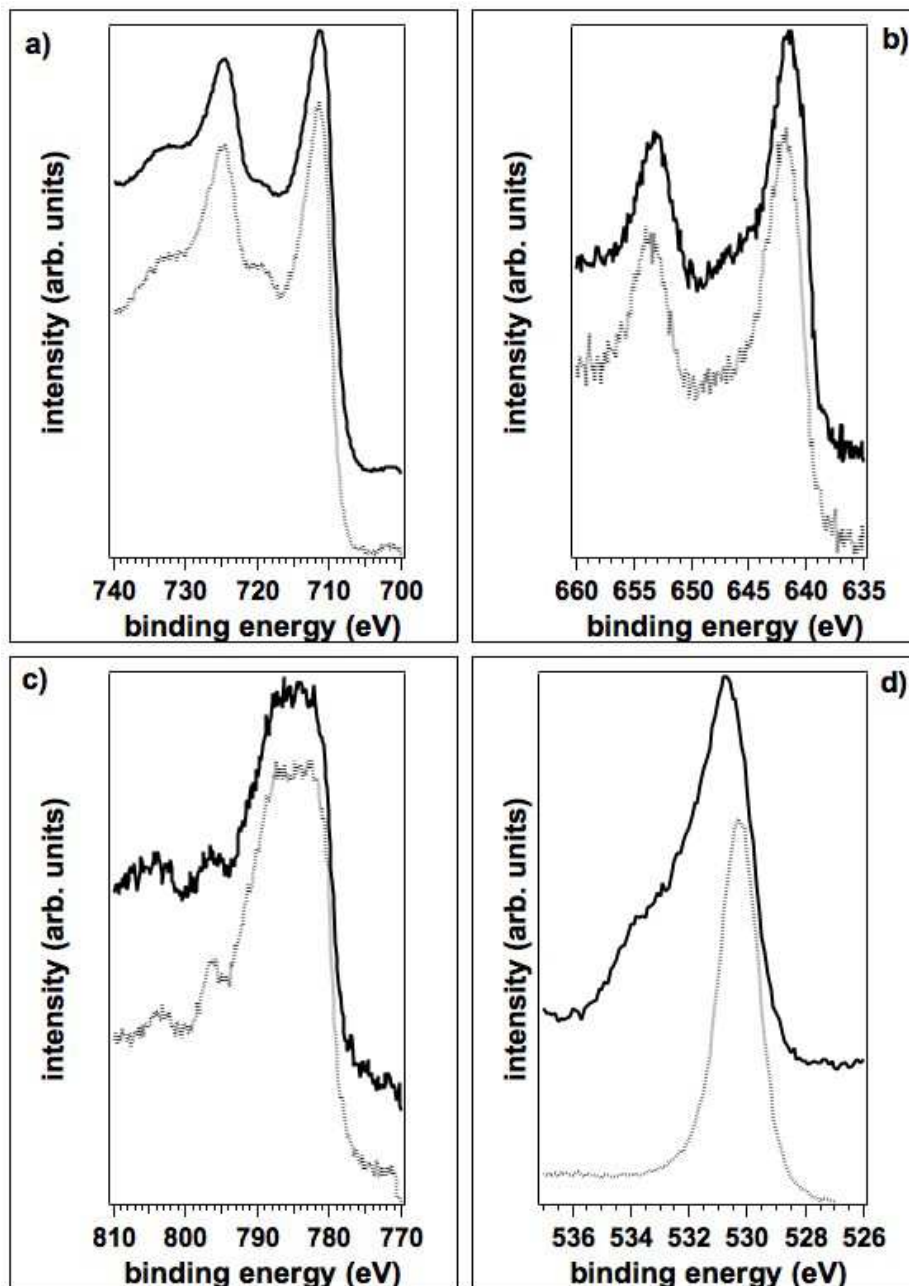

Figure 5-9. (a) Fe 2p,(b) Mn 2p,(c) Co 2p,(d) O1s photoemission spectra of $Co_{0.3}Mn_{0.3}Fe_{2.4}O_Y$ before (solid line) and after (dot line) annealing at 450°C for 30 minutes
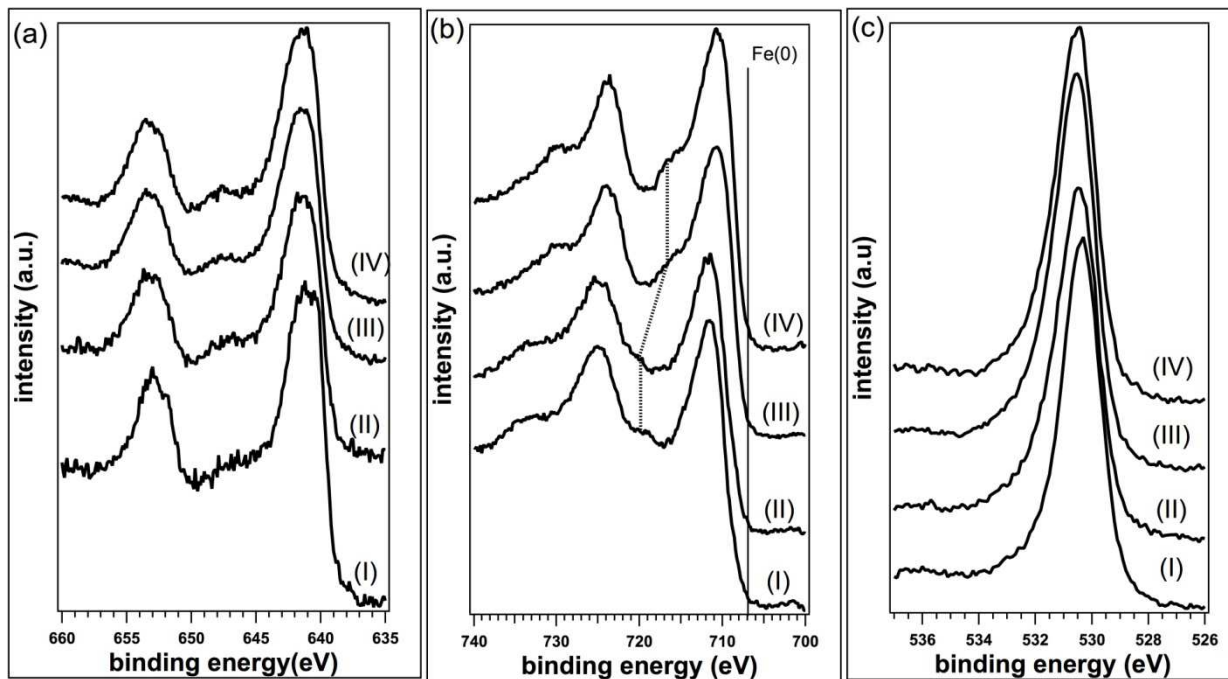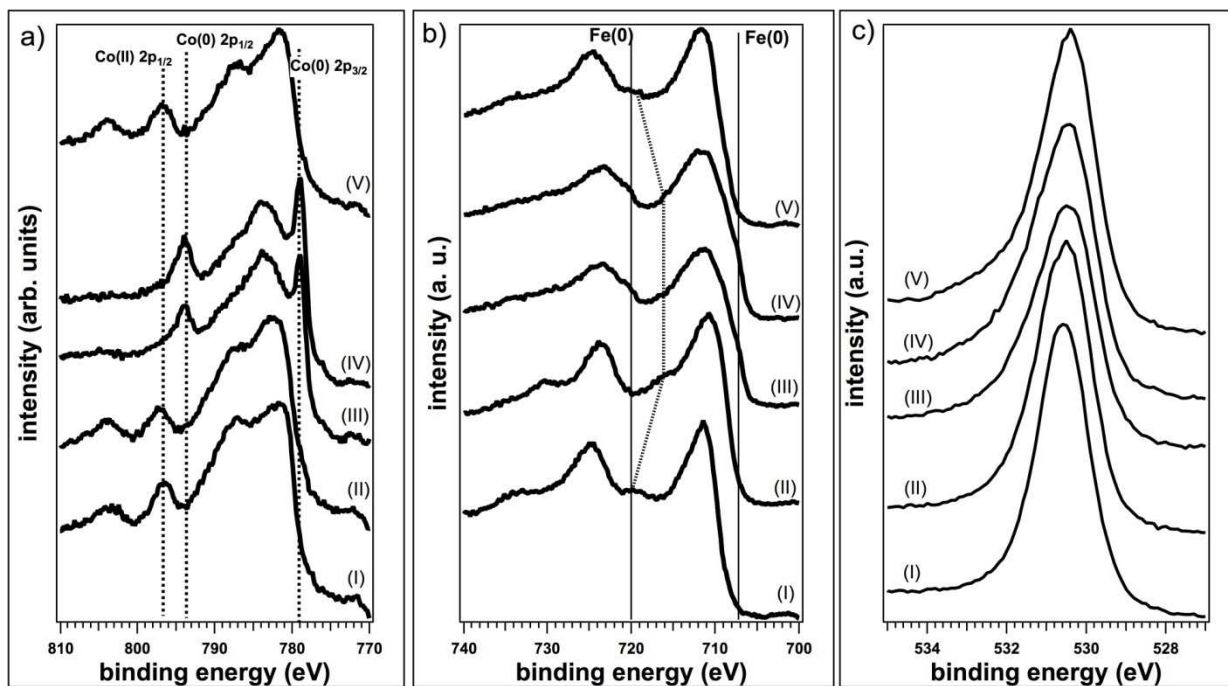
Figure 5-10. (a) Mn 2p (b) Fe 2p (c) O 1s photoemission peak of $Mn_{0.6}Fe_{2.4}O_y$ (i) after annealing at 450°C in UHV for 20 min, and after (II) 20 min, (III) 50, min (IV), 80 min ethanol exposure at 450°C. ($P_{Ethanol}$: 5x10-6 mbar). In (b) the dotted line shows the change in the position of the satellite of the Fe $2p_{3/2}$ line whereas the solid vertical line indicates the BE position of iron metal
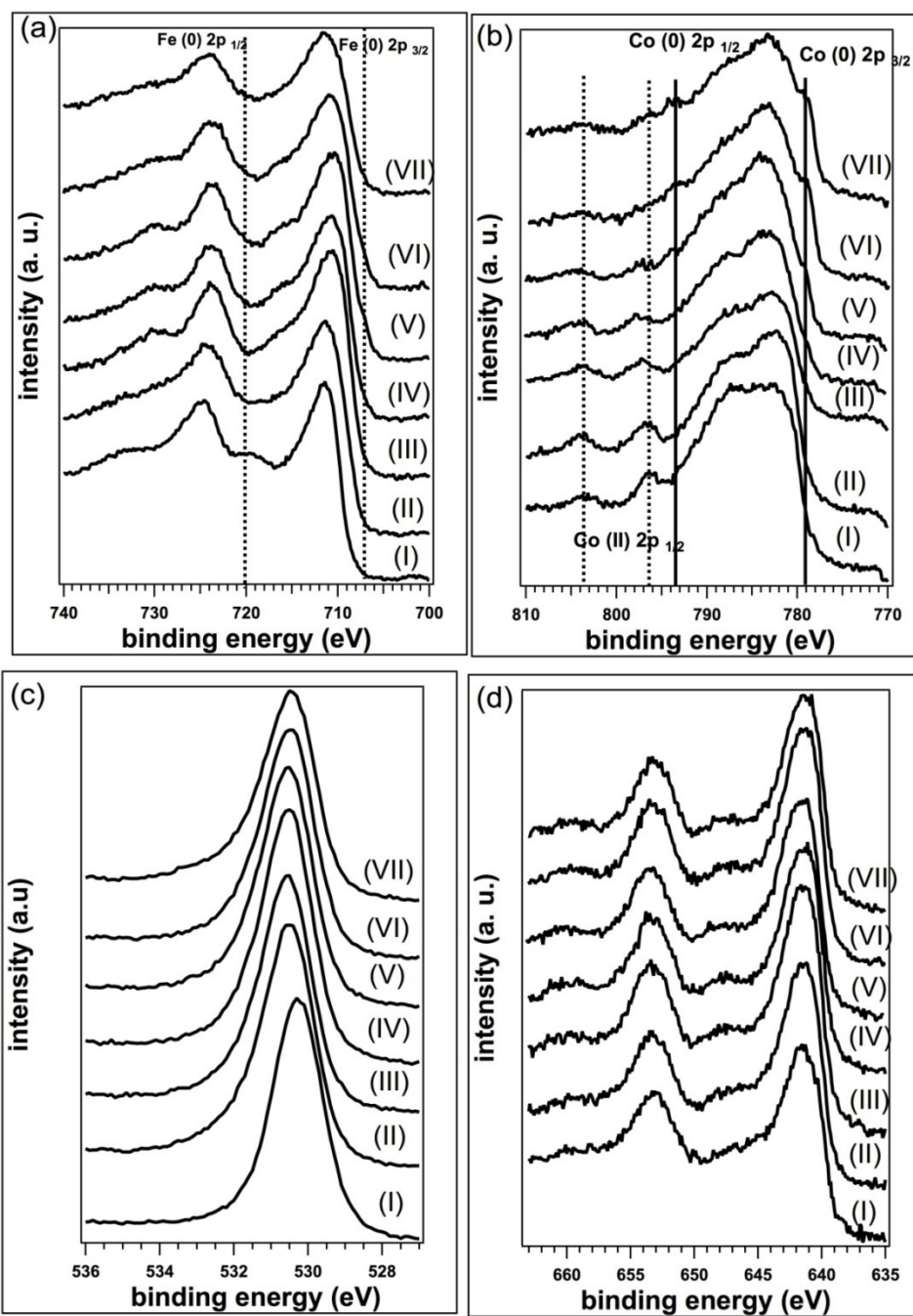
Figure 5-11. (a) Fe 2p (b) Co 2p (c) O 1s(d) Mn 2p photoemission peaks of Co0.3Mn0.3Fe2.4Oy (i) after annealing at 450°C in UHV for 20 min, and after (II) 20 min, (III) 50 min, (IV) 80 min,(V) 120 min ethanol exposure at 450°C(P$_{Ethanol}$: 5x10^{-6} mbar), and after (VI)30 min and (VII) 60 min water exposure at 450°C (P$_{water}$: 2x10^{-4} mbar). In (a) the dotted vertical line indicates the BE position of iron metal, in (b) the BE position of metal component is shown by solid vertical lines, whereas the position of the Co(II) 2p$_{1/2}$ peak maximum position and its satellite are indicated by dotted lines
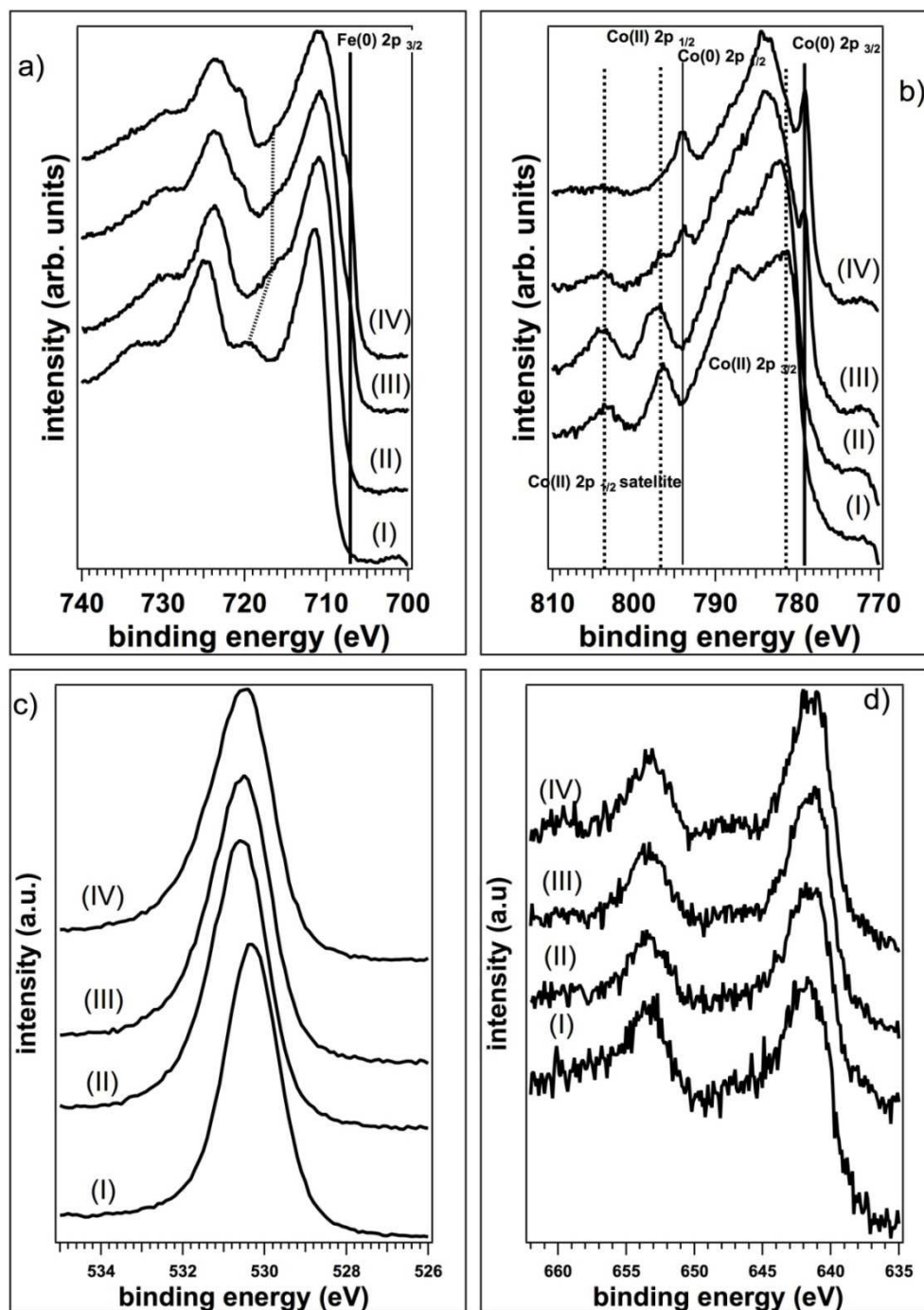
Figure 5-12. (a) Fe 2p (b) Co 2p (c) O 1s(d) Mn 2p photoemission peaks of $Co_{0.3}Mn_{0.3}Fe_{2.4}O_Y$ (i) after annealing at 450°C in UHV for 20min, and after (II) 20 min, (III) 50 min (IV), 80 min ethanol exposure at 450°C($P_{Ethanol}$: 5x10^{-6} mbar). In (a) the dotted vertical line indicates the BE position of iron metal and whereas the dotted line the shift of Fe 2p$_{3/2}$ satellite peak, in (b) the BE position of metal component is shown by solid vertical lines, whereas the position of the Co(II) 2p$_{1/2}$peak maximum position and its satellite are indicated by dotted lines

Figure 5-13. (a) Co 2p (b) Fe 2p (c) O 1s photoemission peaks of $Co_{0.6}Fe_{2.4}O_y$ (i) after annealing at 450°C in UHV for 20 min, and after (II) 20 min, (III) 50, min (IV), 80 min ethanol exposure at 450°C($P_{Ethanol}$: 5x10-6 mbar) and after (VI) 30 min water exposure at 450°C (P_{water}: 2x10^{-4} mbar). In (b) the dotted vertical line indicates the BE position of iron metal and whereas the dotted line the shift of Fe $2p_{3/2}$ satellite peak

Conclusions on the in-situ XPS study

Globally from photoemission we can outline a *scenario* where the reactivity of the ferrospinels is strongly dependent on the type of M introduced in the lattice, which however determines a quite complex reactivity scheme based on a synergetic effect. Manganese in large amount has the effect of slowing down the reduction reaction and in any case it can never be reduced. The high thermodynamic stability of Mn^{2+} is the probable origin of its scarce attitude toward reduction. Cobalt on the contrary can be reduced to the metallic state very quickly, even faster and in a larger extent than iron.

In order to get information on the second step of the chemical loop we have investigated the exposure of ethanol reduced $Co_{0.6}Fe_{2.4}O_y$ and $Co_{0.3}Mn_{0.3}Fe_{2.4}O_y$ to water at 450°C. In both cases Fe 2*p* spectra indicate a fast oxidation process that leads to an almost complete suppression of the metal component. However, it must be noted that the final Fe 2*p* spectrum is rather broad with a smeared fine structure, which can be due to the co-presence of many different phases: not only ferrospinels but also iron suboxides and hydroxides. The presence of these latter is supported by the larger FWHM and increased intensity on the high BE side of the O *1s* peak after water dosing. Similarly in the Co 2*p*

spectra, the quick formation of oxidized species i.e. Co^{2+} can be observed immediately after water exposure. However, whereas in the pure cobalt ferrospinel the oxidation of cobalt is almost quantitative, in the case of the Co/Mn sample such process is partial and a large metal cobalt component is visible even after extended water dosing (60 min). Such difference can be probably traced back to the presence of manganese, which somehow hinders the reaction with water.

5.8. Reactivity tests: $Co_{0.6-x}Mn_xFe_{2.4}O_y$ system

This section includes discussion of the results obtained over $Co_{0.6-x}Mn_xFe_{2.4}O_y$ ferrospinels tested on the laboratory-scale plant. The cycling time was chosen according to the initial results achieved over pristine Fe_3O_4 and M-ferrospinels - $CoFe_2O_4$, $NiFe_2O_4$, reported by Trevisanut and et al[129,126]. It was found that in approximately 20 min of ethanol feeding, the material was constantly reduced until it reached its `steady state` with the stable composition under these reaction conditions. Therefore, we were able to avoid a further coke deposition that occurred over the strongly reduced spinel.
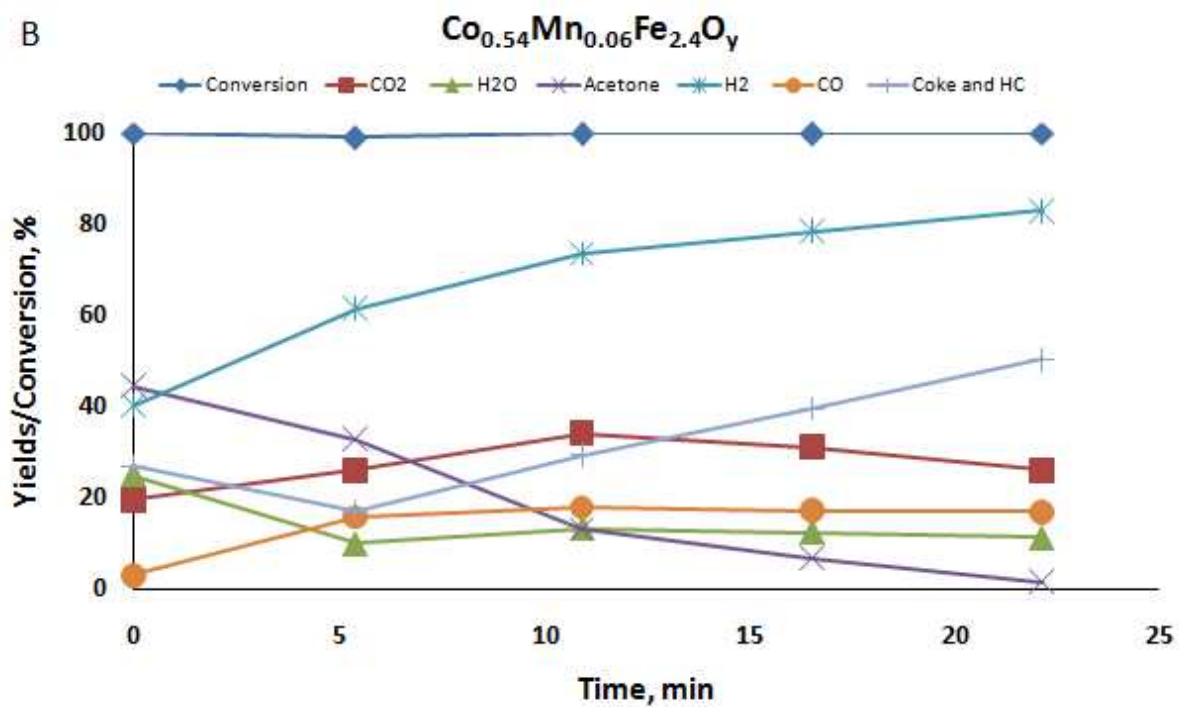
1st step: 20 min reduction with ethanol

Figure 5-14 shows conversion and yield for the main products (yield >5%), obtained during the first step of the chemical loop, where the material is being reduced by ethanol at 450^oC for 20 min. The conversion of ethanol over $Co_{0.6}Fe_{2.4}O_y$ (Figure 5-14, A) reached 100% starting from the first minutes of the reaction, and it was stable during 20 min of ethanol feeding. One of the main products of ethanol conversion was hydrogen, with an initial yield of about 50%, which increased up to 82% while the extent of spinel reduction increased. Also, CO and CO_2 have similar increasing trends as for H_2, thus suggesting that the main reactions during spinel reduction involved the partial oxidation of ethanol:

(1) $C_2H_5OH + MeO_x \rightarrow 2\ CO + 3\ H_2 + MeO_{(x-1)}$

(2) $C_2H_5OH + 3\ MeO_x \rightarrow 2\ CO_2 + 3\ H_2 + 3\ MeO_{(x-1)}$
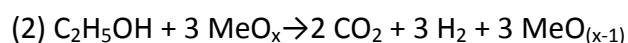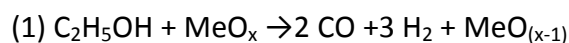
The formation of acetone, which declined with time, can be a result of an aldol condensation of the intermediately formed acetaldehyde, with further isomerization of aldol into hydroxyketone followed by a reverse reaction to form acetone and formaldehyde (converted into CO and H_2). Either, as recently proposed by Rodrigues et al., by ketonization

of carboxylates (acetates) which are obtained by dehydrogenation of this alcohol followed by oxidation[127]. In fact, the formation of acetates over $Co_{0.6-x}Mn_xFe_{2.4}O_y$ samples was confirmed by DRIFTS study. The formation of water (with yield ~11%) involves several possible reactions:

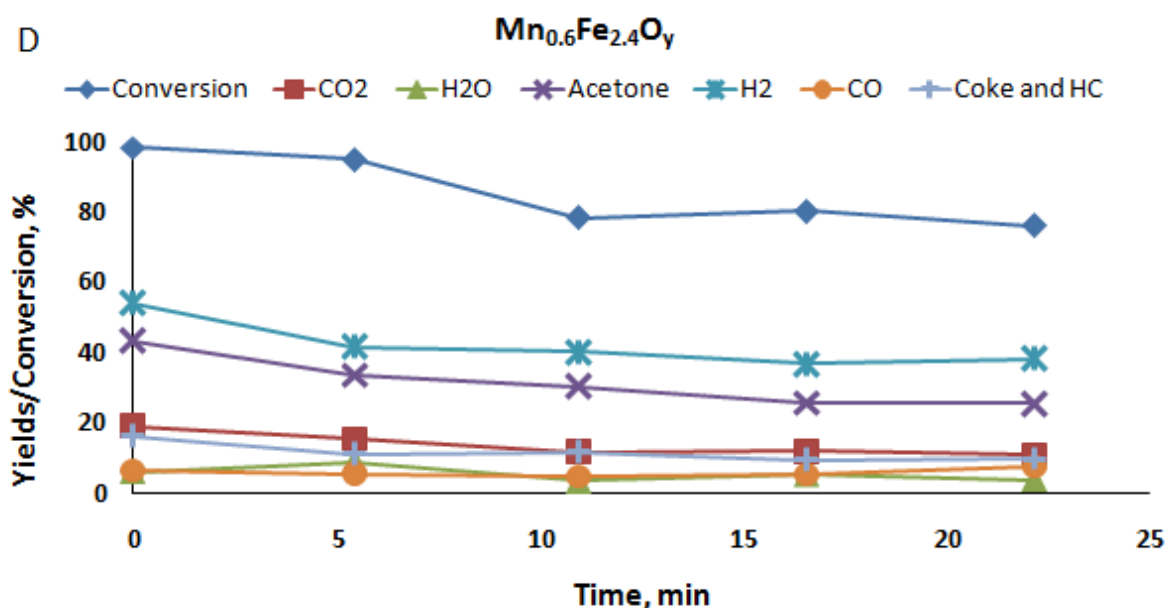(3) $C_2H_5OH + 6\ MeO_x \rightarrow 2\ CO_2 + 3\ H_2O + 6\ MeO_{(x-1)}$

(4) $H_2 + MeO \rightarrow H_2O + Me$

(5) $C_2H_5OH \rightarrow 2\ C + 2\ H_2 + H_2O$

B — Co$_{0.54}$Mn$_{0.06}$Fe$_{2.4}$O$_y$
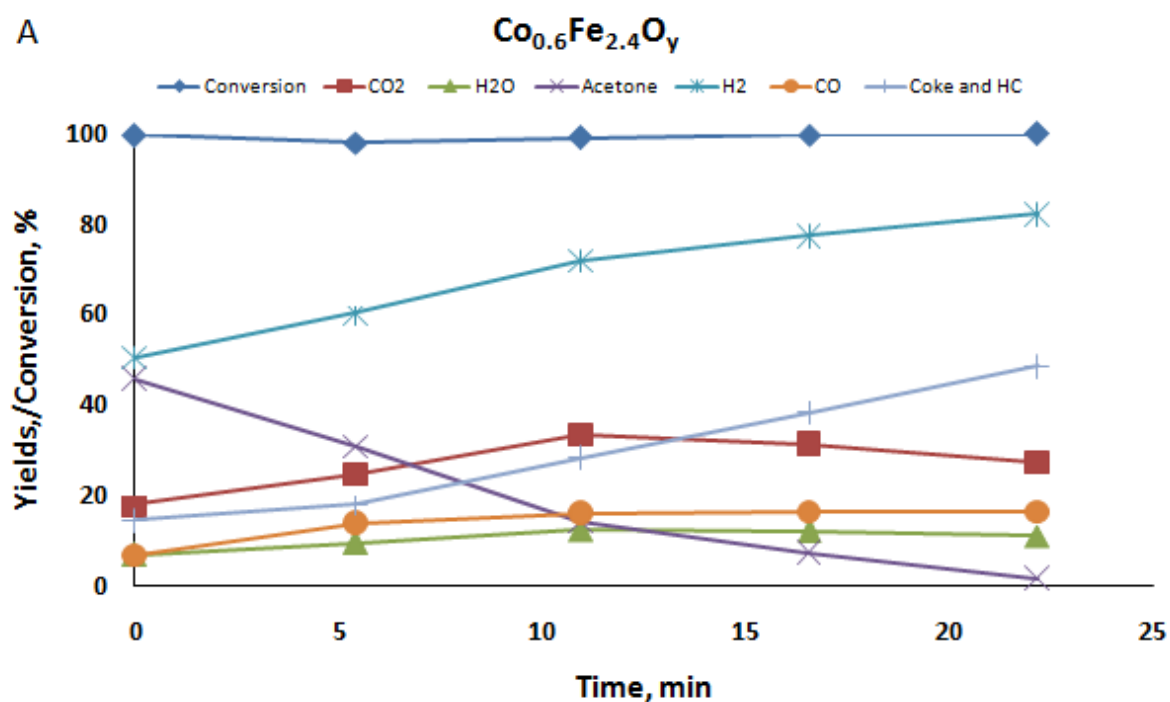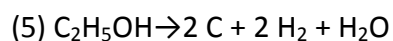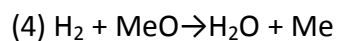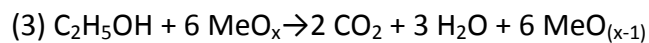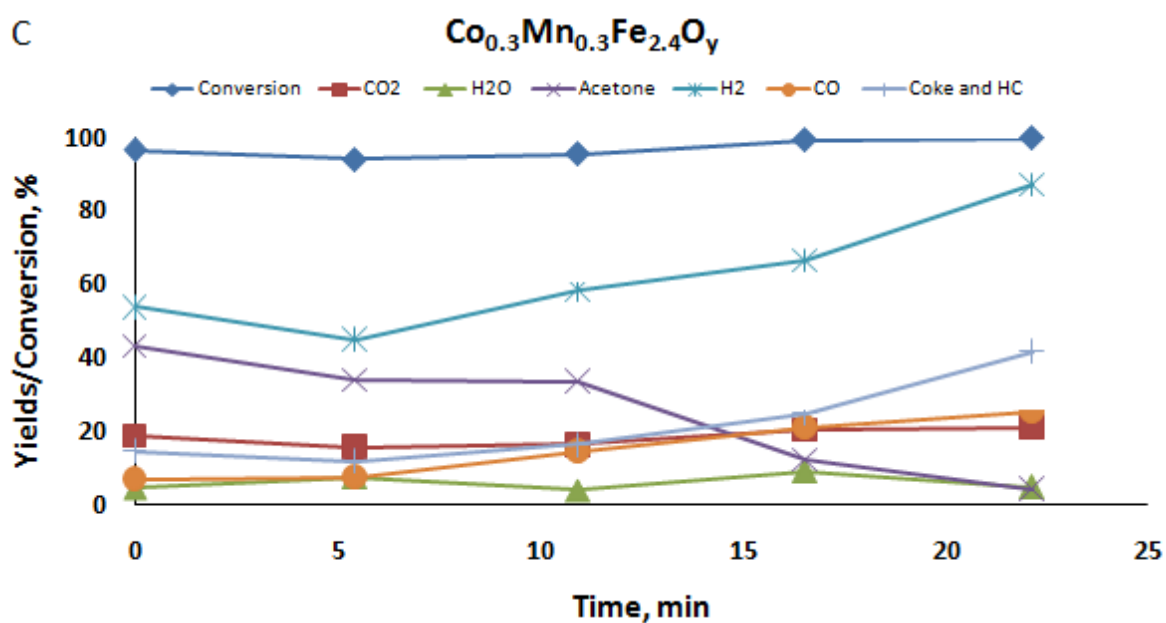
C — Co$_{0.3}$Mn$_{0.3}$Fe$_{2.4}$O$_y$

Figure 5-14. Conversion and yields for the main products during 20 min reduction with ethanol at 450oC over: (A) $Co_{0.6}Fe_{2.4}O_y$; (B) $Co_{0.54}Mn_{0.06}Fe_{2.4}O_y$; (C) $Co_{0.3}Mn_{0.3}Fe_{2.4}O_y$; (D) $Mn_{0.6}Fe_{2.4}O_y$

Coke and heavy compounds (mainly aromatics) also formed starting from the very beginning of the reaction time (~20%), with a progressive increase in yield. Under these reaction conditions it was impossible to avoid the formation of carbonaceous species. The generation of coke was likely due to dehydrogenation and total deoxygenation of ethanol:

(6) $C_2H_5OH \rightarrow C + CO + 3 H_2$

(7) $C_2H_5OH \rightarrow 2 C + H_2O + 2 H_2$
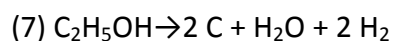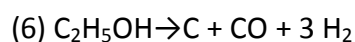
Moreover, disproportionation of CO (Boudouard reaction) can result in coke deposition:

(8) $2 CO \rightarrow CO_2 + C$
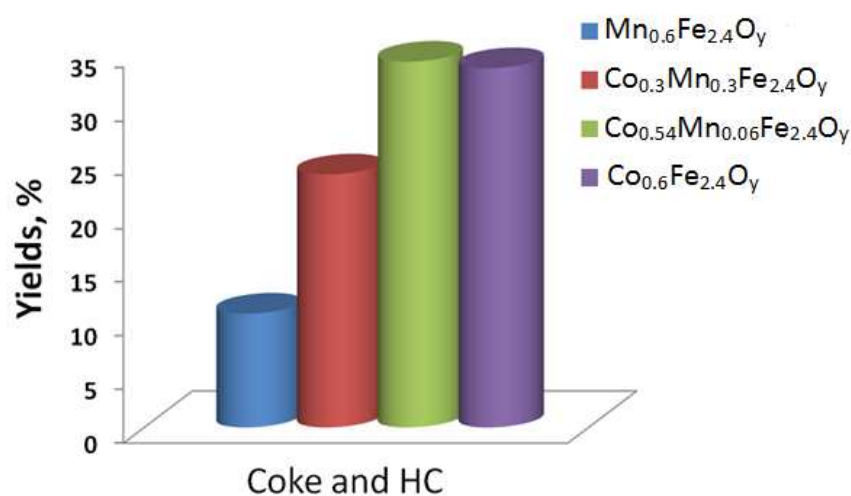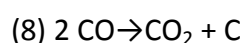
Figure 5-15. Integrated Yields for the coke and heavy compounds during 20 min reduction with ethanol at 450°C

Results obtained with the other samples (Figure 5-14, B,C,D) demonstrate similar trends in the products distribution. However, some significant differences can be seen: with increasing Mn-content the conversion of ethanol was slightly decreasing. The $Mn_{0.6}Fe_{2.4}O_y$ sample (Figure 5-14, D) at first showed 100% of conversion followed by its decrease down to 80%. The main reason for such behavior can be an accumulation of MnO phase in the catalyst, which has a high thermodynamic stability and as a consequence its scarce attitude towards the reduction to metallic component. This result also has been confirmed by TPR, DRIFTS and in-situ XPS measurements.

As discussed above, we could not completely avoid coke formation, but despite this, we were able to significantly reduce its amount by changing the composition of the catalyst, as shown in Figure 5-15, plotting the overall yield to C residues integrated over the 20 min reduction time. Indeed, the presence of Mn had the beneficial effect of decreasing the coke deposition, which is an important issue in order to produce C-free hydrogen. The integrated yields for other products formed during 20 min of reduction with ethanol are plotted in Figure 5-16. In particular, Co-containing ferrospinels ($Co_{0.6}Fe_{2.4}O_y$ and $Co_{0.54}Mn_{0.06}Fe_{2.4}O_y$) have shown high yields to CO_2, CO and H_2O and enhanced reactivity in the anaerobic decomposition/oxidation of ethanol. On the other hand, $Mn_{0.6}Fe_{2.4}O_y$ appeared to be more active in the formation of acetone, which is the result of the reverse aldol condensation reaction.
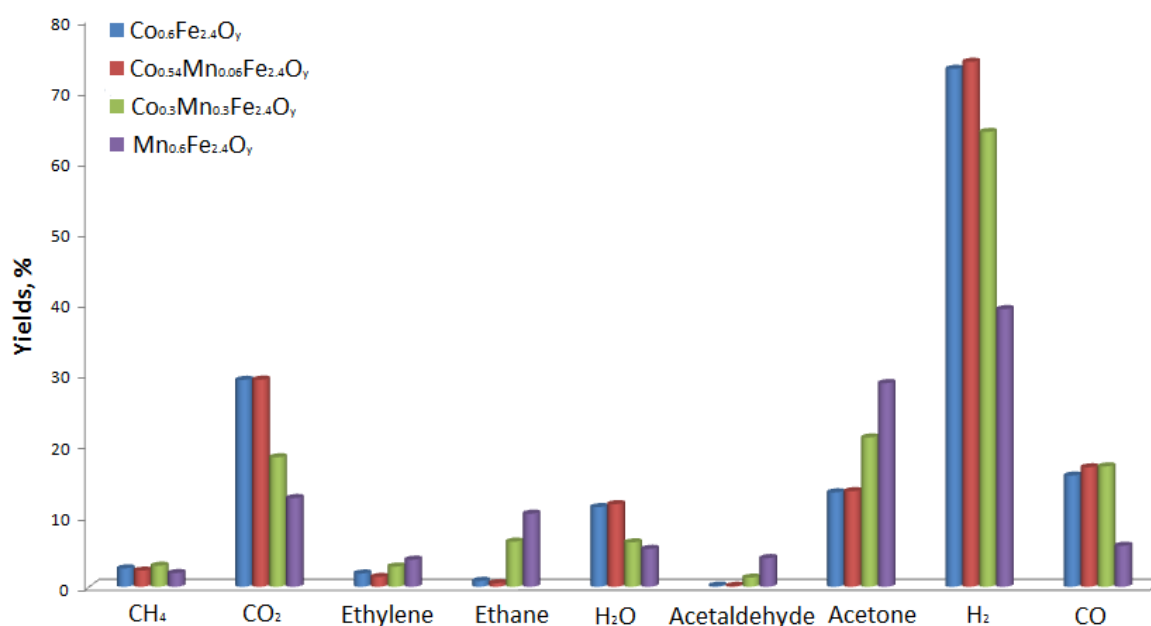

Figure 5-16. Integrated Yields for other compounds during 20 min reduction with ethanol at 450°C

Figure 5-17 shows the degree of reduction for the four catalysts with different ratio Co/Mn as a function of reaction time (20 min), as calculated from the oxygen balance[126]. Even though the highest surface area was shown by $Mn_{0.6}Fe_{2.4}O_y$ catalyst, and it declined with an increase of Co-content, the samples with high content of Co ($Co_{0.6}Fe_{2.4}O_y$ and $Co_{0.54}Mn_{0.06}Fe_{2.4}O_y$) were strongly reduced (almost 100 %) in comparison to only Mn-modified ferrospinel with just app. 20% of reduction extent. This suggests that the difference in the reducibility of the four M-modified ferrospinels is related to the nature of the incorporated M cation and its intrinsic reactivity, which is also confirmed by in-situ XPS results.
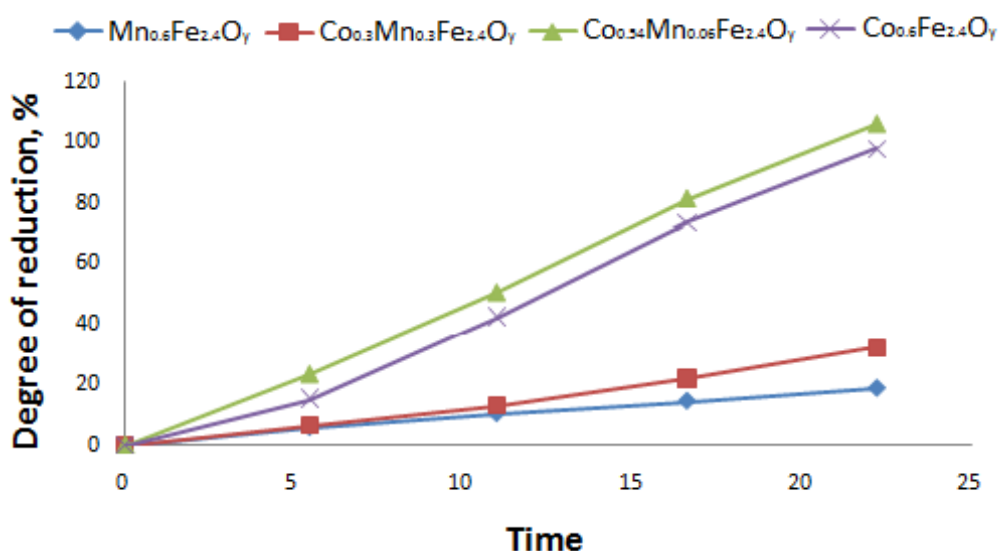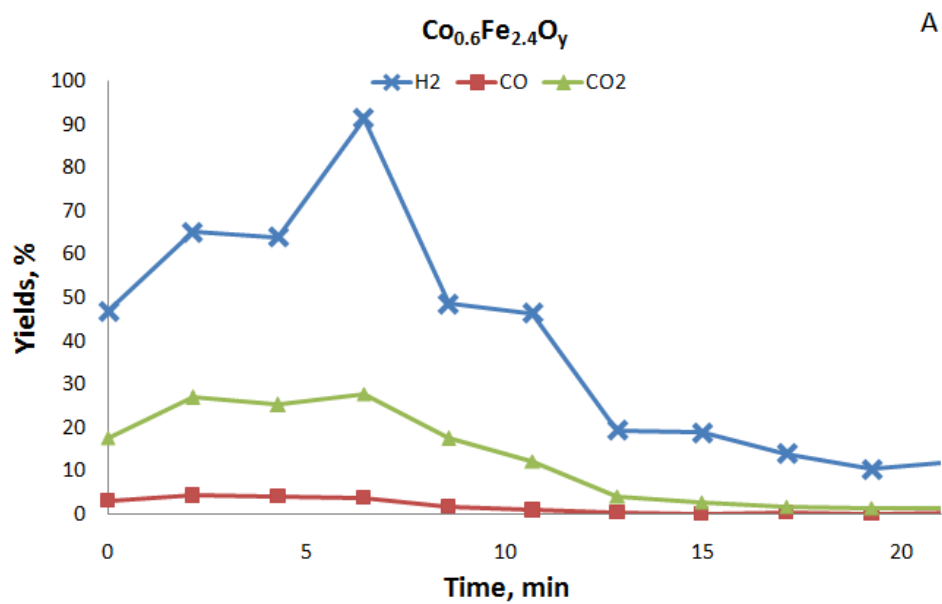

Figure 5-17. Reduction extent of $Co_{0.6-x}Mn_xFe_{2.4}O_y$ samples after 20 min of ethanol exposure (at T-450°C)

2nd step: 20 min re-oxidation with water

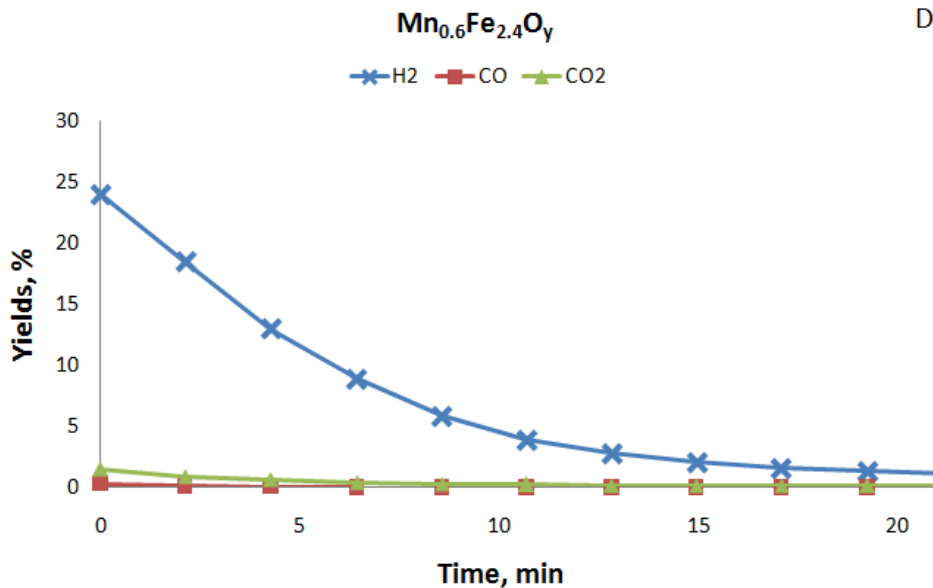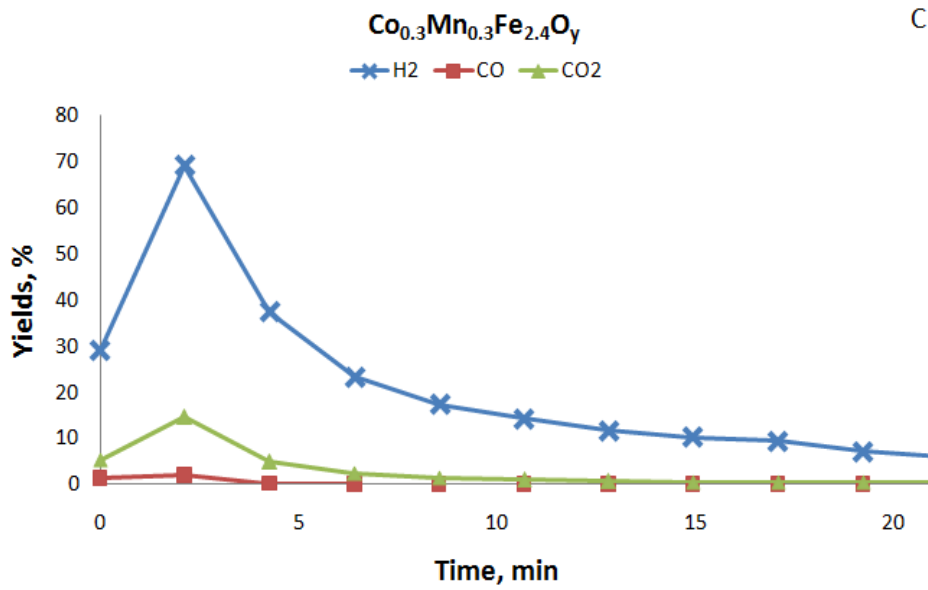***2nd* step: 20 min re-oxidation with water**

Co$_{0.3}$Mn$_{0.3}$Fe$_{2.4}$O$_y$ C
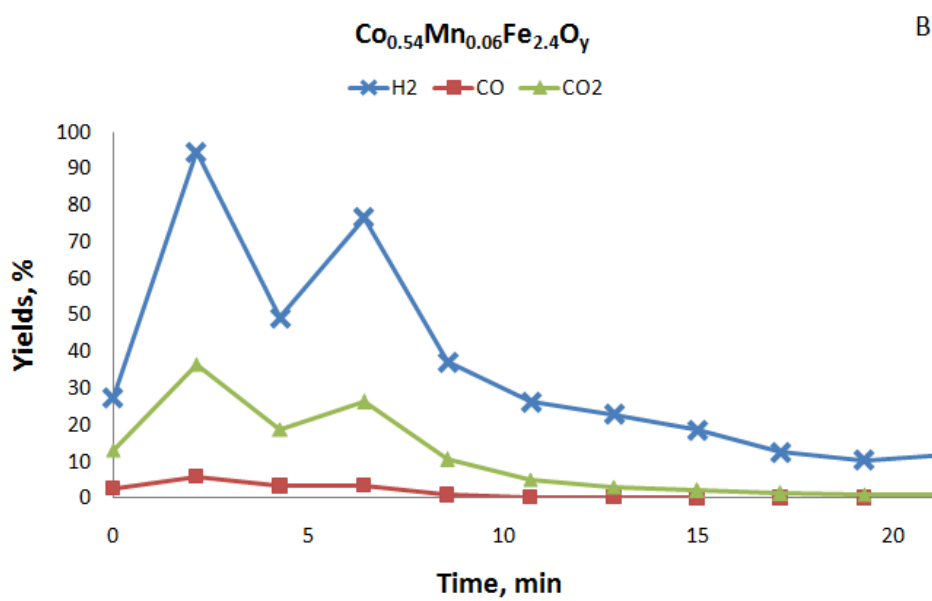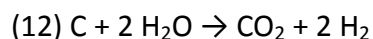

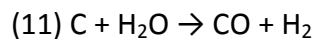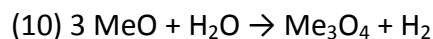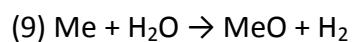**Mn$_{0.6}$Fe$_{2.4}$O$_y$**   D

Figure 5-18. Yields for the H2, CO2 and CO during 20 min re-oxidation with water at 450°C over: (A) Co$_{0.6}$Fe$_{2.4}$O$_y$; (B) Co$_{0.54}$Mn$_{0.06}$Fe$_{2.4}$O$_y$; (C) Co$_{0.3}$Mn$_{0.3}$Fe$_{2.4}$O$_y$; (D) Mn$_{0.6}$Fe$_{2.4}$O$_y$

After the reduction with ethanol, the materials were re-oxidized with steam at 450°C, which corresponds to the second step of the chemical loop. Figure 5-18 (A-D) reports the yield of H_2, CO_2 and CO versus time (yields have been calculated based on the H or O content in products, with respect to the water fed – described in Paragraph 2.11), whereas Figure 5-19 reports the overall yields to H_2, CO and CO_2, integrated over the 20 min oxidation time. High hydrogen yields were obtained over $Co_{0.6}Fe_{2.4}O_y$, $Co_{0.54}Mn_{0.06}Fe_{2.4}O_y$ and $Co_{0.3}Mn_{0.3}Fe_{2.4}O_y$. The common problem of all samples was the formation of CO and CO_2 during the re-oxidation step (Figure 5-18 and Figure 5-19), because of the gasification of carbonaceous

residues, previously formed during the reduction step. The main reactions occur during re-oxidation process are defined as following:

(9) $Me + H_2O \rightarrow MeO + H_2$

(10) $3\ MeO + H_2O \rightarrow Me_3O_4 + H_2$

(11) $C + H_2O \rightarrow CO + H_2$

(12) $C + 2\ H_2O \rightarrow CO_2 + 2\ H_2$

The main difference was in the amount of produced CO_x. According to the obtained results, Mn-containing catalysts were more selective to hydrogen formation, as shown in Table 5-3, reporting the ratio between the overall yield to H_2 and the overall yield to $CO+CO_2$.

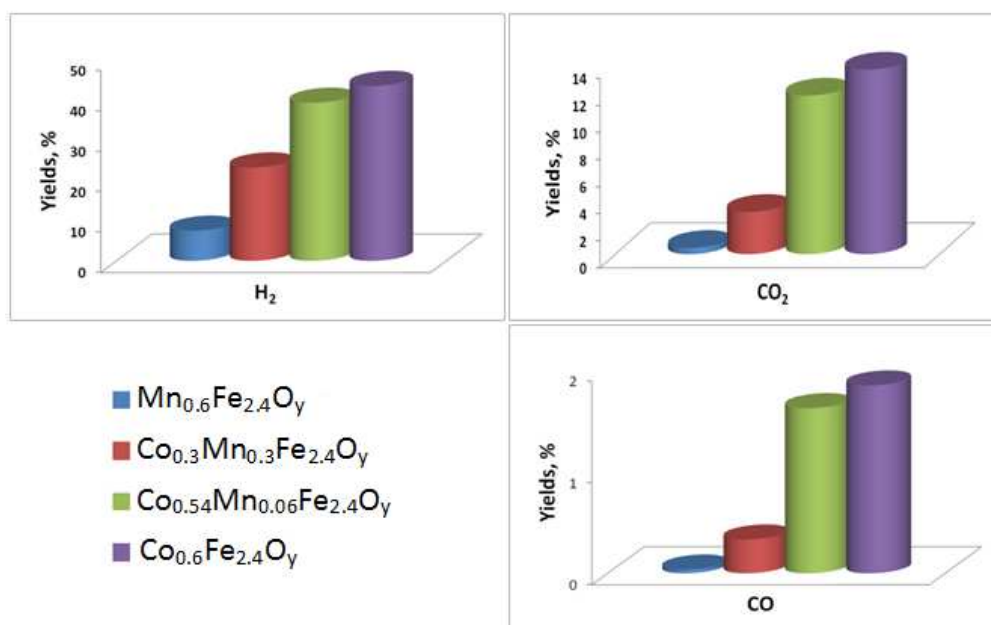Figure 5-19. Integrated values of yields to H_2, CO_2 and CO during the re-oxidation with H_2O

Table 5-3. Ratio $H_2/(CO+CO_2)$ obtained during the re-oxidation step with water

	$H_2/CO+CO_2$
$Mn_{0.6}Fe_{2.4}O_y$	28.0
$Mn_{0.3}Co_{0.3}Fe_{2.4}O_y$	12.2
$Mn_{0.06}Co_{0.54}Fe_{2.4}O_y$	5.2
$Co_{0.6}Fe_{2.4}O_y$	5.0

Determination of carbon content (CHNS analysis)

In order to quantify the real amount of coke formed on the tested materials an elemental analysis (CHNS) was carried out. Table 5-4 shows the obtained results: Mn-containing materials ($Mn_{0.6}Fe_{2.4}O_y$ and $Co_{0.3}Mn_{0.3}Fe_{2.4}O_y$) showed the lowest amount of C residues accumulated during the first reduction step. However, with all materials a part of the coke still remained on the surface after one complete cycle, being not completely re-oxidized with water at that temperature (450^oC). As a consequence, these materials underwent some morphological changes significantly affected by accumulation of coke, sintering (particle size increased to ~90-100 nm) and segregation (Figure 5-20, B,C); these images are of samples which underwent several redox cycles).
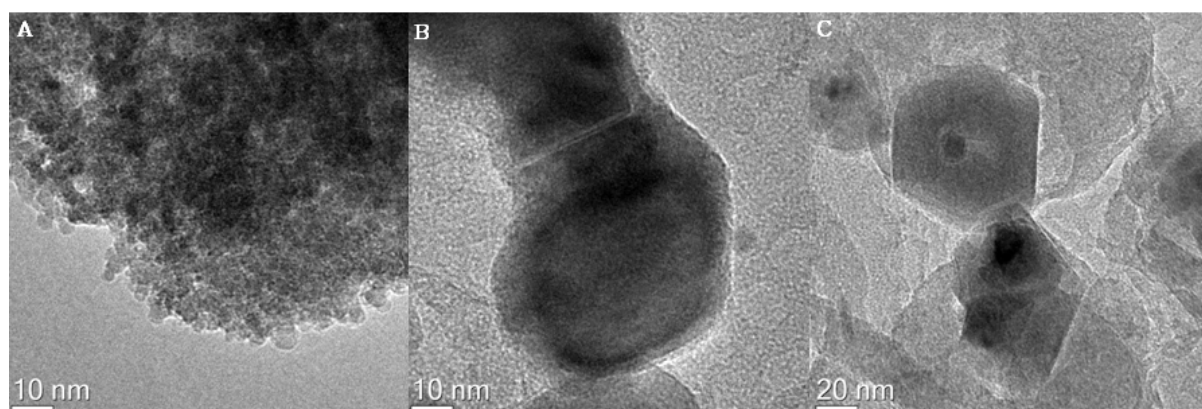

Figure 5-20. TEM images of $Co_{0.3}Mn_{0.3}Fe_{2.4}O_y$: (A) fresh material calcined at 450^oC; (B) after 4 cycles·20 min+ 1red ·20 min; (C) after 20 min·5 cycles

However, the behavior shown by $Co_{0.3}Mn_{0.3}Fe_{2.4}O_y$ can be considered the most promising one, since it forms less coke during the 1st step of ethanol reduction and less CO_x during the 2nd step of re-oxidation with steam, nevertheless it can provide high hydrogen yield. On the other hand, $Mn_{0.6}Fe_{2.4}O_y$ and $Mn_{0.3}Co_{0.3}Fe_{2.4}O_y$ were less efficient in the removal of C residues during the re-oxidation with steam; this means that the low amount of CO and CO_2 formed during the 2nd step are also due to the fact that coke is only in minimal part re-oxidized by steam. This may be due to the lower degree of reduction achieved during the 1st step, since the reduced metal may catalyze the gasification of coke by reaction with steam.

Table 5-4. Amount of coke (C) in weight % obtained over the four investigated samples

SAMPLE	C content(%) after 20 min of reduction (ethanol)	C content(%) after 20 min reduction (ethanol) + 20 min re-oxidation (H_2O)
$Mn_{0.6}Fe_{2.4}O_y$	2.2	2.1
$Co_{0.3}Mn_{0.3}Fe_{2.4}O_y$	7.9	6.5
$Co_{0.54}Mn_{0.06}Fe_{2.4}O_y$	11.0	6.1
$Co_{0.6}Fe_{2.4}O_y$	9.7	6.2

5.9.   Conclusions on the study of $Co_{0.6-x}Mn_xFe_{2.4}O_y$ ferrospinels

The chemical-loop reforming of ethanol for H_2 production was studied by using M-modified ferrospinels of general composition $Co_{0.6-x}Mn_xFe_{2.4}O_y$ ionic oxygen carrier materials. The redox properties of ferrospinels were found to depend strongly on the nature of incorporated cation in addition to its distribution inside the crystal lattice. The four catalysts with different ratio between two supplemented metals (Co/Mn) were investigated. Substitution of Fe^{2+} with Co^{2+} ions led to the formation mainly of an inverse spinel, however the addition of Mn resulted in the substitution of Td coordinated Fe^{3+} ions with Mn^{2+} and as a consequence the formation of new type of active sites. The reduction of M-modified ferrospinels appeared to be a complex process due to the presence of various reduced forms of Fe oxides together with Co and Mn oxides. Besides, it was observed that incorporation of Mn-Co metal cations into magnetite (Fe_3O_4) crystal structure affects its reducibility, depending on the nature of the incorporated metal cation. In particular, Co/Mn systems showed a cooperative influence on each other's reduction profiles. Moreover, in-situ DRIFTS study was performed in order to follow the stepwise reduction of the catalyst surface, which allowed us to detect different adsorbed species and their transformation into the products. Acetates and carbonates appeared to be important surface intermediates over Co- and mixed Co-Mn- ferrospinels and in the case of the only Mn-containing catalyst, there was no evidence of the carbonates formation. Furthermore, according to the results

obtained by means of catalytic tests and CHNS elemental analysis, the addition of Mn hindered carbon deposition, which also caused a decrease of the amount of CO_x generated by oxidation with water steam, which is an important issue to produce clean H_2. However, the Mn containing ferrospinels showed a lower efficiency in the removal of the C residues accumulated during the first step. This may lead to the need of a third step of coke removal by air oxidation, if a clean material is needed to perform a following cycle. In an alternative approach, as already pointed out in the literature, the unreactive coke may be maintained as an inert material, provided (that) during successive cycles the further accumulation of coke occurs at a limited extent only[22,142].

Co-Mn mixed ferrospinels, with high levels of Co, enhanced reactivity in the anaerobic decomposition/oxidation of ethanol. Thus, the behavior shown by $Co_{0.3}Mn_{0.3}Fe_{2.4}O_y$ can be considered to be the most promising one, as this type of M-modified ferrospinel formed less coke during the reduction step (as a result less CO_x generated during the re-oxidation step with water), and still high hydrogen yield could be obtained.

Therefore, one of the key points to improve the proposed process and make it industrially attractive is reducing the amount of carbonaceous species which in principle can be done by changing the catalyst composition and thus tuning its redox properties in order to optimize the ratio between the degree of reduction and the amount of coke deposition.

Hence, the use of bulk M-modified spinel oxides as oxygen carrier materials for the chemical-loop reforming of ethanol has its positive aspects which allow to achieve a good recyclability of the starting material due to the formation of thermodynamically stable spinel oxide phase during cycling using the "same mild temperatures" for both reduction and re-oxidation steps. In comparison to other approaches reported in literature, such as the use of high temperatures[143,144] to limit a coke formation and structured materials with morphologies aimed to confine the negative effects of sintering[145–147].

5.10. Ferrospinels TYPE II: study of $Cu_{0.6-x}Mn_xFe_{2.4}O_y$ system

The study of $Co_{0.6-x}Mn_xFe_{2.4}O_y$ ferrospinels (see previous Paragraph 5.5)have shown that Mn(II) incorporation into the system helps to significantly reduce the amount of coke and hence to avoid a fast deactivation of the material. Therefore, the present section onward explores physicochemical and catalytic properties of the $M^1_{0.6-x}M^2_xFe_{2.4}O_y$ spinel type

systems and the particular interest represents the effect of Mn-incorporation on the morphology, magnetic, redox and catalytic properties of the resulted $Cu_{0.6-x}Mn_xFe_{2.4}O_y$ ferrospinel.

Characterization of fresh $Cu_{0.6-x}Mn_xFe_{2.4}O_y$ ferrites

The section includes a discussion of the results obtained from several characterization techniques: Mössbauer Spectroscopy, Magnetic measurements and TPR over fresh $Cu_{0.6-x}Mn_xFe_{2.4}O_y$ ferrospinels.
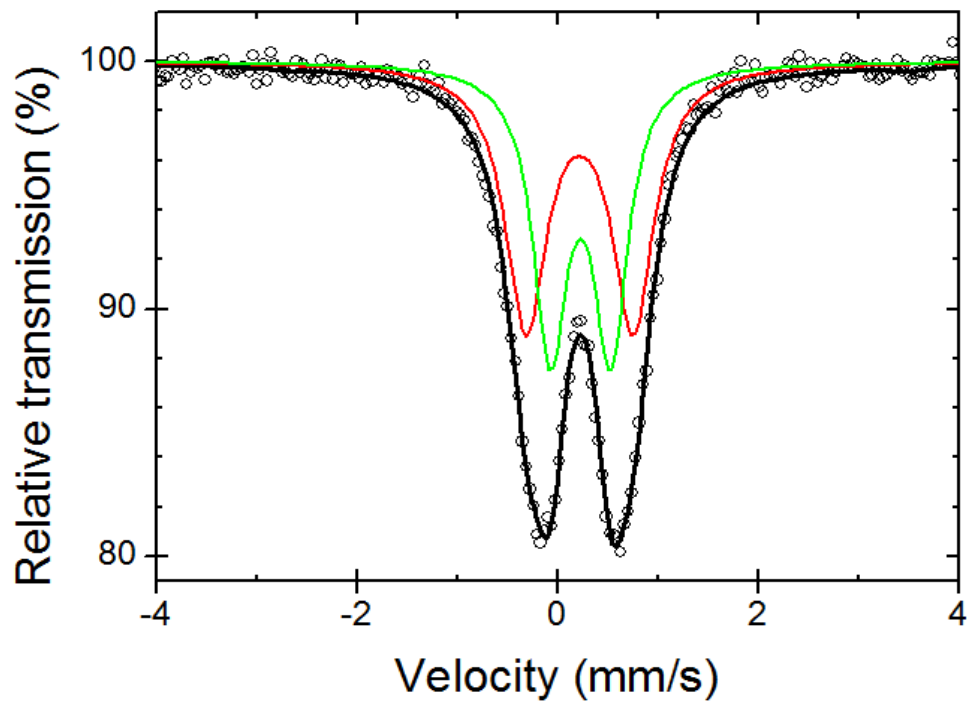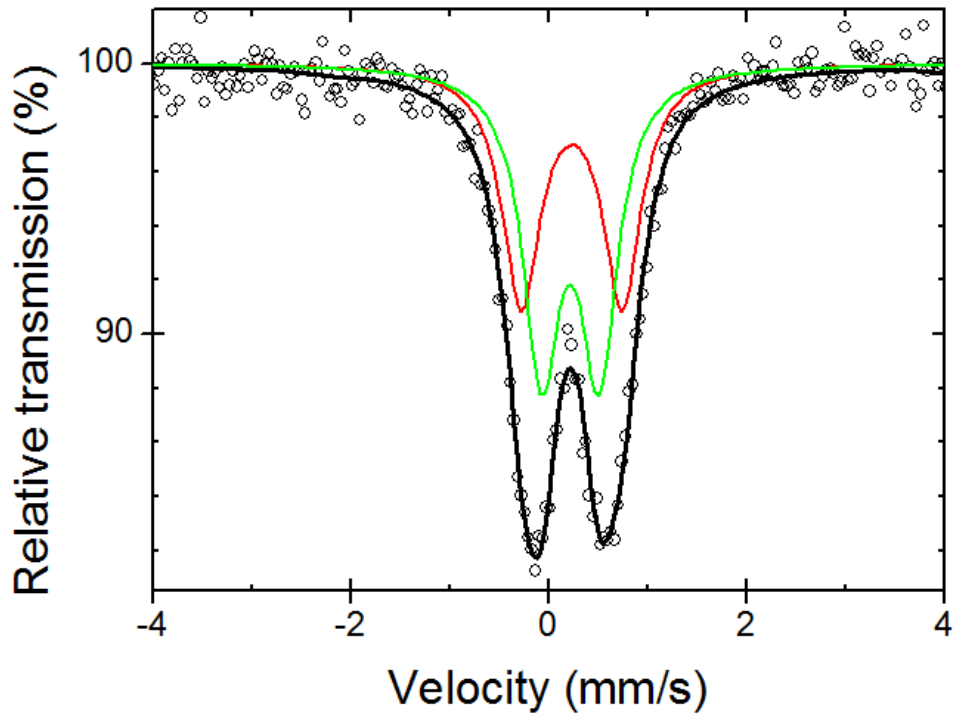
5.11. Mössbauer spectroscopy
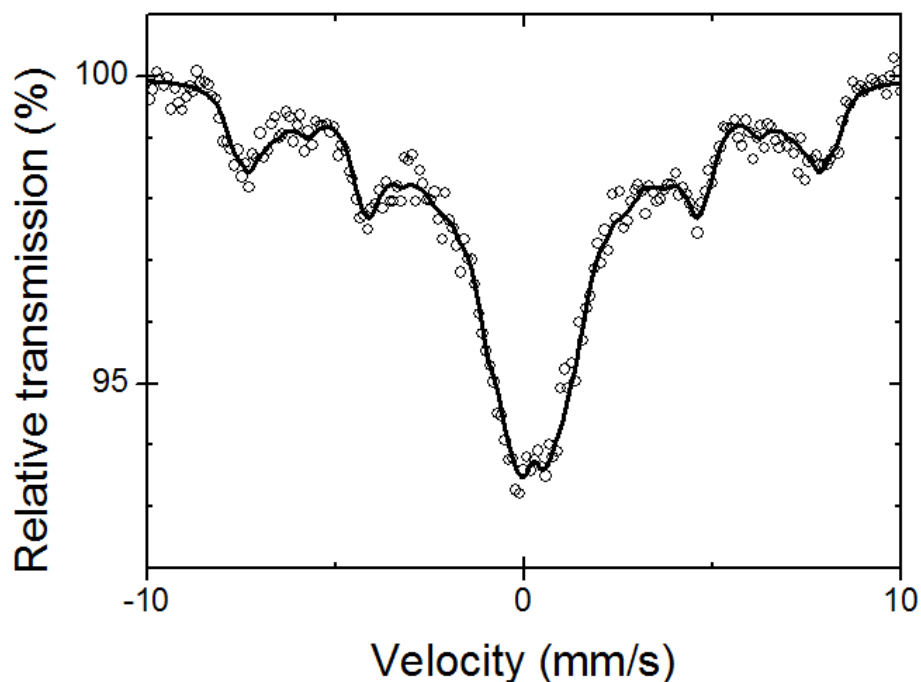
Figure 5-21. Room temperature ^{57}Fe Mössbauer spectra of samples $Cu_{0.6}Fe_{2.4}O_y$, $Cu_{0.3}Mn_{0.3}Fe_{2.4}O_y$ and $Mn_{0.6}Fe_{2.4}O_y$

Table 5-5. Room temperature ^{57}Fe Mössbauer parameters

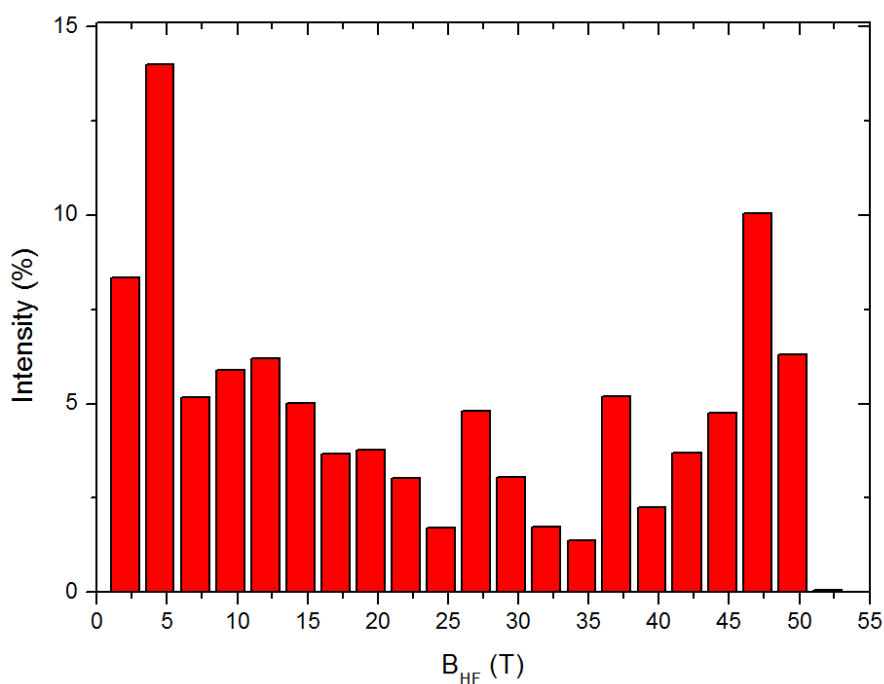| Sample name	δ* (mm/s)	Δ_{EQ} (mm/s)	B_{HF} (T)	Γ (mm/s)	Relative intensity (%)
$Cu_{0.6}Fe_{2.4}O_y$	0.35	0.04	Distribution	0.65	100
$Cu_{0.3}Mn_{0.3}Fe_{2.4}O_y$	0.34	1.02	-	0.47	45
	0.32	0.58		0.45	55
$Mn_{0.6}Fe_{2.4}O_y$	0.32	1.11	-	0.56	34
	0.31	0.61		0.56	66

* Isomer shift referred to α-Fe metal.

Figure 5-22. Internal magnetic field distribution obtained from the best fit of the room temperature ^{57}Fe Mössbauer spectrum of sample $Cu_{0.6}Fe_{2.4}O_y$

The room-temperature Mössbauer spectra of the Mn-Cu-ferrites are shown in Figure 5-21.The three spectra were quite different, because of the magnetic characteristics of the $Cu_{0.6-x}Mn_xFe_{2.4}O_y$ ferrites, which are strongly dependent upon the size of the particles. The Mn-rich ferrite system (sample $Mn_{0.6}Fe_{2.4}O_y$) is characterized by a simple quadrupole split spectrum, which indicates the pure paramagnetic nature of the iron species in the solid. This

observation can be attributed to the presence of superparamagnetic ferrite nanoparticles with sizes below ~5 nm. Such superparamagnetic behavior at room temperature is rather common for nanosized iron oxides, and has already been reported for $MnFe_2O_4$ nanoparticles by C. R. Alves et al[148], among others. Due to relatively large experimental linewidth, the spectrum was fitted by two quadrupole doublets representing either tetrahedrally (A sites) or octahedrally (B sites) coordinated trivalent iron centres. No divalent iron seems to be present in the sample.

The sample with an equal amount of Mn and Cu atoms ($Cu_{0.3}Mn_{0.3}Fe_{2.4}O_Y$) also shows a similar quadrupole split spectrum typical of trivalent iron undergoing superparamagnetic relaxation, in agreement with the results of magnetic studies.

The spectrum of the copper rich sample ($Cu_{0.6}Fe_{2.4}O_Y$), on the other hand, is more complicated and shows the presence of two components in the fitting curve (a doublet and a sextet); it has the typical shape of iron oxides with a relatively large size (or magnetic domains size) distribution undergoing magnetic relaxation. The doublet component is derived from the superparamagnetic contribution of the sample; magnetization randomly changed under the effect of the temperature and only the effect of the electric field gradient at the nucleus is observed which gives rise to a doublet in the total spectra. Besides a doublet, a distribution of sextets is needed to fit the total spectra that derive from the larger ferromagnetic particles that are amorphous. In this case, the fit was performed using a distribution of Internal Magnetic Fields (Figure 5-22).

In summary, the δ values(Table 5-5) for all three M-modified ferrites are in the range from 0.31 to 0.35 mm/s which indicates that all iron is in Fe^{3+} state. The small decrease in the isomer shift with an increase of Mn-content (from 0.35 to 0.31 mm/s) can be explained by the very slight decrease of the s-electron density at the ^{57}Fe nuclei due to the decrease of Fe–O covalency[149].
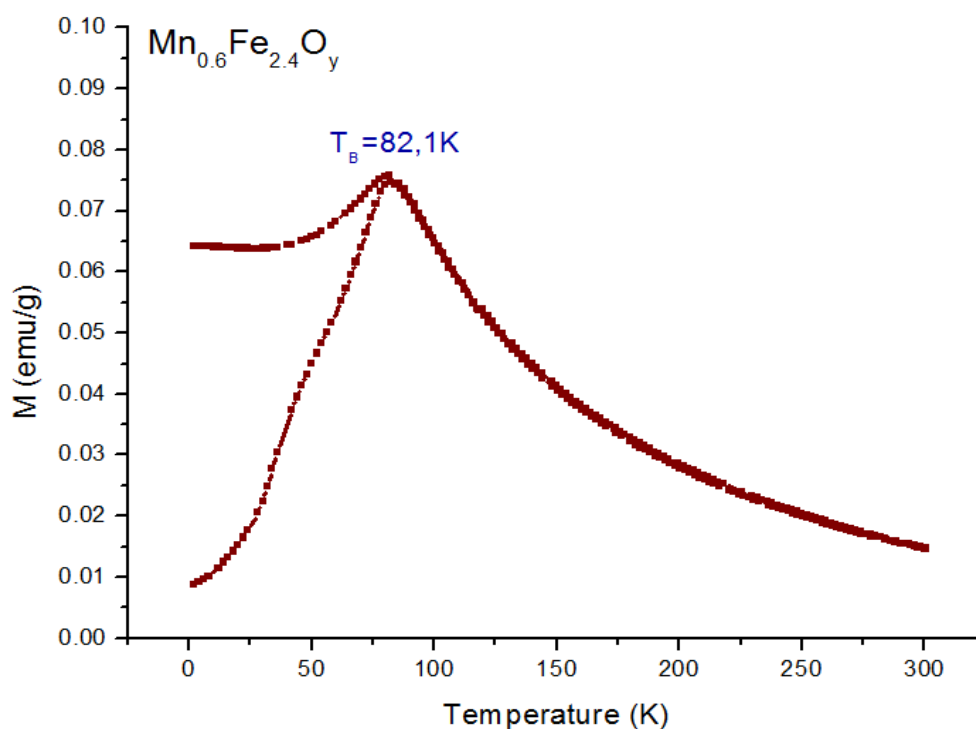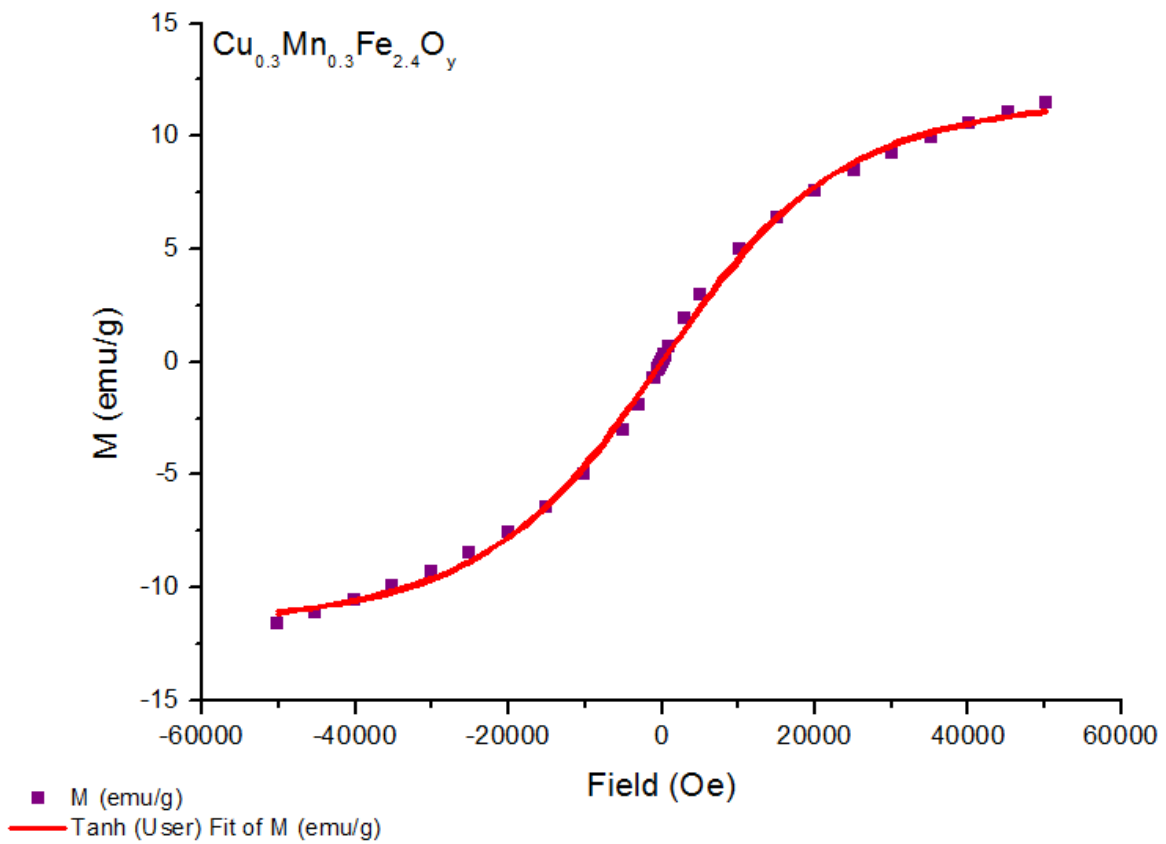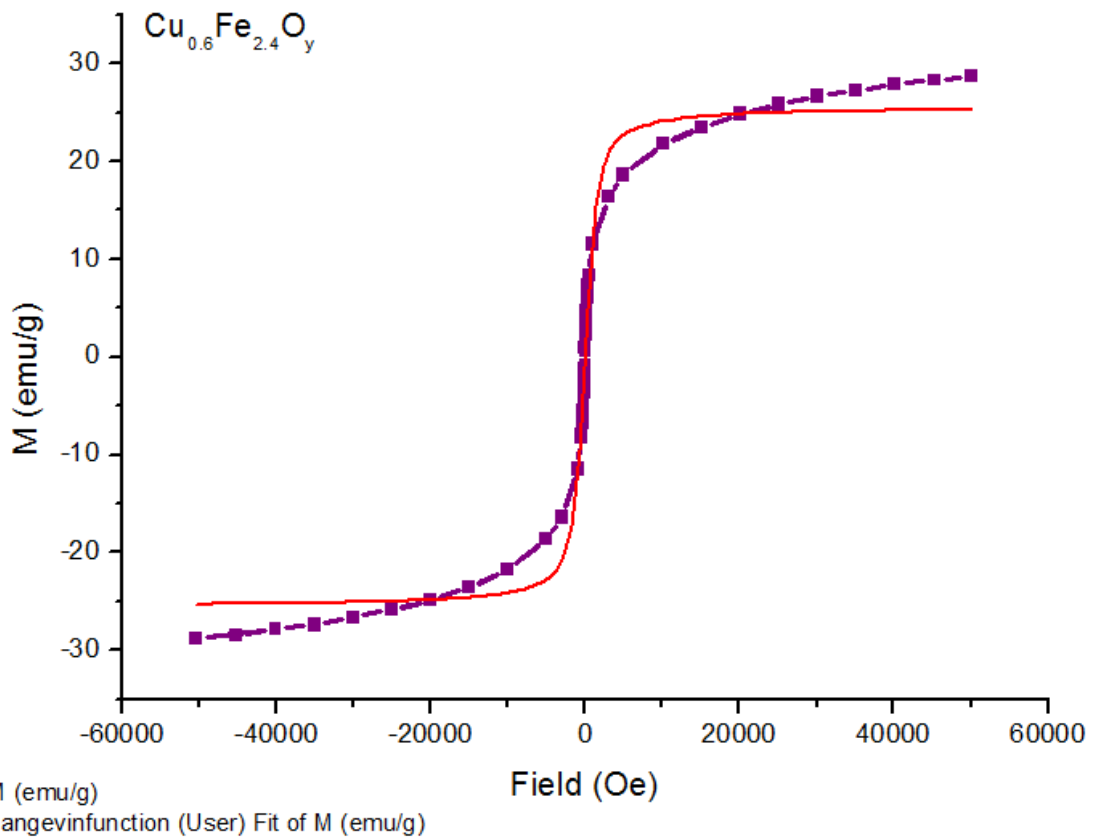
5.12. Magnetic measurements
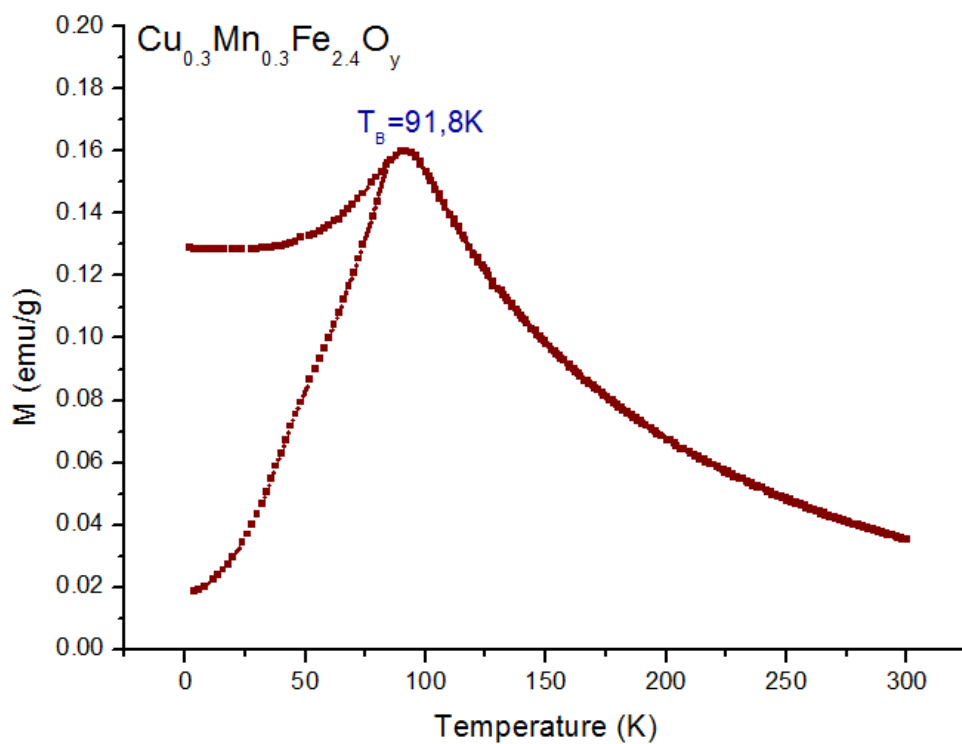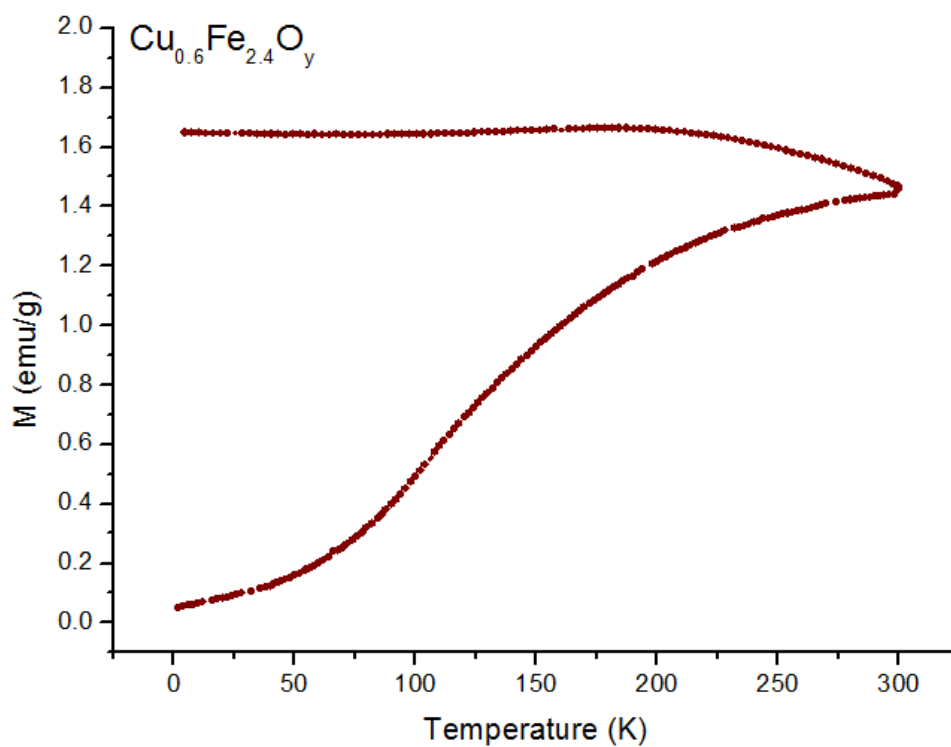
Figure 5-23. ZFC and FC magnetizations of $Cu_{0.6}Fe_{2.4}O_y$, $Cu_{0.3}Mn_{0.3}Fe_{2.4}O_y$ and $Mn_{0.6}Fe_{2.4}O_y$ samples, measured with a magnetic field of H=50 Oe

Zero-field-cooled (ZFC) magnetizations were measured by cooling the $Cu_{0.6}Fe_{2.4}O_y$, $Cu_{0.3}Mn_{0.3}Fe_{2.4}O_y$ and $Mn_{0.6}Fe_{2.4}O_y$ samples in a zero magnetic field and then increasing the temperature in a static field, while field-cooled (FC) curves were obtained by cooling the samples in the same static field. Figure 5-23 shows the temperature dependence of ZFC and FC magnetizations, measured with applied field of 50 Oe. The magnetic properties of the $Mn_{0.6}Fe_{2.4}O_y$ and $Cu_{0.3}Mn_{0.3}Fe_{2.4}O_y$ samples are in a good agreement with previously discussed Mössbauer measurements and characteristic for superparamagnetic particles with blocking temperatures below room temperature. The blocking temperature (T_B), which can be estimated as the position of ZFC maximum, is a threshold temperature between the blocked and the superparamagnetic state whose characterization is closely dependent on the time scale of the measurement method used[150]. In fact, for a particle system with a certain size, T_B is the temperature at which the relaxation time (τ) equals the attempt time (τ_m). The ZFC magnetization shows its maximum at ~82 K for $Mn_{0.6}Fe_{2.4}O_y$ sample and at ~92 K for the $Cu_{0.3}Mn_{0.3}Fe_{2.4}O_y$ sample. However, for the copper rich ferrite ($Cu_{0.6}Fe_{2.4}O_y$) we have not yet reached the blocking temperature which is related to a larger particle size of the sample. This is in a good correlation with the XRD results discussed above (Paragraph 5.2).
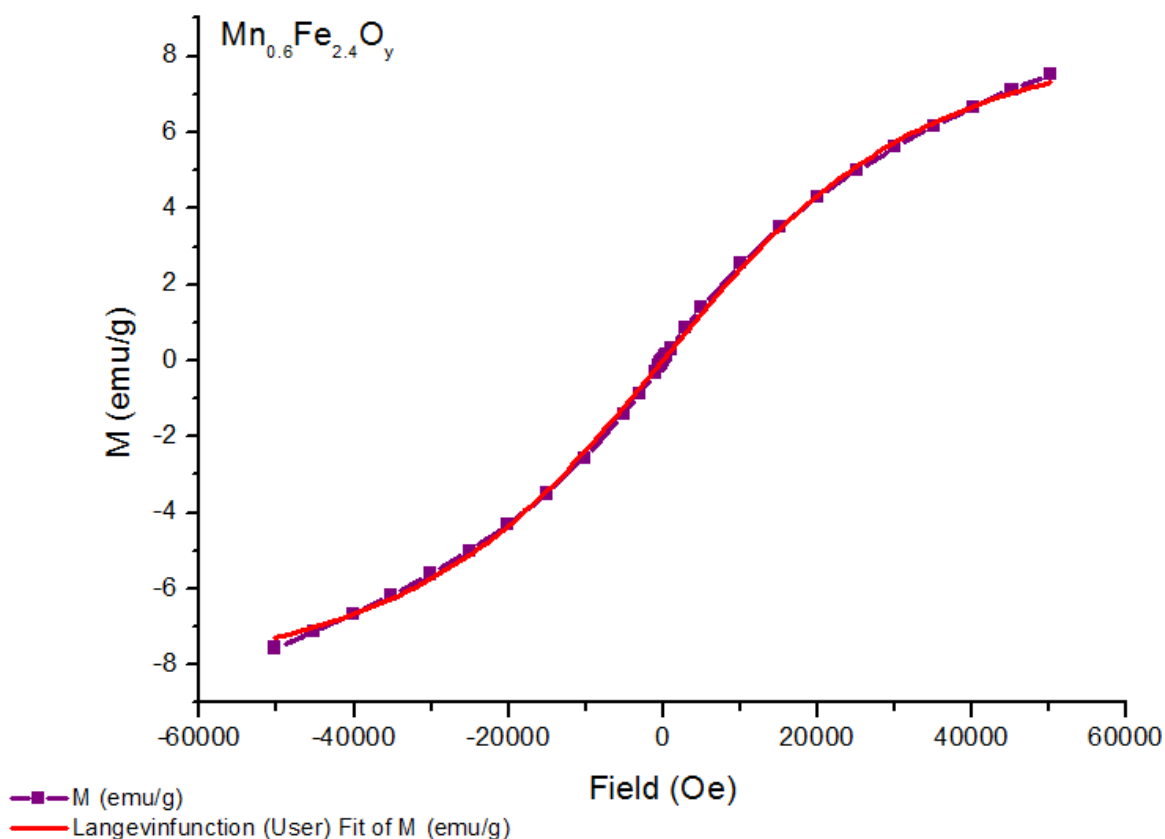
Cu$_{0.6}$Fe$_{2.4}$O$_y$

- M (emu/g)
- Langevinfunction (User) Fit of M (emu/g)

Cu$_{0.3}$Mn$_{0.3}$Fe$_{2.4}$O$_y$

- M (emu/g)
- Tanh (User) Fit of M (emu/g)

Figure 5-24. Hysteresis curves of $Cu_{0.6}Fe_{2.4}O_y$, $Cu_{0.3}Mn_{0.3}Fe_{2.4}O_y$ and $Mn_{0.6}Fe_{2.4}O_y$ samples, collected at T=300 K

The magnetic properties of $Cu_{0.6-x}Mn_xFe_{2.4}O_y$ spinel ferrites have been examined by isothermal magnetization hysteresis curve measurements at 300 K (Figure 5-24).The hysteresis curves of the $Cu_{0.3}Mn_{0.3}Fe_{2.4}O_y$ and $Mn_{0.6}Fe_{2.4}O_y$ samples do not reach complete saturation even at 60 kOe. This is often observed in nanosized materials and can be a result of the spin disordered surface layer which requires a larger field to be saturated together with the concurrent effect of the small mean size of nanoparticles with not too high anisotropy which are still fast relaxing even at 60 kOe[151].On the contrary, for the $Cu_{0.6}Fe_{2.4}O_y$ sample all particles are already blocked and almost completely oriented with a field of ~ 50 kOe. Table 5-6gives the magnetic susceptibility values estimated for three ferrospinels ($Cu_{0.6-x}Mn_xFe_{2.4}O_y$) using the Langevin function. For $Cu_{0.3}Mn_{0.3}Fe_{2.4}O_y$ and $Mn_{0.6}Fe_{2.4}O_y$ samples CHI equals to $5.0 \cdot 10^{-4}$ and $2.5 \cdot 10^{-4}$ m^3kg^{-1} respectively. These values are about four orders of magnitude higher than those typically observed for paramagnetic materials (because magnetic moments of the grains are much larger than magnetic moments of the individual atoms), indicating that Mn-containing materials are in a superparamagnetic state compare to only Cu-ferrospinel. Such difference can be explained by partial substitution of Fe^{3+} cations with Mn^{2+}[106] caused a disorder in the cation distribution between octahedral and

tetrahedral sites which influence such fundamental magnetic properties as saturation magnetization, exchange couplings, and ferromagnetic ordering temperatures[152].

Table 5-6. Magnetic measurements results obtained on $Cu_{0.6-x}Mn_xFe_{2.4}O_y$ ferrites

Sample	A Langevin		B Langevin	Temperature	Mu	n		CHI
	emu/g	A m² kg⁻¹	A m² kg⁻¹	K	A m²	kg⁻¹	m³kg⁻¹	emu/g
$Cu_{0.6}Fe_{2.4}O_y$	25,56	25,56	1,79E-03	300	5,90E+28	4,33E-28	1,53E-02	1,21E+00
$Cu_{0.3}Mn_{0.3}Fe_{2.4}O_y$	13,6	13,6	1,11E-04	300	3,66E+27	3,71E-27	5,04E-04	4,01E-02
$Mn_{0.6}Fe_{2.4}O_y$	9,952	9,952	7,45E-05	300	2,45E+27	4,05E-27	2,47E-04	1,97E-02

5.13. Temperature programmed reduction (TPR) study

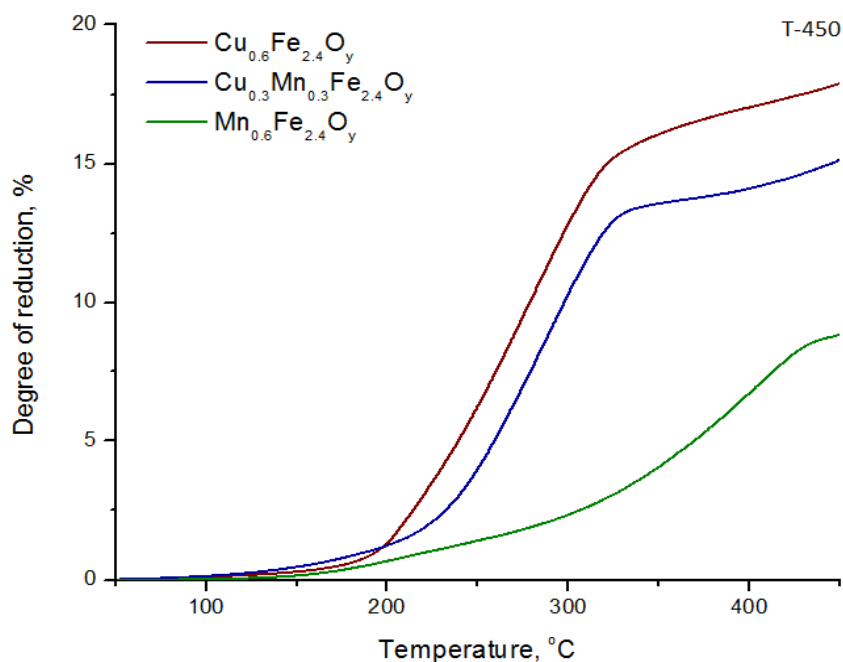**Figure 5-25. Degree of reduction (α) vs temperature (T) for $Cu_{0.6-x}Mn_xFe_{2.4}O_y$ ferrites**

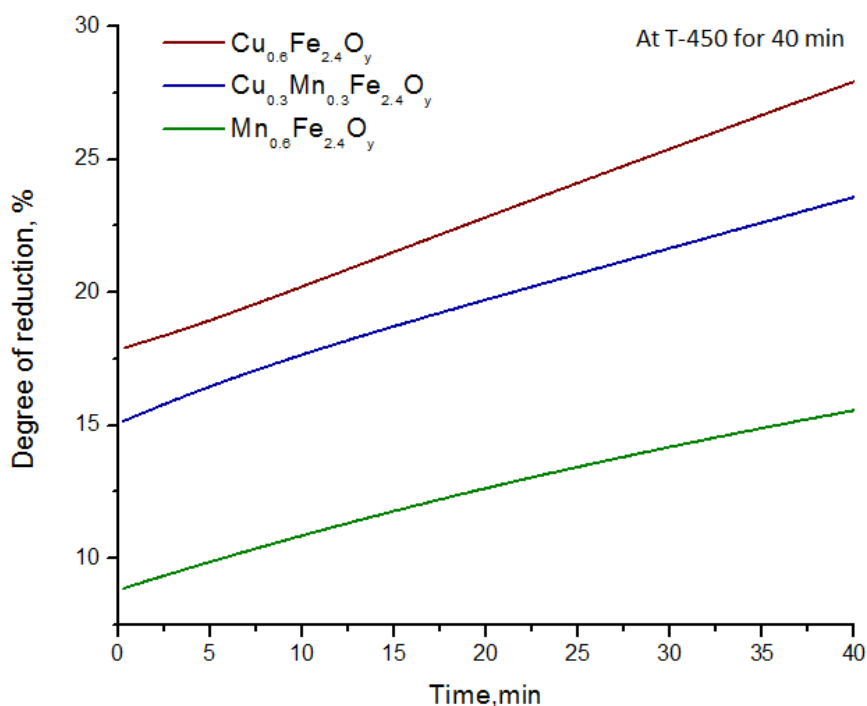**Figure 5-26. Degree of reduction (α) vs time (t) for $Cu_{0.6-x}Mn_xFe_{2.4}O_y$ ferrites**

Figure 5-25 shows *α-versus-T* reduction curves of $Cu_{0.6-x}Mn_XFe_{2.4}O_y$ samples. The shape of this curve can reveal information on the reduction model of the solid, as discussed in details in PART I of the discussion (Paragraph 4.4). Increasing the temperature of the reduction markedly increased the reduction rate of all oxides regardless of the nature of incorporated metal M and this in turn can be justified by Arrhenius equation (exponential relation between K and T). However, looking at the plotted results for Cu-incorporated ferrites ($Cu_{0.6}Fe_{2.4}O_y$-red and $Cu_{0.3}Mn_{0.3}Fe_{2.4}O_y$-blue) this produces an S-shaped (sigmoidal) curve which primarily was assigned as a "nucleation and autocatalytic reduction" model, when reduced metal formed in the early stages of reduction ($Cu^{2+} \rightarrow Cu^{0*}$) catalyzes the reduction by H_2 activation ($H_2 \rightarrow H+H$) which in turn facilitates the reduction of the whole system (details are in the Paragraph 4.4). In contrast to this, the plotted curve for $Mn_{0.6}Fe_{2.4}O_y$ ferrite (Figure 5-25-green) is elongated and resembles more to an "egg-shell" reduction model, which is characterized by a total coverage of the solid oxide particle with a thin layer of newly formed product. Indeed, it appears that $Mn_{0.6}Fe_{2.4}O_y$ sample reduces by a spontaneous nucleation over the entire surface immediately on contact with hydrogen that leads to the formation of the hardly reducible layer of Mn_xFe_yO oxide (like an egg-shell). This elucidates the elongated shape of the reduction curve, since the initially formed compact

Mn_xFe_yO layer may aggravate H_2 diffusion into the bulk (Figure 5-26) leading to starvation and decrease its reduction rate.

To summarize, TPR results indicate the reduction path of the $Cu_{0.6}Fe_{2.4}O_y$ and $Cu_{0.3}Mn_{0.3}Fe_{2.4}O_y$ materials (Figure 5-25) goes through the formation of metallic copper (Cu^0) which generates a high concentration of active hydrogen on the surface and promotes the reduction. In the case of $Mn_{0.6}Fe_{2.4}O_y$ nucleation occurs over entire surface immediately on the contact with hydrogen causing the formation of hardly reducible layer (in form of Mn_xFe_yO) and at this point the reduction is controlled by the H_2-diffusion into the bulk.

Table 5-7 shows the integrated values of consumed H_2 and O_2 during TPR_1/TPO/TPR_2 experiments at 450^oC. Since spinel ferrites may be used as a material for `pure hydrogen` production, the combination of two techniques can provide useful information in the study of reactivity, redox behavior and cycling stability of the resulted ferrospinels. The important conclusion can be drawn: $Cu_{0.6-x}Mn_xFe_{2.4}O_y$ ferrospinels can be reduced (TPR_1), re-oxidized (TPO) and then re-reduced for the second time (TPR_2) with no significant loss in the activity (table, $TPR_1/TPR_2 \sim 1$). However, Cu-containing samples have shown a higher reduction extent in comparison to $Mn_{0.6}Fe_{2.4}O_y$ (Figure 5-26). The main reason for a such behavior can be an accumulation of Mn_xFe_yO phase in the catalyst, which has a high thermodynamic stability and as a consequence its scarce attitude towards the reduction to its metallic component. This result also has been confirmed by in-situ DRIFTS, ex-situ XRD studies and reactivity experiments with ethanol (discussed below).

Table 5-7. Integrated values of consumed H_2/O_2 during TPR/O experiments

SAMPLE	Temperature, ^oC	TPR1, cm^3/g	TPO, cm^3/g	TPR2, cm^3/g	TPR1/TPR2	Surface area, m^2/g
$Cu_{0.6}Fe_{2.4}O_y$	450	115	56	108	1.06	72
$Cu_{0.3}Mn_{0.3}Fe_{2.4}O_y$	450	98	40	91	1.07	131
$Mn_{0.6}Fe_{2.4}O_y$	450	66	31	58	1.14	157

5.14. Surface characterization: in-situ DRIFTS experiments

Figure 5-27 shows DRIFT spectra of $Cu_{0.6-x}Mn_xFe_{2.4}O_y$ ferrites. The spectrum on the bottom corresponds to the adsorption of ethanol at 30°C. According to the literature, ethanol adsorbs on the surface mainly as an ethoxide, formed from the scission of the O-H bond[95–99]. Ethoxy bands (dissociative adsorption) over $Cu_{0.6}Fe_{2.4}O_y$ sample can be observed at 1062 and 1105 cm^{-1} for the C-O/C-C stretching modes together with the bands of the undissociated ethanol (at 1383 cm^{-1} and 1279 cm^{-1} for $CH_3\delta$ and $OH\delta$, respectively).[94,132] The complex absorption in the 2800-2400 cm^{-1} region is due a Fermi resonance of the overtone of the $OH\delta$ vibration mode with the CH- stretching modes at 2970, 2926, and 2859 cm^{-1} (CH_3(as), CH_2(as) and CH_3(s) modes of the ethoxide species).[97,94] The sharp band at 3683 cm^{-1} together with a shoulder at 3636 cm^{-1} is assigned to the –OH stretching vibration of chemisorbed undissociated ethanol over surface Lewis acid sites (M^{n+}).[133–135]

Looking at the adsorption of ethanol at 30°C for $Cu_{0.3}Mn_{0.3}Fe_{2.4}O_y$[(B)] and $Mn_{0.6}Fe_{2.4}O_y$[(C)] ferrites, similar species are formed, with a slightly shifted position. Accordingly, the ethoxy bands observed at 1064/1107[(B)] and 1064/1104[(C)] cm^{-1} for the C-O/C-C stretching modes together with the bands of the undissociated ethanol (at 1381[(B)] and 1384/1272[(C)] cm^{-1} for $CH_3\delta/OH\delta$).[94,132] The CH- stretching modes detected at 2972/2927/2864[(B)] and 2973/2930/2871[(C)] cm^{-1}, were assigned as CH_3(as), CH_2(as) and CH_3(s) modes of the ethoxide species.[97,94] The sharp band centered at 3685[(B)] and 3681[(C)] cm^{-1} is assigned to the –OH stretching of chemisorbed undissociated ethanol, however in contrast to the $Cu_{0.6}Fe_{2.4}O_y$ sample, the shoulder at lower frequency is not well resolved (for $Cu_{0.3}Mn_{0.3}Fe_{2.4}O_y$) due to the broadening of the main peak with a complete disappearance for $Mn_{0.6}Fe_{2.4}O_y$ ferrite (the effect of Mn-incorporation)[106].
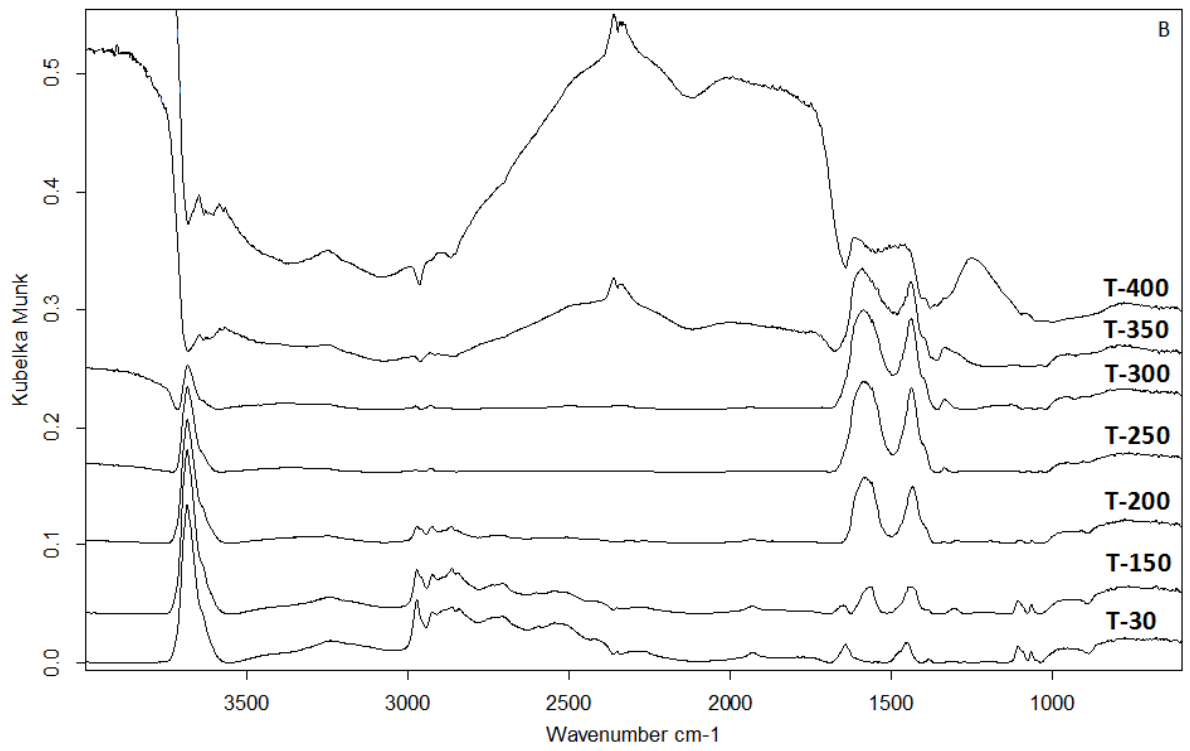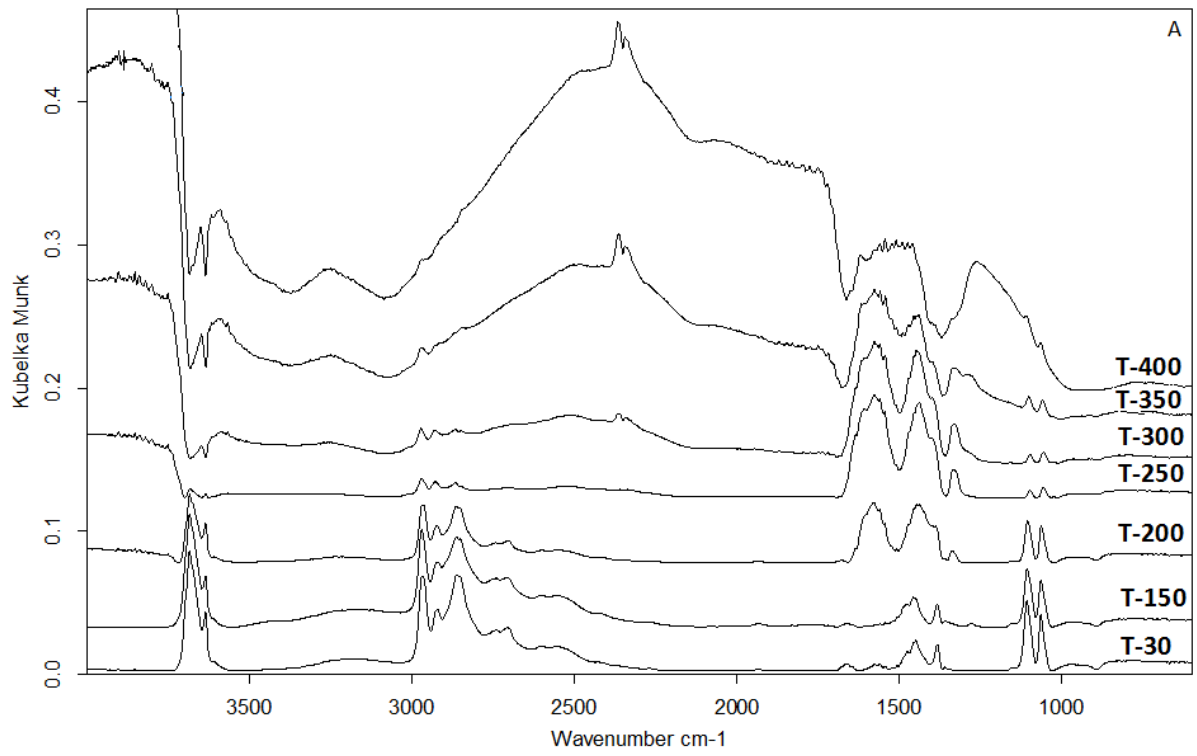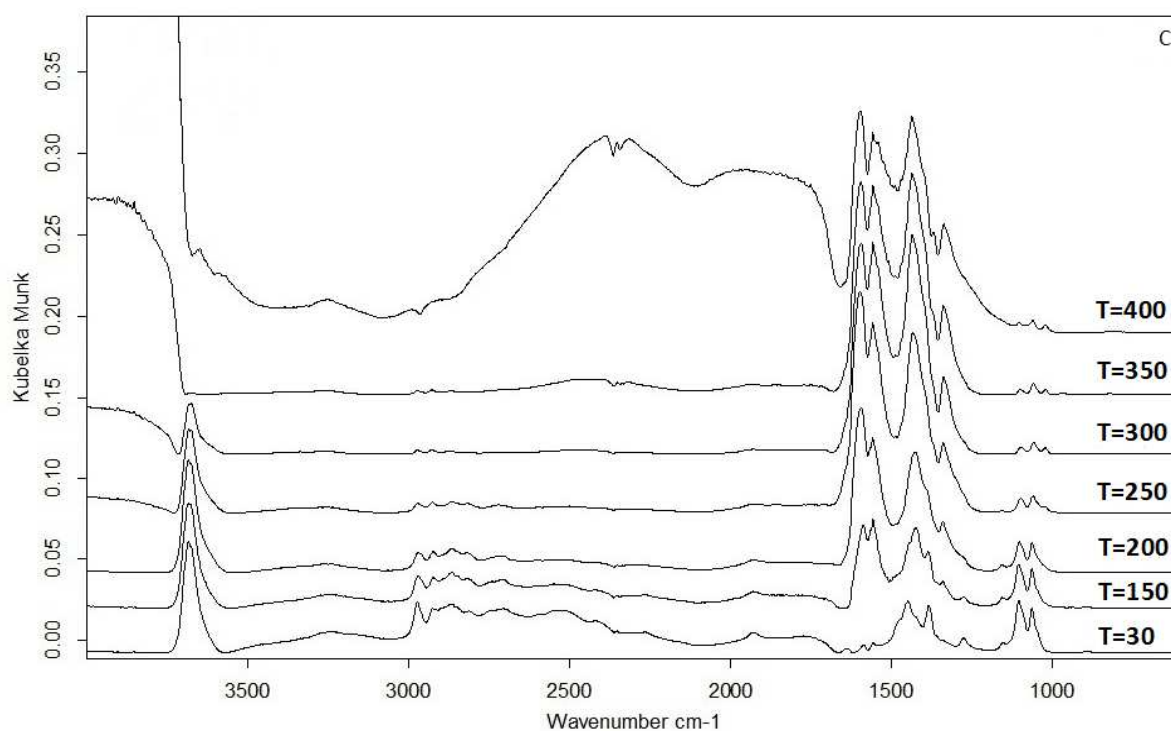
Figure 5-27. DRIFTS spectra: (A)-$Cu_{0.6}Fe_{2.4}O_y$, (B)-$Cu_{0.3}Mn_{0.3}Fe_{2.4}O_y$ and (C)-$Mn_{0.6}Fe_{2.4}O_y$

Some remarkable differences between the DRIFTS spectra of Cu-, Cu-Mn- and Mn-modified ferrites are observed with increasing the temperature from 30-400°C, which is related to the surface chemistry of each compound[94]. Acetate bands (T-200°C) over $Cu_{0.6}Fe_{2.4}O_y^{(A)}$ and $Cu_{0.3}Mn_{0.3}Fe_{2.4}O_y^{(B)}$ (Figure 5-27 - A, B) samples appear at $1333/1440/1577^{(A)}$ and $1341/1437/1582^{(B)}cm^{-1}$ (for the $CH_3\delta$, OCOv(s), and OCOv(as) vibrations, respectively). The broadening of the band at $1577^{(A)}/1582^{(B)}$ cm^{-1} and the apparent complexity of both main components suggest that carbonate species, responsible for bands in the same region, should also form [136]. These species could further produce CO_2, which is detected as the doublet at the 2363-2333 cm^{-1} region and corresponds to adsorbed and/or gaseous CO_2 rotation vibration P and R bands[137]. Moreover, a new band at $1262^{(A)}$ and $1249^{(B)}$ cm^{-1} is observed (for Cu-containing samples only) at higher temperature (T-400°C) and has been attributed to aldehyde adsorbed in η^2 configuration[94]. The DRIFT spectra obtained over the $Mn_{0.6}Fe_{2.4}O_y$ sample (Figure 5-27, C), also exhibited the bands for acetate species, formed by the reaction of ethoxy species with surface oxygen (1598, 1555, 1433 and 1334 cm^{-1}) [98,138]. When the temperature was increased (up to 400°C) the intensity of the bands corresponding to ethoxy species was reduced, whereas the bands associated with acetate species were strongly bounded to the surface and remained practically unchanged.

However, the main difference between the spectra of $Mn_{0.6}Fe_{2.4}O_y$ and other Cu- and Cu-Mn-modified ferrites spectra lies in the absence of the bands associated with carbonate species, as well as the band of the adsorbed linear CO_2 was not observed. Thus, the results may indicate that Cu- and Cu-Mn-modified ferrite systems were more "reactive" than the Mn-modified ferrite sample. This is also followed by the presence of a broad absorbed feature in the 3000-1800 cm^{-1} region, which is attributed to the electronic absorption of the partially reduced sample [94,139].

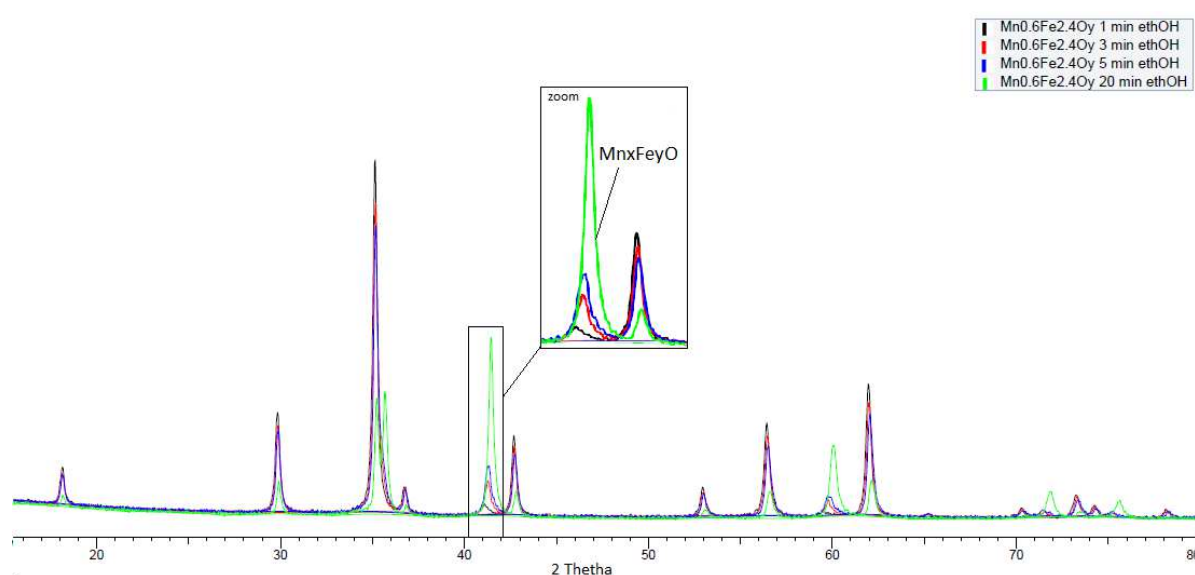## 5.15. Ex-situ XRD study of the reduced samples

Figure 5-28. Stepwise reduction of $Mn_{0.6}Fe_{2.4}O_y$ ferrite with ethanol

Table 5-8. Rietveld refinement of $Mn_{0.6}Fe_{2.4}O_y$ ferrite after stepwise reduction with ethanol

$Mn_{0.6}Fe_{2.4}O_y$

| Reduction time, min	Phase composition	Degree of reduction, %
1	Spinel 95.38% Mn_xFe_yO 7.55%	1.2
3	Spinel 87.47% Mn_xFe_yO 12.53%	3
5	Spinel 80.53%	5

	Mn_xFe_yO 19.47%	
20	Spinel 35.50%	16
	Mn_xFe_yO 64.50%	

The evolution of a phase composition of the $Mn_{0.6}Fe_{2.4}O_y$ sample was studied by mean of XRD using ex-situ approach, which is the most suitable one for a deep understanding of the results obtained on the laboratory-scale plant. Figure 5-28 shows XRD patterns obtained after 1, 3, 5 and 20 min of ethanol exposure over $Mn_{0.6}Fe_{2.4}O_y$ ferrospinel. Table 5-8 summarizes obtained results using Rietveld refinement. The data clearly indicate that after feeding ethanol for 1 min the formation of a new Mn_xFe_yO phase (app. 7%$_w$) was observed. With increasing the reduction time from 1 to 20 min the spinel relative ratio continued decreasing whereas that of the Mn_xFe_yO increased without the appearance of other phases. This apparently shows that the reduction of the $Mn_{0.6}Fe_{2.4}O_y$ goes through the formation of Mn_xFe_yO phase, which is an important proof of the previously discussed TPR results where we proposed the reduction mechanism which goes through the formation of hardly reducible layer of Mn_xFe_yO oxide.

A further investigation of the Cu- and Cu/Mn-incorporated ferrites are reported in Table 5-9. Rietveld refinement of the XRD patterns has been done for the samples $Cu_{0.6}Fe_{2.4}O_y$, $Cu_{0.3}Mn_{0.3}Fe_{2.4}O_y$ and $Mn_{0.6}Fe_{2.4}O_y$. It worth noting, that an addition of Cu^{2+} ions strongly affects its redox properties (detailed discussion in Paragraph 5.4) which in turn determines the reduction mechanism and, as a consequence, the phases which are formed during the reduction step. According to the previously discussed TPR results and ex-situ XRD studies of the TYPE I ferrospinels, the reduction of Cu-containing samples goes through the formation of metallic Cu^0 with further autocatalytic reduction evolution of newly reformed Fe-enriched spinel (with generic formula - $M_{0.6-x}Fe_{2.4+x}O_y$). From the obtained results, it is clear that the reduction of $Cu_{0.6}Fe_{2.4}O_y$ and $Cu_{0.3}Mn_{0.3}Fe_{2.4}O_y$ samples does not go through the formation of Mn_xFe_yO oxide, which acts as a shielding layer and prevents a deep reduction of the following ferrite to its metallic component. Phases detected after 20 min of ethanol exposure over $Cu_{0.6}Fe_{2.4}O_y$ and $Cu_{0.3}Mn_{0.3}Fe_{2.4}O_y$ were identified as follows: spinel- 4.84 %$_w$,

Cu^0-14.7 %$_w$, Fe-0.7 %$_w$, Fe_3C-52.0 %$_w$ and Fe_5C_2-27.76 %$_w$ and spinel-48.40 %$_w$, Fe_5C_2-44.59 %$_w$, Fe_3C-7.01%$_w$, respectively. The absence of Mn_xFe_yO in these two samples makes it possible to clarify the main difference in the reduction paths of $Cu_{0.6-x}Mn_xFe_{2.4}O_y$ ferrites. Since metallic Cu^0 was one of the formed phases in $Cu_{0.6}Fe_{2.4}O_y$; we can suggest that its reduction goes through the formation of metallic copper (Cu^0) which generates a high concentration of active sites on the surface and promotes a further deep reduction to iron carbides: Fe_3C and Fe_2C_5. Moreover, despite that we could not quantify Cu^0 phase in the case of $Cu_{0.3}Mn_{0.3}Fe_{2.4}O_y$ (it should be recall that X-ray diffraction is not extremely sensitive and app. 5% of a new phase could easily not be detected, since Cu content is twice lower), the presence of iron carbides enables us to assume that this sample follows the same reduction path as only Cu-containing one or has a mixed character, since a small amount of Fe^{2+} and Fe^{3+} (as a component of the $Mn_x(Fe^{2+},Fe^{3+})_yO_{x+y}$ phase) nevertheless is present in the sample and was detected with a help of Mössbauer spectroscopy (see Paragraph 5.16). However, in the case of $Mn_{0.6}Fe_{2.4}O_y$ the nucleation occurs over entire surface immediately on the contact with ethanol causing the formation of hardly reducible layer (in form of Mn_xFe_yO) and at this point the reduction is controlled by the ethanol-diffusion into the bulk, since Mn_xFe_yO acts as a core-catalyst of the newly reformed material.

Moreover, in Table 5-9 are listed values of the reduction degree (after 20 min of reduction time) for the $Cu_{0.6-x}Mn_xFe_{2.4}O_y$ ferrites calculated on the basis of Rietveld refinement data. Even though the highest surface area was shown by $Mn_{0.6}Fe_{2.4}O_4$ catalyst (SSA values of the fresh samples reported in Paragraph 5.2), and it declined with an increase of Cu-content, the samples which contain copper cations ($Cu_{0.6}Fe_{2.4}O_y$ and $Cu_{0.3}Mn_{0.3}Fe_{2.4}O_y$) reached higher reduction extent (about 98 and 59%, respectively) in comparison to only Mn-modified ferrospinel (with just 16%). The similar trends were obtained from elaborated TPR results. This suggests that the difference in the reducibility of the resulted M-modified ferrospinels is related to the nature of the incorporated M cation and its intrinsic reactivity.
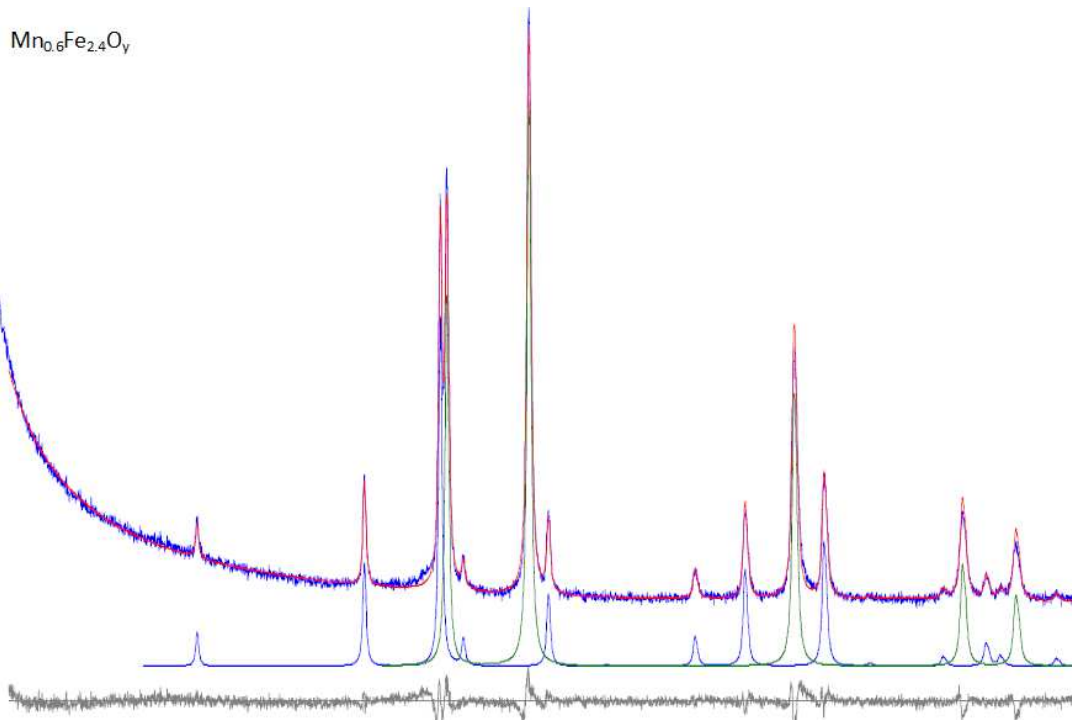
$Cu_{0.6}Fe_{2.4}O_y$

$Cu_{0.3}Mn_{0.3}Fe_{2.4}O_y$
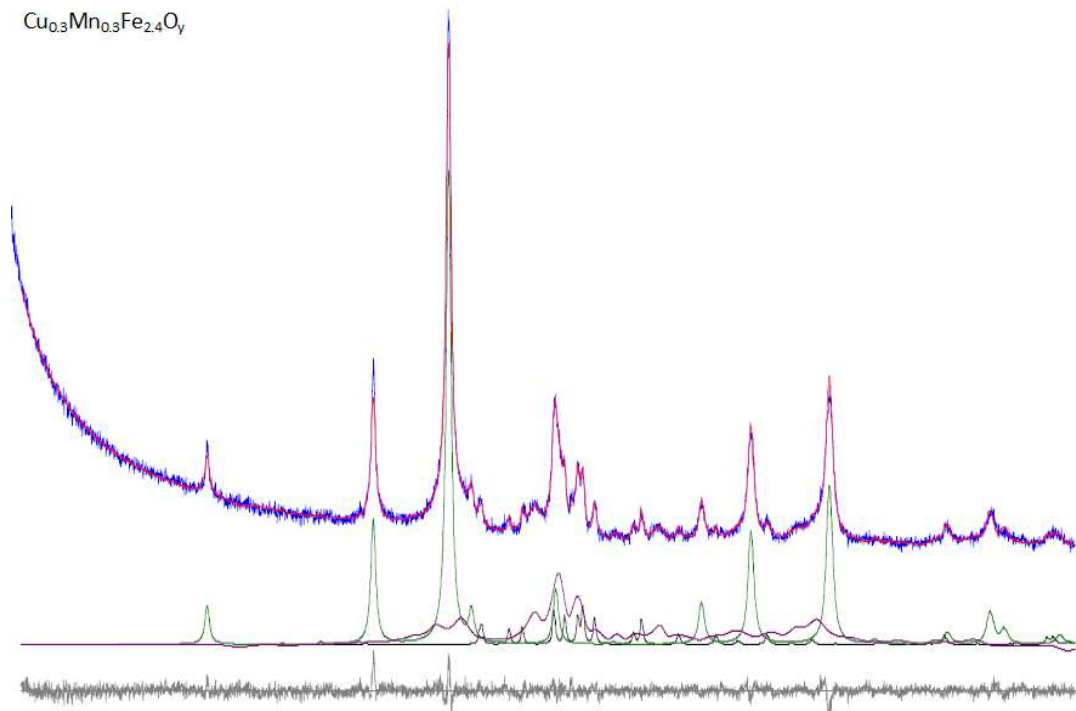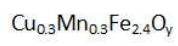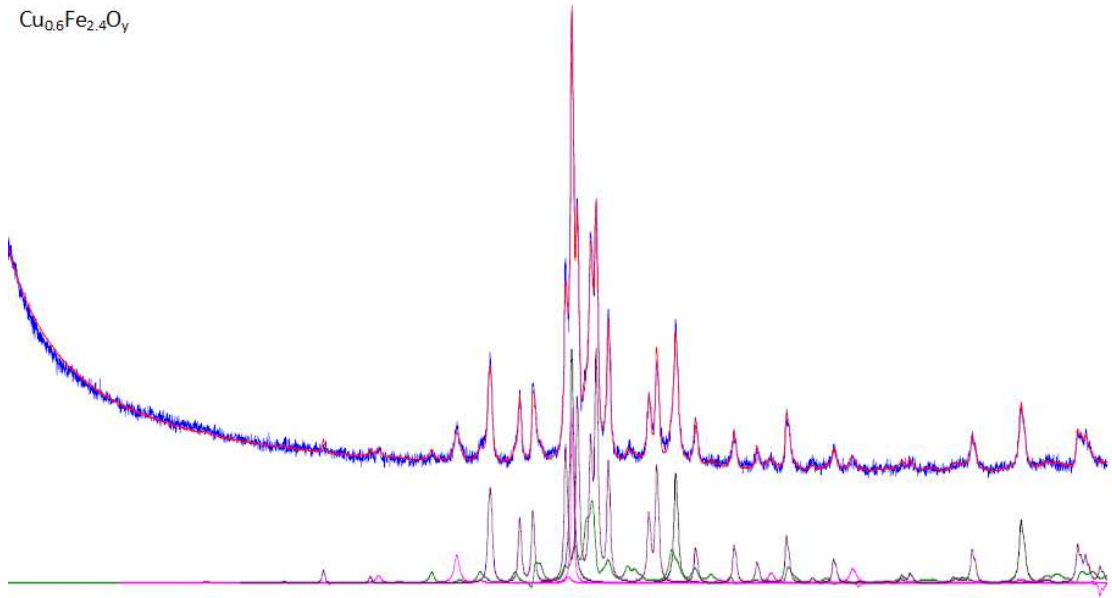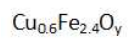
$Mn_{0.6}Fe_{2.4}O_y$

Figure 5-29. Rietveld refinement of XRD patterns taken after 20 min of reduction with ethanol over $Cu_{0.6}Fe_{2.4}O_y$, $Cu_{0.3}Mn_{0.3}Fe_{2.4}O_y$ and $Mn_{0.6}Fe_{2.4}O_y$ ferrites

Table 5-9. Rietveld refinement data of $Cu_{0.6-x}Mn_xFe_{2.4}O_y$ ferrites after 20 min reduction with ethanol

SAMPLE	Degree of reduction, %	Formed phases during ethanol reduction for 20 min, %$_w$
$Mn_{0.6}Fe_{2.4}O_y$	16	SPINEL – 35.5
		Mn_xFe_yO – 64.5
$Cu_{0.3}Mn_{0.3}Fe_{2.4}O_y$	59	SPINEL – 48.4
		Fe_5C_2 – 44.6
		Fe_3C – 7.0
$Cu_{0.6}Fe_{2.4}O_y$	98	SPINEL – 4.8
		Cu - 14.7
		Fe – 0.7
		Fe_3C - 52.0
		Fe_5C_2 - 27.8

5.16. Mössbauer study of the reduced samples

$Cu_{0.6}Fe_{2.4}O_y$ 20 min ethOH
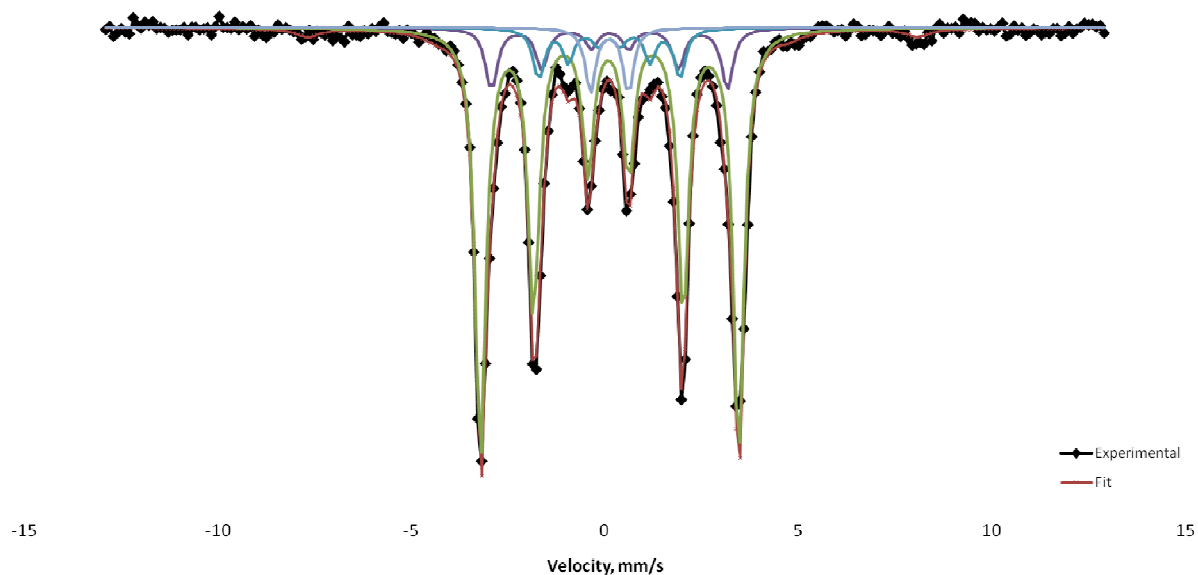
$Cu_{0.3}Mn_{0.3}Fe_{2.4}O_y$ 20 min ethOH

Mn$_{0.6}$Fe$_{2.4}$O$_y$ 20 min ethOH
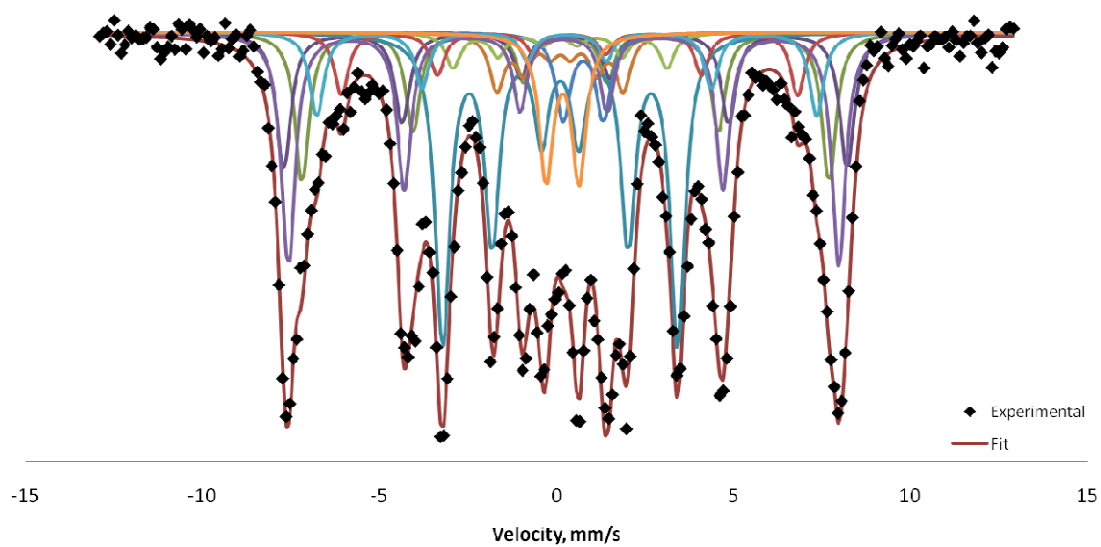
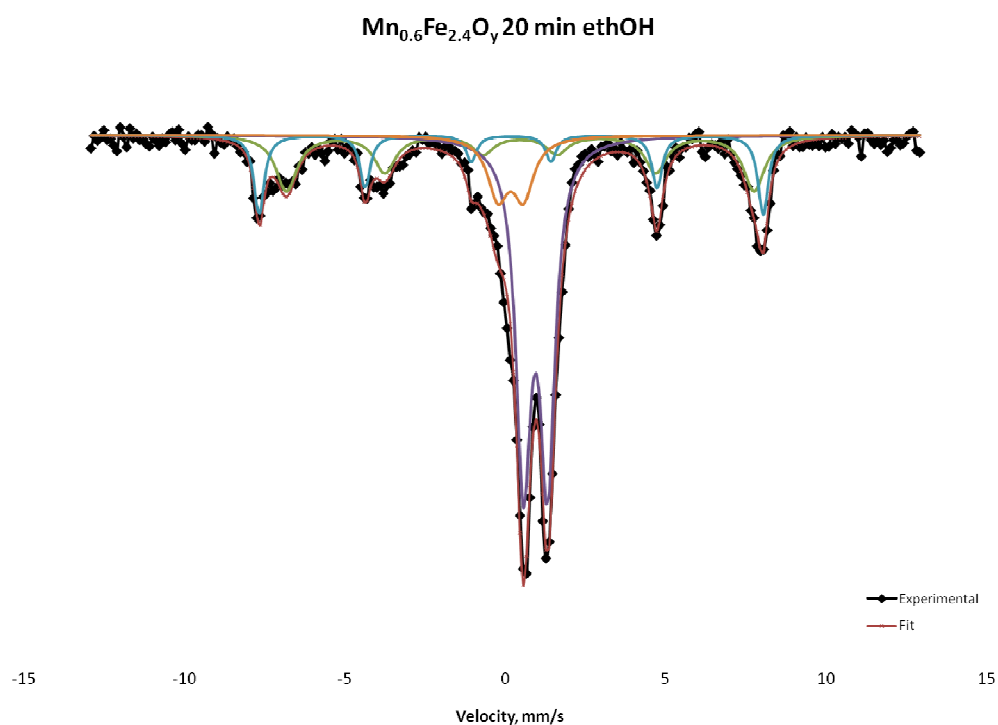**Figure 5-30. Mössbauer spectra of Cu$_{0.6-x}$Mn$_x$Fe$_{2.4}$O$_y$ ferrites taken after 20 min of ethanol reduction**

Mössbauer spectra of the Cu$_{0.6-x}$Mn$_x$Fe$_{2.4}$O$_y$ ferrites after reduction with ethanol at 450°C (20 min) were taken in order to proof the differences in the phase composition discussed previously (Paragraph 5.15). Experimental data and Lorentzian functions, used for the fitting of the spectra for three examined samples, are reported in the following pages.

Figure 5-30 shows Mössbauer spectra of Cu$_{0.6-x}$Mn$_x$Fe$_{2.4}$O$_y$ samples. In the Table 5-10 are listed hyperfine parameters derived from the fitting of the corresponding experimental results. The spectrum of Cu$_{0.6}$Fe$_{2.4}$O$_y$ ferrite was fitted with 4 sextets. The first sextet is characterized by an δ equal to 0.3 mm/s and an Internal magnetic field (H) of 48.7 T with a contribution of only 3%$_{at}$ to the total spectral area; and it was assigned to T$_d$ coordinated Fe^{3+} in the remained re-formed spinel (with generic formula of Cu$_{0.6-x}$Fe$_{2.4+x}$O$_y$). The other 3 sextets correspond to the two iron carbides (Fe$_3$C-cementite and Fe$_5$C$_2$-Hagg carbide), formed during the reduction process. The best fit of the experimental spectrum was obtained with two sextets for Fe$_5$C$_2$, one sextet for Fe$_3$C and the one shared sextet for (Fe$_5$C$_2$+Fe$_3$C). The obtained parameters of the corresponding sextets are in a good agreement with reported literature [122–124]. The large contribution of the iron carbides phase

($Fe_3C + Fe_5C_2$ ~ 97%), as was previously detected by XRD, once again reaffirms that a deep reduction of the M-ferrites (Co, Cu, Ni and Fe)[126,101,129] leads to the formation of Fe_xC_y phase.

The experimental spectrum of $Cu_{0.3}Mn_{0.3}Fe_{2.4}O_y$ with its best fits is shown in Figure 5-30. Two doublets and eight sextets are used to fit the room temperature Mössbauer spectra of the sample. Spinel component (55%$_{at}$) with generic formula: $Cu_{0.3-x}Mn_{0.3-z}Fe_{2.4+x+z}O_y$ composed of 5 sextets; and each one of these sextets correspond to a given environment for the ferric cations in the ferrite compound referred to a different Fe^{3+} in the structure, in accordance with Sawatzky et al[153,154]. Another 3 sextets are similar to those discussed above and were attributed to the existence of a relatively high amount of Fe_xC_y phase ($Fe_3C + Fe_5C_2$ ~ 35%$_{at}$). Remaining two doublets (10%$_{at}$) which represent ferric (Fe^{3+}) and ferrous (Fe^{2+}) iron oxides characterized by an δ: Fe^{2+}- 0.85 mm/s; Fe^{3+}- 0.26 mm/s and a Δ: Fe^{2+}- 1.13 mm/s; Fe^{3+}- 0.92 mm/s and were attributed to the presence of the Mn_xFe_yO solid solution (a small amount of Fe^{3+} in FeO was also seen by Johnson[125]). Eventually, obtained results are indicating an incomplete reduction of the $Cu_{0.3}Mn_{0.3}Fe_{2.4}O_y$ ferrite which assumed to be a direct result of Mn-incorporation (leading to the formation scarcely reducible phase - Mn_xFe_yO).

The last spectrum corresponds to the $Mn_{0.6}Fe_{2.4}O_y$ sample; it reveals information on the reduction path and contribution of Mn-cations to the whole reduction process. The spectrum was fitted with 2 sextets and 2 doublets. The two doublets (60%$_{at}$) attributed to the same ferric (Fe^{3+}) and ferrous (Fe^{2+}) iron oxides as detected in $Cu_{0.3}Mn_{0.3}Fe_{2.4}O_y$ sample (δ: Fe^{2+}- 1.02 mm/s; Fe^{3+}- 0.27 mm/s and a Δ: Fe^{2+}- 0.75 mm/s; Fe^{3+}- 0.79 mm/s. Remaining two sextets are used to fit Fe^{3+} ions in T_d (δ-0.27 mm/s and H-48.5 T) and O_h (δ-0.54 mm/s and H-45.0 T) sites of the reformed spinel phase. From the obtained results, it is clear that the reduction of $Mn_{0.6}Fe_{2.4}O_y$ samples follows a different reduction path which goes through the formation of only two thermodynamically stable phases: $Mn_{0.6-x}Fe_{2.4+x}O_4$ and Mn_xFe_yO. This results support the information obtained from TPR, in-situ DRIFT and ex-situ XRD studies (discussed above).

Table 5-10. Hyperfine parameters derived from the fitting of the Mössbauer spectra

SAMPLE	δ (mm/s)	Δ (mm/s)	H (T)	Rel. Int. (%)	Phase name
$Cu_{0.6}Fe_{2.4}O_y$ after 20 min reduction	0.30	0.00	$48.7_{(Td)}$	3	spinel
	0.21	0.00	$11.2_{(I)}$	9	Fe_5C_2
	0.22	0.00	$18.8_{(II)}$	12	Fe_5C_2
	0.20	0.00	$20.6_{(III+I)}$	76	$Fe_5C_2 + Fe_3C$
$Cu_{0.3}Mn_{0.3}Fe_{2.4}O_y$ after 20 min reduction	0.34		49.2	12	spinel
	0.29		48.0	19	
	0.35		46.0	12	
	0.37		43.6	7	
	0.45		39.8	5	
	0.20		$20.5_{(III+I)}$	27	$Fe_3C + Fe_5C_2$
	0.19		$18.6_{(II)}$	3	Fe_5C_2
	0.19		$11.0_{(I)}$	5	Fe_5C_2
	0.85	1.13	-	4	Fe^{2+}
	0.26	0.92	-	6	Fe^{3+}
$Mn_{0.6}Fe_{2.4}O_y$ after 20 min reduction	0.54		$45.0_{(Oh)}$	24	spinel
	0.27		$48.5_{(Td)}$	16	
	1.02	0.75	-	48	Fe^{2+}
	0.27	0.79	-	12	Fe^{3+}

To finalize the Mössbauer study, it worth noting that: the reduction of the $Cu_{0.6}Fe_{2.4}O_y$ and $Cu_{0.3}Mn_{0.3}Fe_{2.4}O_y$ ferrites have the same nature and goes through the formation of metallic copper (Cu^0) which generates a high concentration of the active sites on the surface and promotes a very deep reduction of the corresponding ferrites. In turn, this results in the formation of the iron carbides (Fe_xC_y) as the main phase of the reduction process. However, in the reduced $Cu_{0.3}Mn_{0.3}Fe_{2.4}O_y$ sample apart of the Fe_xC_y phase, the ferric (Fe^{3+}) and ferrous (Fe^{2+}) iron oxides are also present in a small amount, which may indicate a mixed

reduction character of the following ferrite, which is explained by the presence of Mn-ions (formation of wurstite-like Mn_xFe_yO oxide solid solution). On the other hand, the reduction of $Mn_{0.6}Fe_{2.4}O_y$ occurs over entire surface immediately on the contact with ethanol causing the formation of a hardly reducible layer and at this point the reduction is controlled by the ethanol-diffusion into the bulk, since Mn_xFe_yO may act as a shell-catalyst resulting in a decrease of total reduction of the remained Fe-rich spinel.

5.17. Reactivity tests: $Cu_{0.6-x}Mn_xFe_{2.4}O_y$ system

This section includes discussion of the results obtained over $Cu_{0.6-x}Mn_xFe_{2.4}O_y$ ferrospinels tested on the laboratory-scale plant. The scale is limited to 1 cycle of 20 min (20 min reduction followed by 20 min re-oxidation). The cycling time was chosen according to the results reported by Trevisanut and et al.[129,126].
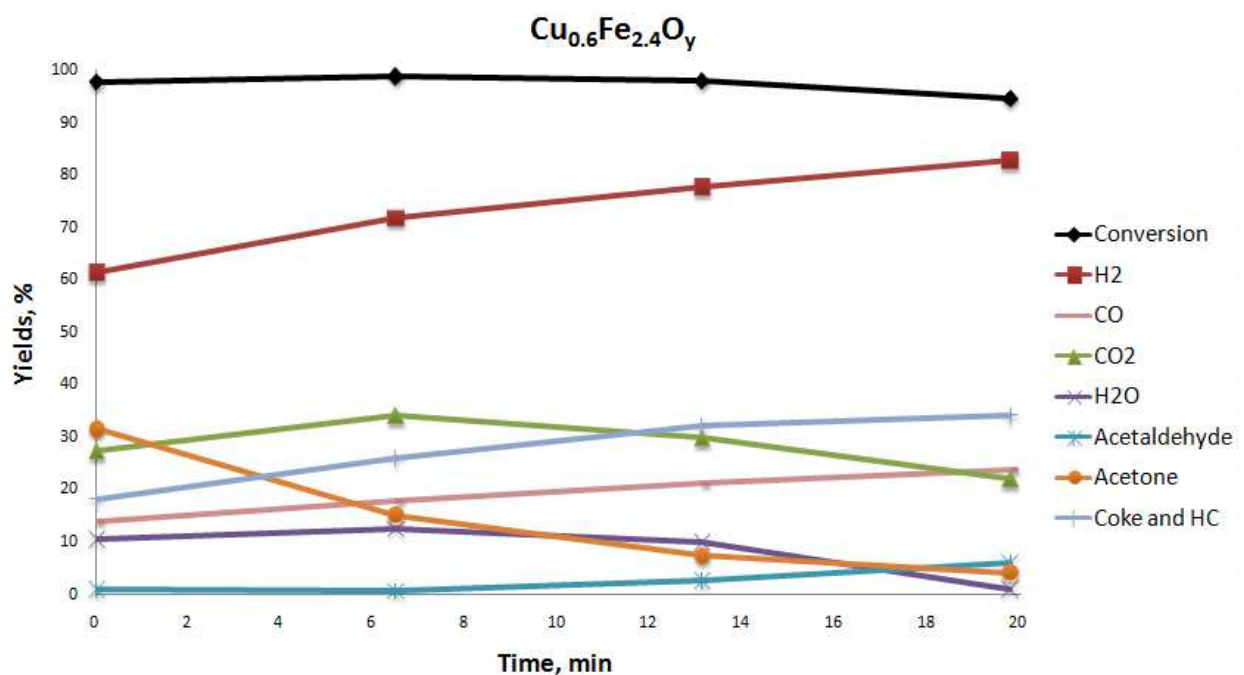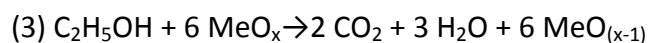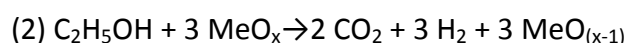
1st step: 20 min reduction with ethanol

Figure 5-31. Conversion and yields for the main products during 20 min reduction with ethanol at 450°C over $Cu_{0.6}Fe_{2.4}O_y$

Figure 5-31 to Figure 5-33 show conversion and yields for the main products (yield >5%), obtained during the ethanol reduction at 450°C for 20 min. $Cu_{0.6}Fe_{2.4}O_y$ ferrite (Figure 5-31) starting from the first minutes of the reaction showed 97% of conversion followed by its decrease down to 95%, while the extent of spinel reduction increased (from 0 to 95 %,

Figure 5-36). One of the main products of ethanol conversion was hydrogen, with an initial yield of about 61%, which increased up to 83%. In addition, CO shows the same increasing trend as for H_2, starting from 14 till 24 %. Looking at CO_2 and H_2O profiles, one may notice a similar decreasing trend (starting yields: CO_2-27% and H_2O-10%, final yields: CO_2-22% and H_2O-1%) with its max yields (34 and 13%, respectively) at about 6 min of reduction time. According to the obtained results we suggest that the main reactions during spinel reduction involved the partial and total oxidation of ethanol:

(1) $C_2H_5OH + MeO_x \rightarrow 2\ CO + 3\ H_2 + MeO_{(x-1)}$

(2) $C_2H_5OH + 3\ MeO_x \rightarrow 2\ CO_2 + 3\ H_2 + 3\ MeO_{(x-1)}$

(3) $C_2H_5OH + 6\ MeO_x \rightarrow 2\ CO_2 + 3\ H_2O + 6\ MeO_{(x-1)}$

In addition, the formation of water involves several possible reactions:

(4) $H_2 + MeO \rightarrow H_2O + Me$

(5) $C_2H_5OH \rightarrow 2\ C + 2\ H_2 + H_2O$
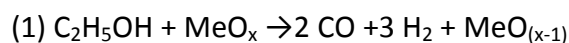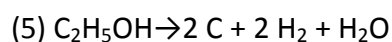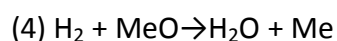
Acetone formation, which declined with time (from 32 to 4%), can be a result of an aldol condensation of the intermediately formed acetaldehyde, with further isomerization of aldol into hydroxyketone followed by a reverse reaction to form acetone and formaldehyde (converted into CO and H_2). Either, as recently proposed by Rodrigues et al., by ketonization of carboxylates (acetates) which are obtained by dehydrogenation of this alcohol followed by oxidation[127]. In fact, the formation of acetates over all $M_{0.6}Fe_{2.4}O_y$ samples was confirmed by DRIFTS study (discussed in the Paragraphs 5.6 and 5.14).

Increasing yields for acetaldehyde (from 1 to 6%) together with hydrogen (from 61 to 83%) on the instantaneously reducing $Cu_{0.6}Fe_{2.4}O_y$ sample, indicates that dehydrogenation/ deoxyhydrogenation of ethanol also occurred:
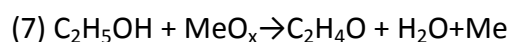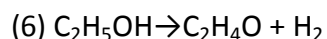
(6) $C_2H_5OH \rightarrow C_2H_4O + H_2$

(7) $C_2H_5OH + MeO_x \rightarrow C_2H_4O + H_2O + Me$

Coke and heavy compounds (mainly aromatics) are formed at the very beginning of the reaction time (~18%), with a progressive increase in yield (to 34%). The generation of coke was likely due to dehydrogenation and total deoxygenation of ethanol:

(8) $C_2H_5OH \rightarrow C + CO + 3\ H_2$

(9) $C_2H_5OH \rightarrow 2\ C + H_2O + 2\ H_2$
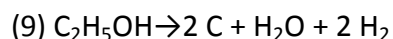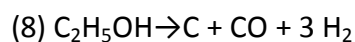
Moreover, a disproportionation of CO (Boudouard reaction) can also lead to a coke deposition:

(10) $2\ CO \rightarrow CO_2 + C$
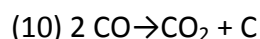
Looking at the conversion and yields evolution over $Cu_{0.3}Mn_{0.3}Fe_{2.4}O_y$ ferrite (Figure 5-32), the results demonstrate similar trends in the products distribution and, as a consequence, a similar reduction path which involves the same set of reactions (eq. 1 to 10). The reduction of $Cu_{0.3}Mn_{0.3}Fe_{2.4}O_y$ sample started with 89 % of ethanol conversion which approached to 95% after 20 min of reduction time. As for the previously discussed ferrite, hydrogen was one of the main products of ethanol conversion, with the following increasing trend: from 49 to 62%. Also, CO and CO_2 have similar increasing trends as for H_2, thus suggesting that the main reactions during spinel reduction involved the partial/total oxidation of ethanol (eq.1-3).
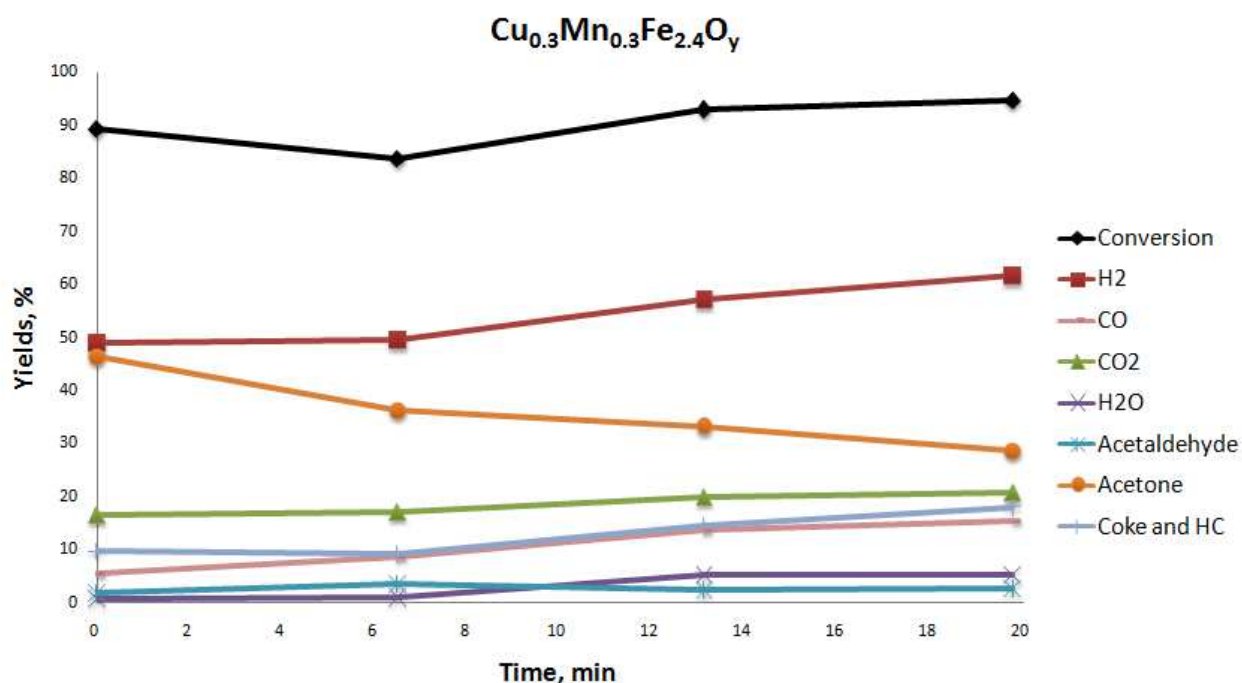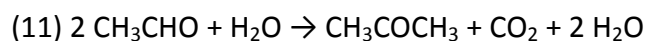

Figure 5-32. Conversion and yields for the main products during 20 min reduction with ethanol at 450°C over $Cu_{0.3}Mn_{0.3}Fe_{2.4}O_y$

The presence of H_2O at the very begging of the reduction time (from 1 to 5%) results from the reactions (eq. 3-5, 8). Acetaldehyde was observed in a small amount (app. 3%). However, yields for the acetone were much higher (increasing in a range: from 46 to 29%) in comparison to $Cu_{0.6}Fe_{2.4}O_y$ ferrite. The overall reaction for the formation of acetone from acetaldehyde may be expressed as follows:

(11) $2\ CH_3CHO + H_2O \rightarrow CH_3COCH_3 + CO_2 + 2\ H_2O$

Coke and heavy compounds (mainly aromatics) are also formed, however in a reasonably small amount (compare to only Cu-incorporated ferrite the values are twice smaller: from 10 to 18%).
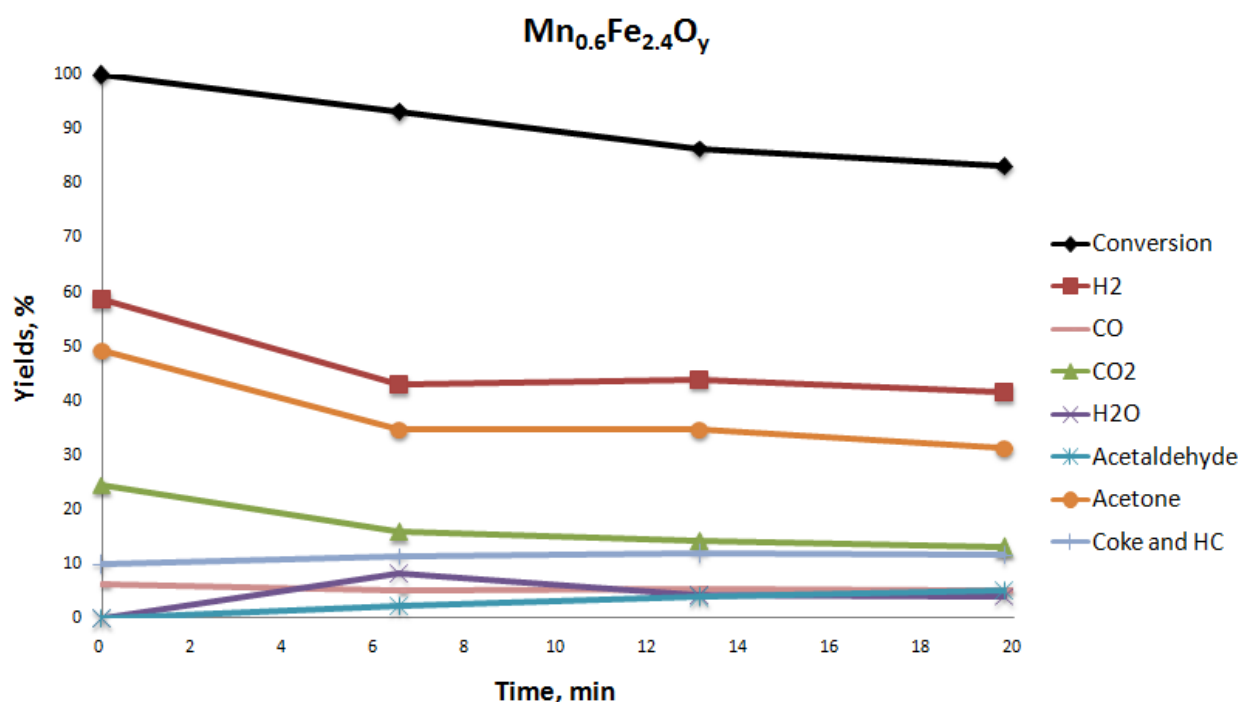
Figure 5-33. Conversion and yields for the main products during 20 min reduction with ethanol at 450oC over $Mn_{0.6}Fe_{2.4}O_y$

Results obtained with the $Mn_{0.6}Fe_{2.4}O_y$ sample (Figure 5-33) demonstrate different trends in the products distribution, with the instantaneously decreasing conversion and decreasing yields of the formed products. According to the XRD and Mössbauer results (discussed previously), the reduction of this sample goes through the formation of two phases: re-formed spinel ($Mn_{0.6-x}Fe_{2.4+x}O_4$) and Mn/Fe solid solution (Mn_xFe_yO). Thus, we should take into account this information. A significant decrease of the conversion (from 100 to 83%)

over $Mn_{0.6}Fe_{2.4}O_y$ sample is attributed to an accumulation of Mn_xFe_yO phase in the catalyst, which has a high thermodynamic stability and, as a consequence, its scarce attitude towards the reduction to the metallic component. Moreover, it also explains the decrease in yields (since conversion ↓) for the main products: H_2 (from 59 to 42%), CO_2 (24-13%), CO (6 to 5%), H_2O (0 to 4%), acetaldehyde (from 0 to 5 %) and acetone (49-31 %). However, the formation of acetone directly from ethanol is not excluded, especially in the case of $Mn_{0.6}Fe_{2.4}O_y$ (formed Mn_xFe_yO acts as a catalyst; it worth noting that MnO may catalyze the direct transformation: ethanol→acetone, as was reported by Dolgychand et al[155]). Coke and heavy compounds were formed in a small amount (9 to 11%).
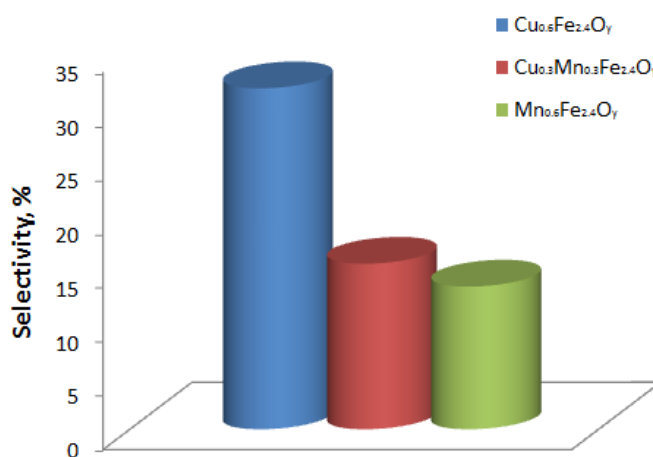
Figure 5-34. Integrated selectivity to coke

As discussed above, we could not completely avoid the coke formation (in Figure 5-34 are plotted integrated selectivity for $Cu_{0.6-x}Mn_xFe_{2.4}O_y$ ferrites), but despite this, we were able to significantly reduce its amount by changing the composition of the catalyst (see CHNS results below). Indeed, the presence of Mn had a beneficial effect of decreasing the coke deposition, which is an important issue in order to produce C-free hydrogen. The integrated yields for the other products formed in minor quantities during 20 min of reduction with ethanol are plotted in Figure 5-35.
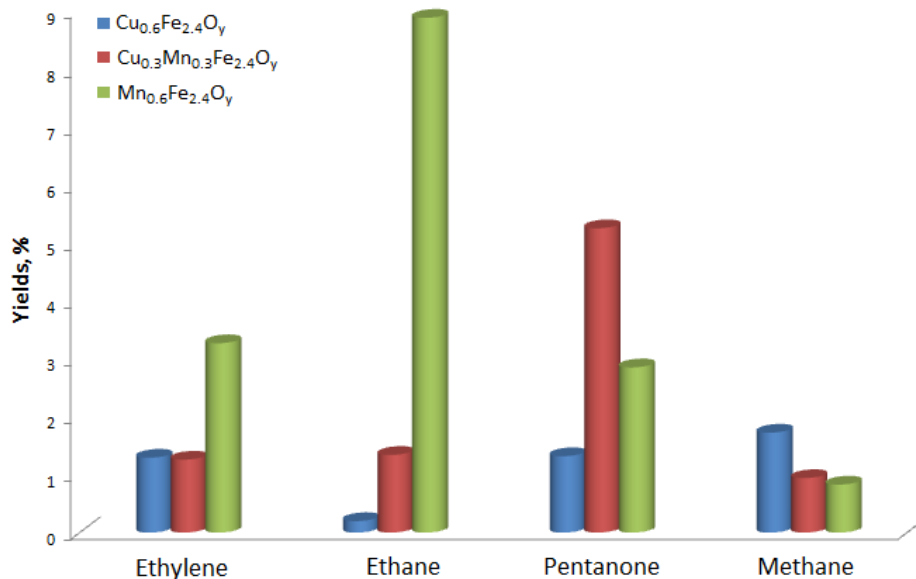
Figure 5-35. Integrated yields for the other products formed during 20 min reduction with ethanol at 450°C over $Cu_{0.6-}Mn_xFe_{2.4}O_y$ ferrites
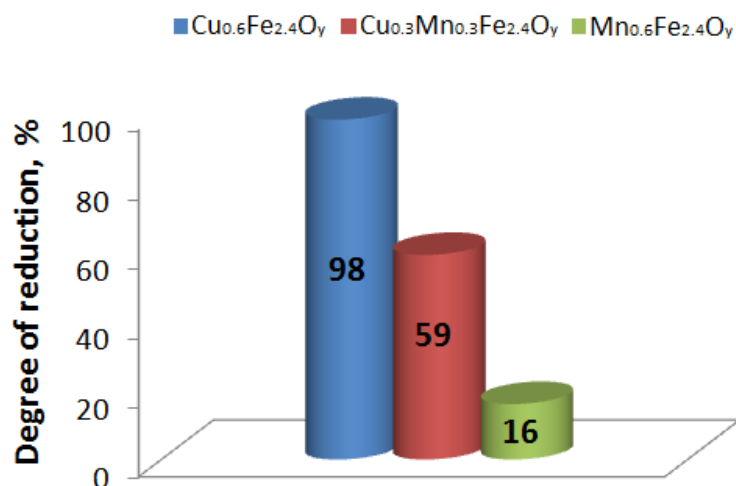
Figure 5-36. Reduction extent calculated on the basis of Rietveld refinement for $Cu_{0.6-x}Mn_xFe_{2.4}O_y$ ferrites

In the Figure 5-36 are shown values of the reduction extent for the $Cu_{0.6-x}Mn_xFe_{2.4}O_y$ ferrites, as calculated on the basis of Rietveld refinement results. Even though the highest surface area was shown by $Mn_{0.6}Fe_{2.4}O_4$ catalyst, and it declined with an increase of Cu-content, the samples which contain copper cations ($Cu_{0.6}Fe_{2.4}O_y$ and $Cu_{0.3}Mn_{0.3}Fe_{2.4}O_y$) reached higher reduction extent (about 98 and 59%, respectively) in comparison to only Mn-modified ferrospinel (with just 16%). The similar trends were obtained from elaborated TPR results. This suggests that the difference in the reducibility of the resulted M-modified ferrospinels is related to the nature of the incorporated M cation and its intrinsic reactivity.

2ⁿᵈ step: 20 min re-oxidation with water

After the reduction with ethanol, the materials were re-oxidized with steam at 450°C, which corresponds to the second step of the chemical loop. Tests were carried out on the same apparatus used for the reduction step, feeding water by means of a syringe pump at 450°C, for 20min, after the reduction step. The gas mixture out flowing from the reactor was first passed through a water trap, in order to avoid a higher water concentration which could be harmful for the micro-GC columns. The analytical method used allowed us to carry out an analysis every few minutes. Reaction conditions are detailed in Paragraph 2.11.

SAMPLE	Integrated yields		
	H_2	CO_2	CO
$Cu_{0.6}Fe_{2.4}O_y$	51	14	2
$Cu_{0.3}Mn_{0.3}Fe_{2.4}O_y$	19	5	0.6
$Mn_{0.6}Fe_{2.4}O_y$	7	0.8	0.04
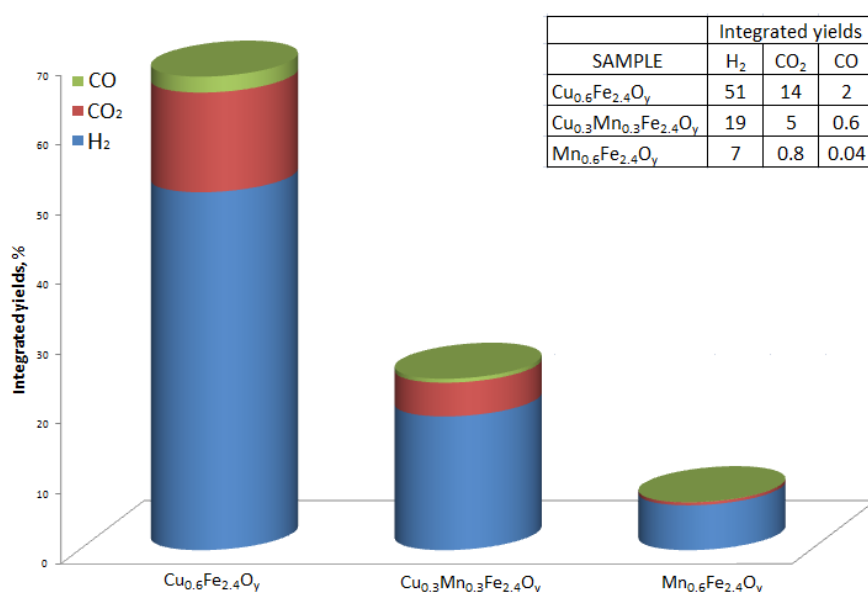
Figure 5-37. Integrated yields for H_2, CO_2 and CO produced during the 2ⁿᵈ re-oxidation step with steam at 450°C over $Cu_{0.6-x}Mn_xFe_{2.4}O_y$ ferrites
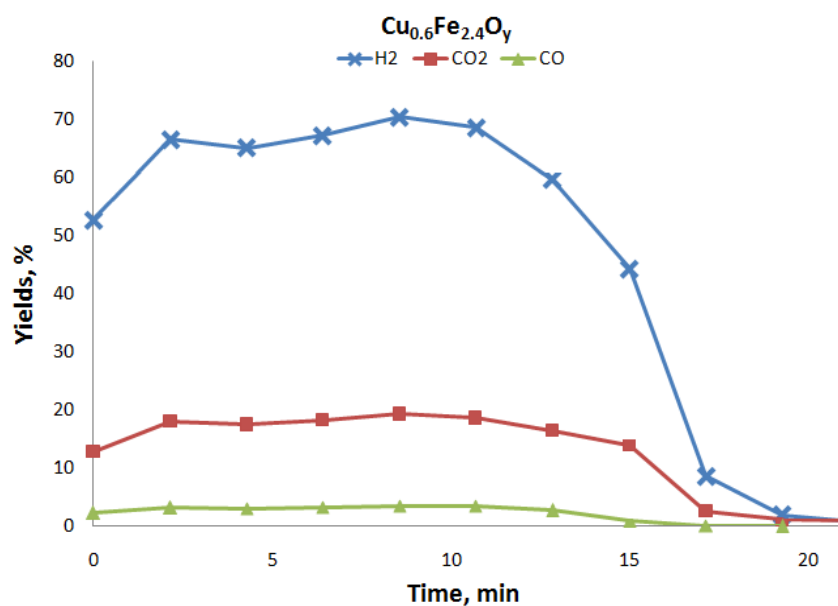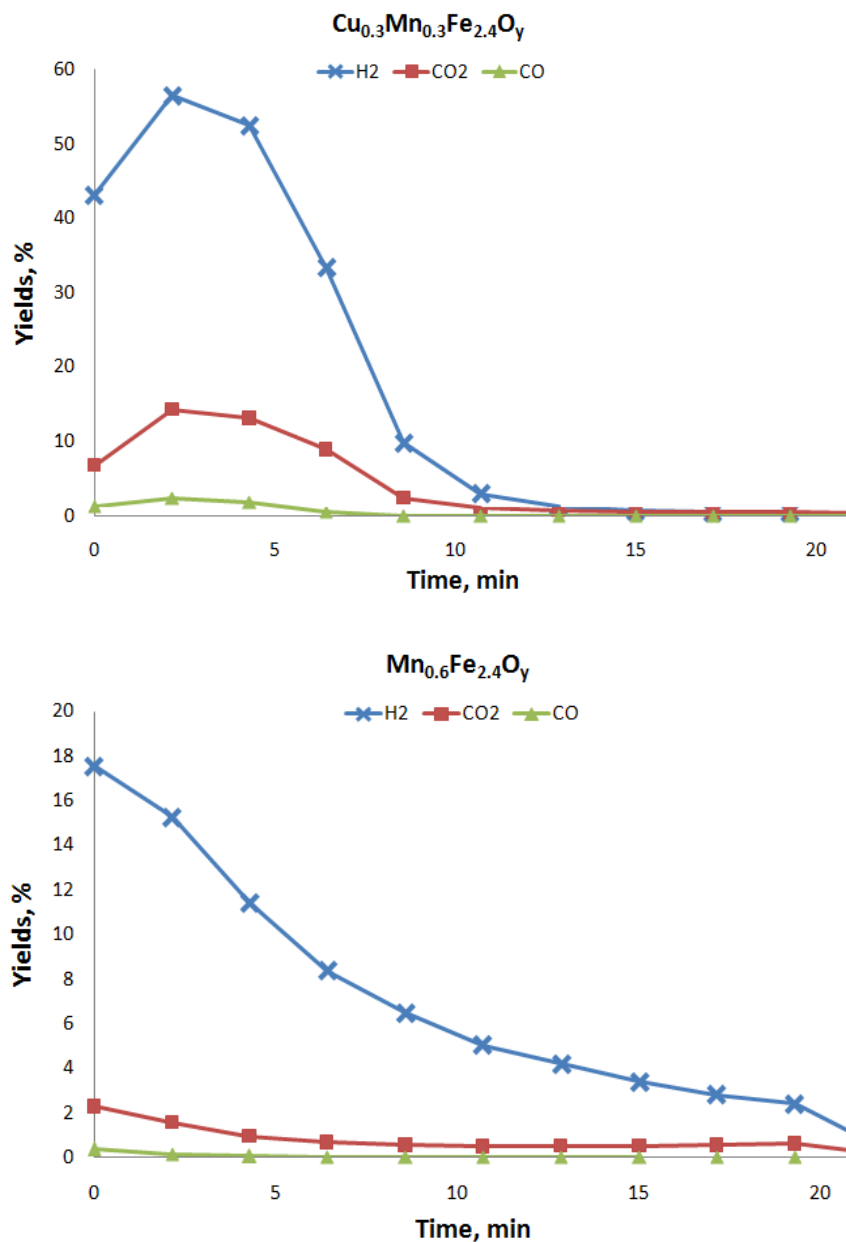
Figure 5-38. H_2, CO_2 and CO yields vs time obtained during the 2nd re-oxidation step with steam at 450^oC over $Cu_{0.6-x}Mn_xFe_{2.4}O_y$ ferrites

Figure 5-38 reports the yield of H_2, CO_2 and CO versus time (yields have been calculated based on the H or O content in products, with respect to the water fed – described in Paragraph 2.11), whereas Figure 5-37 reports the overall yields to H_2, CO and CO_2, integrated over the 20 min oxidation time. It is important to notice, that the increasing trends (within 0-5 min) shown in Figure 5-38 for $Cu_{0.6}Fe_{2.4}O_y$ and $Cu_{0.3}Mn_{0.3}Fe_{2.4}O_y$ samples, most probably arise from the following fact: the stream, containing unconverted steam and products, needs a few minutes to reach the catalyst and then the on-line GC apparatus after

the start-up of the reaction. A common behavior for all three samples was a complete re-oxidation of the material in the chosen timeframe - app. in 20 min.

High hydrogen yield (51%) was detected for $Cu_{0.6}Fe_{2.4}O_y$ sample; whereas a lower amount of hydrogen produced during the re-oxidation process was obtained over Mn-incorporated samples: $Cu_{0.3}Mn_{0.3}Fe_{2.4}O_y$ (19%) and $Mn_{0.6}Fe_{2.4}O_y$ (7%) ferrites. This can be explained, taking into account the values of the reduction extent, calculated on the basis of Rietveld refinement: $Cu_{0.6}Fe_{2.4}O_y$ and $Cu_{0.3}Mn_{0.3}Fe_{2.4}O_y$ reached a higher reduction extent (about 98 and 59%, respectively) in comparison to only Mn-modified ferrospinel (with just 16%). Apart of produced hydrogen, the common feature for all the samples was the formation of CO and CO_2 during the re-oxidation step (Figure 5-37 and Figure 5-38), because of the gasification of carbonaceous residues, previously formed during the reduction step. The main reactions occur during re-oxidation process are defined as following:

(12) $Me + H_2O \rightarrow MeO + H_2$

(13) $3 MeO + H_2O \rightarrow Me_3O_4 + H_2$

(14) $C + H_2O \rightarrow CO + H_2$

(15) $C + 2 H_2O \rightarrow CO_2 + 2 H_2$
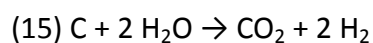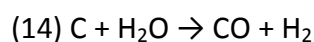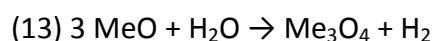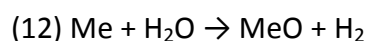
The main difference was in the amount of produced CO_x. According to the obtained results, Mn-containing catalysts produced less CO_x which resulted from a lower amount of deposited carbon during the reduction step (results on the carbon content are summarized in Table 5-11 , see CHNS analysis).

Determination of carbon content (CHNS analysis)

In order to evaluate the amount of coke formed during the reduction step with ethanol (within 20 min), an elemental analysis (CHNS) on the different materials was carried out. Table 5-11 summarizes the results of CHNS analysis over $Cu_{0.6}Fe_{2.4}O_y$ ferrospinels. According to the obtained results, the highest amount of coke accumulated during the ethanol reduction was detected over $Cu_{0.6}Fe_{2.4}O_y$ sample and it declines with Mn-incorporation ($Cu_{0.6}Fe_{2.4}O_y > Cu_{0.3}Mn_{0.3}Fe_{2.4}O_y > Mn_{0.6}Fe_{2.4}O_y$). Such trend: ↑coke with ↑Cu-incorporation, confirms previously discussed values of coke accumulation, calculated on the basic of GC analysis (integrated yields: $Cu_{0.6}Fe_{2.4}O_y$- 32%>$Cu_{0.3}Mn_{0.3}Fe_{2.4}O_y$- 15%>$Mn_{0.6}Fe_{2.4}O_y$ - 13%).

Table 5-11. CHNS results over $Cu_{0.6-x}Mn_xFe_{2.4}O_y$ ferrites after 20 min reduction

SAMPLE	C content(%) after 20 min of reduction (ethanol)
$Mn_{0.6}Fe_{2.4}O_y$	2.2
$Cu_{0.3}Mn_{0.3}Fe_{2.4}O_y$	5.0
$Cu_{0.6}Fe_{2.4}O_y$	9.8

5.18. Conclusions on the study of $Cu_{0.6-x}Mn_xFe_{2.4}O_y$ system

The chemical-loop reforming of ethanol for H_2 production was studied by using $Cu_{0.6-x}Mn_xFe_{2.4}O_y$ ferrospinels as ionic oxygen carrier materials. The magnetic properties of Cu/Mn-modified ferrites, prepared via co-precipitation method, were examined by mean of Magnetic Study and Mössbauer Spectroscopy. According to the Mössbauer results, $Cu_{0.3}Mn_{0.3}Fe_{2.4}O_y$ and $Mn_{0.6}Fe_{2.4}O_y$ samples are characterized by doublet-like spectra which arises due to the effect of the electric field gradient at the nucleus. This observation was explained by the presence of superparamagnetic ferrite nanoparticles with sizes below ~5 nm. A characteristic feature of superparamagnetic nanoparticles was confirmed by Magnetic Measurements: the CHI values estimated for three ferrospinels ($Cu_{0.6-x}Mn_xFe_{2.4}O_y$) have shown that $Cu_{0.3}Mn_{0.3}Fe_{2.4}O_y$ and $Mn_{0.6}Fe_{2.4}O_y$ materials are in the superparamagnetic state compared to only Cu-ferrospinel. This effect was correlated with the increase of Mn-incorporation and attributed to a disorder in the cation distribution between O_h and T_d sites, caused by a partial substitution of Fe^{3+} cations with Mn^{2+}ions.

The redox properties of ferrospinels were found to depend strongly on the nature of incorporated cation in addition to its distribution inside the crystal lattice. On this basis, the reduction of $Cu_{0.6-x}Mn_xFe_{2.4}O_y$ ferrites is further complicated and proceeds through the concurrent reactions of instantaneously formed new reduced phases until the system reaches its 'steady state' at these reaction conditions. Study of the H_2-reduction curves (α-*versus*-T) brought us to an important conclusion on the reduction paths of the samples: the $Cu_{0.6}Fe_{2.4}O_y$ and $Cu_{0.3}Mn_{0.3}Fe_{2.4}O_y$ materials reduces through the formation of metallic copper (Cu^0) which generates a high concentration of active hydrogen on the surface and

promotes the reduction, so called "autocatalytic" model. In the case of $Mn_{0.6}Fe_{2.4}O_y$ nucleation occurs over entire surface immediately on the contact with hydrogen causing the formation of hardly reducible layer (in the form of Mn_xFe_yO) and at this point the reduction is controlled by the H_2-diffusion into the bulk, as in the "egg-shell" model.

Apart of H_2-reduction, the particular interest represented also the reduction behavior of $Cu_{0.6-x}Mn_xFe_{2.4}O_y$ samples using ethanol as a probe molecule (as a 1st step of the chemical-loop process). In-situ DRIFTS study was performed in order to follow the stepwise reduction of the catalyst surface, which allowed us to detect different adsorbed species and their transformation into the products. Acetates and carbonates appeared to be important surface intermediates over Cu- and mixed Cu-Mn- ferrospinels and in the case of the only Mn-containing catalyst, there was no evidence of the carbonates formation.

The evolution of a phase composition of the $Mn_{0.6}Fe_{2.4}O_y$ sample was studied by mean of XRD using ex-situ approach. The data clearly indicated that after feeding ethanol for 1 min the formation of a new Mn_xFe_yO phase (app. 7%$_w$) was observed. With increasing the reduction time from 1 to 20 min the spinel relative ratio continued decreasing whereas that of the Mn_xFe_yO increased without the appearance of other phases. This apparently showed that the reduction of the $Mn_{0.6}Fe_{2.4}O_y$ went through the formation of Mn_xFe_yO phase, which is an important proof of the TPR results with an "egg-shell" reduction model. Furthermore, the Mössbauer study of the C_2H_5OH-reduced materials indicated a similar phase distributions. The only difference between H_2 and C_2H_5OH reduction paths was observed for $Cu_{0.3}Mn_{0.3}Fe_{2.4}O_y$ ferrite, where the ferric (Fe^{3+}) and ferrous (Fe^{2+}) iron oxides were also present in a small amount, which may indicate a "mixed reduction character" with a partial contribution from both "autocatalytic" (shown by $Cu_{0.6}Fe_{2.4}O_y$) and "egg-shell" (shown by $Mn_{0.6}Fe_{2.4}O_y$) mechanisms.

Moreover, the chemical-loop reforming was performed using $Cu_{0.6}Fe_{2.4}O_y$ ferrites as looping materials. The obtained results have shown that samples which contain copper cations ($Cu_{0.6}Fe_{2.4}O_y$ and $Cu_{0.3}Mn_{0.3}Fe_{2.4}O_y$) reached higher reduction extent (about 98 and 59%, respectively) in comparison to only Mn-modified ferrospinel (with just 16%). In addition, conducted CHNS elemental analysis has shown the relationship between a ferrite composition and a carbon deposition: "↑%$_{Cu}$" → "↑%$_C$". Thus, the addition of Mn hindered carbon deposition, which also caused a decrease of the amount of CO_x generated by

oxidation with water steam, which is an important issue to produce clean H_2. However, Mn-incorporation led to a lower efficiency of the 1st step due to the formation of thermodynamically stable Mn_xFe_yO which prevents a further deep reduction. This in turn reduces the yields for H_2 produced on the 2nd re-oxidation step. Cu-incorporation has shown an opposite effect, leading to a higher reduction extent and as a consequence higher yields for H_2 produced during the steam re-oxidation stage.

6. CHEMICAL-LOOP REFORMING: REACTIVITY TESTS→$M_{0.6}Fe_{2.4}O_y$

The previous two chapters have included some results on the reactivity of $Co_{0.6-x}Mn_xFe_{2.4}O_y$ and $Cu_{0.6-x}Mn_xFe_{2.4}O_y$ ferrospinels: 1 complete cycle of 20 min (1st step – ethanol reduction – 20 min/ 2nd step – water re-oxidation – 20 min). This chapter contains a further discussion on the reactivity of $M_{0.6}Fe_{2.4}O_y$ materials, using a different cycling time and a sample composition as an important tool to improve the overall effectiveness of the chemical-loop reforming (CLR) process.

The choice of reaction conditions and cycling time was adopted according to the study of Cocchi (reducing agent: methanol, T_{red} – 300 and 420°C/T_{re-ox} – 420°C, looping materials: Fe_3O_4, $CoFe_2O_4$ and $NiFe_2O_4$)[100] and Trevisanut (reducing agent: ethanol, $T_{screen\ red}$ – 400 and 450°C/T_{re-ox} – 450°C, looping materials: Fe_3O_4, $CoFe_2O_4$ and $NiFe_2O_4$)[101]. Important to note, that the essential aim of the reduction step was to maximize the reduction extent with a minimum deactivation (an effect of coke accumulation) of the looping material along with an improving of its cycling stability. Hence, previously obtained results suggested the best reaction conditions to be as follows: 1st step – ethanol reduction at T_{red}-450°C and 2nd step – water re-oxidation at T_{re-ox}-450°C. Cycling time was chosen on the same basis and can be subdivided into: long cycles (duration time of one complete cycle: 1 h red/1 h re-ox) and short cycles (duration time of one complete cycle: 20 min $_{red}$/20 min $_{re-ox}$, 6 min $_{red}$/6 min $_{re-ox}$).The optimum time for both steps was set up as 20 min per each cycle (however, a comparison of the integrated mol of produced H_2 during the 2nd step for the same total *tos* has been made, for example 1h (total→60 min) = 3 cyc·20 min (total→60 min) = 10 cyc·6 min (total→60 min).

The composition of $M_{0.6}Fe_{2.4}O_y$ ferrospinel was also varied in between transition metals: Co, Mn, Cu and alkaline earth metals: Ca, Mg. The aim of the following modifications was to pursue a higher selectivity to some valuable chemicals produced on the 1st reduction step along with a high purity H_2 produced during the 2nd re-oxidation step (Figure 1-10).
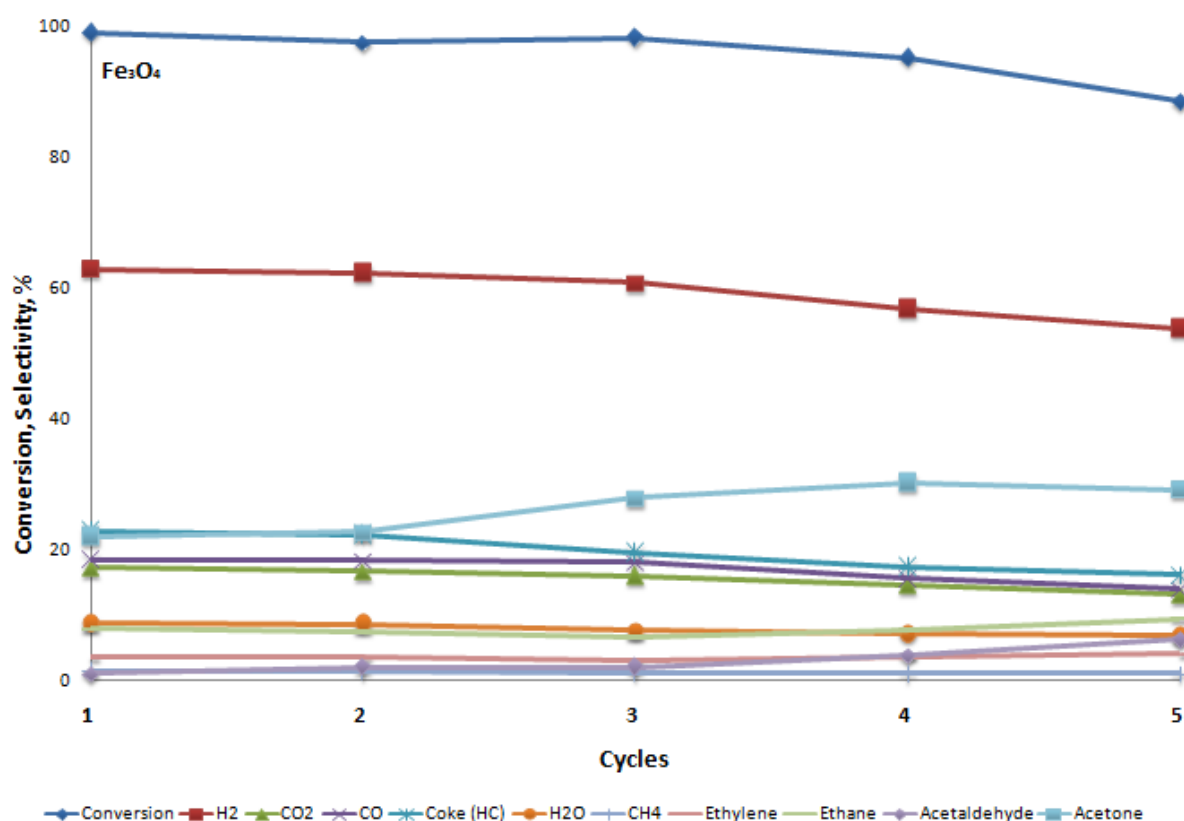
6.1. 1st step: reduction with ethanol at T-450°C

Figure 6-1. Conversion and Selectivity to the main products obtained for Fe$_3$O$_4$ during the 20 min cycling at T-450°C

Figure 6-2 shows the results obtained over M$_{0.6}$Fe$_{2.4}$O$_y$ samples (where M-Cu, Co, Mn, Ca and Mg) during 5 complete cycles of 20 min (plotted selectivity and conversion represent an integrated value and this has been done per each cycle). For comparison of any important differences with changing the composition of the ferrospinels, Fe$_3$O$_4$ was taken as a reference (studied in details by Trevisanut[101]). In Figure 6-1 plotted results obtained with bare magnetite over 5 complete cycles. As was seen by Trevisanut and others, the main drawback of the pure-Fe$_3$O$_4$ is a low cycling stability which derives from deep modifications of the looping material occurred during the redox cycles, such as: sintering, segregation, coke deposition (partly remains after each cycle due to an incomplete gasification with a steam) and incomplete re-oxidation, etc. As a consequence of the lost in the activity, the amount of produced H$_2$ on the 2nd step (see the next paragraph) over magnetite decreased with every repeated cycle, leading to a lower efficiency of the CLR process. As discussed previously in the Chapters 4 and 5, a slight change in the composition may strongly affect the final redox properties and catalytic behavior of the resulted sample. Thus, looking at the

plotted results in Figure 6-2, an average conversion of ethanol over Mn-/Mg-/Ca-modified samples showed the lowest values compared to Cu-/Cu-Mn-/Co-Mn- materials with a decreasing trend for almost all the samples. This can be explained by sintering ($\uparrow$ of particle size $\downarrow$ of SSA, see TEM images for some cycled samples in the Chapter 5), segregation (mainly in the form of metal (M) and metal oxide (MO), as detected by XRD, see the next Paragraphs 6.2 and 6.4) and coke deposition (part of which remains after each cycle, see Raman spectroscopic study in the next Paragraph 6.5).

Looking at the selectivity to the different products (Figure 6-2), H_2 appears to be the main product of the reduction process over all M-modified ferrospinels. However, its selectivity affected by the nature of a foreign metal and in addition by the phase composition of a newly reformed material (the composition is changing continuously until the reduction extent reaches its plateau (its max at chosen reaction conditions). Incorporation of Mn and alkaline metals (like, Ca and Mg) gives a lower selectivity to H_2: $Mn_{0.6}Fe_{2.4}O_y$ (with a decreasing trend from 49 to 34%), $Ca_{0.6}Fe_{2.4}O_y$ (with a decreasing trend from 54 to 41%) and $Mg_{0.6}Fe_{2.4}O_y$ (with a decreasing trend from 52 to 32%). On the contrary, a highest selectivity to hydrogen was obtained with incorporation of transition metals, such as Cu and Cu/Mn, Co/Mn: $Cu_{0.6}Fe_{2.4}O_y$ (with $\downarrow$ trend from 80 to 60%), $Cu_{0.3}Mn_{0.3}Fe_{2.4}O_y$ (from 62 to 60%, with a max at 69% for a 2nd cycle) and $Co_{0.3}Mn_{0.3}Fe_{2.4}O_y$ (with $\uparrow$ trend from 66 to 78%). Moreover, other products formed during the ethanol reduction also have shown some differences in the selectivity distributions which vary according to the nature of the incorporated cations. High selectivity to acetone have shown the following ferrospinels: $Mn_{0.6}Fe_{2.4}O_y$ (from 38 to 31%), $Mg_{0.6}Fe_{2.4}O_y$ (from 35 to 22%) and $Ca_{0.6}Fe_{2.4}O_y$ (from 38 to 21%). In addition, CO_x (see Chapter 5, eq. 1-3, 7, 9-10) and H_2O (see Chapter 5, eq. 3-5, 8, 10) formed over all tested materials, however the higher selectivity observed with Cu-, Cu/Mn- and Co/Mn-incorporated samples, which appear to achieve a higher reduction extents. The formation of coke (+heavy compounds) was also one of the products formed with all looping materials. The lowest selectivity to coke production have shown by Mn-, Ca- and Mg-incorporated samples. Hence, according to the present study, incorporation of Cu-, Cu/Mn- and Co/Mn- catalyze the reactions of total and partial oxidation of ethanol giving rise to higher selectivity to CO_x (or based on the calculation from H balance: to H_2 and H_2O). From the other hand, Mn-, Ca- and Mg-modification predominantly catalyze

dehydrogenation and condensation reactions leading to the formation of higher amount of acetaldehyde, acetone and pentanone.
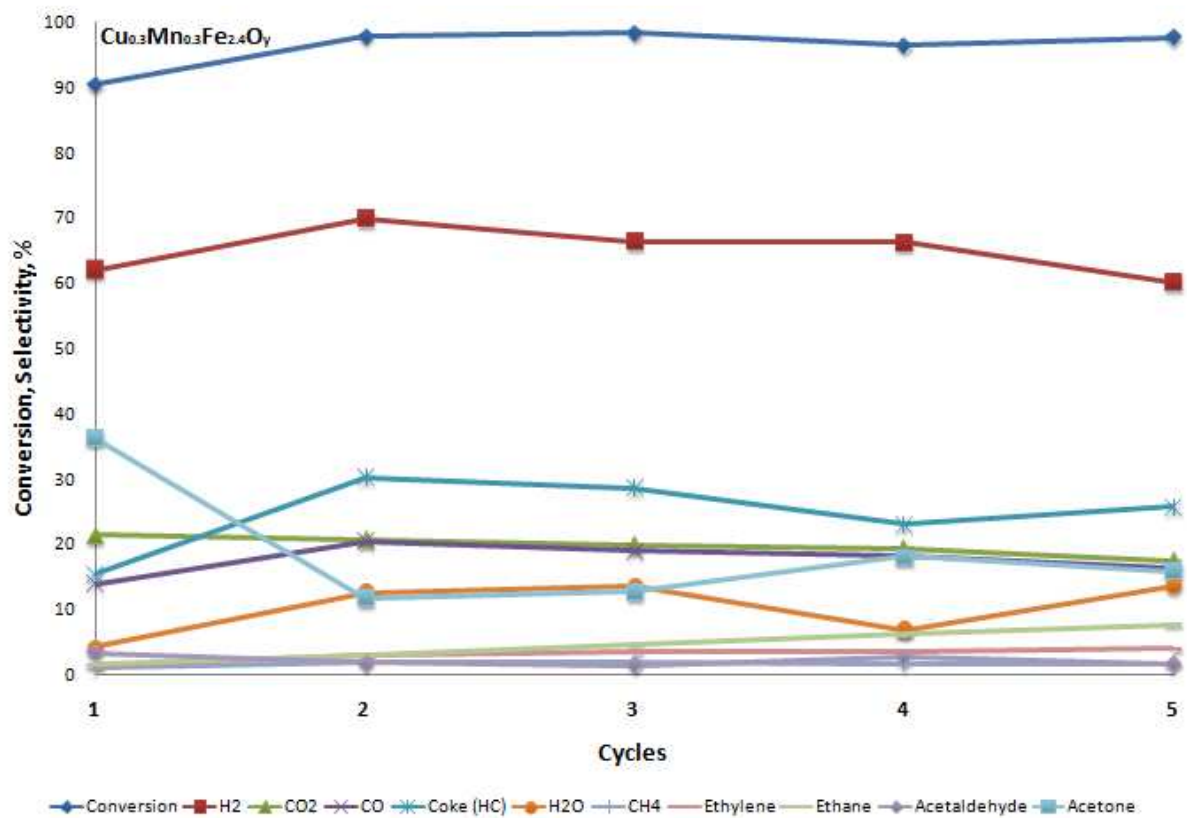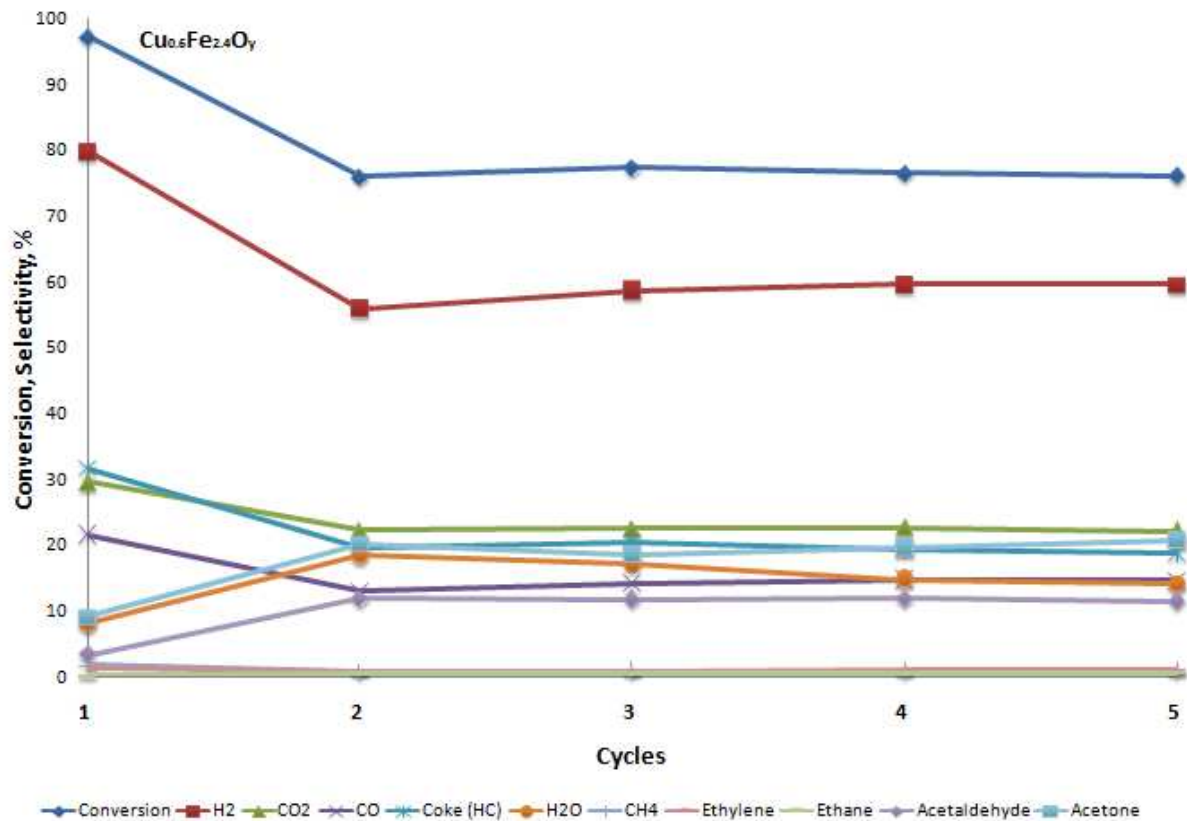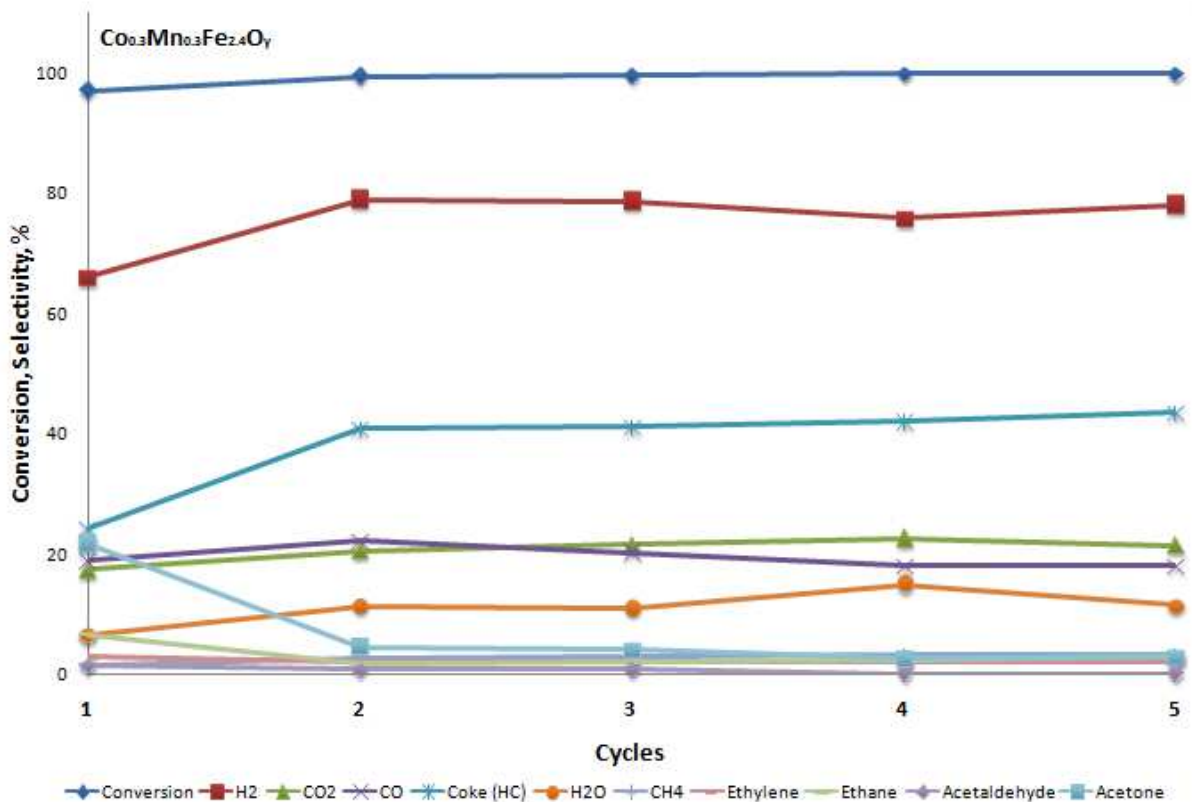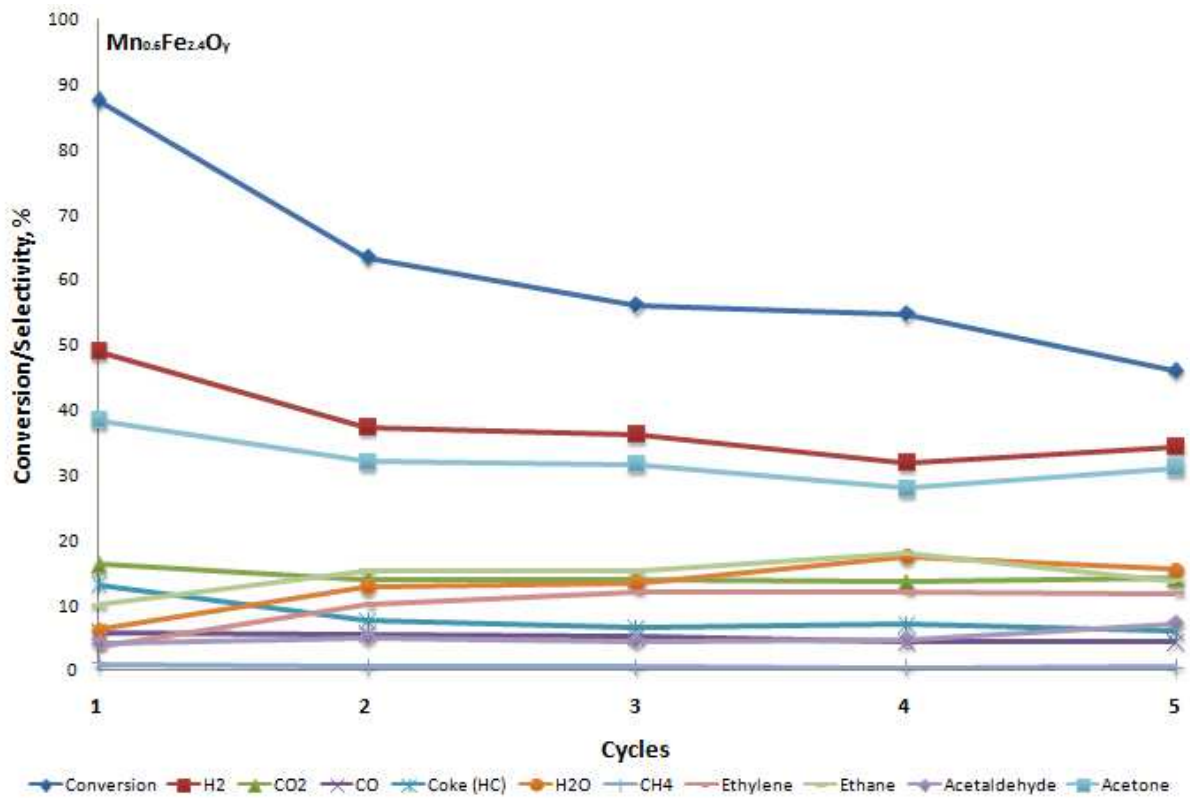
Figure 6-2. Conversion and Selectivity to the main products obtained for TYPE II ferrospinels ($M_{0.6}Fe_{2.4}O_y$) during the 20 min cycling at T-450°C
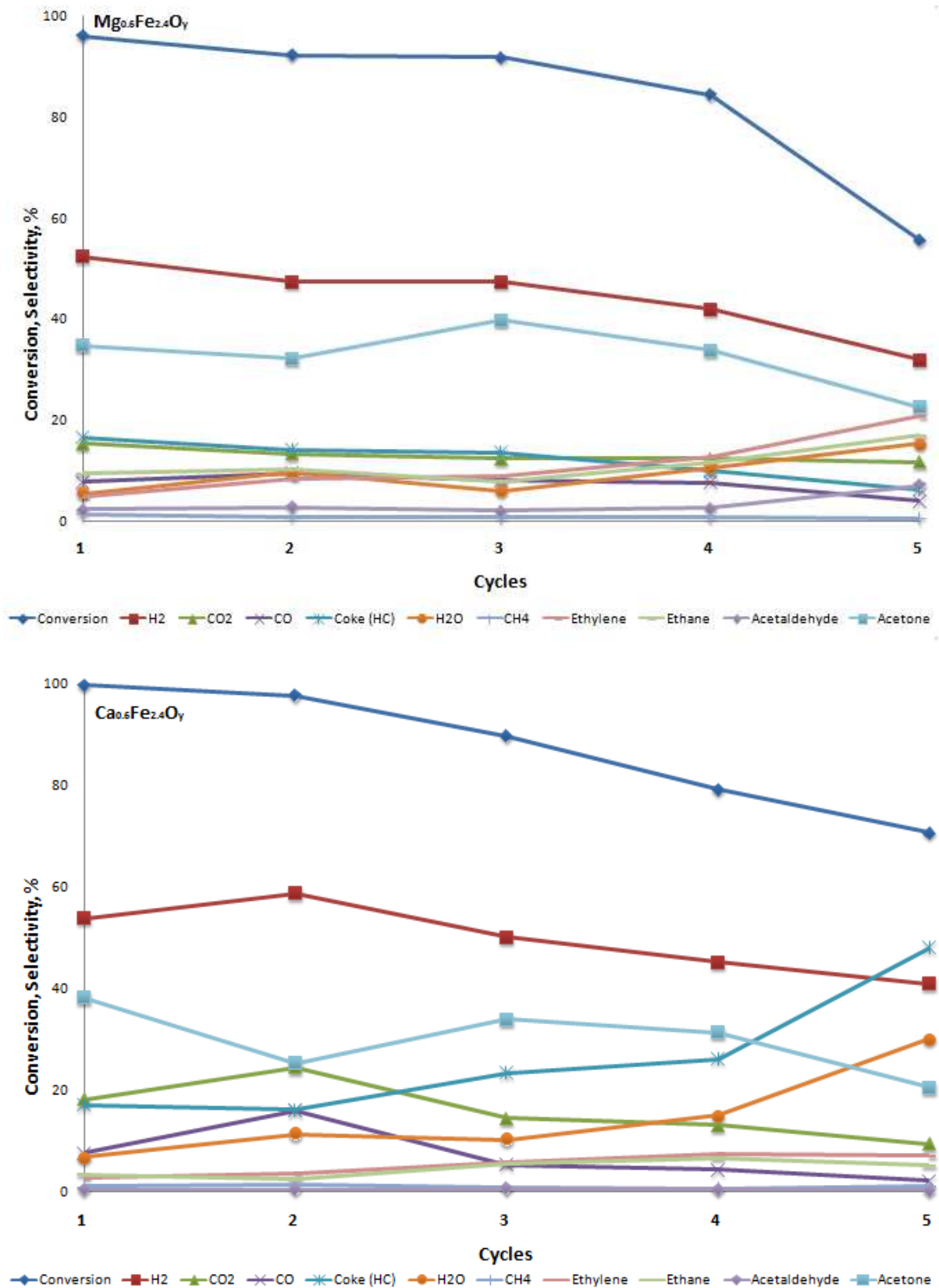
6.2. Ex-situ XRD study over cycled materials after 4 cyc·20 min+1 ^{red}

Characterization of the cycled materials by mean of XRD is an important tool to elucidate several aspects on the stability of the spinel phase and its re-formation after each redox cycle. Moreover, identification of the phases during the reduction process can help to understand the results obtained from the catalytic tests.

Figure 6-3 shows XRD patterns for $M_{0.6}Fe_{2.4}O_y$ ferrospinels which are taken after 4 complete cycles (20 min each step) + 1 ethanol reduction (20 min). At the first sight, a presence of the spinel phase (as a reformed phase: $M_{0.6-x}Fe_{2.4+x}O_4$) indicates an incomplete reduction which appears after cycling (possibly as a result of the sintering ($\uparrow$particle size and $\downarrow$SSA) and the partly remaining coke (the spinel phase is encapsulated inside). Moreover, the ethanol reduction of already cycled material led to the formation of the other phases, like metal (M) and metal oxide (MO). Reduction with ethanol led to the formation of: _$Co_{0.3}Mn_{0.3}Fe_{2.4}O_y$_ (reformed spinel ($Co_{0.3-x}Mn_{0.3-y}Fe_{2.4+x+y}O_4$) and metal oxides solid solution (Mn_xFe_yO); _$Cu_{0.3}Mn_{0.3}Fe_{2.4}O_y$_ (reformed spinel ($Cu_{0.3-x}Mn_{0.3-y}Fe_{2.4+x+y}O_4$), metal oxides solid solution (Mn_xFe_yO) and metal (Cu^0)), _$Cu_{0.6}Fe_{2.4}O_y$_ (reformed spinel ($Cu_{0.6-x}Fe_{2.4+x}O_4$), iron carbides (Fe_3C and Fe_5C_2) and metal (Cu^0)), _$Mg_{0.6}Fe_{2.4}O_y$_ (reformed spinel ($Mg_{0.6-x}Fe_{2.4+x}O_4$) and metal oxides solid solution (Mg_xFe_yO)) and _$Mn_{0.6}Fe_{2.4}O_y$_(reformed spinel ($Mn_{0.6-x}Fe_{2.4+x}O_4$) and metal oxides solid solution (Mn_xFe_yO)). As explained in the previous Chapter 5, the formation and further accumulation of a hardly reducible and thermodynamically stable M_xFe_yO oxide (mainly, as Mn_xFe_yO and Mg_xFe_yO) elucidates a decrease in the conversion for $Mg_{0.6}Fe_{2.4}O_y$ and $Mn_{0.6}Fe_{2.4}O_y$ samples (see Paragraph 6.1). Moreover, the formation of much higher amount of acetone (stable within 20 min) over these two samples could be also correlated to the presence of the thermodynamically stable M_xFe_yO phase, which may catalyze the following reaction of the condensation of acetaldehyde with its further transformation to acetone (Chapter 5, eq. 11).

Co$_{0.3}$Mn$_{0.3}$Fe$_{2.4}$O$_y$
4 cycles+1 red (20min)
▲ MnxFeyO

Position [°2Theta] (Copper (Cu))

Cu$_{0.3}$Mn$_{0.3}$Fe$_{2.4}$O$_y$
4 cycles+1 red (20min)
▲ MnxFeyO
▲ Cu
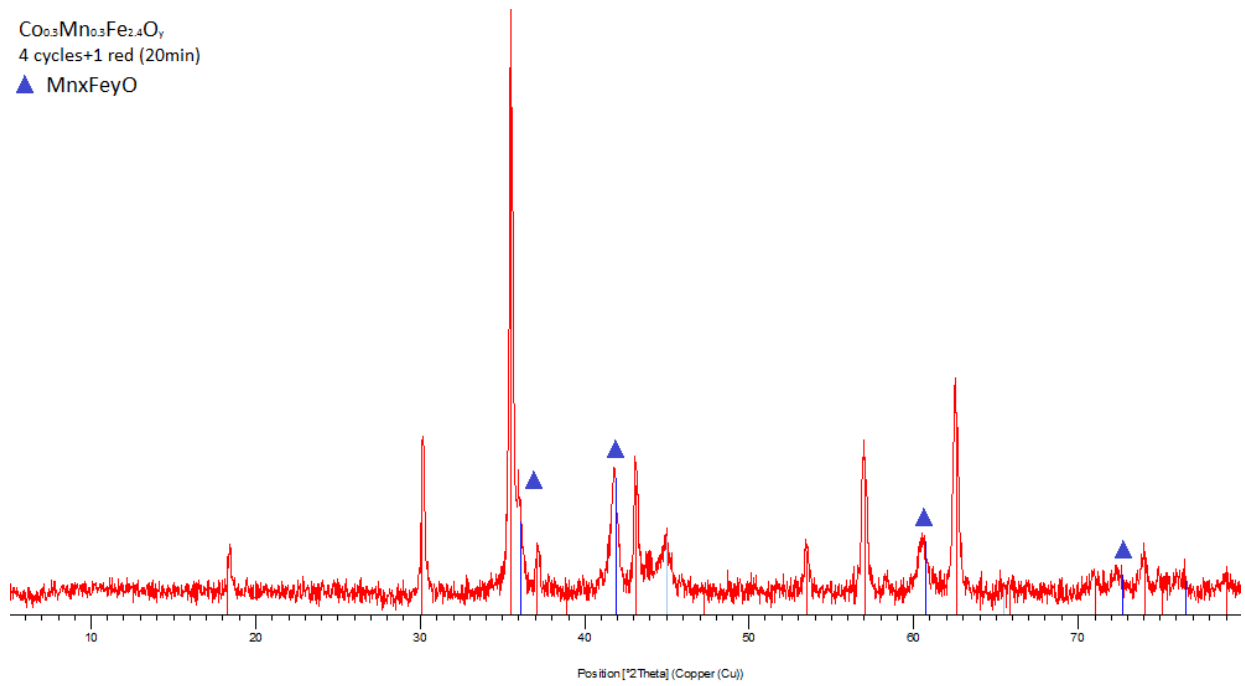
Position [°2Theta] (Copper (Cu))
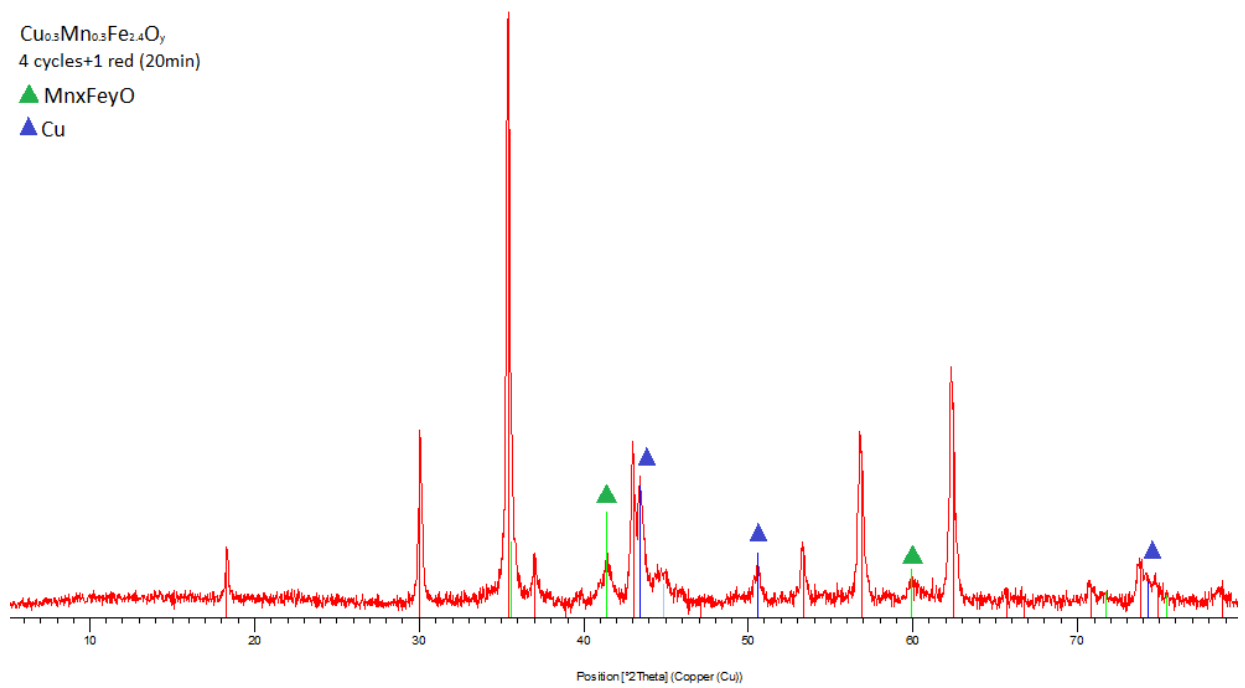
Cu$_{0.6}$Fe$_{2.4}$O$_y$
4 cycles+1 red (20min)
▲ Fe
▲ Cu
▲ Carbides (Fe$_3$C and Fe$_5$C$_2$)

Position [°2Theta] (Copper (Cu))
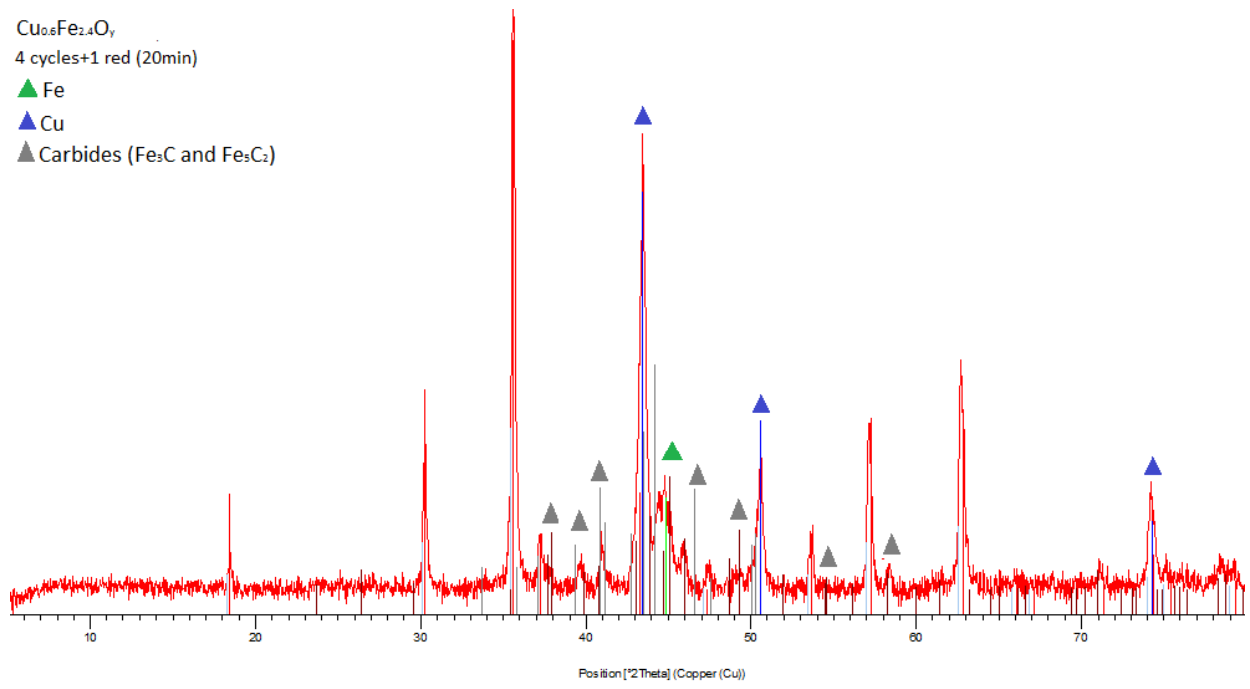
Mg$_{0.6}$Fe$_{2.4}$O$_y$
4 cycles+1 red (20min)
▲ MgxFeyO

Position [°2Theta] (Copper (Cu))
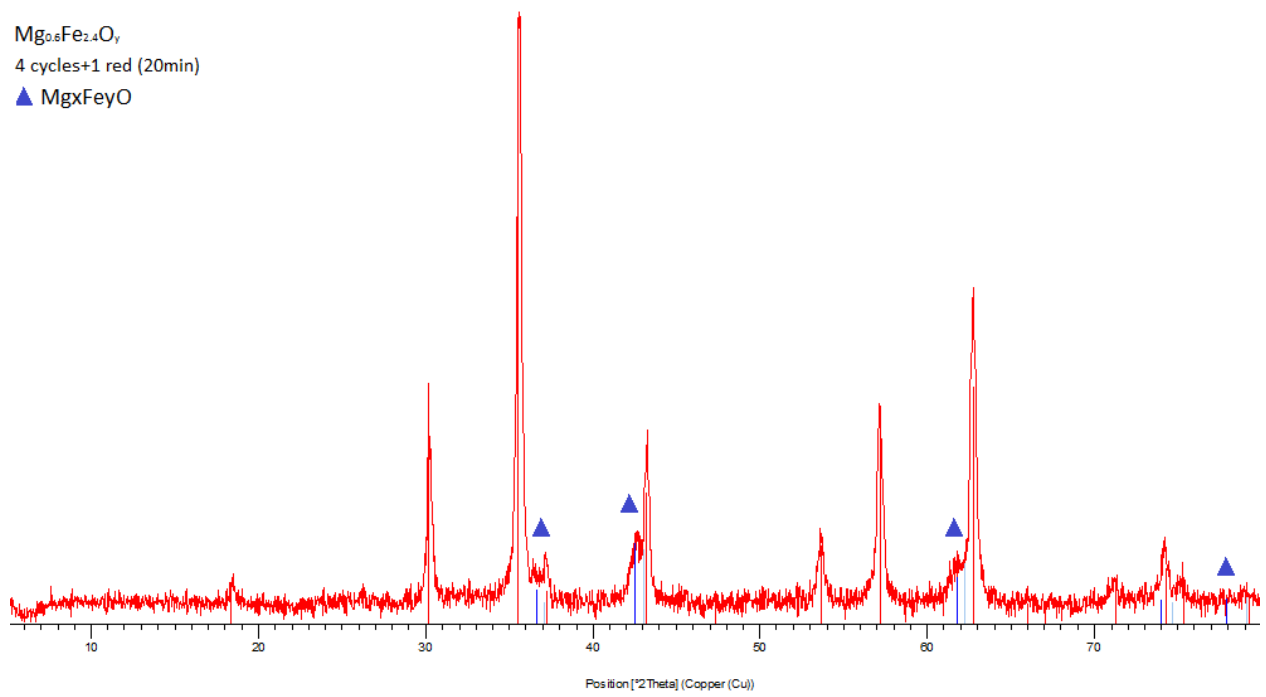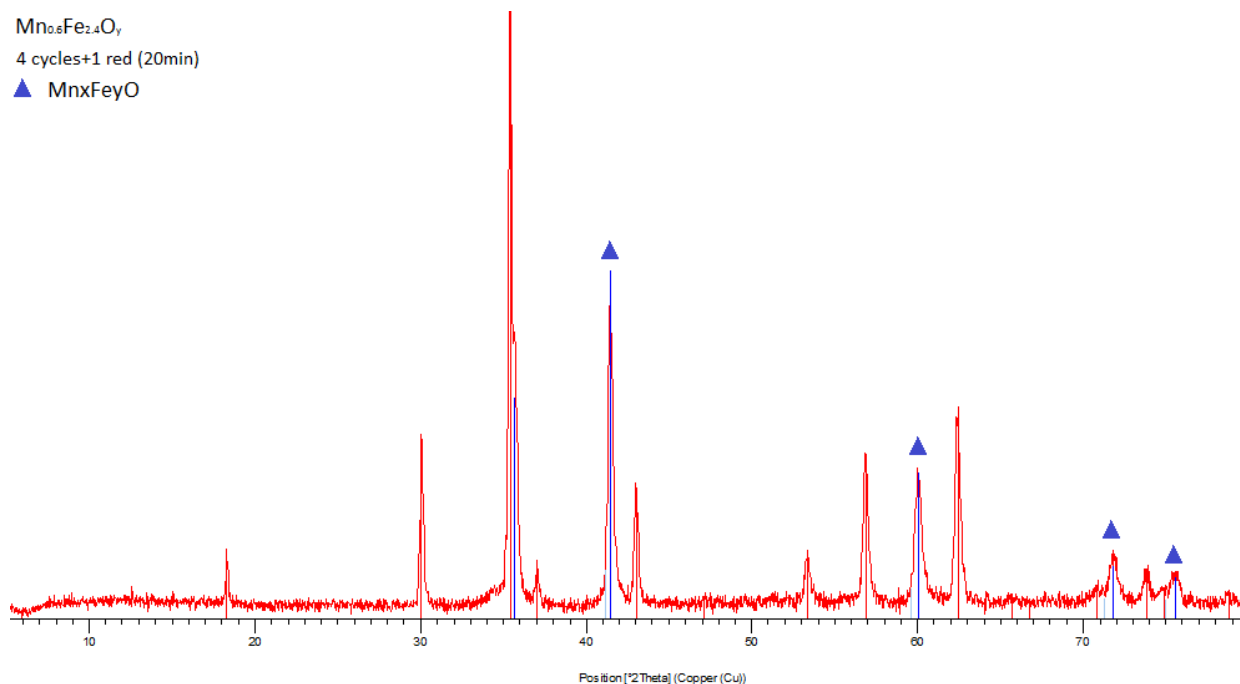
Figure 6-3. XRD patterns for $M_{0.6}Fe_{2.4}O_y$ ferrospinels which are taken after 4 complete cycles (20 min each step) + 1 ethanol reduction (20 min)

6.3. 2nd step: re-oxidation with water at T-450°C

After the reduction with ethanol, the materials were re-oxidized with water steam at 450°C, which corresponds to the second step of the chemical loop. Tests were carried out with the same $M_{0.6}Fe_{2.4}O_y$ materials using different cycling conditions (with duration of 1h, 20 min and 6 min). Important to note, that the Paragraph 6.1 includes the discussion on the 20 min reduction steps (as an optimum cycling time), however this part will touch on the results obtained from 1 h and 6 min cycles, in order to compare the integrated mol of produced H_2 during the 2nd step for the same total *tos*: 1h (total→60 min) = 3 cyc·20 min (total→60 min) = 10 cyc·6 min (total→60 min).

Figure 6-4 shows integrated values for the produced H_2 and CO_x obtained during the 3 complete cycles of 20 min (equal to the total *tos* of 60 min), where bare-Fe_3O_4 was taken as a reference. The obtained results confirm a previously made statement that the nature of the M-incorporated metal affects the redox properties, stability, catalytic activity and overall effectiveness in CLR process of the resulted looping material. Thus, a higher amount of H_2 was obtained over Co-, Cu-, Cu/Mn- and Co/Mn-modified ferrites in comparison to a much lower amount produced over Mn-, Mg- and Ca-modified and non-modified Fe_3O_4 samples. These results lie in parallel with the results obtained during the reduction step

carried out with ethanol; the materials containing in its composition as a foreign metal Co-, Cu-, Cu/Mn- and Co/Mn-cations reached a deeper reduction extent in comparison to Mn-, Ca- and Mg-cations, which in turn leads to a higher amount of H_2 produced on the re-oxidation step with water steam. However, the reduction by ethanol led to a coke deposition and a metal carbides formation. This turned into the generation of CO and CO_2 during the re-oxidation step (Figure 6-4), because of the gasification of carbonaceous residues. Partly, the problem of coke deposition can be overcome by tuning the M-ferrite composition (this effect has been for $Co_{0.6-x}Mn_xFe_{2.4}O_y$ and $Cu_{0.6-x}Mn_xFe_{2.4}O_y$ systems, see CHNS results discussed in the Chapter 5) or by shortening the cycling time of each step to avoid a strong reduction to Fe_xC_y carbides (up to 6 min per 1 cycle). The latter in turn decreases the total amount of produced H_2 due to the incomplete reduction (the effectiveness of CLR process ↓), Figure 6-5. The experiments performed at longer cycling time (much longer than approximately 20 min→ like 1 h cycles) did not show a positive impact on the H_2 production (Figure 6-5), producing much less hydrogen (compare to 20 min cycles) and accumulating more coke (↑ amount of CO_x on the 2nd step and ↑ deactivation due to the incomplete gasification).
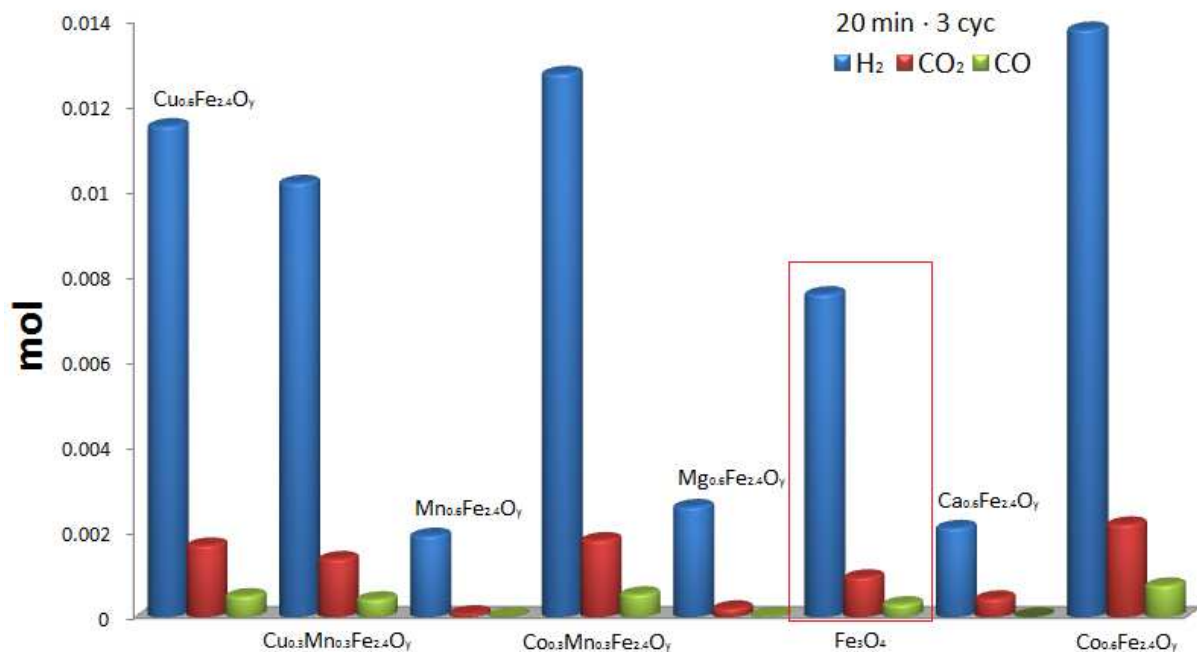
Figure 6-4. Integrated mol of produced H_2 and CO_x during 3 cyc·20 min over $M_{0.6}Fe_{2.4}O_y$ ferrites
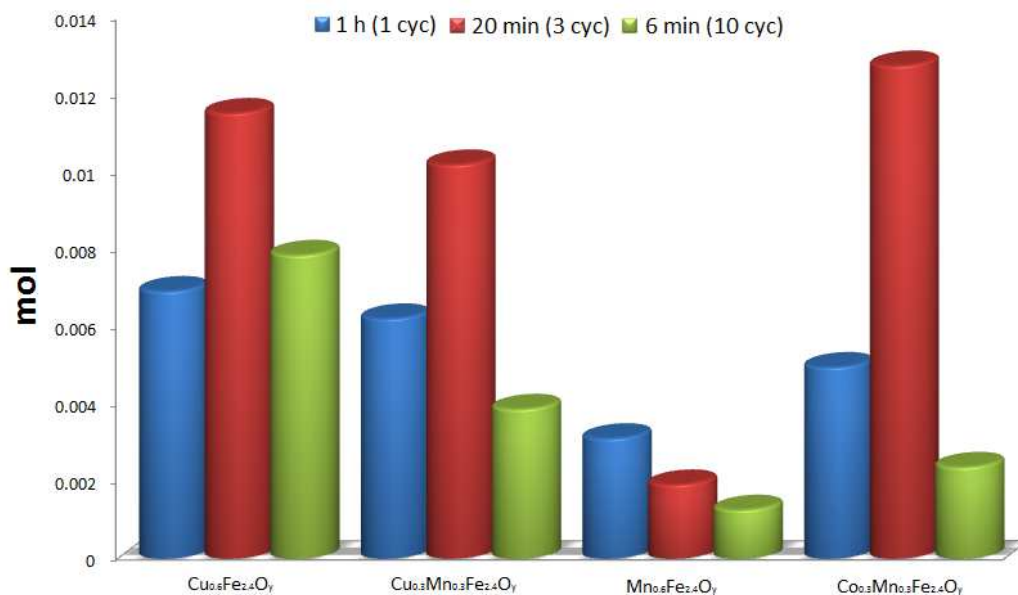
Figure 6-5. Comparison of the H_2-integrated mol produced over $M_{0.6}Fe_{2.4}O_y$ ferrites during the same total tos of 60 min with a different duration time per each cycle (6, 20 and 60 min)

6.4. Ex-situ XRD study over cycled materials after 5 cyc·20 min
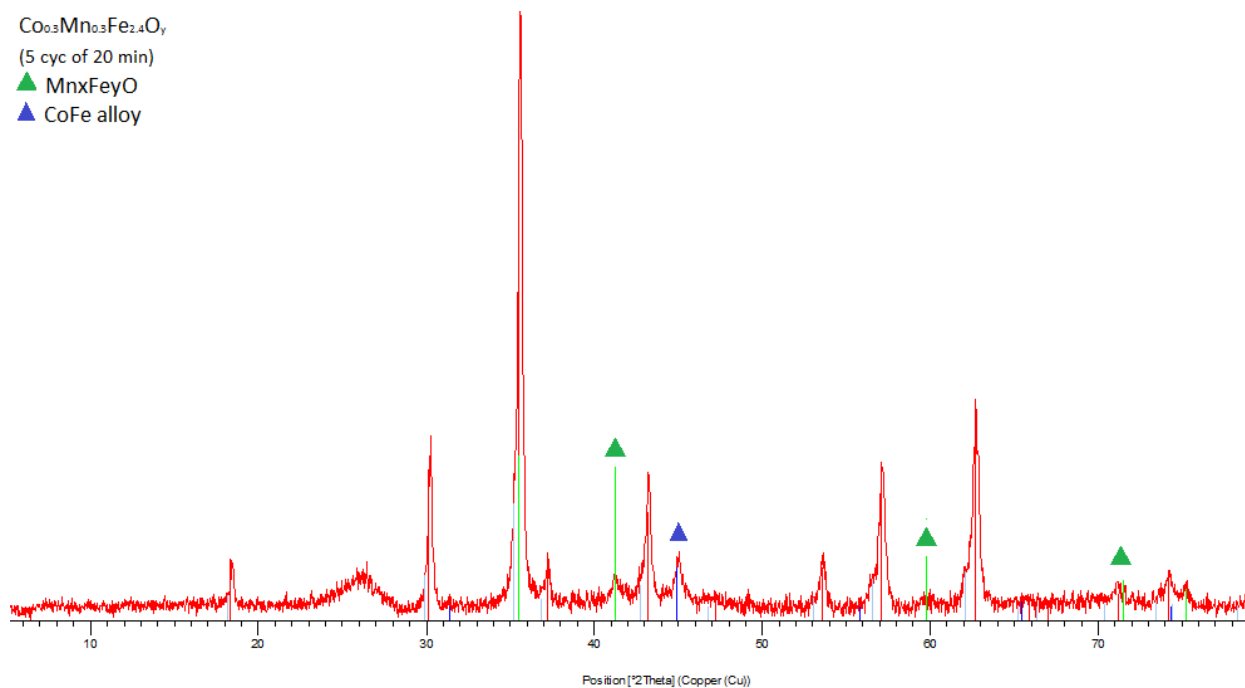
Cu$_{0.3}$Mn$_{0.3}$Fe$_{2.4}$O$_y$
(5 cyc of 20 min)
▲ Cu
▲ MnxFeyO

Position [°2Theta] (Copper (Cu))

Cu$_{0.6}$Fe$_{2.4}$O$_y$
(5 cyc of 20 min)
▲ Cu
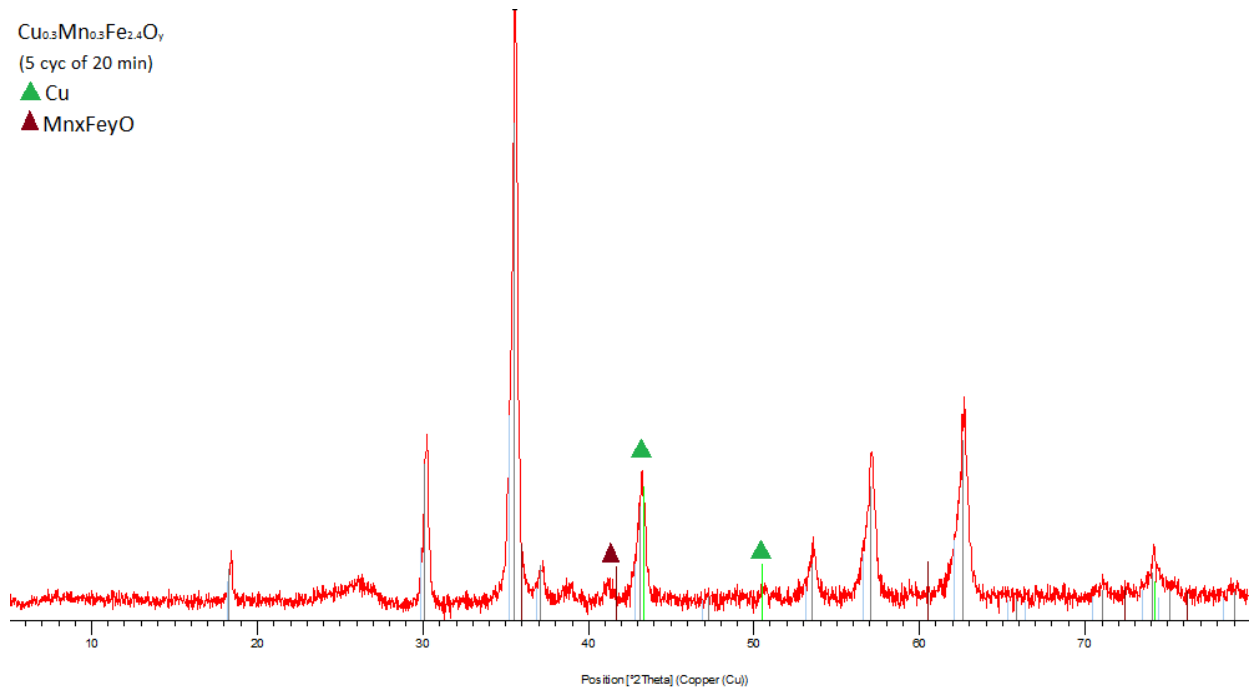
Position [°2Theta] (Copper (Cu))
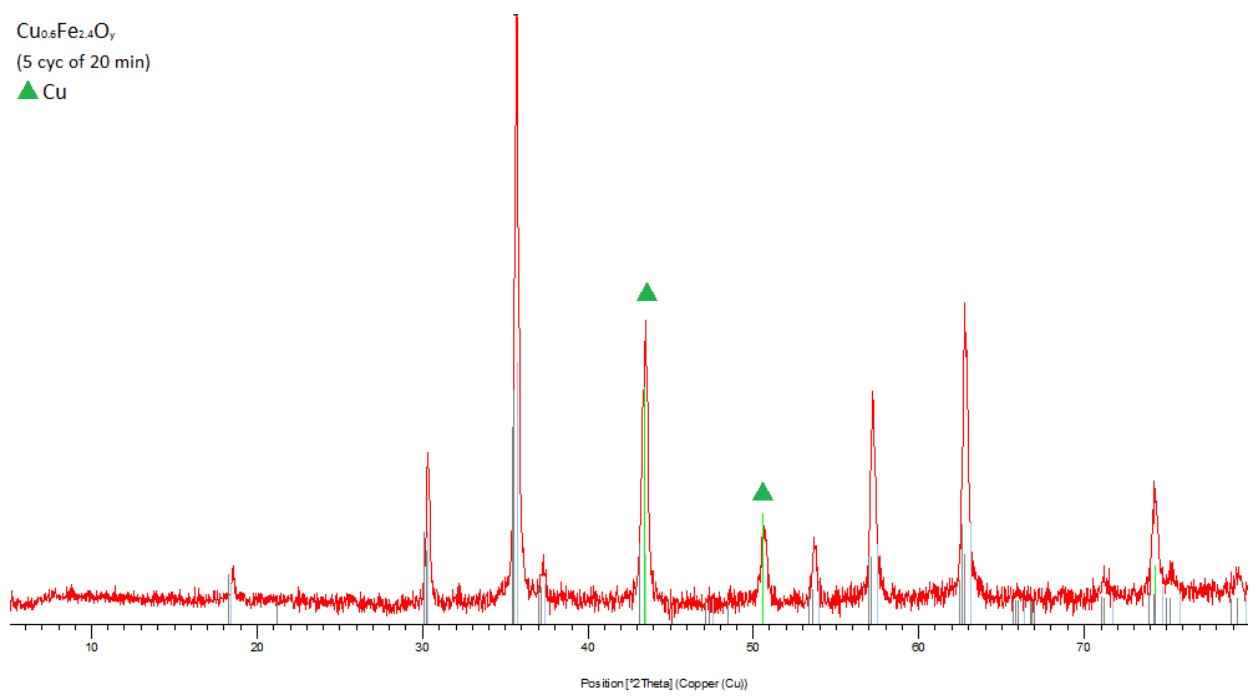
$Mn_{0.6}Fe_{2.4}O_y$
(5 cyc of 20 min)
▲ MnxFeyO

Position [°2Theta] (Copper (Cu))

$Mg_{0.6}Fe_{2.4}O_y$
(5 cyc of 20 min)

Position [°2Theta] (Copper (Cu))
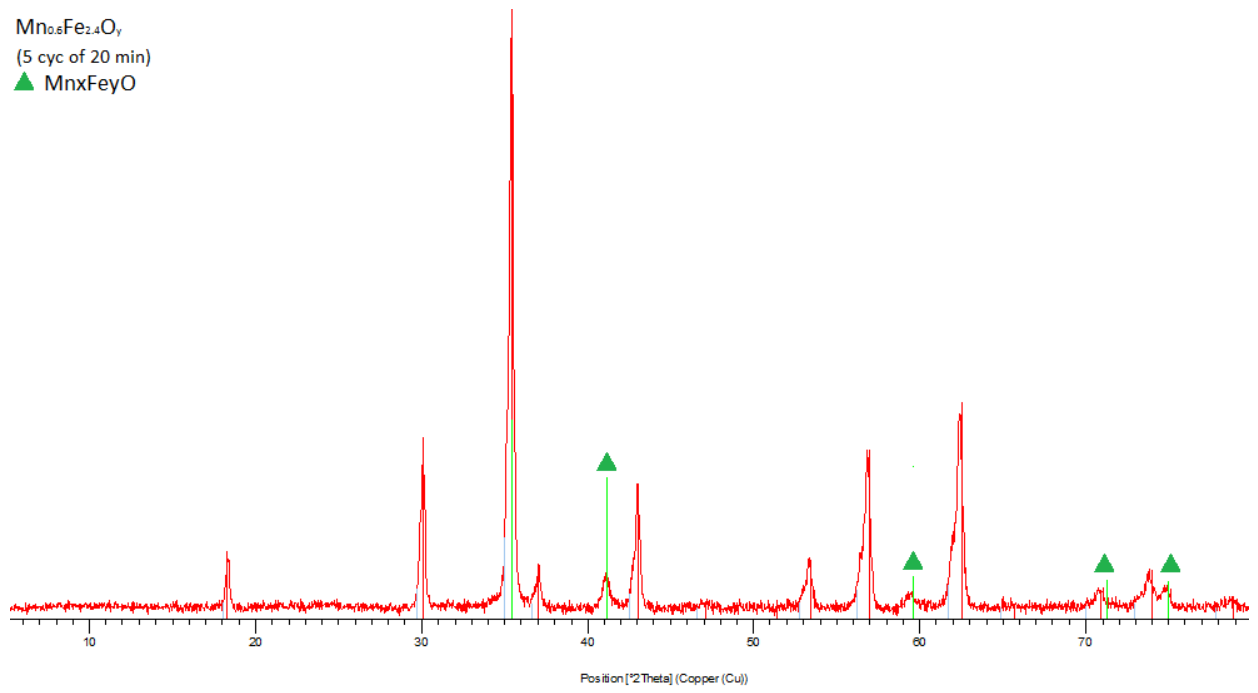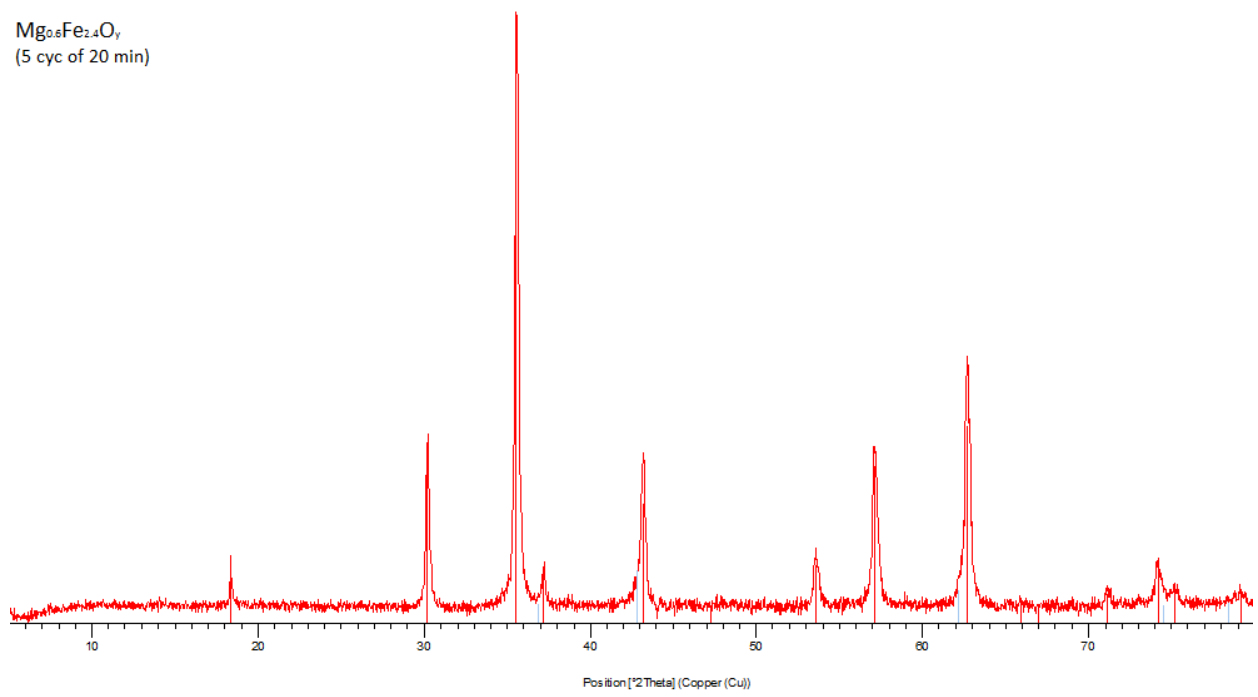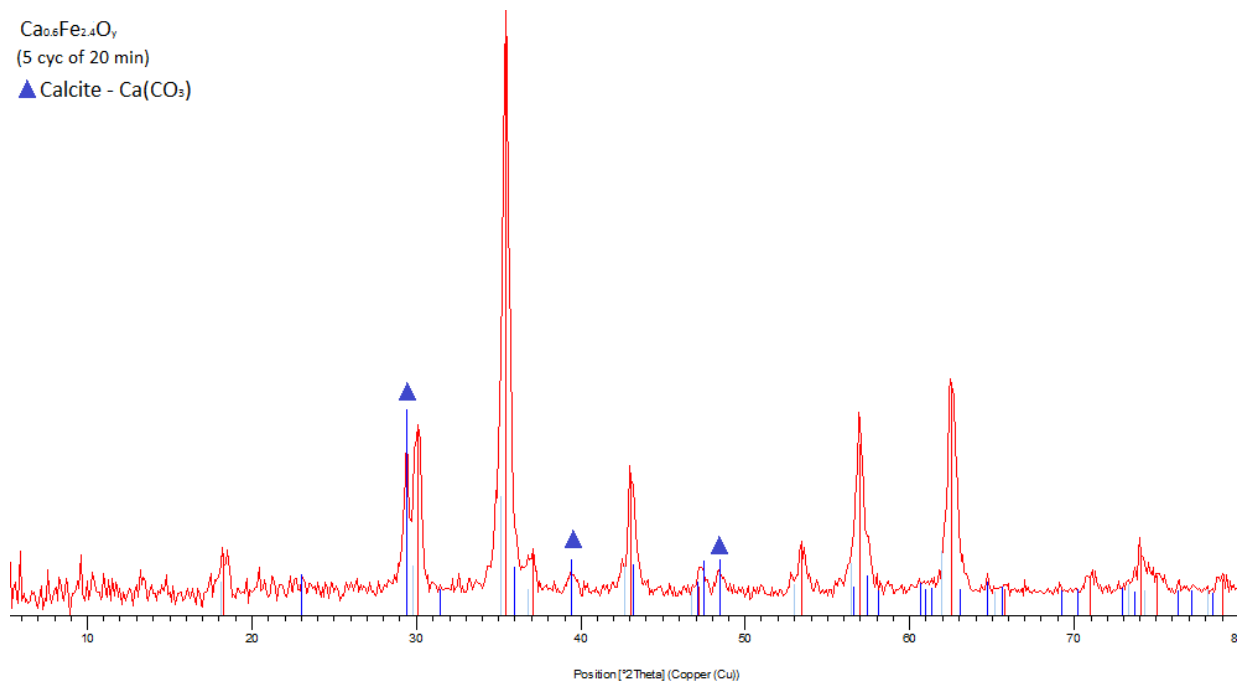
Figure 6-6. XRD patterns for $M_{0.6}Fe_{2.4}O_y$ ferrospinels which are taken after 5 complete cycles (20 min each step)

One of the key points to obtain an efficient CLR process lies in the use of potentially stable (with ability to reform a spinel phase after each complete cycle) and highly active (with no significant loss in the redox performance with cycling) materials. By mean of the ex-situ XRD study, performed on the used $M_{0.6}Fe_{2.4}O_y$ materials, identification of the reformed phases after several complete cycles gave important information on the stability of the spinel phase. Figure 6-6 shows the XRD results taken on the cycled samples after 5 complete cycles. It can be seen that all tested materials underwent some morphological changes and were significantly affected by sintered temperature (narrowing of the patterns), segregation (presence of M and MO phases in addition the spinel one) and coke deposition (for some samples a broad reflection at ~26° (2θ)).

Re-oxidation with water steam at 450°C led to the formation of the following phases: $Co_{0.3}Mn_{0.3}Fe_{2.4}O_y$ (reformed spinel, CoFe alloy and Mn_xFe_yO), $Cu_{0.3}Mn_{0.3}Fe_{2.4}O_y$ (reformed spinel, Cu^0 and Mn_xFe_yO), $Cu_{0.6}Fe_{2.4}O_y$ (reformed spinel and Cu^0), $Mn_{0.6}Fe_{2.4}O_y$ (reformed spinel and Mn_xFe_yO), $Mg_{0.6}Fe_{2.4}O_y$ (reformed spinel) and $Ca_{0.6}Fe_{2.4}O_y$ (reformed spinel and calcite – $Ca(CO_3)$). Nevertheless, all $M_{0.6}Fe_{2.4}O_y$ ferrites have shown that the reformed spinel ($M_{0.6-x}Fe_{2.4+x}O_4$) with a main 100% reflection of (311) plane at 35.5° (2θ) prevails to the other M and MO expelled phases. That is an important prove of the thermodynamic stability of a spinel oxide which allow us to re-obtain the initial spinel phase upon the cycling and in turn

increase the stability of looping material (as seen for $Cu_{0.6}Fe_{2.4}O_y$, $Cu_{0.3}Mn_{0.3}Fe_{2.4}O_y$ and $Co_{0.3}Mn_{0.3}Fe_{2.4}O_y$, in the Paragraph 6.1). Moreover, the evidence of the lower amount of coke deposition over Mn-, Mg- and Ca-containing materials can be seen from the less intensive reflection of carbonaceous species at ~26° (2θ), supported by CHNS analysis (see Chapters 5). The presence of coke indicates that carbon was accumulating during cycling and cannot be simply eliminated by sending a water steam at 450°C. One of the possible solutions to overcome this problem is to add the 3rd step (O_2-feeding to clean the looping material after each complete cycle) (see PART I).

6.5. Raman spectroscopy over cycled materials

Raman spectroscopy was used to identify different kind of carbonaceous species (such as diamond, graphite, and etc.) formed on the surface of the reduced $M_{0.6}Fe_{2.4}O_y$ materials (Figure 6-7 and Figure 6-8). Ordered and disordered carbon may be identified in Raman spectra by its characteristic bands. The spectroscopic study of the cycled materials showed the formation of two types of carbonaceous species, which partly remained intact after the re-oxidation step:

- G band at 1580 cm^{-1}: crystalline graphite (E_{2g2}). This band is due to the stretching of C sp^2 atoms, which are present as an aromatic layer.

- D1 band at 1350 cm^{-1}: diamond-like (A_{1g}). This band is due to C sp^3 atoms present in the diamond structure, but also in defects present in C sp^2 structures[156].
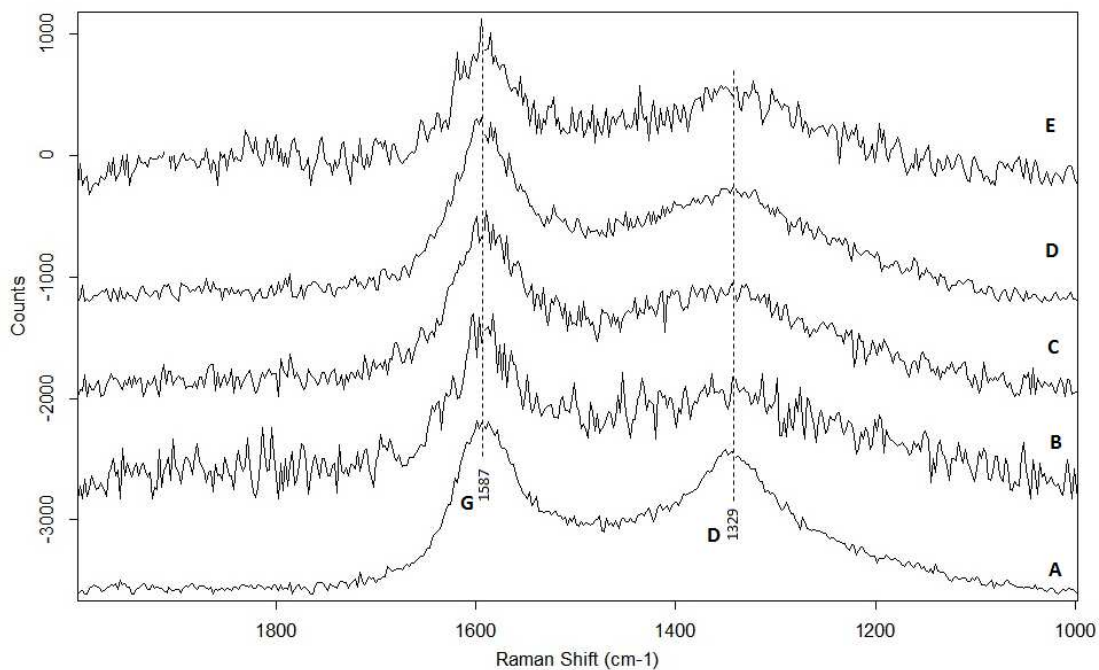
Figure 6-7. Raman spectra of exhausted materials after 6 min·10 cycles over: (A) $Co_{0.6}Fe_{2.4}O_y$; (B) $Mn_{0.3}Co_{0.3}Fe_{2.4}O_y$; (C) $Mn_{0.6}Fe_{2.4}O_y$; (D) $Cu_{0.3}Mn_{0.3}Fe_{2.4}O_y$; (E) $Cu_{0.6}Fe_{2.4}O_y$
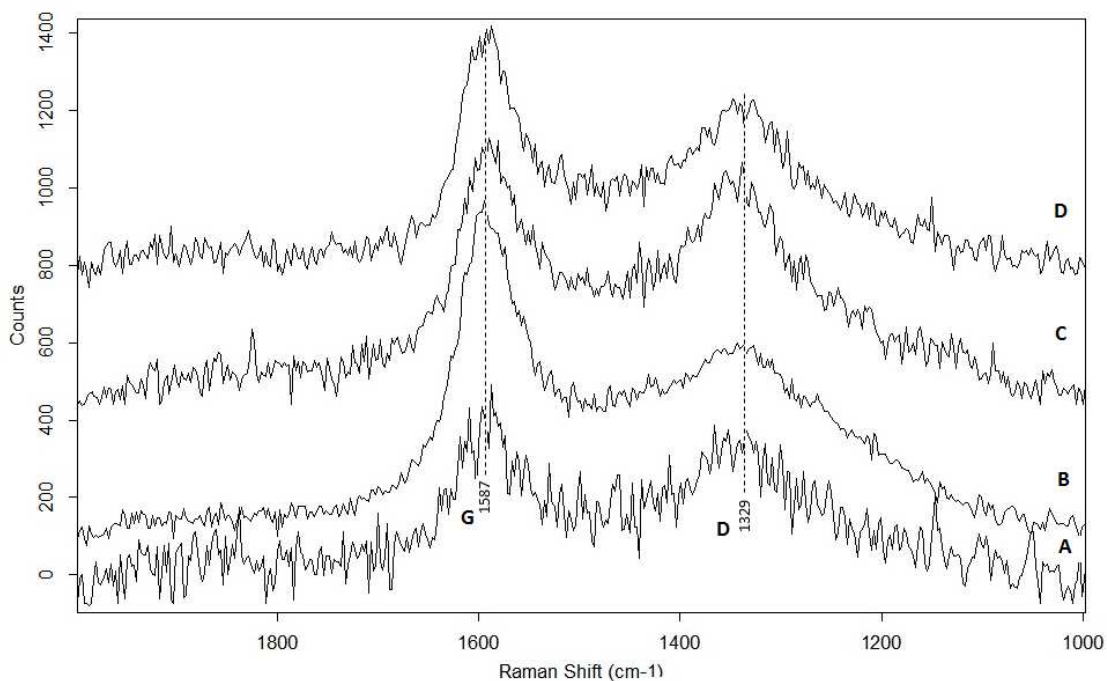

Figure 6-8. Raman spectra of exhausted materials after 20 min·5 cycles over: (A) $Mn_{0.3}Co_{0.3}Fe_{2.4}O_y$; (B) $Mn_{0.6}Fe_{2.4}O_y$; (C) $Cu_{0.3}Mn_{0.3}Fe_{2.4}O_y$; (D) $Cu_{0.6}Fe_{2.4}O_y$

6.6. Conclusions on the study of $M_{0.6-x}Fe_{2.4}O_y$ ferrospinels

The catalytic activity in the ethanol chemical-loop reforming was studied by using TYPE II ferrospinels ($M_{0.6}Fe_{2.4}O_y$) as oxygen carrier looping materials. The composition of $M_{0.6}Fe_{2.4}O_y$ ferrospinel was varied in between the transition metals: Co, Mn, Cu and the alkaline earth metals: Ca and Mg, in order to pursue a higher selectivity to some valuable chemicals produced on the 1st reduction step along with a high purity H_2 produced during the 2nd re-oxidation step. The redox properties of ferrospinels were found to depend strongly on the nature of incorporated cation, which has its affect on the productivity of the 2nd step.

The reduction of M-modified ferrospinels appeared to be a complex process due to the presence of various metal - M (where M is Cu^0, CoFe alloy) and metal oxide-MO (where MO is Mn_xFe_yO and Mg_xFe_yO) reduced forms. Besides, it was observed that the incorporation of Cu-, Mn/Co- or Mn/Cu- cations into a magnetite (Fe_3O_4) crystal structure have a beneficial effect on its stability. An important prove of the thermodynamic stability of spinel oxide was confirmed by XRD study which allow us to re-obtain the initial spinel phase upon the cycling and in turn increase the stability of looping material (as seen for $Cu_{0.6}Fe_{2.4}O_y$, $Cu_{0.3}Mn_{0.3}Fe_{2.4}O_y$ and $Co_{0.3}Mn_{0.3}Fe_{2.4}O_y$).

Moreover, the addition of Mn hindered carbon deposition, which also caused a decrease of the amount of CO_x generated by oxidation with water steam, which is an important issue to produce clean H_2. However, the Mn containing ferrospinels showed a lower efficiency in the removal of the C residues accumulated during the first step. This may lead to the need of a third step of coke removal by air oxidation, if a clean material is needed to perform a following cycle. In an alternative approach, as already pointed out in the literature, the unreactive coke may be maintained as an inert material, provided (that) during successive cycles the further accumulation of coke occurs at a limited extentonly[22,53].

7. TYPE I *vs.* TYPE II FERROSPINELS

The previous Chapters included the results on reactivity tests and material characterizations of TYPE I (Chapter 4) and TYPE II (Chapters 5 and 6) ferrospinels. Consequently, it was necessary to make a general comparison between the various materials in order to make an overall conclusion.

Figure 7-1 summarizes the integrated values for H_2 produced during the 2nd re-oxidation step (referred to 1 complete cycle of 20 min) carried out with the water steam over MFe_2O_4 and $M_{0.6}Fe_{2.4}O_y$ ferrospinels. For understanding the results from different prospective, some important properties are provided in Table 7-1. There are several aspects that have to be underlined, taking into account the primary proposed looping material - Fe_3O_4:

- Mn-incorporation into the $MFe_2O_4/M_{0.6}Fe_{2.4}O_y$ ferrites showed its positive aspect on the lowering the amount of produced coke which tends to accumulate during the 1st reduction step carried out with ethanol stream, see $C\%_w$ (CHNS) in Table 7-1;

- Mn-incorporation increased the $\mathbf{H_2/CO_x}$ ratio, which follows from the previously made statement (*to note*: the higher is the $\mathbf{H_2/CO_x}$ ratio the more 'pure' H_2 is generated during the 2nd re-oxidation step); for comparison Fe_3O_4 itself accounts for $\mathbf{H_2/CO_x=3.5}$, whereas TYPE I: $MnFe_2O_4$ ($\mathbf{H_2/CO_x=15}$), $Co_{0.5}Mn_{0.5}Fe_2O_4$ ($\mathbf{H_2/CO_x=15}$) and TYPE II: $Mn_{0.6}Fe_{2.4}O_y$ ($\mathbf{H_2/CO_x=14}$), $Co_{0.3}Mn_{0.3}Fe_{2.4}O_y$ ($\mathbf{H_2/CO_x=7}$), all the other $\mathbf{H_2/CO_x}$ values are listed in Table 7-1;

- Incorporation of the transition metals, as Cu/Co/Mn (Fe:Cu or (-Co,-Mn) is equal to 2 or 4), has its beneficial effect on the total amount of produced H_2 derived from H_2O in comparison to a non-modified Fe_3O_4 spinel. Hence, the best performance was shown by the following binary/ternary M-modified ferrospinels: TYPE I - $CuFe_2O_4$ (Y-52%), $Cu_{0.5}Co_{0.5}Fe_2O_4$ (Y-46%), $Cu_{0.5}Mn_{0.5}Fe_2O_4$ (Y-37%) and TYPE II – $Cu_{0.6}Fe_{2.4}O_y$ (Y-50%), $Co_{0.6}Fe_{2.4}O_y$;

- Cu/Co- incorporation leads to the increase of $\mathbf{n_{H2}/n_{Eth}}$ ratio, as for TYPE I: $CuFe_2O_4$ ($\mathbf{n_{H2}/n_{Eth}=1.2}$), $Cu_{0.5}Co_{0.5}Fe_2O_4$ ($\mathbf{n_{H2}/n_{Eth}=1.0}$) and TYPE II: $Cu_{0.6}Fe_{2.4}O_y$ ($\mathbf{n_{H2}/n_{Eth}=1.1}$), $Co_{0.6}Fe_{2.4}O_y$ ($\mathbf{n_{H2}/n_{Eth}=1.0}$); which roughly could be correlated to the feasibility of producing H_2 starting from bio-ethanol being based on the H_2 vs. Ethanol heating values (referred to **LHV (Lower Heating Value)**, MJ/kg): **119,96** and **28.86**,

respectively (*note*: in the case of using bio-ethanol as a potential fuel). In another words, the higher is n_{H2}/n_{Eth} the higher is the potential efficiency of CLR (ethanol) process. Of course, there many more aspects that have to be undertaken in order to calculate the actual cost of the CLR process and to estimate a final price of H_2 produced via CLR technology and compare it to the existing ones (*not encompassed in this study*).
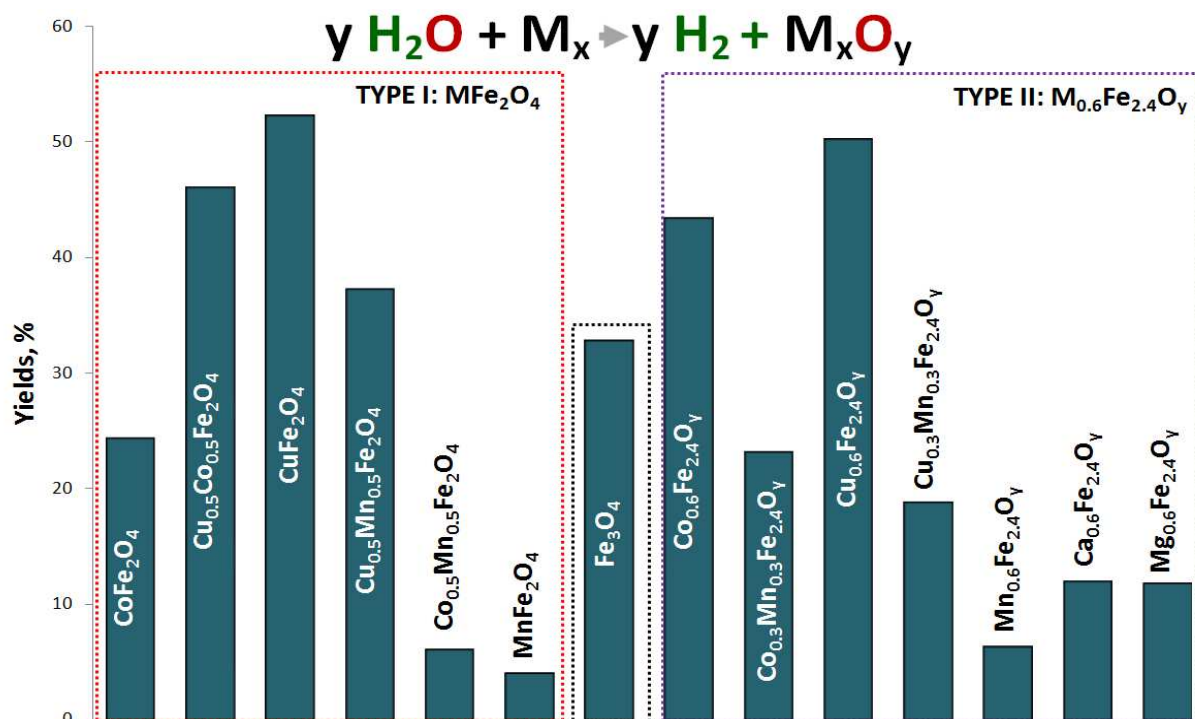
Figure 7-1. Integrated Yields for H_2 produced during 2nd re-oxidation step carried out with steam at $450^{o}C$ over MFe_2O_4 and $M_{0.6}Fe_{2.4}O_y$ ferrospinels (*note*: listed data correspond to the values obtained after 1 complete cycle of 20 min)

Table 7-1. Parameters calculated for MFe_2O_4 and $M_{0.6}Fe_{2.4}O_y$ ferrites (*note*: listed data correspond to the values obtained after 1 complete cycle of 20 min)

	$C \%_w$ after 20 min red with ethanol	H_2/CO_x	Moles of H_2/Moles of Ethanol (n_{H2}/n_{Eth})
TYPE I: MFe_2O_4			
$CoFe_2O_4$	11.6	6	0.5
$Cu_{0.5}Co_{0.5}Fe_2O_4$	16.3	3	1.0
$CuFe_2O_4$	**6.9**	**3**	**1.2**
$Cu_{0.5}Mn_{0.5}Fe_2O_4$	6.1	3	0.8
$Co_{0.5}Mn_{0.5}Fe_2O_4$	1.5	15	0.1

$MnFe_2O_4$	1.7	15	0.09
REFERENCE MATERIAL			
Fe_3O_4	**5.3**	**3.5**	**0.7**
TYPE II: $M_{0.6}Fe_{2.4}O_y$			
$Co_{0.6}Fe_{2.4}O_y$	**9.7**	**3**	**1.0**
$Co_{0.3}Mn_{0.3}Fe_{2.4}O_y$	7.9	7	0.5
$Cu_{0.6}Fe_{2.4}O_y$	9.8	3	1.1
$Cu_{0.3}Mn_{0.3}Fe_{2.4}O_y$	5.0	4	0.4
$Mn_{0.6}Fe_{2.4}O_y$	2.2	14	0.1
$Ca_{0.6}Fe_{2.4}O_y$	-	3	0.3
$Mg_{0.6}Fe2.4Oy$	-	7	0.3

Being guided by the data presented above, Figure 7-2 and Table 7-2 resume a further comparison between TYPE I and TYPE II ferrospinels, in particularly focusing on the H_2 produced during several consecutive cycles (referred to 3 complete cycles of 20 min). From this point, the samples been narrowed to the ones which gave the max yields to hydrogen (see Figure 7-1). Hence, the following statements can be made:

- consecutive utilization of TYPE I: $CoFe_2O_4$, $CuFe_2O_4$, $Cu_{0.5}Co_{0.5}Fe_2O_4$ and TYPE II: $Co_{0.6}Fe_{2.4}O_y$, $Co_{0.3}Mn_{0.3}Fe_{2.4}O_y$, $Cu_{0.6}Fe_{2.4}O_y$, $Cu_{0.3}Mn_{0.3}Fe_{2.4}O_y$, $Co_{0.3}Mn_{0.3}Fe_{2.4}O_y$ ferrospinels as looping materials resulted in higher amounts of produced hydrogen (*given in moles*) which surpass the value obtained over the reference material – Fe_3O_4, see Figure 7-2;

- Increasing the total *tos* from 20 to 60 min (accounts the total time for the reduction/re-oxidation step) leads to the decreasing of **H_2/CO_x**ratio, which in its turn affects the final purity of the target gas – H_2 (*note*: this problem can be overcome by implementation of 3 steps CLR process with the 3rd step being carried out with air, as discussed in Chapter 4);

- **$CuFe_2O_4$** (as representative of **TYPE I** ferrospinel group of materials) and **$Co_{0.6}Fe_{2.4}O_y$** (as representative of **TYPE II** ferrospinel group of materials) showed the higher **n_{H2}/n_{Eth}** ratio of **1** (referred to the total value for 3 consecutive cycles) which is in fact twice as much as obtained with Fe_3O_4 (**$n_{H2}/n_{Eth}=0.5$**).
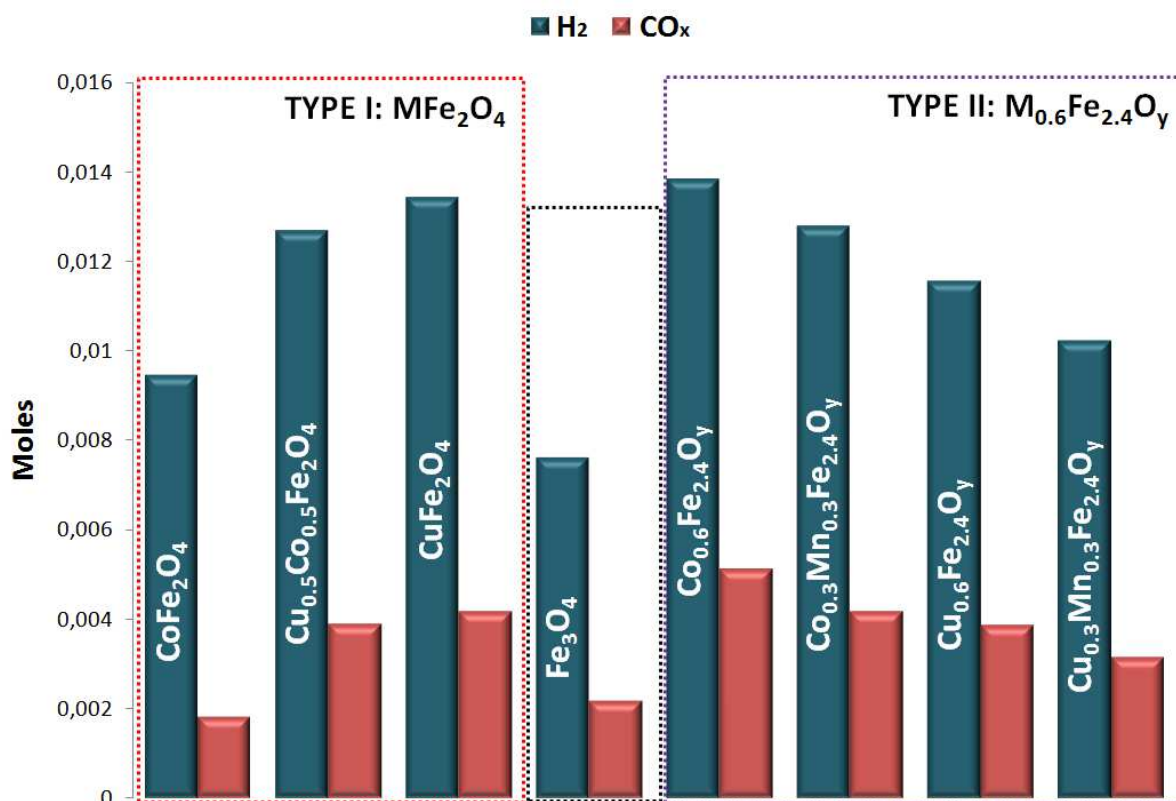
Figure 7-2. Integrated moles for H$_2$ and CO$_x$ produced during 2nd re-oxidation step carried out with steam at 450°C over MFe$_2$O$_4$ and M$_{0.6}$Fe$_{2.4}$O$_y$ ferrospinels (*note*: listed data correspond to the values obtained after 3 complete cycle of 20 min)

Table 7-2. Parameters calculated for MFe$_2$O$_4$ and M$_{0.6}$Fe$_{2.4}$O$_y$ ferrites (*note*: listed data correspond to the values obtained after 3 complete cycle of 20 min)

	H$_2$/CO$_x$	Moles of H$_2$/Moles of Ethanol
TYPE I: MFe$_2$O$_4$		
CoFe$_2$O$_4$	5	0.7
Cu$_{0.5}$Co$_{0.5}$Fe$_2$O$_4$	3	0.9
CuFe$_2$O$_4$	**3**	**1.0**
REFERENCE MATERIAL		
Fe$_3$O$_4$	**3**	**0.5**
TYPE II: M$_{0.6}$Fe$_{2.4}$O$_y$		
Co$_{0.6}$Fe$_{2.4}$O$_y$	**3**	**1.0**
Co$_{0.3}$Mn$_{0.3}$Fe$_{2.4}$O$_y$	3	0.9
Cu$_{0.6}$Fe$_{2.4}$O$_y$	3	0.8
Cu$_{0.3}$Mn$_{0.3}$Fe$_{2.4}$O$_y$	3	0.7

7.1. Conclusions: TYPE I *vs.* TYPE II ferrospinels

To finalize the comparison between TYPE I (MFe_2O_4, where Fe/M=2/1) *vs.* TYPE II ($M_{0.6}Fe_{2.4}O_y$, where Fe/M=4/1) ferrospinels and the reference material – Fe_3O_4:

- M-incorporation (such as Cu, Co, Mn or Cu/Co, Co/Mn, Cu/Mn) strongly affects the final redox properties of the resulted materials → MFe_2O_4 and $M_{0.6}Fe_{2.4}O_y$ ferrospinels. Besides, the presence of M in its smaller amount (as in the TYPE II - $M_{0.6}Fe_{2.4}O_y$ with Fe/M=4/1) was already sufficient to see positive results on the production of H_2 via 2 steps CLR of bio-ethanol compared to the non-modified Fe_3O_4. Further increase of the M amount didn't contribute to any additional improvements of the materials performance (as in the TYPE I - MFe_2O_4 with Fe/M=2/1), but, even on the contrary, had shown an opposite effect (as in the case of $CoFe_2O_4$ and $Co_{0.6}Fe_{2.4}O_y$ ferrites and explained by scarce attitude of the Co^0 to be re-oxidized by means of water as the only oxidant). *That is to say,* the utilization of TYPE II - $M_{0.6}Fe_{2.4}O_y$ ferrospinels, as oxygen and electrons carrier materials, appears to be more appealing for the 2 steps CLR of bio-ethanol, since the 2nd step carried out with water steam leads to incomplete re-oxidation of the previously reduced M^{2+} to its metallic component (Co^0 and Cu^0), which in its turn results in the conclusion that as much of Co and Cu are present in the final M-modified ferrite as less material in its re-oxidized form is available for further reduction in the consecutive cycles.

In conclusion→ despite that several improved looping materials have been identified, complete appraisals of their performance and further optimization studies are required in order to give information on the overall conversion efficiencies, process design and economics.

LITERATURE

1   R. M. Navarro, M. C. Sánchez-Sánchez, M. C. Alvarez-Galvan, F. Del Valle and J. L. G. Fierro, *Energy Environ. Sci.*, 2009, **2**, 35–54.

2   G. Tsekouras, D. Neagu and J. T. S. Irvine, *Energy Environ. Sci.*, 2013, **6**, 256–266.

3   B. K. Boggs, R. L. King and G. G. Botte, *Chem. Commun. (Camb).*, 2009, 4859–4861.

4   T. Lazarides, M. Delor, I. V Sazanovich, T. M. McCormick, I. Georgakaki, G. Charalambidis, J. A. Weinstein and A. G. Coutsolelos, *Chem. Commun. (Camb).*, 2014, **50**, 521–523.

5   J. W. Jurss, R. S. Khnayzer, J. A. Panetier, K. A. El Roz, E. M. Nichols, M. Head-Gordon, J. R. Long, F. N. Castellano and C. J. Chang, *Chem. Sci.*, 2015, **6**, 4954–4972.

6   M. Ni, D. Y. C. Leung and M. K. H. Leung, *Int. J. Hydrogen Energy*, 2007, **32**, 3238–3247.

7   L. Chen, C. K. S. Choong, Z. Zhong, L. Huang, T. P. Ang, L. Hong and J. Lin, *J. Catal.*, 2010, **276**, 197–200.

8   F. Fresno, T. Yoshida, N. Gokon, R. Fernández-Saavedra and T. Kodama, *Int. J. Hydrogen Energy*, 2010, **35**, 8503–8510.

9   P. Charvin, S. Abanades, G. Flamant and F. Lemort, *Energy*, 2007, **32**, 1124–1133.

10   N. Hanada, S. Hino, T. Ichikawa, H. Suzuki, K. Takai and Y. Kojima, *Chem. Commun. (Camb).*, 2010, **46**, 7775–7.

11   P. Gupta, L. G. Velazquez-Vargas and L. Fan, *Energy and Fuels*, 2007, **21**, 2900–2908.

12   V. Hacker, R. Fankhauser, G. Faleschini, H. Fuchs, K. Friedrich, M. Muhr and K. Kordesch, *J. Power Sources*, 2000, **86**, 531–535.

13   V. Hacker, G. Faleschini, H. Fuchs, R. Fankhauser, G. Simader, M. Ghaemi, B. Spreitz and K. Friedrich, *J. Power Sources*, 1998, **71**, 226–230.

14   R. Sime, J. Kuehni, L. D. Souza, E. Elizondo and S. Biollaz, *Int. J. Hydrogen Energy*, 2003, **28**, 491–498.

15   V. Hacker, *J. Power Sources*, 2003, **118**, 311–314.

16   K. Go, S. Son, S. Kim, K. Kang and C. Park, *Int. J. Hydrogen Energy*, 2009, **34**, 1301–1309.

17   K. Go, S. Son and S. Kim, *Int. J. Hydrogen Energy*, 2008, **33**, 5986–5995.

18 K. Otsuka, A. Mito, S. Takenaka and I. Yamanaka, 2001, **26**, 191–194.

19 V. V. Galvita, H. Poelman and G. B. Marin, *Top. Catal.*, 2011, **54**, 907–913.

20 M. Bleeker, S. Gorter, S. Kersten, L. van der Ham, H. van den Berg and H. Veringa, *Clean Technol. Environ. Policy*, 2009, **12**, 125–135.

21 M. F. Bleeker, S. R. a. Kersten and H. J. Veringa, *Catal. Today*, 2007, **127**, 278–290.

22 R. Campo, P. Durán, J. Plou, J. Herguido and J. a. Peña, *J. Power Sources*, 2013, **242**, 520–526.

23 J. A. Peña, E. Lorente, E. Romero and J. Herguido, *Catal. Today*, 2006, **116**, 439–444.

24 E. Lorente, J. A. Peña and J. Herguido, *J. Power Sources*, 2009, **192**, 224–229.

25 S. A. Ghoneim, R. A. El-salamony and S. A. El-temtamy, 2016, 116–139.

26 M. A. Pefia, 1996, **144**, 7–57.

27 J. Adanez, A. Abad, F. Garcia-Labiano, P. Gayan and L. F. de Diego, *Prog. Energy Combust. Sci.*, 2012, **38**, 215–282.

28 P. Cho, T. Mattisson and A. Lyngfelt, *Ind. Eng. Chem. Res.*, 2005, **44**, 668–676.

29 V. Galvita and K. Sundmacher, *Appl. Catal. A Gen.*, 2005, **289**, 121–127.

30 L. Protasova and F. Snijkers, *Fuel*, 2016, **181**, 75–93.

31 D. Yamaguchi, L. Tang and N. Burke, .

32 K.-S. Cha, H.-S. Kim, B.-K. Yoo, Y.-S. Lee, K.-S. Kang, C.-S. Park and Y.-H. Kim, *Int. J. Hydrogen Energy*, 2009, **34**, 1801–1808.

33 K.-S. Kang, C.-H. Kim, W.-C. Cho, K.-K. Bae, S.-W. Woo and C.-S. Park, *Int. J. Hydrogen Energy*, 2008, **33**, 4560–4568.

34 D. Yamaguchi, L. Tang, L. Wong, N. Burke, D. Trimm, K. Nguyen and K. Chiang, *Int. J. Hydrogen Energy*, 2011, **36**, 6646–6656.

35 S. Takenaka, N. Hanaizumi, V. Son and K. Otsuka, *J. Catal.*, 2004, **228**, 405–416.

36 K.-S. Kang, C.-H. Kim, K.-K. Bae, W.-C. Cho, W.-J. Kim, Y.-H. Kim, S.-H. Kim and C.-S. Park, *Int. J. Hydrogen Energy*, 2010, **35**, 568–576.

37 T. Kodama, T. Shimizu, T. Satoh and M. Nakata, *sola*, 2003, **73**, 363–374.

38   K. Otsuka, T. Kaburagi, C. Yamada and S. Takenaka, *J. Power Sources*, 2003, **122**, 111–121.

39   E. Lorente, J. a. Peña and J. Herguido, *Int. J. Hydrogen Energy*, 2011, **36**, 7043–7050.

40   S. Takenaka, T. Kaburagi, C. Yamada, K. Nomura and K. Otsuka, *J. Catal.*, 2004, **228**, 66–74.

41   S. Takenaka, K. Nomura, N. Hanaizumi and K. Otsuka, *Appl. Catal. A Gen.*, 2005, **282**, 333–341.

42   J. C. Ryu, D. H. Lee, K. S. Kang, C. S. Park, J. W. Kim and Y. H. Kim, *J. Ind. Eng. Chem.*, 2008, **14**, 252–260.

43   K. Otsuka, C. Yamada, T. Kaburagi and S. Takenaka, *Int. J. Hydrogen Energy*, 2003, **28**, 335–342.

44   V. J. Aston, B. W. Evanko and A. W. Weimer, *Int. J. Hydrogen Energy*, 2013, **38**, 9085–9096.

45   S. Bhavsar, B. Tackett and G. Veser, *Fuel*, 2014, **136**, 268–279.

46   F.-X. Chiron and G. S. Patience, *Int. J. Hydrogen Energy*, 2012, **37**, 10526–10538.

47   F.-X. Chiron, G. S. Patience and S. Rifflart, *Chem. Eng. Sci.*, 2011, **66**, 6324–6330.

48   C.-C. Cormos, *Int. J. Hydrogen Energy*, 2010, **35**, 2278–2289.

49   K. Go, S. Son, S. Kim, K. Kang and C. Park, *Int. J. Hydrogen Energy*, 2009, **34**, 1301–1309.

50   M. Källén, P. Hallberg, M. Rydén, T. Mattisson and A. Lyngfelt, *Fuel Process. Technol.*, 2014, **124**, 87–96.

51   K.-S. Kang, C.-H. Kim, W.-C. Cho, K.-K. Bae, S.-W. Woo and C.-S. Park, *Int. J. Hydrogen Energy*, 2008, **33**, 4560–4568.

52   S. Lorentzou, a. Zygogianni, K. Tousimi, C. Agrafiotis and a. G. Konstandopoulos, *J. Alloys Compd.*, 2009, **483**, 302–305.

53   M. Luo, S. Wang, L. Wang and M. Lv, *J. Power Sources*, 2014, **270**, 434–440.

54   M. G. Rosmaninho, F. C. C. Moura, L. R. Souza, R. K. Nogueira, G. M. Gomes, J. S. Nascimento, M. C. Pereira, J. D. Fabris, J. D. Ardisson, M. S. Nazzaro, K. Sapag, M. H. Araújo and R. M. Lago, *Appl. Catal. B Environ.*, 2012, **115-116**, 45–52.

55   M. Rydén, M. Källén, D. Jing, A. Hedayati, T. Mattisson and A. Lyngfelt, *Energy Procedia*, 2014, **51**, 85–98.

56   S. Yang, K. Kim, J. Baek, J. Kim, J. B. Lee, C. K. Ryu and G. Lee, 2012.

57   M. North-holland, A. Materials and G. B. Aktiengesellschaft, 2005, **74**, 2005.

58   W. Ponhan and S. Maensiri, *Solid State Sci.*, 2009, **11**, 479–484.

59   D. Gao, Z. Shi, Y. Xu, J. Zhang, G. Yang, J. Zhang, X. Wang and D. Xue, *Nanoscale Res. Lett.*, 2010, **5**, 1289–1294.

60   V. G. Harris, A. Geiler, Y. Chen, S. D. Yoon, M. Wu, A. Yang, Z. Chen, P. He, P. V. Parimi, X. Zuo, C. E. Patton, M. Abe, O. Acher and C. Vittoria, *J. Magn. Magn. Mater.*, 2009, **321**, 2035–2047.

61   M. Pardavi-Horvath, *J. Magn. Magn. Mater.*, 2000, **215**, 171–183.

62   E. Auzans, D. Zins, E. Blums and R. Massart, *J. Mater. Sci.*, 1999, **34**, 1253–1260.

63   F. A. Tourinho, R. Franck and R. Massart, *J. Mater. Sci.*, 1990, **25**, 3249–3254.

64   S. Rana, a. Gallo, R. S. Srivastava and R. D. K. Misra, *Acta Biomater.*, 2007, **3**, 233–242.

65   C. Sun, J. Lee and M. Zhang, *Adv. Drug Deliv. Rev.*, 2008, **60**, 1252–1265.

66   P. Pradhan, J. Giri, R. Banerjee, J. Bellare and D. Bahadur, *J. Magn. Magn. Mater.*, 2007, **311**, 208–215.

67   J. a. Toledo-Antonio, N. Nava, M. Martínez and X. Bokhimi, *Appl. Catal. A Gen.*, 2002, **234**, 137–144.

68   R. J. Rennard and W. L. Kehl, *J. Catal.*, 1971, **21**, 282–293.

69   C. G. Ramankutty, S. Sugunan and B. Thomas, *J. Mol. Catal. A Chem.*, 2002, **187**, 105–117.

70   E. Manova, T. Tsoncheva, D. Paneva, I. Mitov, K. Tenchev and L. Petrov, *Appl. Catal. A Gen.*, 2004, **277**, 119–127.

71   N. Ma, Y. Yue, W. Hua and Z. Gao, *Appl. Catal. A Gen.*, 2003, **251**, 39–47.

72   S. K. Pardeshi and R. Y. Pawar, *Mater. Res. Bull.*, 2010, **45**, 609–615.

73   M. Florea, M. Alifanti, V. I. Parvulescu, D. Mihaila-Tarabasanu, L. Diamandescu, M. Feder, C. Negrila and L. Frunza, *Catal. Today*, 2009, **141**, 361–366.

74   C. U. Aniz, *Open J. Phys. Chem.*, 2011, **01**, 124–130.

75   C. Nordhei, K. Mathisen, I. Bezverkhyy and D. Nicholson, *J. Phys. Chem. C*, 2008, **112**, 6531–6537.

76   N. Rezlescu, E. Rezlescu, P. D. Popa, C. Doroftei and M. Ignat, *Appl. Catal. B Environ.*, 2014, **158-159**, 70–75.

77   A. Urdă, A. Herraïz, Á. Rédey and I.-C. Marcu, *Catal. Commun.*, 2009, **10**, 1651–1655.

78   H. Xi, X. Hou, Y. Liu, S. Qing and Z. Gao, *Angew. Chem. Int. Ed. Engl.*, 2014, 1–5.

79   P. Lahiri and S. K. Sengupta, *Can. J. Chem.*, 1991, **69**, 33–36.

80   A. I. Onuchukwu, *J. Chem. Soc. Faraday Trans. 1*, 1984, **80**, 1447.

81   S. Briceno, H. Del Castillo, Sagredo, W. Bramer-Escamilla and P. Silva, *Appl. Surf. Sci.*, 2012, **263**, 100–103.

82   A. Khan and P. G. Smirniotis, *J. Mol. Catal. A Chem.*, 2008, **280**, 43–51.

83   A. Khan, P. Chen, P. Boolchand and P. Smirniotis, *J. Catal.*, 2008, **253**, 91–104.

84   R. Ramanathan and S. Sugunan, *Catal. Commun.*, 2007, **8**, 1521–1526.

85   S. K. Pardeshi and R. Y. Pawar, *Mater. Res. Bull.*, 2010, **45**, 609–615.

86   J. Tong, L. Bo, Z. Li, Z. Lei and C. Xia, *J. Mol. Catal. A Chem.*, 2009, **307**, 58–63.

87   M. Kooti and M. Afshari, *Sci. Iran.*, 2012, **19**, 1991–1995.

88   1–29.

89   U. Muller, *Inorganic structural chemistry*, Wiley, second edi., 2001, vol. 40.

90   B. D. Hosterman, 2011.

91   M. E. Melinda Darby Dyar and Gunter, *Mineralogy and Optical Mineralogy*, Mineralogical Society of America, 2008.

92   G. Leofanti, G. Tozzola, M. Padovan, G. Petrini, S. Bordiga and A. Zecchina, 1997, **34**, 307–327.

93   Z. M. Khoshhesab, in *Infrared Spectroscopy - Materials Science, Engineering and Technology*, ed. T. Theophile, INTECH, 2012, p. 510.

94   J. V. Ochoa, C. Trevisanut, J.-M. M. Millet, G. Busca and F. Cavani, *J. Phys. Chem. C*, 2013, **117**, 23908–23918.

95   C. Resini, T. Montanari, L. Barattini, G. Ramis, G. Busca, S. Presto, P. Riani, R. Marazza, M. Sisani, F. Marmottini and U. Costantino, *Appl. Catal. A Gen.*, 2009, **355**, 83–93.

96   S. S. Ata-Allah, *J. Magn. Magn. Mater.*, 2004, **284**, 227–238.

97 M. Domok, M. Toth, J. Rasko and a Erdohelyi, *Appl. Catal. B Environ.*, 2007, **69**, 262–272.

98 K. Rintramee, K. Föttinger, G. Rupprechter and J. Wittayakun, *Appl. Catal. B Environ.*, 2012, **115-116**, 225–235.

99 G. Busca, U. Costantino, T. Montanari, G. Ramis, C. Resini and M. Sisani, *Int. J. Hydrogen Energy*, 2010, **35**, 5356–5366.

100 S. Cocchi, *Tesi*, 2012, 215.

101 C. Trevisanut, Università di Bologna, 2014.

102 N. Ballarini, F. Cavani, S. Passeri, L. Pesaresi, A. F. Lee and K. Wilson, *Appl. Catal. A Gen.*, 2009, **366**, 184–192.

103 S. Cocchi, M. Mari, F. Cavani and J.-M. M. Millet, *Appl. Catal. B Environ.*, 2014, **152-153**, 250–261.

104 A. C. A. Reed S.J.B., *Microprobe Analysis*, Wiley, New York, 1973.

105 J. P. Chen and C. M. Sorensen, 1996, **54**, 9288–9296.

106 O. Vozniuk, S. Agnoli, L. Artiglia, A. Vassoi, N. Tanchoux, F. Di Renzo, G. Granozzi and F. Cavani, *Green Chem.*, 2015.

107 P. Chandramohan, M. P. Srinivasan, S. Velmurugan and S. V. Narasimhan, *J. Solid State Chem.*, 2011, **184**, 89–96.

108 B. D. Hosterman, 2011.

109 V. D'Ippolito, G. B. Andreozzi, D. Bersani and P. P. Lottici, *J. Raman Spectrosc.*, 2015, **46**, 1255–1264.

110 N. Z. Lazarevic, Z, Jovalekic, C, Milutinovic, A, Romcevic, M.J, Romcevic, *Acta Phys. Pol. A*, 2012, **121**, 682–686.

111 J. J. Graves, P.R., Johnston, C., Campaniello, *Mater. Res. Bull.*, 1988, **23**, 1651–1660.

112 a. Pineau, N. Kanari and I. Gaballah, *Thermochim. Acta*, 2006, **447**, 89–100.

113 a. Pineau, N. Kanari and I. Gaballah, *Thermochim. Acta*, 2007, **456**, 75–88.

114 W. K. Jozwiak, E. Kaczmarek, T. P. Maniecki, W. Ignaczak and W. Maniukiewicz, *Appl. Catal. A Gen.*, 2007, **326**, 17–27.

115 B. Hou, H. Zhang, H. Li and Q. Zhu, *Chinese J. Chem. Eng.*, 2012, **20**, 10–17.

116   G. K. Reddy, P. Boolchand and P. G. Smirniotis, *J. Phys. Chem. C*, 2012, **116**, 11019–11031.

117   A. Khan, P. Chen, P. Boolchand and P. Smirniotis, *J. Catal.*, 2008, **253**, 91–104.

118   K. Kandel, U. Chaudhary, N. C. Nelson and I. I. Slowing, *ACS Catal.*, 2015, **5**, 6719–6723.

119   M. J. Tiernan, P. A. Barnes and G. M. B. Parkes, 2001, 220–228.

120   J. Alan and D. M. Brian, *Tempature-Programmed Reduction for Solid Materials Characterization*, 1986.

121   J. Alan and D. M. Brian, *Temperature-Programmed Reduction for Solid Materials Characterization*, 1986.

122   X.-W. Liu, S. Zhao, Y. Meng, Q. Peng, A. K. Dearden, C.-F. Huo, Y. Yang, Y.-W. Li and X.-D. Wen, *Sci. Rep.*, 2016, **6**, 26184.

123   G. B. Raupp and W. N. Delgass, *J. Catal.*, 1979, **58**, 348–360.

124   J. W. Niemantsverdriet, a. M. Van der Kraan, W. L. Van Dijk and H. S. Van der Baan, *J. Phys. Chem.*, 1980, **84**, 3363–3370.

125   D. P. Johnson, *Solid State Commun.*, 1969, **7**, 1785–1788.

126   C. Trevisanut, M. Mari, J.-M. M. Millet and F. Cavani, *Int. J. Hydrogen Energy*, 2015, **40**, 5264–5271.

127   C. P. Rodrigues, P. C. Zonetti, C. G. Silva, A. B. Gaspar and L. G. Appel, *Appl. Catal. A Gen.*, 2013, **458**, 111–118.

128   D. He, Y. Ding, W. Chen, Y. Lu and H. Luo, *J. Mol. Catal. A Chem.*, 2005, **226**, 89–92.

129   C. Trevisanut, F. Bosselet, F. Cavani and J. M. M. Millet, *Catal. Sci. Technol.*, 2015, **5**, 1280–1289.

130   I. Chemicals, 2013.

131   C. S. S. R. Kumar, Ed., *Raman Spectroscopy for Nanomaterials Characterization*, Springer Berlin Heidelberg, Berlin, Heidelberg, 2012.

132   M. Schmal, D. V. Cesar, M. M. V. M. Souza and C. E. Guarido, *Can. J. Chem. Eng.*, 2011, **89**, 1166–1175.

133   T. W. Birky, J. T. Kozlowski and R. J. Davis, *J. Catal.*, 2013, **298**, 130–137.

134   T. Mathew, B. B. Tope, N. R. Shiju, S. G. Hegde, B. S. Rao and C. S. Gopinath, *Phys. Chem. Chem. Phys.*, 2002.

135   G.Busca, *Phys. Chem. Chem. Phys.*, 1999, **1**, 723–736.

136   L. Mattos and F. Noronha, *J. Catal.*, 2005, **233**, 453–463.

137   A. Boudjemaa, C. Daniel, C. Mirodatos, M. Trari, A. Auroux and R. Bouarab, *Comptes Rendus Chim.*, 2011, **14**, 534–538.

138   L. V. Mattos and F. B. Noronha, *J. Power Sources*, 2005, **152**, 50–59.

139   G. Busca, *Catal. Today*, 1996, **27**, 457–496.

140   M. C. Biesinger, B. P. Payne, A. P. Grosvenor, L. W. M. Lau, A. R. Gerson and R. S. C. Smart, *Appl. Surf. Sci.*, 2011, **257**, 2717–2730.

141   A. P. Grosvenor, B. A. Kobe, M. C. Biesinger and N. S. McIntyre, *Surf. Interface Anal.*, 2004, **36**, 1564–1574.

142   E. Hormilleja, P. Durán, J. Plou, J. Herguido and J. a. Peña, *Int. J. Hydrogen Energy*, 2014, **39**, 5267–5273.

143   J. R. Scheffe, M. D. Allendorf, E. N. Coker, B. W. Jacobs, A. H. McDaniel and A. W. Weimer, *Chem. Mater.*, 2011, **23**, 2030–2038.

144   K. S. Kang, C. H. Kim, K. K. Bae, W. C. Cho, S. H. Kim and C. S. Park, *Int. J. Hydrogen Energy*, 2010, **35**, 12246–12254.

145   L. Neal, A. Shafiefarhood and F. Li, *Appl. Energy*, 2015.

146   B. M. Corbella, L. F. De Diego, F. García-Labiano, J. Adánez and J. M. Palacios, *Energy & Fuels*, 2005, **19**, 433–441.

147   Z. Sarshar, Z. Sun, D. Zhao and S. Kaliaguine, *Energy & Fuels*, 2012, **26**, 3091–3102.

148   C. R. Alves, R. Aquino, J. Depeyrot, F. a. Tourinho, E. Dubois and R. Perzynski, *J. Mater. Sci.*, 2007, **42**, 2297–2303.

149   M. Banerjee, N. Verma and R. Prasad, *J. Mater. Sci.*, 2007, **42**, 1833–1837.

150   S. Yoon, *J. Magn. Magn. Mater.*, 2012, **324**, 2620–2624.

151   D. Carta, M. F. Casula, A. Falqui, D. Loche, G. Mountjoy, C. Sangregorio and A. Corrias, 2009, **4**, 8606–8615.

152   M. a Willard, Y. Nakamura, D. E. Laughlin and M. E. McHenry, *J. Am. Ceram. Soc.*, 1999, **82**, 3342–3346.

153   G. a. Sawatzky, F. Van Der Woude and a. H. Morrish, *Phys. Rev.*, 1969, **187**, 747–757.

154   G. a. Sawatzky, F. Van Der Woude and a. H. Morrish, *J. Appl. Phys.*, 1968, **39**, 1204–1205.

155   I. L. Stolyarchuk, I. V Vasylenko, Y. I. Pyatnitsky, P. E. Strizhak and P. Nauky, 2013, **49**, 172–177.

156   C. Lucarelli, G. Pavarelli, C. Molinari, S. Albonetti, W. Mista, D. Di Domenico and A. Vaccari, *Int. J. Hydrogen Energy*, 2014, **39**, 1336–1349.

ACKNOWLEDGMENTS

Personally, I think that 3 years of my research work was driven by 3 forces: perception, curiosity and uncertainty. That is why I would like to refer to the statements of two great men:

"Science is perhaps the only human activity in which errors are systematically criticized and, in time, corrected."
-- Karl Popper (philosopher)

"As far as the laws of mathematics refer to reality, they are not certain, and as far as they are certain, they do not refer to reality. "
-- Albert Einstein (theoretical physicist)

And, being inspired by the people who have contributed to the great discoveries, enabled me to *"reach the end" of the endless.*